

DIODE-LASER-BASED DIRECT-DETECTION DOPPLER WIND LIDAR

by

Luke Colberg

A proposal submitted in partial fulfillment
of the requirements for the degree

of

Doctor of Philosophy

in

Electrical Engineering

MONTANA STATE UNIVERSITY
Bozeman, Montana

February 2024

©COPYRIGHT

by

Luke Colberg

2024

All Rights Reserved

TABLE OF CONTENTS

1. INTRODUCTION	1
Overview of Doppler Wind Lidar	2
Measurement Techniques.....	3
Direct-Detection Doppler Wind Lidar	3
Edge Technique	4
Fringe-Imaging Technique.....	7
ALADIN (Atmospheric Laser Doppler Instrument)	10
Laser-Induced Fluorescence Technique.....	11
Heterodyne Doppler Wind Lidar	12
Millijoule-Pulse Heterodyne Doppler Wind Lidar	12
Microjoule-Pulse Heterodyne Doppler Wind Lidar	13
Continuous-Wave Heterodyne Doppler Wind Lidar	13
The MPD (MicroPulse Differential Absorption Lidar)	14
Statement of Objectives	16
2. BACKGROUND THEORY	17
The Optical Doppler Effect	18
Atmospheric Scattering.....	19
Molecular Scattering.....	19
Aerosol Scattering	21
The Double-Edge Technique	22
The Problem of a Two-Component Atmosphere.....	27
A Proposed Solution to the Problem of a Two-Component Atmosphere	27
Instrument Description	28
Potential Alternative Solutions	30
3. COMPLETED WORK.....	31
Laser Stabilization	31
Summary	31
Introduction.....	31
Design	32
Laser Enclosure	35
Rubidium Cell Enclosure	36
Servo Circuit	37
Results	38
Laser Transmitter and First-Stage Receiver	39
Summary	39

TABLE OF CONTENTS – CONTINUED

Introduction.....	39
TSOA Assembly.....	40
Axicon Assembly.....	41
T/R Assembly	43
Etalon Temperature Stabilization	44
Summary	44
Introduction.....	44
Mechanical Design.....	46
Electronic Design	50
Testing	51
Second-Stage Receiver.....	53
Summary	53
Introduction.....	53
Design	54
 4. RESEARCH PLAN	56
Instrument Development (February 2024 - June 2024).....	56
Laser Transmitter (February 2024 - May 2024).....	56
Temperature-Stabilized Etalon Mount (February 2024 - April 2024)	57
Lidar Receiver (February 2024 - May 2024).....	57
Assemble and Align the Lidar (May 2024 - June 2024)	58
Software Development (July 2024 - September 2025).....	58
Instrument Control and Data Acquisition Software (July 2024 - September 2024).....	58
Retrieval Algorithm (October 2024 - August 2025)	59
Testing and Validation (October 2024 - December 2025)	61
Testing and Troubleshooting (October 2024 - August 2025)	61
Horizontal Testing and Validation (September 2025 - Decem- ber 2025)	61
 5. PUBLICATIONS	62
Completed Publications	62
Planned Publications	64
 REFERENCES CITED.....	66
APPENDIX: List of Acronyms	85
APPENDIX: Laser Stabilization Solidworks Drawings.....	

TABLE OF CONTENTS – CONTINUED

APPENDIX: Transmitter Solidworks Drawings.....

APPENDIX: Temperature-Stabilized Etalon Mount Solidworks Drawings.....

APPENDIX: Second-Stage Receiver Solidworks Drawings.....

LIST OF FIGURES

Figure	Page
2.1 The Cabannes spectrum of air in the U.S. Standard Atmosphere at altitudes of 0 km (left), 5 km (center), and 50 km (right).....	21
2.2 The total scattering spectrum of air molecules and aerosol particles in the U.S. Standard Atmosphere at an altitude of 0 km with a backscatter ratio of 1.01 (left) and 2 (center and right). The scattering intensity is portrayed on a log scale in the plot to the right.....	22
2.3 A block diagram of a simplified double-edge receiver. The solid black lines are the atmospheric scattering spectra, the dot-dashed blue line is the transmission spectrum for etalon a, and the dotted red line is the transmission spectra of etalon b.....	23
2.4 Top: The atmospheric scattering spectrum, the etalon transmission spectra, and the signal strength at the detectors with zero LOS wind. The black solid line is the atmospheric scattering spectrum, the blue dot-dashed line is the transmission spectrum of etalon a, the red dotted line is the transmission spectrum of etalon b, and the shaded regions underneath the transmission spectra represent the portion of the atmospheric scattering signal that reaches the detector. Bottom: The same as the top plot with a $100\frac{m}{s}$ LOS wind (256-MHz Doppler shift) applied. The unshifted atmospheric scattering signal is shown as the black dashed line for reference.	24
2.5 A schematic of the DLB direct-detection DWL.	28
3.1 FMS control loop. The red arrows indicate optical paths, and the blue arrows indicate electrical signals. $\lambda/4$ = Quarter Waveplate, $\lambda/2$ = Half Waveplate, θ = Phase, BPF = Bandpass Filter, DBM = Double-Balanced Mixer, DBR = Distributed Bragg Reflector Laser, Det. = Detector, EOM = Electro-Optic Modulator, FP = FiberPort (Fiber Collimator), ISO = Faraday Isolator, LPF = Lowpass Filter, M = Mirror, PBS = Polarizing Beamsplitter, Rb = Rubidium, RF Amp. = Radio-Frequency Amplifier.	33

LIST OF FIGURES – CONTINUED

Figure	Page
3.2 Top-Left: The saturated absorption spectrum for ^{87}Rb near 780.246 nm. Top-Right: A close-up view of the top-left. Bottom-Left: The error signal generated by the FMS stabilization scheme. Bottom-Right: A close-up view of the bottom-left. The labeled hyperfine features are 1 :($F = 2, F' = 3$), 2 :($F = 2, F' = C2, 3$), 3 :($F = 2, F' = C1, 3$), 4 :($F = 2, F' = 2$), 5 :($F = 2, F' = 1$), 6 :($F = 2, F' = 0$).....	34
3.3 A photo of the laser enclosure.....	35
3.4 A photo of the rubidium cell enclosure.....	36
3.5 Left: The servo circuit diagram. Right: A photo of the servo inside the shielded electronic box.....	37
3.6 Left: A time-series plot of the beat note of two DBR lasers stabilized to adjacent crossover lines in the saturated absorption spectrum of rubidium [$^{87}Rb(5^2S_{1/2}, F = 2) \rightarrow (5^2P_{3/2}, F' = C1, 3)$ and $^{87}Rb(5^2S_{1/2}, F = 2) \rightarrow (5^2P_{3/2}, F' = C2, 3)$]. The blue line indicates the beat note frequency, the black dashed line indicates the mean beat note frequency of 82.2847 MHz, and the red dashed lines are frequencies 500 kHz greater and less than the mean. Right: A histogram of the time series. The beat note standard deviation was 97.226 kHz, indicating a laser stability of 68.749 kHz.....	38
3.7 The laser transmitter block diagram.....	39
3.8 A photo of the TSOA assembly.....	40
3.9 A photo of the axicon assembly.....	42
3.10 A photo of the T/R assembly.....	43
3.11 Left: A photo of the temperature-stabilized etalon mount prototype. Right: A SolidWorks drawing of the left, including a cross-sectional view.....	46
3.12 Left: A photo of the second stage of the temperature-stabilized etalon mount. Right: A SolidWorks drawing of the left, including a cross-sectional view.....	47

LIST OF FIGURES – CONTINUED

Figure	Page
3.13 Left: A photo of the second stage of the temperature-stabilized etalon mount and its heat sink interfacing with the lid of the first stage. Right: A SolidWorks drawing of the left, including a cross-sectional view.....	48
3.14 Left: A photo of the inner chamber of the first stage of the temperature-stabilized etalon mount. Right: A SolidWorks drawing of the left, including a cross-sectional view. The drawing is shown with the lid and the cover.....	49
3.15 Left: A photo of the second stage of the receiver inside the first stage of the temperature-stabilized etalon mount. Right: A SolidWorks drawing of the left, including a cross-sectional view. The drawing shows the first stage chamber without insulation.....	49
3.16 A block diagram of the temperature control electronics.....	51
3.17 The best temperature stability performance of the temperature-stabilized etalon mount. This test recorded a stability of 1.15 mK over 96 hours.....	52
3.18 The long-term drift of the temperature-stabilized etalon mount caused by mechanical drift.	53
3.19 The second-stage receiver block diagram.....	54

ABSTRACT

Researchers at Montana State University have developed diode-laser-based (DLB) lidar instruments to provide continuous vertical profiling for atmospheric science and weather forecasting. Lidar profiles are immensely valuable to atmospheric scientists because of the high resolution and continuity of the vertical profiles. The MicroPulse Differential Absorption Lidar (MPD) can provide continuous range-resolved profiles of thermodynamic parameters (water vapor and temperature) and aerosols. This work seeks to expand the suite of measurements by incorporating vertical wind speeds.

This document contains an introduction, a progress report, and a completion plan for designing, constructing, and testing the DLB direct-detection Doppler Wind Lidar (DWL). The DLB direct-detection DWL is based on a novel combination of the double-edge DWL and High Spectral Resolution Lidar (HSRL) techniques. This instrument is based on prior MPD designs, with modifications for measuring wind speeds. Two major additions to the MPD architecture are a frequency-stabilized laser transmitter and thermally-stabilized etalon mounts for a double-edge receiver. The laser transmitter and the double-edge receiver design and progress in constructing and testing them will be outlined. A research plan for completing the project will be proposed, including assembling the lidar, writing data acquisition software and retrieval algorithms, and validating the retrieved wind profiles compared to in-situ observations.

INTRODUCTION

In atmospheric science, the wind field describes the motion of air masses. It is a fundamental parameter for describing atmospheric circulation patterns, weather dynamics, and turbulent mixing processes. Wind velocity measurements are, therefore, necessary for all aspects of atmospheric science, including weather forecasting [1]. However, obtaining precise measurements of winds is particularly challenging in the planetary boundary layer (PBL), where most weather exists. In this lowest part of the atmosphere, the wind field is characterized by dynamic and turbulent air movements [2, 3]. The lower troposphere's wind field impacts various societal applications, including high-impact meteorology, climate modeling, air quality forecasting, renewable energy, and aviation, so obtaining these measurements is of high priority [4–8].

Tropospheric wind speed measurements can be made in situ by tracking the horizontal motion of ascending weather balloons or measuring wind speeds with aircraft. However, in-situ wind field measurements have limitations. Radiosondes from the global radiosonde network are launched only twice daily (00:00 and 12:00 UTC) from a spatially sparse network of radiosonde stations. Their infrequent launches make them unsuitable for capturing a dynamic wind field, and their spatial sparseness makes them unsuitable for capturing mesoscale- γ (2-20 km), mesoscale- β (20-200 km), and some mesoscale- α (200-2000 km) phenomena. In-situ measurements by airplanes are effective at sampling the wind field near airports or in targeted campaigns. However, the cruising altitude of airplanes is in the upper troposphere (9 to 12 km), so most observations are far above the dynamic PBL and airplane-based campaigns are too expensive for regular use. Remote-sensing techniques provide a promising alternative to address these limitations, as they can provide continuous vertical profiles of the wind field.

Tropospheric wind speeds can be measured with a high resolution through several remote-sensing technologies, including Doppler Wind Lidar (DWL), Doppler radar, and sodar (sonic detection and ranging). These instruments all rely on observing the Doppler effect caused by the motion of atmospheric molecules and particles. In all cases, the instrument emits a wave (light, radio, or sound) into the atmosphere and observes the frequency of the Doppler-shifted return signal. The observed frequency shift can be converted to the line-of-sight (LOS) wind speed (the vector component of wind along the vector

of the transmitted wave). All these instruments are valuable for atmospheric research, depending on the specific research goals. DWLs stand out for their ability to provide wind field measurements with high temporal and spatial resolution in clear atmospheric conditions. These high-resolution measurements can resolve the rapidly changing wind field in the troposphere, making these observations helpful for refining and validating atmospheric models.

The following section provides a literature review of DWLs and their measurement techniques. It also reviews the Diode-Laser-Based (DLB) MicroPulse Differential absorption lidar (MPD), from which the instrument described in this document—the DLB direct-detection DWL—receives its heritage. The introduction will conclude with a statement of objectives for the proposed dissertation.

Overview of Doppler Wind Lidar

Optical remote sensing with DWL instruments is a powerful method for observing the 3-dimensional wind field in the atmosphere. Lidar instruments function by sending light toward a target or volume of targets—such as air molecules or aerosol particles—and detecting a scattered return signal [9]. The electromagnetic radiation from the transmitted light wave illuminates the target, whether a single atom, molecule, or solid/liquid particle. The incident electromagnetic radiation accelerates charged particles within the target and sets them into oscillatory motion. Charged particles emit electromagnetic radiation when accelerated, and this secondary radiation is the scattered light [10].

In elastic scattering, the most common type of scattering in the atmosphere, the scattered radiation is at the exact frequency as the incident radiation from the perspective of the scattering target. However, if the scattering target moves with respect to the observer (the lidar instrument), the scattered radiation will appear to have shifted in frequency from the observer's perspective. This apparent frequency shift is known as the optical Doppler effect. DWLs leverage this effect to measure the wind field. In DWLs, the targets are a volume of air molecules and aerosol particles that move at an average velocity equal to the wind velocity. Therefore, the average Doppler shift from these targets can be measured and converted to the LOS wind speed. A more complete discussion of the optical Doppler effect will be presented in Chapter 2.

The wind field is a vector field composed of three orthogonal components. It can also be described by a vertical wind velocity (positive for an updraft), a horizontal wind speed, and a

horizontal wind direction. An upward-pointing DWL can observe the vertical component of the vector field. The lidar must use multiple views with horizontal components to determine the horizontal wind speed and direction, achieved by scanning the transmit beam. The wind-velocity vector can be determined at some altitude by observing multiple (at least three) LOS components of the wind vector at that same altitude.

Different implementations of the DWL technique allow wind-field measurements in different levels of the atmosphere, ranging from the surface layer (10 m) to the lower thermosphere (105 km) with varying temporal and spatial resolutions. DWL instruments can generally be separated into direct-detection and heterodyne DWLs. Direct-detection DWLs rely on direct observations of the lidar signal, whereas heterodyne DWLs measure the frequency and phase of the backscattered signal. Heterodyne DWLs are commonly known as coherent DWLs. However, all DWL instruments coherently detect a Doppler shift, not just those that use the heterodyne technique. Notable reviews of DWL instruments can be found in Werner [11], Reitebuch [12], Reitebuch and Hardesty [13], and Shangguan et al. [14].

The following literature review summarizes DWL instruments, focusing on direct-detection DWL, particularly emphasizing the double-edge technique used by the DLB direct-detection DWL. Heterodyne DWL will be covered sparingly. This literature review will provide a background of the existing technologies, providing context for the DLB direct-detection DWL.

Measurement Techniques

Direct-Detection Doppler Wind Lidar

A direct-detection DWL is a wind speed measuring instrument that relies on observing the intensity of the returning lidar signal. These instruments use some type of spectrometer as a frequency-discriminating element. Benedetti-Michelangeli et al. [15] made the first lidar-based wind speed measurements in 1972 using a direction-detection DWL that incorporated a scanning Fabry-Pérot interferometer. This DWL observed the radial wind speed within a single range bin (300 m wide at an altitude of 750 m) by gating the interferometer. Subsequently, Eloranta et al. [16] demonstrated a wind speed measuring lidar in 1975, which tracked the speed of inhomogeneities in aerosol profiles, utilizing them as tracers for the LOS wind speeds. Since then, several methods have been developed to measure vertical wind profiles continuously.

Noteworthy direct-detection techniques for profiling winds include the edge (filter), fringe-imaging (interferometric), and laser-induced fluorescence (LIF) techniques, each of which will be described further. Additionally, ALADIN (Atmospheric LAser Doppler INstrument), a satellite-based instrument that combines the edge and fringe-imaging techniques, will be explored. Among these methods, the double-edge technique, a specific implementation of the edge technique, and the fringe-imaging technique stand out for their ability to measure winds in the troposphere with high precision. Modeling studies show that they have nearly identical performance in the lower troposphere [17–19]. The edge technique can also profile winds up to an altitude of 80 km. The LIF technique, on the other hand, is restricted to altitudes from 80 to 105 km.

Edge Technique The edge technique uses one or more narrowband filters (NBFs) and measures the transmitted signal strength through these filters. The spectral filters can be either Fabry-Pérot etalons or atomic-vapor absorption filters. The laser frequency is positioned on the steep slope of the transmission spectrum of the filter, so a Doppler shift causes large changes in transmission through the filter. In the single-edge technique, the laser frequency is tuned to the sideline of either an etalon or an atomic vapor filter. In the commonly used double-edge technique, two etalons are tuned to place their peaks above and below the laser frequency. The double-edge technique can also be achieved with an atomic vapor filter by transmitting two laser wavelengths (one on each side of the spectrum) or by Zeeman-splitting the absorption feature by applying a strong magnetic field.

The first double-edge wind speed measurements were made by a group at OHP (Observatoire de Haute-Provence [Haute-Province Observatory]) [20, 21]. This lidar, operating at 532 nm, was designed to observe radial wind speeds in the middle stratosphere to the middle mesosphere (ranging from 25 to 60 km). This lidar relied on the molecular backscatter signal and could not operate in parts of the atmosphere containing aerosols.

Another early edge DWL was created by a group at NASA (National Aeronautics and Space Administration). In a modeling paper, Korb et al. [22] modeled a DWL using an etalon in the single-edge technique and a transmitted wavelength of 1064 nm. They found that for a 20-m vertical resolution and a 100-shot average, the radial wind speeds could be retrieved with a precision of $0.2 \frac{m}{s}$ below 2 km and $0.5 \frac{m}{s}$ below 5 km. This lidar was created, and it measured wind speeds with a precision of $0.11 \frac{m}{s}$ for a 500-shot average and a 22-m vertical resolution at night. The instrument relied on the presence of aerosols [23].

In the late 90s, a series of modeling papers explored the double-edge technique using etalons as filters based on the harmonic wavelengths of the Nd:YAG laser (i.e., 1064 nm, 532 nm, and 355 nm) [17, 19, 24, 25]. The consensus was that the double-edge technique was superior to the single-edge technique due to an increased sensitivity to small frequency shifts. Also, these studies found two clear options for creating a double-edge DWL with a Nd:YAG laser: a 355-nm lidar that primarily uses backscatter from molecules and a 1064-nm lidar that primarily uses backscatter from aerosols. In the stratosphere and mesosphere, a 532-nm that primarily uses backscatter from molecules could be advantageous over a 355-nm lidar due to the lower optical depth and signal attenuation of the 532-nm wavelength. The etalons for the 355-nm and 532-nm lidar should be carefully designed so that the wind speed retrieval is insensitive to the presence of aerosols, and the etalons for the 1064-nm lidar should be designed so that the wind speed retrieval is insensitive to molecular scattering. This desensitizing involves careful optimization of the etalon parameters and the offset between the etalons and the emitted wavelength.

After the Mount Pinatubo eruption sent a plume of volcanic ash 35 km into the atmosphere in 1991, the pure molecular scattering assumption was no longer valid in the stratosphere. Consequently, the molecular signal of the OHP lidar was contaminated by aerosol scattering, rendering the lidar unable to retrieve accurate winds in the stratosphere. To address this, the OHP group redesigned their etalons to minimize the sensitivity of the wind speed retrieval to the presence of aerosols [26, 27]. This lidar used a double-Fabry-Pérot cavity featuring two mirrors, where one-half of one of the mirrors has a step coating deposited on it. This step coating creates two apertures, where each sub-aperture has a slightly different path length, creating two edge filters. In a recent paper by Khaykin et al. [28], the OHP group reports wind speed measurements from 5 to 75 km with a random error of $6 \frac{m}{s}$ at the top of the stratosphere (~ 50 km) with a spatial resolution of 1 km and an averaging time of 5.5 hr at night. These impressive results are made possible by a frequency-doubled Nd:YAG laser sending 800-mJ pulses into the atmosphere at 30 Hz and three 50-cm diameter telescopes (one for each pointing direction).

A group at NASA Goddard developed a mobile double-edge DWL at 355 nm [29] called the Tropospheric Wind Lidar Technology Experiment (TWiLiTE) as part of the Goddard Lidar Observatory for Winds (GLOW). This lidar utilized a triple-Fabry-Pérot interferometer with two parallel mirrors, one having three sub-apertures with slightly different lengths created by depositing small-step reflective coatings. Two sub-apertures create the double-edge receiver, and the third is a locking channel that allows active laser locking to the etalons.

The details of this interferometer are given by Gentry et al. [30]. A ground-based mobile version of TWiLiTE was validated compared to radiosondes in 2002 [31], which led to the development of an airborne system [30].

A group at the University of Science and Technology of China (USTC) created a pair of double-edge DWLs. The first instrument emitted a 1064-nm wavelength, relied exclusively on the aerosol backscatter signal, and could retrieve wind speeds with a standard deviation between the lidar and radar measurements of $0.45 \frac{m}{s}$ for a 100-m range bin and a 30-min averaging time [32] below 2.5 km. A second instrument was created to profile winds using molecular backscatter [33]. It used 355-nm light, a triple-Fabry-Pérot interferometer similar to TWiLiTE, and a three-telescope transmitter similar to the OHP group. This lidar can profile winds from 15 to 60 km with random errors of less than $7.6 \frac{m}{s}$ at 60 km with a temporal resolution of 30 min. Observational experiments agreed closely with the European Center for Medium-Range Weather Forecasting (ECMWF) models [34].

An alternative solution to using etalons as narrowband transmission filters is atomic-vapor absorption filters as notch filters. In a pair of modeling papers, She et al. [35, 36] compared double-edge DWLs using Fabry-Pérot etalons with single-edge filters based on iodine absorption filters, like the ones used in the University of Wisconsin High Spectral Resolution Lidar (HSRL) system [37]. The major advantage of the absorption filter is that an atomic transition determines the frequency of the spectrometer, which is absolutely stable. In contrast, the frequency of an etalon is determined by mirror spacing, requiring precise stabilization methods. She et al. found that a DWL using a double-edge etalon at 1064 nm outperforms one using an iodine filter for high aerosol loading, and a DWL using a double-edge etalon operating at 355 nm outperforms one using an iodine filter for pure molecular scattering. However, the iodine-filter lidar had good performance for high and low aerosol loading, allowing it to operate at all atmospheric altitudes, unlike the double-edge DWLs [36].

Researchers from the Ocean University of Qingdao and Colorado State University (CSU) developed lidars based on iodine absorption cells operating at 532 nm [38–40]. These lidars were unique in that they could simultaneously measure the aerosol-to-molecular backscatter ratio and the LOS wind speed. These measurements were achieved by alternating the transmitted laser frequency to the center of the absorption band and the sideline. When the laser was tuned to the center of the absorption band, the receiver measured the backscatter ratio using the HSRL technique [37, 41]. When the laser was tuned to the sideline of the absorption band, the receiver could measure the LOS wind speeds with the edge technique.

This simultaneous measurement of the backscatter ratio and LOS wind speeds allows the iodine filter DWL to operate in regions with high or low aerosol loading. Liu et al. [40] report wind speed measurements from 100 m to 15 km at night and 100 m to 12 km during the day with a vertical resolution of 136 m and a temporal resolution of 30 min. The lidar was compared to radiosonde profiles, and it was found that the standard deviation between the measurements was $3.1 \frac{m}{s}$ at night and $3.2 \frac{m}{s}$ during the day.

Several other iodine-filter-based DWLs have been created for high-altitude wind speed profiling, including one at the Arecibo Observatory [42] and another at ALOMAR (Arctic Lidar Observatory for Middle Atmosphere Research) [43]. The one at Arecibo can measure winds from 18 to 45 km with a 1.5-km vertical resolution and a 20-min temporal resolution. The lidar at ALOMAR can profile temperature and winds from 30 to 80 km. With a temporal resolution of 2 hr and a vertical resolution of 2 km, the random wind speed error at 49 km and 80 km is $0.6 \frac{m}{s}$ and $10 \frac{m}{s}$, respectively. These impressive results were achieved using two lasers with a mean power output of 14 W, each transmitted through two telescopes with 1.8-m diameter primary mirrors.

A group at CSU created a double-edge filter by placing a sodium vapor cell in a strong permanent magnet [44]. The magnetic field induced Zeeman splitting in the absorption filter, with each half absorbing one of the circularly polarized states of light. This filter had the advantage of the natural stability of atomic vapor cells and increased sensitivity provided by the double-edge technique. The filter was integrated into the receiver of a three-frequency sodium lidar, typically used for a LIF lidar (see LIF Technique), and simultaneously retrieved wind, temperature, and aerosol-to-molecular backscatter ratio from 5 to 50 km. With a 60-min integration time and a 1-km vertical resolution, reliable temperature and wind speed measurements close to modeled values were retrieved from 10 to 45 km [45].

Fringe-Imaging Technique The fringe-imaging technique uses an interferometer to measure LOS wind speeds. This technique can be achieved by interfering beams using many waves, such as in a Fabry-Pérot or Fizeau interferometer, or by splitting into two waves and interfering them together, as in a Mach-Zehnder or a Michelson interferometer. With a constant path length in the interferometer, any changes in the phase and, therefore, the spatial pattern of the inference fringes can be related to a change in the frequency of the backscattered light and converted to LOS wind speeds. The molecular backscatter signal has a short coherence length (a few centimeters). In contrast, the aerosol backscatter signal has a coherence length approximately equal to that of the laser (up to tens of meters). Therefore,

in an interferometer optimized for aerosols (i.e., one with a path difference greater than 10 cm), the molecular signal is not resolved and does not create fringes, adding only an offset. This property allows an interferometric lidar to use aerosol backscatter only or aerosol and molecular backscatter to retrieve LOS wind speeds.

The first fringe-imaging DWLs were demonstrated by a group at the Space Physics Research Laboratory (SPRL) at the University of Michigan [46–48]. The early versions of their instrument used a pulsed Nd:YAG laser at 532 nm with a $1\text{-}\mu\text{s}$ pulse length, a 50-Hz repetition rate, and an average power of 3 W. Daytime measurements were achieved using a high-resolution Fabry-Pérot interferometer that resolved the backscattered signal from aerosols. The interferometer was an optically contacted plane etalon (i.e., a plane etalon with the plates held in a monolithic structure) in a pressure-controlled canister filled with dry nitrogen. The receiver could be adapted to measure winds using the molecular signal by changing the bandwidth of the etalon. For an averaging time of 4 min, this lidar showed errors of less than $2 \frac{m}{s}$ compared to radiosondes below 1.5 km.

Notably, this group was also the first to use charge-coupled devices (CCDs) to detect the spatial changes in the fringe pattern [49], now commonplace in fringe-imaging DWLs. They created a system operating at 355 nm that captured both aerosol scattering and molecular scattering by recapturing light reflected off of the aerosol-discriminating Fabry-Pérot interferometer and passing that through a broader bandpass Fabry-Pérot interferometer. They also picked off a tiny amount of the outgoing laser light and sent it through the receiver as a reference to observe instrument biases. This 355-nm lidar had an error of less than $0.5 \frac{m}{s}$ for a 3.5-min averaging time in the lowest 6 km of the atmosphere but required calibration to radiosonde profiles to remove a systematic bias.

In modeling papers, McKay [17, 18] and McGill and Spinhirne [19] demonstrated that a fringe-imaging system with a Fabry-Pérot interferometer had a much greater dynamic range than a comparable double-edge system, and had similar errors while operating within the PBL. McKay also modeled a Fizeau interferometer in a fringe-imaging system [50]. He found that it had practical advantages compared to a Fabry-Pérot interferometer, like its linear fringe pattern, but required a much smaller field of view (25 μrad for a Fizeau interferometer compared to 120 μrad for a Fabry-Pérot interferometer). The ALADIN lidar successfully implemented a Fizeau wedge in their aerosol interferometer (see the ALADIN section).

Liu and Kobayashi modeled a Mach-Zehnder interferometer for retrieving winds using the aerosol signal [51], and Bruneau modeled the performance of a Mach-Zehnder interferometer for retrieving winds with the molecular signal [52]. Both papers found that wind speed measurements with a Mach-Zehnder interferometer have a lower error than that of a Fabry-Pérot interferometer in the shot noise limit. Bruneau and Pelon further expanded on using Mach-Zehnder interferometers and modeled that they can be used to measure aerosol backscatter and extinction [53]. They estimated that wind speeds with an error of 0.5 $\frac{m}{s}$ could be made in the PBL with a 355-nm airborne DWL featuring a Mach-Zehnder interferometer with a 50-cm optical path difference when averaged over 100 shots and using a 500-m vertical resolution. In another modeling study, Cezard found that a Michelson interferometer can be optimized to retrieve wind speeds from aerosols or molecules. While they are 50% less efficient than a Mach-Zehnder interferometer, Michelson interferometers are more straightforward to build [54].

Bruneau et al. [55] demonstrated the first wind speed measurements using a Mach-Zehnder interferometer. They used the OHP double-edge DWL [26, 27] and split the received light 50/50, with 50% going to the double-edge receiver and 50% going to the Mach-Zehnder interferometer. The Mach-Zehnder interferometer made accurate wind speed measurements (compared to the double-edge receiver) with half the noise of the double-edge receiver (during nighttime measurements) between 10 and 40 km. However, it was sensitive to the presence of aerosols. More recently, this work continued into the LNG (Lidar aérosols Nouvelle Génération [Next-Generation aerosol Lidar]) group's 355-nm HSRL, which can measure aerosol backscatter, extinction, and wind speeds [56]. This lidar features a quadrature Mach-Zehnder interferometer made of fused silica and utilizes a zero-wind reference for bias correction. It can measure wind speeds in favorable conditions with a precision of 1 to 2 $\frac{m}{s}$.

A state-of-the-art fringe-imaging DWL that uses a Mach-Zehnder interferometer is represented by the Optical Autocovariance Wind Lidar (OAWL) [57]. OAWL features a field-widened, quadrature Mach-Zehnder interferometer. It uses a tiny portion of the outgoing laser pulse as a frequency reference, so the laser does not need to be stabilized to the interferometer. Also, the optical path difference of the interferometer can vary between pulses without signal degradation, making OAWL ideal for airplane- or satellite-based operation. The interferometer is designed so that the optical path difference is the same for any ray entering the system, regardless of angle. This field widening allows the system to use light scattered from wide angles, which occurs in the region of incomplete overlap. Additionally,

the OAWL interferometer can be adapted for retrieving winds from the aerosol signal or the molecular signal by changing the optical path difference of the Mach-Zehnder interferometer. The OAWL receiver can also operate at any laser wavelength, adding flexibility.

OAWL instruments have shown close agreement to heterodyne DWL, radar wind profilers, and dropsondes in validation campaigns. During the Green OAWL (GrOAWL) (an OAWL operating with a Nd:YAG laser at 532 nm) airborne performance and validation, it retrieved wind speeds with mean biases under $0.1 \frac{m}{s}$ and an R^2 value exceeding 0.9 for 2-min-averaged profiles in comparisons to dropsondes [58].

Another interferometric DWL is being built by a group at DLR (Deutsches Zentrum für Luft- und Raumfahrt [German Aerospace Center]) for profiling winds in the near field (50-300 m) in front of aircraft for a control system to preemptively react to turbulence observed by the lidar [59, 60]. It operates at 355 nm and features a monolithic field-widened Michelson interferometer. Like OAWL, this lidar captures a small fraction of the outgoing laser pulse and uses it as a zero-wind speed reference. A demonstrator prototype for this lidar was compared to a Vaisala/Leosphere WindCube. The random wind error of the demonstrator was found to be as low as $0.4 \frac{m}{s}$ to $0.65 \frac{m}{s}$ at 50 m and 76 m for a 40-pulse average and a 30-m range resolution with no significant slope error.

ALADIN (Atmospheric Laser Doppler Instrument) ALADIN, a satellite-based direct-detection DWL created by ESA (European Space Agency) under the Atmospheric Dynamics Mission-Aeolus (ADM-Aelous) [61–63], marked a significant milestone as the first DWL in space and the first instrument capable of profiling atmospheric winds on a global scale. Before ADM-Aeolus, limited observations of the atmospheric wind fields in the southern hemisphere, above the oceans, and in the stratosphere hindered numerical weather prediction (NWP) and climate modeling [64, 65].

ALADIN employs a sophisticated setup combining the double-edge and fringe-imaging techniques, leveraging two spectrometers, the Rayleigh and the Mie, which use backscatter from molecules and aerosols, respectively [66]. The signal is first incident on the Mie Spectrometer, a Fizeau wedge that acts as a notch filter, which allows the narrowband aerosol signal to pass and analyzes wind speeds from aerosols (Mie winds) using the fringe-imaging technique. The molecular signal is reflected off the Mie Spectrometer, split, and passed through the Rayleigh Spectrometer, a Fabry-Pérot cavity, with each beam taking a different path through the etalon, effectively creating a double-edge filter. This signal is analyzed to determine wind speeds from the molecular backscatter signal (Rayleigh winds).

Using aerosol and molecular signals to determine wind speeds allows ALADIN to retrieve wind speeds in the aerosol-dense PBL up to an altitude of about 30 km. The synergy between these techniques also significantly increases the receiver efficiency. Individually, each method would only use a fraction of the return signal.

During a pre-flight validation campaign, the Airborne ALADIN Demonstrator (A2D) [66, 67], a prototype mirroring the ALADIN design but with a smaller telescope, demonstrated wind speed retrievals with systematic errors of less than $0.5 \frac{m}{s}$ and random errors of $1.5 \frac{m}{s}$ for the Mie spectrometer and $2.7 \frac{m}{s}$ for the Rayleigh spectrometer [68]. Algorithmic corrections and additional quality control reduced these errors to $1.5 \pm 0.3 \frac{m}{s}$ for both spectrometers [69].

Upon its launch in 2018, ALADIN demonstrated its capability to take wind speed measurements on a global scale. Initial mission results showed higher random error than the mission requirements [70, 71]. Subsequently, an extensive post-launch validation campaign was conducted, comparing ALADIN’s wind speeds to various instruments (e.g., [69, 72, 73]). Many error sources were mitigated through algorithm correction and quality control (e.g., [74, 75]). Evaluations conducted by Rennie et al. [76], Laroche and St-James [77], and Garrett et al. [78] indicate that ALADIN’s profiles have a significant positive impact on NWP models, specifically in the tropical upper troposphere and lower stratosphere, the polar troposphere, and in predicting the steering currents of tropical cyclones.

Laser-Induced Fluorescence Technique In the upper atmosphere, layers of metal ions, including sodium, potassium, and iron, are deposited by meteoric ablation, form consistent layers from 80 to 105 km in the mesopause and lower thermosphere. Below this, the air density is too high, and the ions react with other atmospheric constituents. The LIF technique can observe the presence of the ions and, by observing the spectrum of the return signal, measure temperature and LOS wind speeds [79].

In this technique, a laser is precisely tuned to a spectral line of the metal constituent. The ions absorb the incident laser light, and the lidar detects the subsequent fluorescent re-emission. The absorption cross-section for resonant absorption in metal ions significantly exceeds non-resonant molecular scattering (by 15 orders of magnitude), resulting in a much higher signal from metal resonant scattering compared to non-resonant molecular scattering (by 5 orders) in the mesopause [80]. Temperatures can be observed by measuring the Doppler broadening of the fluorescent re-emission spectrum, and LOS wind speeds can be observed by measuring the Doppler shift.

A cutting-edge instrument that utilizes the LIF lidar technique is the CSU Sodium lidar [81, 82]. This technology can profile temperature and wind in the mesopause region during daytime and nighttime and has been widely replicated. The CSU Na Lidar emits three frequencies on and near the peak of the sodium D2 line (589 nm) and employs multiple telescopes to observe the horizontal wind components. During the day, it utilizes an ultra-narrow Faraday filter to remove the solar background.

LIF lidars have proven effective for long-term monitoring of temperature and winds in the mesopause and lower thermosphere region. These observations are particularly valuable because the only in-situ observations from this region are from rocket soundings. LIF lidars have been instrumental in observing various phenomena, including long-term changes in the mesopause, mesosphere and lower thermosphere tidal waves, and anomalies in wind and temperature caused by geomagnetic storms [83].

Recently, signals have been retrieved from iron ions up to 170 km, calcium ions up to 200 km, and helium ions up to 700 km, indicating that LIF lidars have the potential to extend temperature and wind profiling into the upper thermosphere [84].

Heterodyne Doppler Wind Lidar

Heterodyne DWL instruments are based on an optical heterodyne technique, where the return signal is mixed with a local oscillator beating at the same (homodyne) or similar (heterodyne) frequency as the emitted wavelength. This mixing results in a beat note between the backscattered atmospheric signal and the local oscillator. Homodyne detection cannot differentiate between positive and negative LOS wind speeds, so the heterodyne technique is almost always used. Heterodyne DWL instruments rely on the presence of aerosols, as the molecularly backscattered signal is too broad to be resolved in a heterodyne detection system. A detailed exploration of heterodyne DWLs is outside of the scope of this review, and they will be covered here sparingly. In general, heterodyne DWL can be classified into high-powered pulsed instruments (mJ-pulse energy), low-powered pulsed instruments (μ J-pulse energy), and low-powered continuous-wave (CW) instruments.

Millijoule-Pulse Heterodyne Doppler Wind Lidar High-powered pulsed heterodyne DWLs are generally used to measure phenomena where high temporal resolution is needed, like in airplane wake vortices or from high-altitude airplane-based platforms, where backscatter coefficients are low. A notable example is the DAWN (Doppler Aerosol WiNd) lidar system developed at NASA Langley [85–87]. This lidar is based on an injection-seeded Ho:Tm:LuLiF pulsed solid-state laser operating at $2.05 \mu m$, emitting 250-mJ pulses with a

5- to 10-Hz repetition rate. The CW seed laser also operates as the local oscillator. The $2\text{-}\mu\text{m}$ wavelength allows eye-safe operation. In ground-based testing, DAWN showed close agreement with radiosondes, with residuals of $1.06 \frac{\text{m}}{\text{s}}$ and 5.78° for magnitude and direction [86]. In airplane-based testing, DAWN showed close agreement with dropsondes in regions of high aerosol loading [87]. DAWN can even retrieve winds in the free troposphere where aerosol loading is low from the tiny amount of aerosols there [72, 86].

Microjoule-Pulse Heterodyne Doppler Wind Lidar Low-powered pulsed heterodyne DWLs are commercially available from companies like HALO Photonics and Vaisala/Leosphere. These instruments typically operate near $1.5 \text{ }\mu\text{m}$, leveraging the cost-effective photonics developed by the telecom industry. They operate at high pulse repetition rates of 10-20 kHz and pulse energies of 50-100 μJ . Halo Photonics Streamline DWLs are deployed at Atmospheric Radiation Measurement (ARM) facilities [88]. A study comparing the Streamline DWLs with sonic anemometers 400 m from the lidar found an R^2 coefficient greater than 0.96, a standard deviation of $0.413 \frac{\text{m}}{\text{s}}$, and biases of $5.8 \frac{\text{cm}}{\text{s}}$. In a comparison study with radiosondes, Leosphere (now Vaisala) WindCubes showed an R^2 coefficient between lidar and radiosonde observations of 0.99 from 500-1325 m altitude for a 75-m range resolution and a 10-min averaging time [89]. These instruments can make meteorological-quality observations of wind speed and direction within the PBL. Due to their commercial availability and cost-effectiveness ($\sim \$250\text{k}-\400k), low-powered pulsed heterodyne DWLs have been widely deployed in networks (e.g., [90, 91]) and field experiments (e.g., [92–94]).

Continuous-Wave Heterodyne Doppler Wind Lidar CW heterodyne DWL instruments excel at short ranges, providing high-temporal-resolution winds close to the lidar instrument. Profiles can be obtained by scanning the focus of the telescope. The lidar will measure the wind speed at the telescope's focus, as the wavefront can be matched with the local oscillator at that range. The wavefront at other ranges is not matched with the local oscillator wavefront and, therefore, is not resolved. These systems are commercially available (e.g., METEK GmbH and ZX) and have been used widely by the wind energy industry. The limitation of this system is the poor range resolution at long ranges. For example, the Wind Scout from METEK has a range resolution of 0.16 m at 10 m, 16 m at 100 m, and 1.6 km at 1 km [95].

The MPD (MicroPulse Differential Absorption Lidar)

A team of researchers at Montana State University (MSU) and the National Center for Atmospheric Research (NCAR) has developed an innovative lidar system called the MicroPulse DIAL (MPD). This lidar architecture uses cost-effective DLB technology, enabling continuous and long-term vertical profiling of atmospheric thermodynamics (water vapor and temperature) through the Differential Absorption Lidar (DIAL) technique [96]. The MPD instruments can also employ the High Spectral Resolution Lidar (HSRL) technique [41] to profile aerosols. Additionally, this lidar uses the micro-pulse technique [97, 98], enabling eye-safe operation. The DLB design makes MPD instruments particularly well-suited for extended deployment, and they have demonstrated over a year of continuous operation with minimal downtime.

Early versions of the MPD were created by a team of researchers at MSU, utilizing the DIAL technique to profile water vapor. Details about these instruments can be found in Nehrir et al. [99], Nehrir et al. [100], and Nehrir et al. [101]. These laboratory prototypes demonstrated impressive accuracy from a low-powered instrument. Recognizing the MPD's potential, a collaboration with researchers at NCAR was formed, and a field-deployable fourth-generation instrument was developed, as detailed in Repasky et al. [102] and Spuler et al. [103]. The fourth-generation MPD was validated compared to radiosondes and other water vapor profiling instruments [104]. A network of five of these MPDs was created and is available to the research community. Further information about the latest version of the MPD instruments can be found in Spuler et al. [105] and Spuler et al. [106].

The MPD architecture is flexible and can be adapted for measuring aerosols using the HSRL technique. A rubidium-based HSRL [107] and a potassium-based HSRL [108, 109] were created and demonstrated aerosol profiling. Temperature measurements were demonstrated using the DIAL technique and a temperature-sensitive oxygen absorption line. Details about the temperature retrieval can be found in Repasky et al. [110], with the initial demonstrations presented in Stillwell et al. [108].

At the time of writing, NCAR operates a network of five field-deployable instruments. Three instruments can profile water vapor, temperature, and aerosols, and two can only profile water vapor. Additionally, a laboratory instrument at MSU can profile temperature and aerosols.

The MPD aims to provide an instrument for implementing a network of thermodynamic profiling instruments with a spacing of about 125 km to address mesoscale forecasting needs [4, 5, 8, 111, 112]. The instruments must be cost-effective to achieve this horizontal spacing. A suitable technology must meet the following criteria:

1. delivers continuous and range-resolved thermodynamic profiling,
2. operates unattended for long periods of time,
3. operates without ancillary calibrations (i.e., to a radiosonde or radiometer) to keep operational costs low, and
4. poses no safety threat to the community.

Instruments with exceptional accuracy and precision do not address the forecasting needs as they are expensive and require high-powered, non-eye-safe lasers. The MPD, however, fulfills these requirements.

Recently, a direct-detection DWL was conceptualized using the MPD architecture [113]. The instrument described in this document corresponds to the one modeled in Repasky et al. [113], with additional details provided in the Instrument Description. If successful, this work would add kinematic profiling to the MPD system, enabling a low-cost thermodynamic and kinematic profiling instrument.

Furthermore, the DLB direct-detection DWL would be useful as a stand-alone instrument. While there are cost-effective, commercially available heterodyne DWLs for profiling winds within the PBL, most DWLs that can profile winds in the free troposphere are sophisticated and expensive research instruments, many of which cannot observe winds in the aerosol-dense PBL, and many others that are not eye-safe. Unlike the commercially available heterodyne DWLs, the DLB direct-detection DWL would be able to profile winds in the PBL and the lower free troposphere, which would make the DLB direct-detection DWL helpful in studies of PBL-free troposphere coupling and long-distance transport of aerosols and trace gases. Furthermore, the DLB direct-detection DWL would provide these measurement capabilities while maintaining cost-effectiveness and eye-safe operations, unlike the sophisticated direct-detection DWLs. These features allow the DLB direct-detection DWL to fill a niche between the commercially available heterodyne DWLs and the high-cost direct-detection DWLs.

Statement of Objectives

The objectives for his research effort are:

- **Objective 1 (Main Objective):** Develop and demonstrate a direct-detection DWL system for vertical wind profiling in the lower atmosphere based on the DLB MPD architecture.
- **Objective 2:** Develop technologies for advancing the MPD architecture and DLB lidar.
- **Objective 3:** Demonstrate scientific research capabilities by observing mixing heights with the DLB direct-detection DWL.

The remainder of this document is divided into four chapters. The Background Theory chapter will provide the background and context necessary to understand the work in this dissertation. Then, the Completed Work chapter will describe the work completed at the time of writing of this document. After that, the Research Plan will provide a plan for completing the objectives. Finally, the Publications chapter will list past and planned publications related to this work.

BACKGROUND THEORY

This chapter provides the background necessary for understanding the working mechanism for the DLB direct-detection DWL. Each section aims to explain a key topic. This chapter is structured as follows:

1. **The Optical Doppler Effect:** Providing an overview of the optical Doppler effect, foundational to all DWL instruments.
2. **Atmospheric Scattering:** Describing atmospheric scattering, focusing on the difference between the spectra from scattering by gaseous molecules and aerosol particles.
3. **The Double-Edge Technique:** Presenting the technique used by the DLB direct-detection DWL, the double-edge technique, and deriving the wind speed retrieval starting with the lidar equation.
4. **The Problem of a Two-Component Atmosphere:** Describing the difficulties of using the double-edge technique in a mixed atmosphere of gaseous molecules and aerosol particles (e.g., in the PBL).
5. **A Proposed Solution to the Problem of a Two-Component Atmosphere:** Offering a solution that combines the double-edge and HSRL techniques, solving the problem of a two-component atmosphere with greater efficiency than traditional double-edge receivers.
6. **Instrument Description:** Offering a description of the DLB direct-detection DWL design.
7. **Potential Alternative Solutions:** Discussing alternative solutions to the problem of a two-component atmosphere.

The Optical Doppler Effect

The Doppler effect refers to the perceived change in frequency of a wave due to the relative motion of the source and observer. When the source of the wave moves toward the observer, the wave appears to have a higher frequency, and vice versa if the source moves away. The Doppler effect is responsible for the apparent change in pitch of a siren as an ambulance rushes past a listener and the shifts in the spectra from distant stars.

In the optical Doppler effect, there is no distinction between a moving source and a moving observer, and only the relative velocity component along the vector between them matters. If a source emits light of frequency, f_0 , and the relative speed along the line of sight between the source and observer is v , then the observed frequency, f^* , is

$$f^* = f_0 \left(1 + \frac{v}{c}\right), \quad (2.1)$$

where c is the speed of light. The relative speed is defined so that a positive value indicates that the source and observer are moving together, leading to a higher observed frequency (i.e., a blueshift).

In nonresonant scattering (i.e., scattering away from a resonant absorption line), light emitted from and re-detected by a lidar system has two emission events with identical frequency shifts. The lidar emits light toward a target, and the frequency observed by the target is f^* . The charged particles in the target are accelerated, re-emitting light at f^* in the target's reference frame. The lidar observes a second Doppler shift, where the observed frequency, f , is

$$f = f^* \left(1 + \frac{v}{c}\right) = f_0 \left(1 + 2\frac{v}{c} + \left(\frac{v}{c}\right)^2\right). \quad (2.2)$$

The second-order term, $(\frac{v}{c})^2$, is negligible at the speeds of atmospheric winds, so the observed frequency can be approximated as

$$f = f_0 \left(1 + 2\frac{v}{c}\right). \quad (2.3)$$

Expressing the Doppler effect as the original frequency plus a frequency shift, known as the Doppler shift (i.e., $f = f_0 + \Delta f$, where $\Delta f = 2f_0 \frac{v}{c}$), allows for measurement of the LOS velocity between a lidar and a target through

$$v = \frac{1}{2} \Delta f \frac{c}{f_0} = \frac{1}{2} \Delta f \lambda_0, \quad (2.4)$$

where λ_0 is the transmitted wavelength ($\lambda_0 = \frac{c}{f_0}$).

In DWLs, the Doppler shift is small compared to optical frequencies. If a lidar emitting light with a wavelength of 780 nm (384.6 THz) is incident on a volume of air moving at 1 $\frac{m}{s}$ toward the lidar, the Doppler shift would be 2.56 MHz or 1 part in 150 million. Hence, DWLs must have a high spectral resolution and a stable transmitted laser frequency to detect such subtle frequency shifts.

Atmospheric Scattering

The two-component atmosphere model states that there are two primary types of scattering targets that light will interact with in the atmosphere: gaseous molecules and aerosol particles. When a volume of air contains both aerosols and molecules, the average frequency shift observed by the DWL is the Doppler shift caused by the wind speed. However, the frequency shift of a single scattered photon is determined by the motion of the individual scattering target, not the mean of a volume of targets. Consequently, the velocity distribution determines the spectrum of light scattered by a volume of targets.

In quiescent air at room temperature, air molecules exhibit thermal motion with mean speeds from 300 to 400 $\frac{m}{s}$. In contrast, aerosols move with Brownian motion with speeds usually below 1 $\frac{cm}{s}$. The width of the spectrum from aerosols in lidar is negligible compared to the linewidth of the transmitted laser. However, the broadening from the thermal motion of gaseous molecules cannot be neglected. Spectrally-resolving lidar instruments, including the DLB direct-detection DWL, require careful modeling of the molecular scattering spectrum for accuracy [114, 115].

Molecular Scattering

Witschas [116] and She [117] provide comprehensive overviews of molecular scattering in the atmosphere. The molecular scattering theory relevant to a DWL will be presented here.

In an ideal gas, individual molecular speeds follow a Maxwellian distribution determined by temperature. The molecules move in a random direction, resulting in a Gaussian distribution for LOS velocity. The spectrum of light scattered by these molecules is Doppler broadened according to the LOS velocity distribution. The Doppler broadening effect is purely elastic, meaning there is no frequency shift in the reference frame of the scattering target. However, in a real gas, inelastic scattering effects emerge due to interactions between the optical frequency, density fluctuations in the gaseous medium, and internal frequencies

of the molecule. These inelastic scattering effects include Brillouin, vibrational Raman, and rotational Raman scattering.

The largest source of inelastic scattering in the atmosphere is Brillouin scattering, which can be thought of as the beat of the optical frequency with pressure (sound) waves and entropy fluctuations within the molecules. Real gases at high pressure form a Brillouin triplet with a narrow central peak from entropy fluctuations and two broader Stokes (lower frequency) and anti-Stokes (higher frequency) shifted lines from pressure fluctuations.

While monoatomic molecules like Helium do not rotate or vibrate at their electronic ground state, diatomic (or multi-atomic) molecules like atmospheric nitrogen or oxygen do. Scattering from these vibrational or rotational motions is called Raman scattering, the second largest source of inelastic scattering in the atmosphere. Vibrational Raman scattering causes substantial wavelength shifts (hundreds of nanometers), which are filtered out before they get to the detector in a DWL. Similarly, the Stokes and anti-Stokes bands of rotational Raman scattering (ranging from 1-10 nm) are filtered out before the detector. However, the Q branch of rotational Raman, caused by small amounts of rotational energy within the rotational ground state, scattering causes frequency shifts smaller than the Doppler broadened spectrum's linewidth.

Doppler-broadening, Brillouin scattering, and the Q branch of rotational Raman scattering comprise the quasi-elastic molecular scattering spectrum that reaches the detector. Collectively, this spectrum is known as the Cabannes spectrum, often referred to as the Rayleigh-Brillouin Spectrum [117–119].

The Tenti-S6 model [120] is widely considered the most accurate representation of the Cabannes spectrum for atmospheric scattering. It requires the temperature, pressure, molecular mass, and transport coefficients of air as inputs. The Cabannes spectral lineshape for the U.S. Standard Atmosphere at several altitudes is shown in Figure 2.1. It resembles a Gaussian distribution with a flattened top at high pressures and becomes indistinguishable from a Gaussian distribution at low pressures.

Despite its ubiquity, the Tenti-S6 model has theoretical shortcomings [121]. Nevertheless, the spectra generated by the Tenti-S6 model closely match the observed spectra at the temperatures and pressures typically found in the atmosphere [122, 123], and the model is sufficient for highly accurate wind speed retrievals.

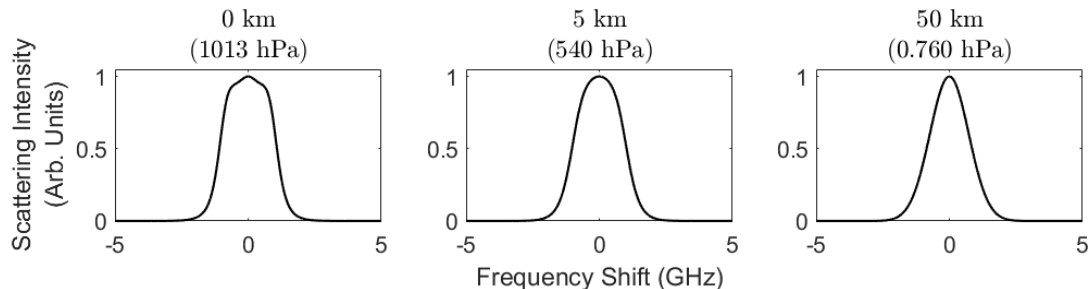


Figure 2.1: The Cabannes spectrum of air in the U.S. Standard Atmosphere at altitudes of 0 km (left), 5 km (center), and 50 km (right).

Aerosol Scattering

Aerosols are solid or liquid particles suspended in a gaseous mixture. Aerosols exhibit Brownian motion in quiescent air with velocities typically less than $1 \frac{\text{cm}}{\text{s}}$. The corresponding Doppler shift for a $1 \frac{\text{cm}}{\text{s}}$ LOS velocity at 780 nm is 25 kHz.

The Fourier-limited linewidth of a laser with a $1-\mu\text{s}$ square pulse is 1.2 MHz, and the measured CW linewidth of the lasers used in the MPD is about 1.4 MHz. The pulsed spectrum of the transmitter is approximately 1.84 MHz. Therefore, in quiescent air, the Doppler shift from aerosols compared to the linewidth of the laser is negligible, allowing the aerosol spectrum to be approximated as the laser linewidth.

Aerosols, suspended in air, move with the bulk velocity of the mixture. Their settling speeds are generally $\sim 1 \frac{\text{mm}}{\text{s}}$, so the backscattering spectrum of aerosols from the atmosphere can be approximated by the laser linewidth Doppler-shifted by the mean wind speed.

In the PBL, aerosol scattering is prevalent and cannot be neglected. It is useful to define a term describing the portion of backscatter that is caused by aerosols. The backscatter ratio as a function of range, defined as the ratio of the total backscatter (aerosols and molecules) to the backscatter from aerosols only, can be expressed as

$$B(r) = \frac{\beta_a(r) + \beta_m(r)}{\beta_m(r)}, \quad (2.5)$$

where r is the range, $B(r)$ is the backscatter ratio, $\beta_a(r)$ is the aerosol backscatter coefficient, and $\beta_m(r)$ is the molecular backscatter coefficient. The backscatter coefficient multiplied by the optical path length represents the probability that a photon is scattered backward.

The backscatter ratio at 780 nm can range from nearly 1 (pure molecular scattering) after intense precipitation or in the free troposphere to over 20 in thick forest-fire smoke

conditions. In Bozeman, MT, the backscatter ratio at 780 nm is generally between 1.5 and 3 in clear conditions within the PBL and approaches 1 in the free troposphere [124].

In an atmosphere with molecules and aerosols, the total atmospheric scattering spectrum is the superposition of the Cabannes spectrum and the aerosol spectrum, resulting in the total spectrum shown in Figure 2.2. The aerosol scattering spectrum, depicted as a Lorentzian function with a 2 MHz linewidth, appears like a sharp spike at the center of the molecular scattering spectrum. The plot to the left shows nearly pure molecular scattering, while the two plots to the center and right show a realistic backscatter ratio for the PBL. With a realistic backscatter ratio, the molecular scattering is distinguishable only when shown on a logarithmic scale. Although the spectrum in the left plot is unrealistic in the PBL, it effectively illustrates the narrow aerosol spectrum at the center of the molecular spectrum. It will represent the total atmospheric scattering spectrum in the remainder of this document.

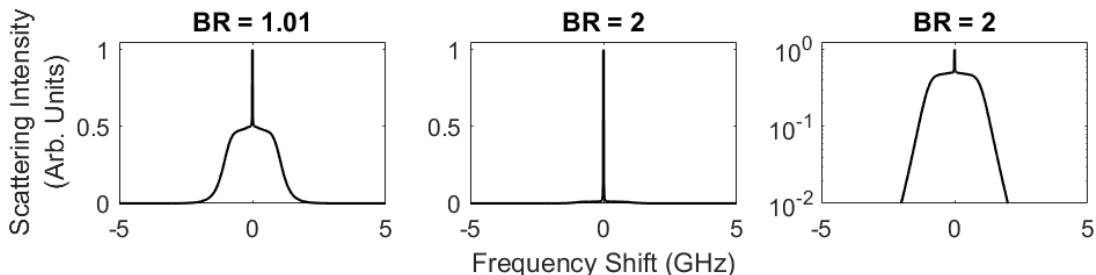


Figure 2.2: The total scattering spectrum of air molecules and aerosol particles in the U.S. Standard Atmosphere at an altitude of 0 km with a backscatter ratio of 1.01 (left) and 2 (center and right). The scattering intensity is portrayed on a log scale in the plot to the right.

In the two-component atmosphere, the magnitude of the molecular scattering spectrum can be accurately modeled. On the other hand, the magnitude of the aerosol spectrum varies widely and changes rapidly, and it can only be found through measurement.

The Double-Edge Technique

A simplified block diagram of a double-edge receiver using etalons as filters is shown in Figure 2.3. In the classic double-edge technique, the lidar signal is split into two components by a 50/50 beam splitter, each of which is passed through a spectrally-discriminating filter

(etalons in Figure 2.3). Detectors behind each filter measure the atmospheric scattering spectrum that passes through.

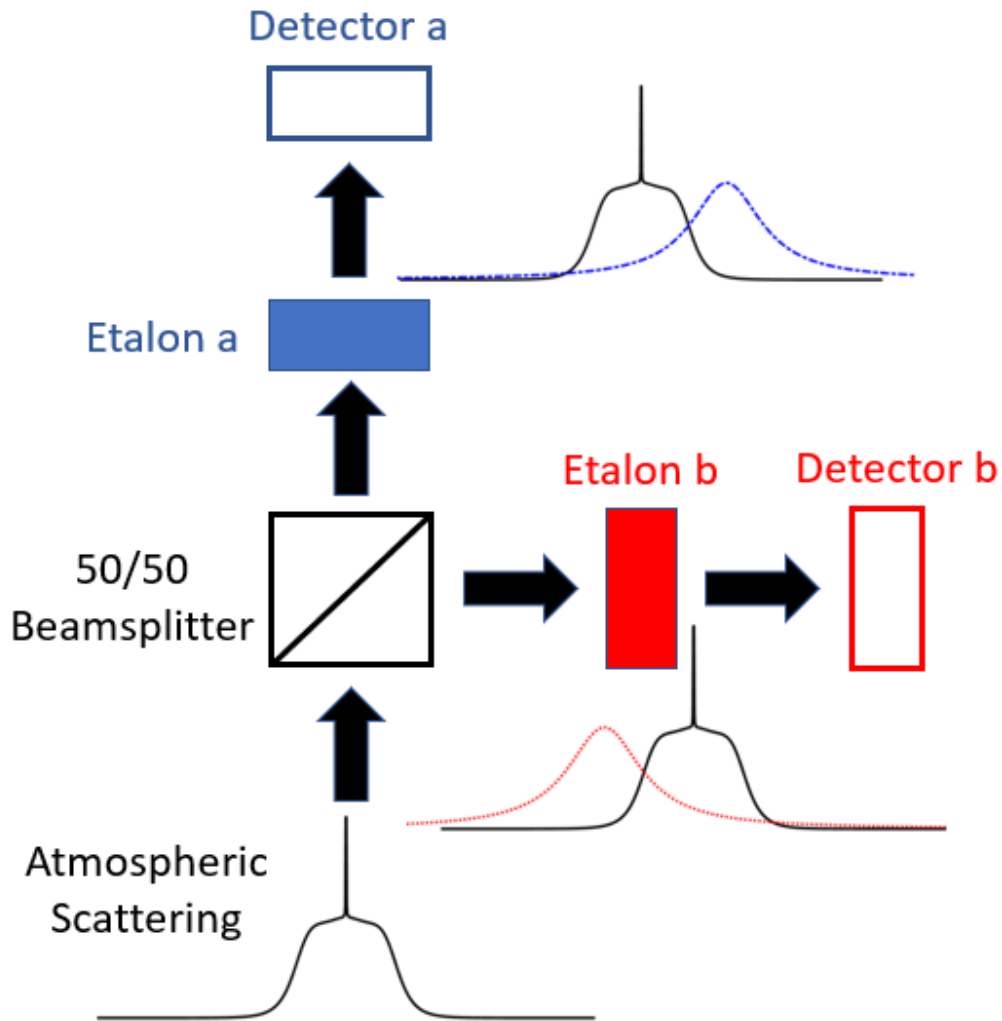


Figure 2.3: A block diagram of a simplified double-edge receiver. The solid black lines are the atmospheric scattering spectra, the dot-dashed blue line is the transmission spectrum for etalon a, and the dotted red line is the transmission spectra of etalon b.

The top plot in Figure 2.4 shows the atmospheric scattering spectrum with no applied Doppler shift (a LOS wind speed of $0 \frac{m}{s}$) and the etalon transmission spectra. Shaded regions beneath the etalon transmission curves represent the portion of the atmospheric scattering signal reaching the detector. With zero Doppler shift, the signal strength at each detector

is equal. The second plot in Figure 2.4 shows the atmospheric scattering spectrum with an applied Doppler shift that would occur for $100\frac{m}{s}$ LOS winds away from the receiver. The strength of the signal that reaches detector b is greater than the signal that reaches detector a. Although $100\frac{m}{s}$ is an unrealistically high wind speed, it is chosen so that the signal change is obvious.

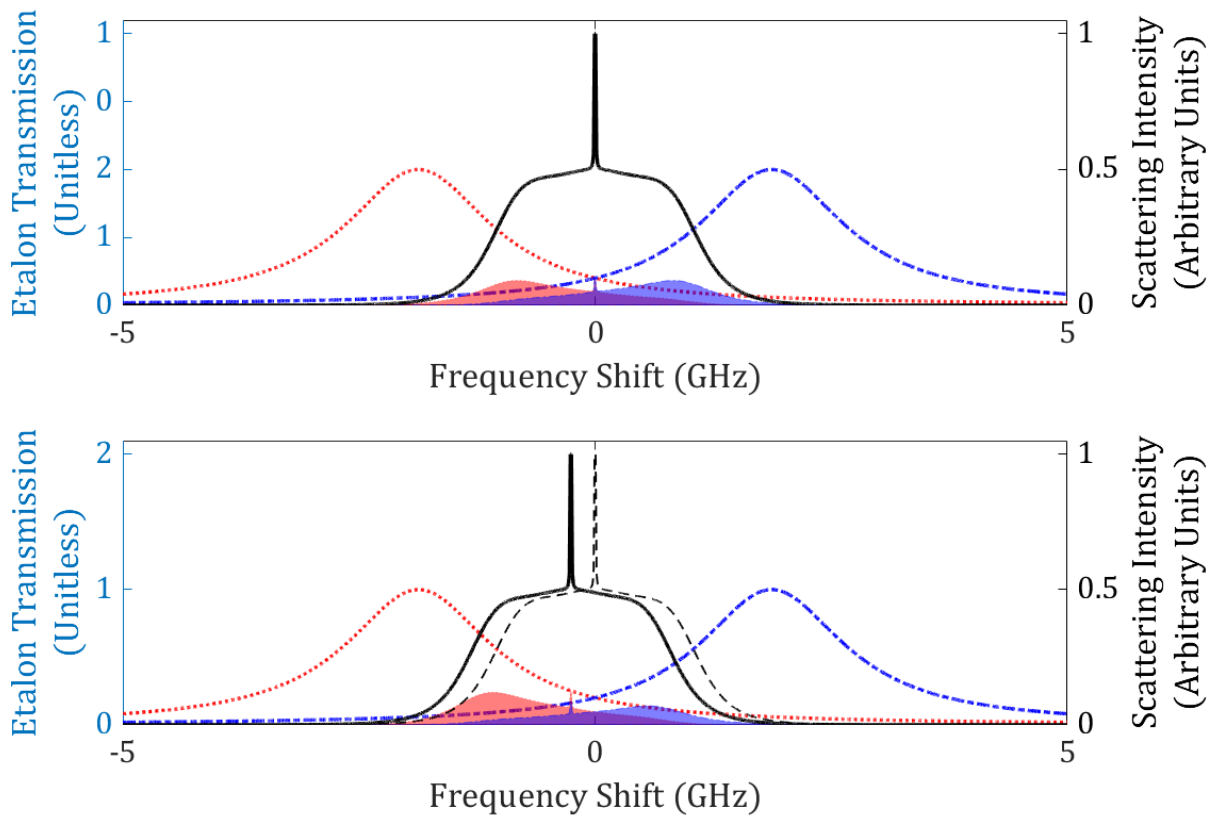


Figure 2.4: Top: The atmospheric scattering spectrum, the etalon transmission spectra, and the signal strength at the detectors with zero LOS wind. The black solid line is the atmospheric scattering spectrum, the blue dot-dashed line is the transmission spectrum of etalon a, the red dotted line is the transmission spectrum of etalon b, and the shaded regions underneath the transmission spectra represent the portion of the atmospheric scattering signal that reaches the detector. Bottom: The same as the top plot with a $100\frac{m}{s}$ LOS wind (256-MHz Doppler shift) applied. The unshifted atmospheric scattering signal is shown as the black dashed line for reference.

The ratio of the signal received by detector a to detector b is directly related to the LOS wind speed. This relationship will be demonstrated using the background-subtracted lidar equation for a photon-counting lidar [125], following the derivation in Repasky et al. [113].

$$N_x(r, f) = N_0 \frac{c\tau}{2} \frac{A_0}{r^2} T_{atm}^2 O(r) \beta(r, f) \eta_x T_{e,x}(f) \quad (2.6)$$

The undefined term x is a placeholder that can be either a or b depending on the receiver channel, $N_x(r, f)$ is the number of photons received as a function of range and frequency, N_0 is the number of photons in the outgoing laser pulse, c is the speed of light, τ is the pulse duration, A_0 is the receiver area, T_{atm}^2 is the two-way atmospheric transmission, $O(r)$ is the overlap function, $\beta(r, f)$ is the total backscatter spectrum, η_x is the receiver channel efficiency, and $T_{e,x}(f)$ is the etalon transmission. Equation 2.6 assumes that each receiver channel has the same overlap function.

The backscatter term, $\beta(r, f)$, can be separated into aerosol and molecular components.

$$\beta(r, f) = \beta_a(r) \delta(f_0 + \Delta f - f) + \beta_m(r) g(r, f_0 + \Delta f(r), f) \quad (2.7)$$

Here, $\delta(f_0 + \Delta f(r) - f)$ is a delta function centered at $f_0 + \Delta f(r)$ (the aerosol scattering spectrum can be assumed to be a delta function) and $g(r, f_0 + \Delta f(r), f)$ is the Cabannes lineshape centered at $f_0 + \Delta f(r)$.

Equation 2.6 then becomes

$$N_x(r, f) = N_0 \frac{c\tau}{2} \frac{A_0}{r^2} T_{atm}^2 O(r) [\beta_a(r) \delta(f_0 + \Delta f(r) - f) + \beta_m(r) g(r, f_0 + \Delta f(r), f)] \eta_x T_{e,x}(f). \quad (2.8)$$

Substituting $\beta_a(r) = (B(r) - 1)\beta_m(r)$ from Equation 2.5 and rearranging yields

$$N_x(r, f) = N_0 \frac{c\tau}{2} \frac{A_0}{r^2} T_{atm}^2 O(r) \beta_m(r) \left([B(r) - 1] \delta(f_0 + \Delta f(r) - f) + g(r, f_0 + \Delta f(r), f) \right) \eta_x T_{e,x}(f). \quad (2.9)$$

For brevity, let

$$F(r) = N_0 \frac{c\tau}{2} \frac{A_0}{r^2} T_{atm}^2 O(r) \beta_m(r). \quad (2.10)$$

Equation 2.9 can be rewritten as

$$N_x(r, f) = F(r) \left([B(r) - 1] \delta(f_0 + \Delta f(r) - f) + g(r, f_0 + \Delta f(r), f) \right) \eta_x T_{e,x}(f). \quad (2.11)$$

The total signal observed can be found by integrating over frequency.

$$N_x(r) = F(r) \eta_x \left([B(r) - 1] T_{e,x}(f = f_0 + \Delta f(r)) + \int g(r, f_0 + \Delta f(r), f) T_{e,x}(f) df \right) \quad (2.12)$$

The direct-detection Doppler signal is given by Equation 2.13, where $M(r)$ is the direct-detection Doppler signal, $N_a(r)$ is the signal detected by detector a, and $N_b(r)$ is the signal detected by detector b.

$$M(r) = \frac{N_a(r) - N_b(r)}{N_a(r) + N_b(r)} \quad (2.13)$$

Substituting Equation 2.12 into 2.13 yields

$$M(r) = \frac{[B(r) - 1] (\eta_a T_{e,a}(f = f_0 + \Delta f(r)) - \eta_b T_{e,b}(f = f_0 + \Delta f(r))) + \int g(r, f_0 + \Delta f(r), f) (\eta_a T_{e,a}(f) - \eta_b T_{e,b}(f)) df}{[B(r) - 1] (\eta_a T_{e,a}(f = f_0 + \Delta f(r)) + \eta_b T_{e,b}(f = f_0 + \Delta f(r))) + \int g(r, f_0 + \Delta f(r), f) (\eta_a T_{e,a}(f) + \eta_b T_{e,b}(f)) df}. \quad (2.14)$$

This equation can be solved numerically if all the parameters but $\Delta f(r)$ are known. Once $\Delta f(r)$ is known, the LOS wind speed can be retrieved with Equation 2.4.

The Problem of a Two-Component Atmosphere

In Equation 2.14, $M(r)$, η_a , η_b , $T_{e,a}(f)$, $T_{e,b}(f)$ can be measured and $g(r, f)$ can be modeled accurately. There are two unknowns: $B(r)$ and $\Delta f(r)$.

This issue has two solutions:

1. desensitize the lidar to $B(r)$, (i.e., minimize $\frac{dM(r)}{dB(r)}$)
2. or measure $B(r)$ with ancillary measurements.

Many successful double-edge DWLs (e.g., [26, 27, 31, 33, 34]) chose option 1. The etalons are spaced to minimize $\frac{dM(r)}{dB(r)}$, enabling the DWL to operate in regions with variable aerosol content. Some edge DWLs (e.g., [23, 32]) only use the aerosol scattering signal, using high-finesse etalons positioned on the edge of the aerosol signal (e.g., [32]), effectively making $\frac{dM(r)}{dB(r)} = 0$. The drawback of option 1 is that the DWL either relies on the presence of aerosols or sacrifices receiver efficiency to make $\frac{dM(r)}{dB(r)} = 0$.

A Proposed Solution to the Problem of a Two-Component Atmosphere

The DLB direct-detection DWL proposes a new solution to the problem of a two-component atmosphere. Combining a double-edge DWL with an atomic-vapor absorption HSRL operating at a nearby wavelength, this instrument measures the backscatter ratio profiles and uses them in the wind speed retrieval. The HSRL operates on the Potassium D1 line at 770 nm, and the double-edge DWL operates at 780 nm, which allows stabilization to the D2 line of Rubidium. These wavelengths are near enough that a close estimate of the backscatter ratio at 780 nm can be made from the measurement at 770 nm. However, the wavelengths are far enough apart that the beams can be separated and combined using dichroic mirrors.

There are several benefits of measuring the backscatter ratio instead of designing the system so that $\frac{dM(r)}{dB(r)} = 0$. This approach avoids the need for custom etalons, lowering instrument costs. Also, the etalons can be placed closer together, which leads to greater receiver efficiency and lower random error.

The novel combination of an atomic absorption HSRL and a double-edge DWL using etalons as filters was conceptualized in Repasky et al. [113]. Combining an HSRL with another lidar technique resembles the temperature- and aerosol-profiling MPD, which leverages the backscatter ratio measured by an atomic absorption HSRL in the DIAL retrieval of temperature [108].

Instrument Description

This work will describe a prototype instrument that operates on a similar concept as the one described in Repasky et al. [113]. However, the first iteration of this lidar will not precisely match the one used in the paper. Instead, the 780-nm DWL will be built as a stand-alone system, and a combined O_2 DIAL and HSRL, as described in [108] will be used to measure the backscatter ratio at 770 nm. This instrument has demonstrated reliable backscatter ratio retrievals [109] and will not be extensively discussed in this document.

The instrument in this thesis will be similar to the one conceptualized in Repasky et al. [126], with a few subtle differences. The schematic for this instrument is shown in Figure 2.5.

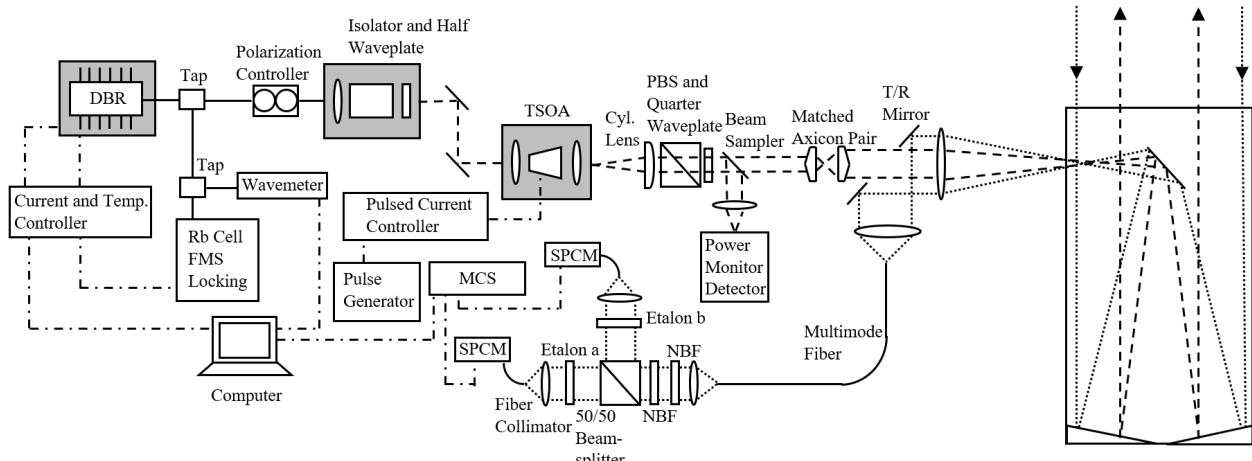


Figure 2.5: A schematic of the DLB direct-detection DWL.

A fiber-coupled distributed Bragg reflector (DBR) laser (Photodigm) serves as the seed laser in a master oscillator power amplifier (MOPA) configuration with a tapered semiconductor optical amplifier (TSOA) acting as the amplifier. A small portion of the seed laser is directed to a frequency modulation spectroscopy (FMS) locking system, which will be described in the Completed Work section, and a wavemeter for broadband wavelength tuning. A fiber polarization controller, an isolator, and a half waveplate prevent feedback into the DBR laser and control the polarization of the input into the TSOA. An aspheric lens couples the light into the TSOA (Eagleyard Photonics). The TSOA is overdriven, which means that it is pulsed at a low duty cycle ($\sim 1\%$) to achieve high peak powers (up to several Watts) without causing catastrophic optical mirror damage (COMD) [100, 127]. The TSOA

is pulsed at 10 kHz with $1\text{-}\mu\text{s}$ pulse widths, generating the lidar pulse train.

The astigmatic output of the TSOA is collimated and circularized using an aspheric lens and a cylindrical lens. The cylindrical lens is tilted 3° downward to avoid retroreflection into the TSOA. The beam passes through a polarizing beamsplitter (PBS) and a quarter-waveplate, with the PBS aligned to allow transmission, and is converted into circularly polarized light by the quarter-waveplate. The PBS rejects retroreflection from downstream of the quarter-waveplate.

After the quarter-waveplate, the beam is sampled, and a small amount is sent to a power monitor. The remaining beam continues to an axicon, converting the circular beam to an annular one. The annular beam passes through the middle of the transmit/receive (T/R) mirror (an elliptical mirror with a 10-cm hole bored through it). It is incident on a lens, which forms a shared focal point system with the Newtonian telescope (Meade F-4.5). The hole through the center of the T/R mirror is imaged onto the inner diameter of the telescope's 40-cm primary mirror. The annular beam is shaped to pass the light around the secondary mirror to the atmosphere.

On the return path, light is collected by the outer half of the telescope's primary mirror, which is imaged onto the T/R mirror and reflected to a beam reducer and fiber collimator. Light is collected into a multimode fiber ($105\text{-}\mu\text{m}$ core diameter), which effectively scrambles the modes and causes there to be no angular dependence in the receiver. The light is then taken to the second stage of the receiver.

The light is launched into the system using a fiber collimator and a 2.25x beam expander. After collimation and expansion, the beam passes through two NBFs (Alluxa) to remove the sky background and is incident on a 50/50 non-polarizing beamsplitter (N-PBS). Half of the light is incident on etalon a, and half of the light is incident on etalon b. These etalons are fused-silica solid etalons (Light Machinery). They are temperature-stabilized and held inside a temperature-stabilized chamber. After passing through the etalons, each leg is incident on a fiber collimator and coupled into a multimode fiber, directed to a fiber-coupled single-photon-counting module (SPCM) (Perkin-Elmer Avalanche Photodiode [APD]).

The signal from the SPCMs is collected by a multichannel scaler (MCS) made by NCAR. The timing is controlled by a pulse generator (Quantum Composers), the DBR current is controlled by a laser controller (Newport), the DBR temperature and TSOA temperature are controlled by a temperature controller module (Thorlabs), and the TSOA current is controlled by a pulsed current controller (Berkley Nucleonics). A computer controls the entire system with a LabVIEW program.

Potential Alternative Solutions

This section briefly discusses the application of other DWL techniques using the MPD architecture.

A key design criterion for the DLB direct-detection DWL is compatibility with the water vapor- and temperature-profiling MPD instruments. This criterion means that the DLB direct-detection DWL must operate at a wavelength that can be separated from the 828-nm water vapor DIAL and the 770-nm temperature DIAL. Also, TSOAs and DBRs are restricted to approximately 700nm-1 μ m.

One potential alternative solution is the single-edge method using a Rubidium vapor cell, as proposed by She for a Potassium vapor cell [128]. This method could be used with a laser transmitter capable of alternating the laser frequency between the sideline to measure winds with the edge technique and the center of the absorption spectrum to measure the backscatter ratio with the HSRL technique, similar to the iodine-filter-based instruments built by the group at the Ocean University of Qingdao and CSU [38–40]. This approach provides a stable spectrometer but would have a lower sensitivity to changes in wind speed.

Fringe-imaging methods (e.g., [49, 57, 66]) could theoretically be integrated with an MPD. However, these methods use complicated interferometers and require CCD-array or multi-pixel SPCM detectors. The preference in this context is to use commercially available fused-silica solid etalons and SPSCMs that work well with the existing data acquisition software, avoiding the need to build an interferometer and develop new software.

Heterodyne detection is theoretically viable with an MPD but cannot profile winds above the PBL. Also, it would be difficult to match the wavefront of the return signal with the local oscillator in a system with a large telescope, like the MPD. Implementing a heterodyne detection system would require a significant change to the MPD control software to incorporate a spectrum analyzer.

Other instruments have been conceptualized to measure wind speeds and aerosol backscatter simultaneously that could theoretically be used with an MPD (e.g., [129–131]). However, these techniques require sophisticated instrumentation, and none have been implemented in a working prototype at the time of writing.

COMPLETED WORK

This chapter describes the design and fabrication of the DLB direct-detection DWL. Two critical subsystems needed to be developed: laser frequency stabilization and etalon temperature stabilization. These subsystems are discussed in-depth. Additionally, this chapter describes the assembly of the laser transmitter and laser receiver. The chapter is organized as follows:

- **Laser Stabilization:** Describing the design and fabrication of the laser stabilization control loop. This subsystem has been completed.
- **Laser Transmitter and First-Stage Receiver:** Discussing progress in fabricating and assembling the laser transmitter and first-stage receiver (the telescope to the multimode fiber, refer to Figure 2.5). The laser transmitter and first-stage receiver still need to be fully assembled.
- **Etolon Temperature Stabilization:** Detailing progress in designing, fabricating, and testing the etalon temperature stabilization. Several temperature-stabilized etalon mount prototypes have been made, and testing is underway.
- **Second-Stage Receiver:** Discussing the progress in designing and fabricating the second-stage receiver (the multimode fibers to the detectors, refer to Figure 2.5). The second-stage receiver still needs to be fully assembled.

Laser Stabilization

Summary

The DLB direct-detection DWL requires a laser with an absolute frequency stability of 500 kHz. The modeling paper for the DLB direct-detection DWL found that this stability would contribute $0.2 \frac{m}{s}$ to the wind speed retrieval error [113]. The laser was stabilized to a saturated absorption line of ^{87}Rb using FMS, and a stability of 68.749 kHz was achieved for a 48-hour test.

Introduction

In many applications requiring precise frequency control, a free-running laser falls short of the stability requirements, and active stabilization is needed. Stabilization schemes using FMS [132, 133] to atomic absorption lines provide active stabilization to an absolutely stable

frequency reference. This method is similar to the Pound-Drever-Hall (PDH) [134, 135] technique, except the frequency reference in the FMS method is the transmission spectrum of a vapor absorption cell instead of the reflection from a high-finesse Fabry-Pérot cavity, as in the PDH method.

FMS to an atomic vapor cell has the advantage over the PDH technique as the spectral lines are absolutely stable and do not require as stringent temperature control, an evacuated chamber, or vibration isolation. Examples of lidars that use FMS for laser stabilization include the NASA airborne HSRL [136] and the DLR airborne HSRL [137], both employing it with a Nd:YAG laser at 532 nm and using an iodine vapor cell as a reference. Diode lasers have been stabilized to saturated absorption resonances in the rubidium D2 line using FMS to create frequency references for atomic clocks with reported stabilities in the Hz (10^{-14}) level [138–142]. While not achieving these levels of stability, this work demonstrates a laser with long-term stability under 100 kHz (3.84×10^{-9}). The optical and electronic design will be given in the following sections.

Design

The laser stabilization employs an FMS scheme, as shown in Figure 3.1. The setup includes a DBR laser (Photodigm PH780DBR040BF-ISO) thermally controlled by a built-in thermo-electric cooler (TEC) and enclosed within a thermally-stabilized enclosure (see the Laser Enclosure subsection) to reduce the effects of low-frequency temperature drifts. The laser output passes through an isolator and a half waveplate and is reflected by a PBS to produce linearly polarized light. This light is modulated by an electro-optic modulator (EOM) (New Focus 4001 phase modulator [12 MHz resonant frequency]) driven by a function generator and a radio-frequency (RF) amplifier (New Focus 3363-B) at 12 MHz, adding sidebands to the light wave. It should be noted that the choice of 12 MHz due to the availability of EOMs at that resonant frequency is not optimal for stabilization to a Lamb peak in FMS.

The beam then passes through a half waveplate, a PBS, a rubidium cell (Thorlabs) enclosed in an insulated enclosure (see the Rubidium Cell Enclosure subsection), and a quarter waveplate. The beam is then reflected back through the waveplate and the Rb cell along the same path. The counter-propagating beam configuration acts as a pump-probe system, revealing the Doppler-free Lamb peaks, as seen in Figure 3.2. The DLB direct-detection DWL will be stabilized to the $^{87}\text{Rb}(5^2\text{S}_{1/2}, F = 2) \rightarrow (5^2\text{P}_{3/2}, F' = C2, 3)$ hyperfine crossover transition.

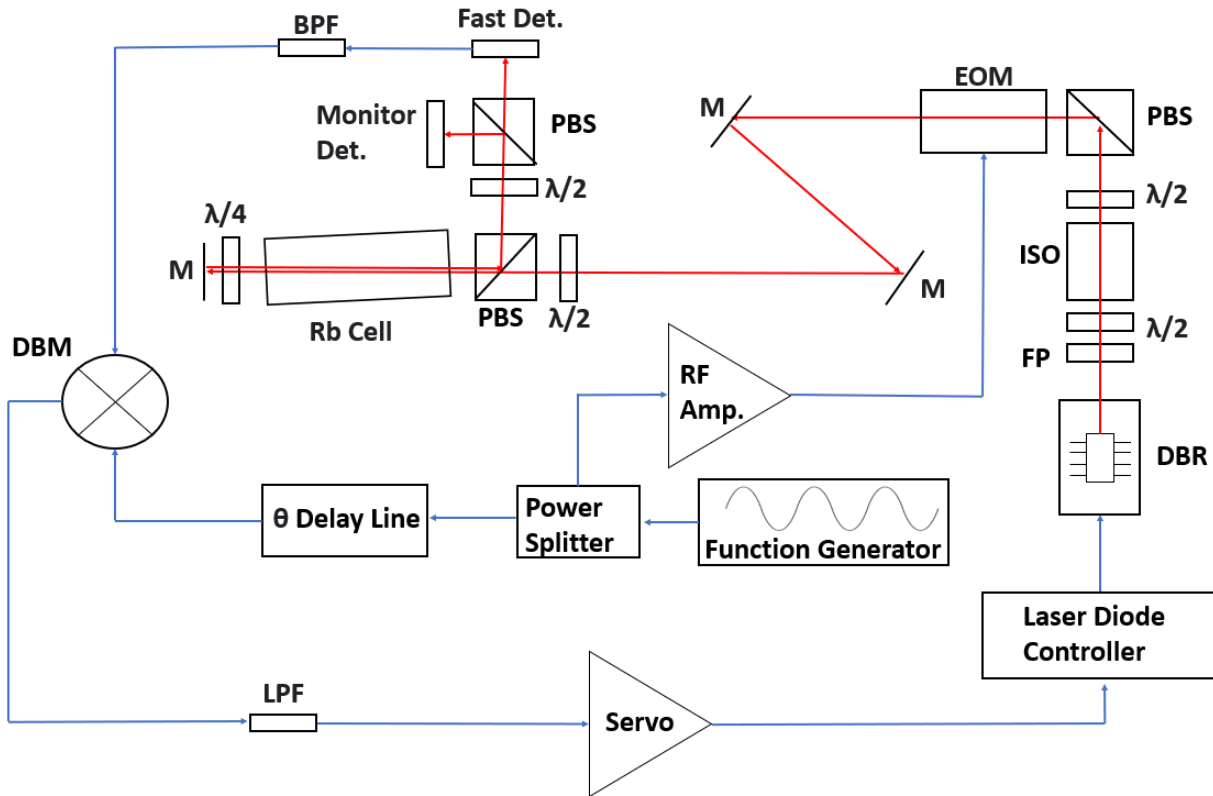


Figure 3.1: FMS control loop. The red arrows indicate optical paths, and the blue arrows indicate electrical signals. $\lambda/4$ = Quarter Waveplate, $\lambda/2$ = Half Waveplate, θ = Phase, BPF = Bandpass Filter, DBM = Double-Balanced Mixer, DBR = Distributed Bragg Reflector Laser, Det. = Detector, EOM = Electro-Optic Modulator, FP = FiberPort (Fiber Collimator), ISO = Faraday Isolator, LPF = Lowpass Filter, M = Mirror, PBS = Polarizing Beam splitter, Rb = Rubidium, RF Amp. = Radio-Frequency Amplifier.

The reflected beam undergoes a phase shift in the reflection and at the quarter waveplate, making its polarization orthogonal to the counter-propagating beam. Therefore, the PBS reflects the beam 90° . It is then directed to a fast detector for locking and a monitor detector. The sidebands and the main lobe create an optical beat note (12 MHz) at the detector. The beat note is filtered (to remove the 24-MHz signals) by an inline bandpass filter and mixed with the local oscillator from the function generator, which is split from the signal driving the EOM with a power splitter (Minicircuits ZSC-2-1). A phase delay line, a BNC cable cut to the correct length for the desired phase delay, ensures that the detected signal is in phase with the local oscillator. The mixer (Minicircuits ZAD-1) converts the two 12-MHz signals into the DC error signal, as seen in Figure 3.2.

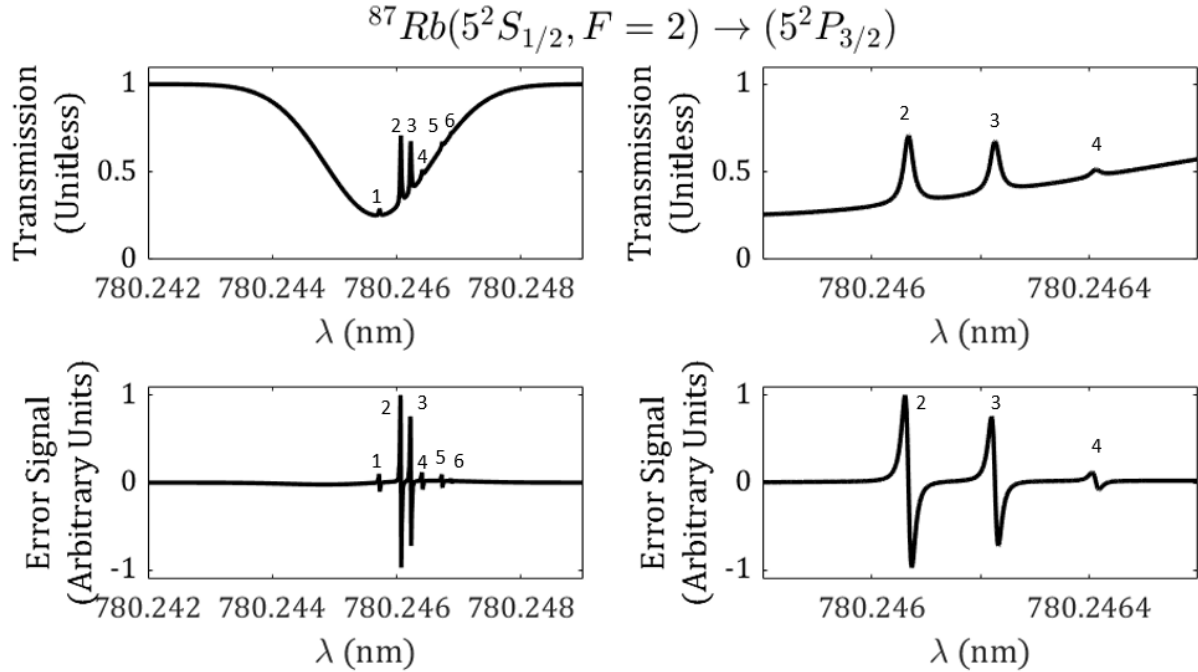


Figure 3.2: Top-Left: The saturated absorption spectrum for ^{87}Rb near 780.246 nm. Top-Right: A close-up view of the top-left. Bottom-Left: The error signal generated by the FMS stabilization scheme. Bottom-Right: A close-up view of the bottom-left. The labeled hyperfine features are **1**:($F = 2, F' = 3$), **2**:($F = 2, F' = C2, 3$), **3**:($F = 2, F' = C1, 3$), **4**:($F = 2, F' = 2$), **5**:($F = 2, F' = 1$), **6**:($F = 2, F' = 0$).

The error signal is filtered by an inline lowpass filter to isolate the DC signal. This filtered signal is amplified by the custom-built servo (see the Servo Circuit subsection) and fed back into the laser controller, providing active feedback stabilization to the Lamb peaks of the hyperfine absorption spectrum.

The laser stabilization scheme can be conceptualized as a control problem (Chapter 2 of [143]), where the laser is the plant, the FMS scheme is the discriminator, the servo controls the closed-loop gain, and the laser controller is the actuator.

Three devices were created to increase the laser's frequency stability.

1. **Thermally Stabilized Laser Enclosure:** An actively stabilized enclosure designed to reduce external temperature forcings to the laser (plant).
2. **Insulated Rubidium Cell Enclosure:** An enclosure that reduces temperature drift in the rubidium cell (discriminator).
3. **Servo Circuit:** A custom-built amplifier that provides the correct closed-loop gain for a stable control system.

The following subsections will detail each custom-built component.

Laser Enclosure The laser cavity length determines the frequency of emitted laser light. In a diode laser, the temperature alone determines the cavity length. Consequently, room temperature fluctuations are the primary source of frequency noise. A laser enclosure was created to increase the thermal stability of the laser to reduce this noise.

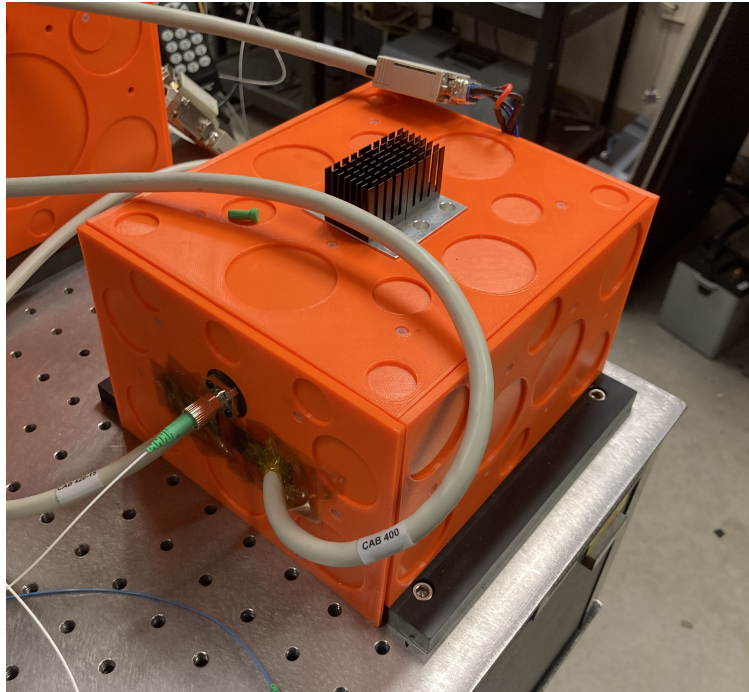


Figure 3.3: A photo of the laser enclosure.

The laser enclosure is depicted in Figure 3.3. It is constructed from Delrin, has an actively temperature-controlled aluminum lid, and is insulated with rubber foam and 3D-printed ABS. The aluminum lid is controlled with a TEC and a temperature controller module. It is set to the same temperature as the laser, effectively isolating the air inside the enclosure from external variations. Refer to Appendix B for assembly drawings of the laser enclosure.

Rubidium Cell Enclosure The rubidium cell acts as the discriminator for the laser stabilization system. Therefore, any change to the rubidium cell changes the lock point. The temperature probes in the resistive heating element (Thorlabs GCH25-75) were set to a constant temperature. However, a temperature gradient formed along the length of the cell because it exchanged heat with the ambient environment. Therefore, when the temperature of the room changed, the temperature of the faces of the cell changed, causing changes to the etalon effects associated with these faces.

Consequently, these changes caused drifts in the lock point, causing the laser frequency to change with the room temperature. Additionally, when the cell heaters were turned off, rubidium was deposited on the faces of the cell, which did not vaporize when the cell was reheated, blocking transmission. An insulated enclosure was built for the cell to insulate its temperature from the room's temperature to mitigate these problems.

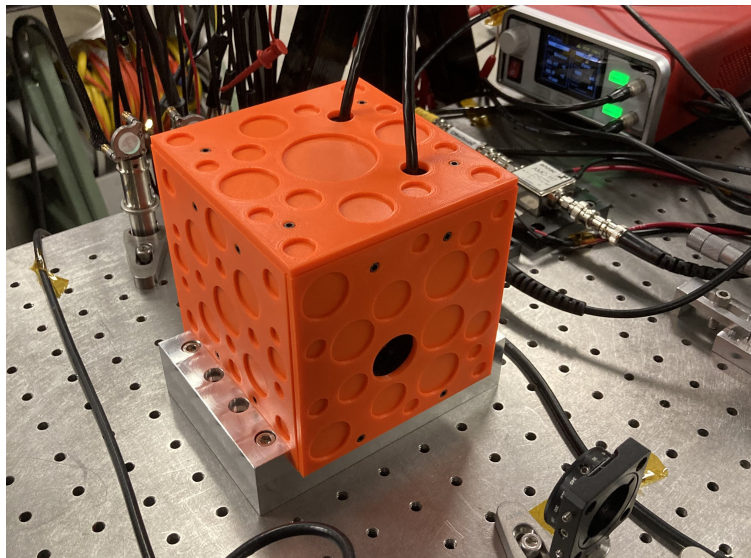


Figure 3.4: A photo of the rubidium cell enclosure.

The enclosure, depicted in Figure 3.4, is constructed from acetal plastic and is insulated with rubber foam and 3D-printed ABS. Antireflective-coated windows allow light transmission through the enclosure. An aluminum heat sink, pressed against the side of the rubidium cell, forces the rubidium to condense on the side of the cell instead of the faces when the cell cools, preventing solid rubidium from depositing on the faces. A soft thermal pad interfaces the heat sink with the Pyrex cell, preventing direct metal-to-glass contact. Refer to Appendix B for assembly drawings of the rubidium cell enclosure.

Servo Circuit An ideal servo for laser stabilization has a high DC gain, a wide bandwidth, and a transfer function that causes no closed-loop instabilities when incorporated with the rest of the electronics. A discussion of servo design is given by Zhu [144] and Roos (Chapter 5 of [145]).

The servo was created using a custom pcb and draws inspiration from those created by previous graduate students in the Montana State Physics Department [145–147]. The schematic of the servo circuit is shown in Figure 3.5. The servo is a voltage follower and an integrating amplifier with a variable gain controlled by a wire-wound potentiometer. The output voltage is limited with a diode clipper. The servo was designed to maximize gain at low frequency instead of aiming for wide bandwidth. The DC gain is 60 dB, and the bandwidth is 2 kHz. The pcb is mounted inside a shielded electronics box with BNC inputs and outputs. The servo is powered by a regulated power supply (Acopian), and all electronics are powered by an uninterruptible power supply (UPS) to prevent line noise. An image of the circuit inside the shielded electronic box is shown in Figure 3.5.

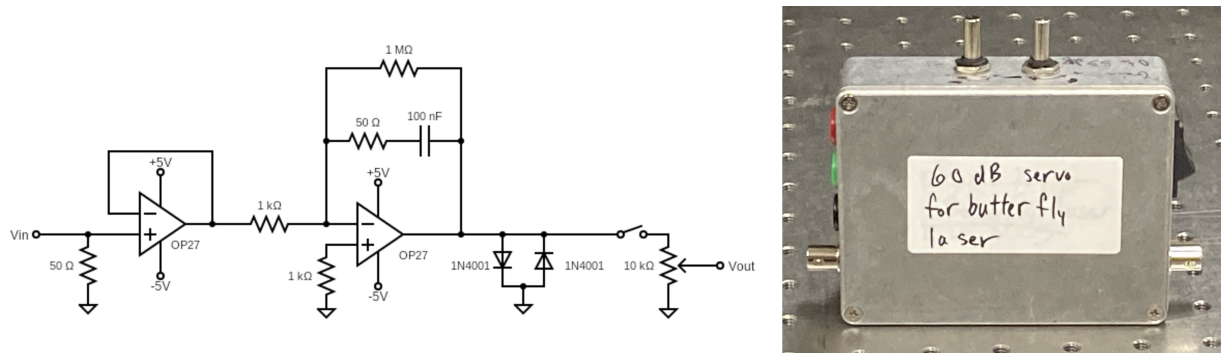


Figure 3.5: Left: The servo circuit diagram. Right: A photo of the servo inside the shielded electronic box.

Results

The stability of a laser cannot be measured directly. A reliable method of determining the stability of a laser is to beat two identical lasers together and monitor the beat note stability. Assuming that the fluctuations in the two lasers are uncorrelated, laser stability is the square root of the beat note stability.

In this study, two DBR lasers were stabilized to adjacent crossover lines in the saturated absorption spectrum of a rubidium vapor cell [$^{87}Rb(5^2S_{1/2}, F = 2) \rightarrow (5^2P_{3/2}, F' = C1, 3)$ and $^{87}Rb(5^2S_{1/2}, F = 2) \rightarrow (5^2P_{3/2}, F' = C2, 3)$]. These crossover lines are nominally 78.47 MHz apart [148], but the lock point of the FMS locking scheme is not the exact frequency of the atomic transition and can range from 77 to 83 MHz apart depending on the relative phase delay of the local oscillator and the beat note from the detector. For example, the beat note in Figure 3.6 is 82.3 MHz.

The beat note stability was monitored for 48 hours, as shown in Figure 3.6. The beat note stability for the system was 97.226 kHz, indicating a laser stability of 68.749 kHz. This stability is much lower than the needed stability of 500 kHz. The lasers have been left unattended and stabilized for over a week without issue.

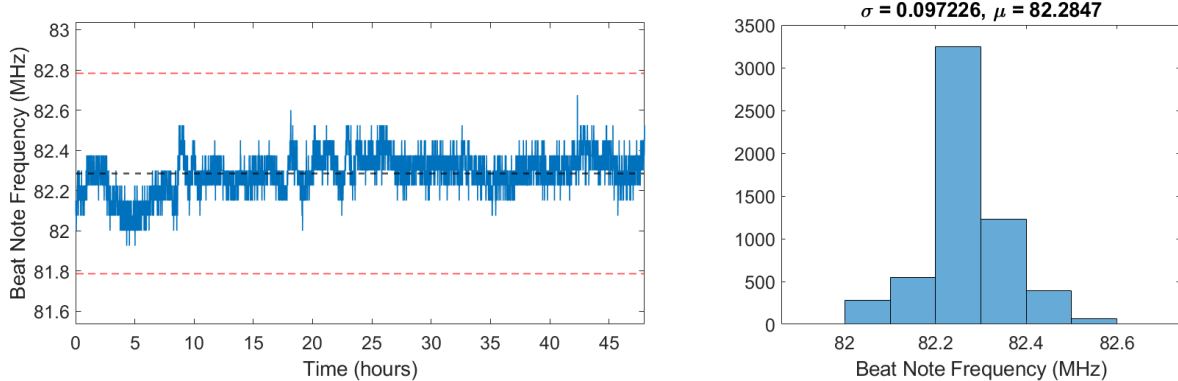


Figure 3.6: Left: A time-series plot of the beat note of two DBR lasers stabilized to adjacent crossover lines in the saturated absorption spectrum of rubidium [$^{87}Rb(5^2S_{1/2}, F = 2) \rightarrow (5^2P_{3/2}, F' = C1, 3)$ and $^{87}Rb(5^2S_{1/2}, F = 2) \rightarrow (5^2P_{3/2}, F' = C2, 3)$]. The blue line indicates the beat note frequency, the black dashed line indicates the mean beat note frequency of 82.2847 MHz, and the red dashed lines are frequencies 500 kHz greater and less than the mean. Right: A histogram of the time series. The beat note standard deviation was 97.226 kHz, indicating a laser stability of 68.749 kHz.

Laser Transmitter and First-Stage Receiver

Summary

The DBR laser transmitter (the laser to the telescope, refer to Figure 2.5) and first-stage receiver (the telescope to the multimode fiber, refer to Figure 2.5) were designed using previous MPD instruments as a template. Assemblies for components in the laser transmitter have been designed, machined, and assembled. The laser transmitter still needs to be completed.

Introduction

The laser transmitter and first stage receiver are similar to the DLB-HSRL designs [107–109], with some improvements developed since the last publications. An overview of the laser transmitter was given in the Instrument Description section, and SolidWorks drawings of the transmitter and the first stage of the receiver are available in Appendix C. A block diagram of the transmitting optics before the telescope and first-stage receiving optics is shown in Figure 3.7.

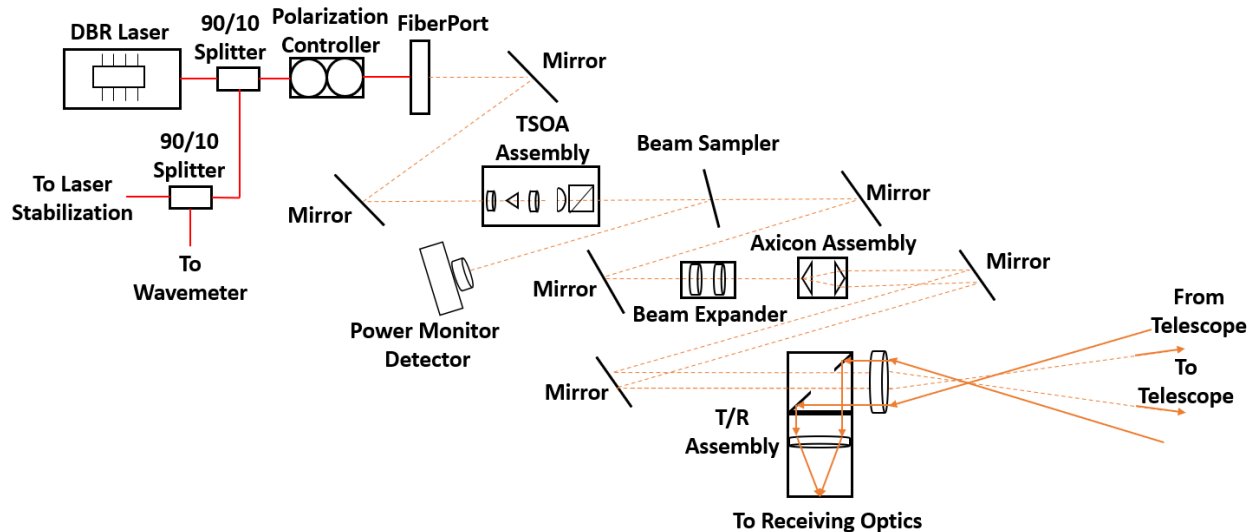


Figure 3.7: The laser transmitter block diagram.

Several assemblies were created to improve previous MPD designs. These include:

1. the **TSOA assembly**,
2. the **Axicon assembly**,
3. and the **T/R assembly**.

The details of these subsystems will be described in the following subsections. SolidWorks drawings for other transmitter components are also shown in Appendix C.

TSOA Assembly

The TSOA assembly (refer to Figure 3.7 for reference) focuses laser light into the TSOA, amplifies it, and collimates the output. It consists of a TSOA, two aspheric lenses on either side of the amplifier held in fiber positioners, a cylindrical lens, and a circular polarizer. SolidWorks drawings of the TSOA assembly are available in Appendix C, and a photo of it is shown in Figure 3.8.

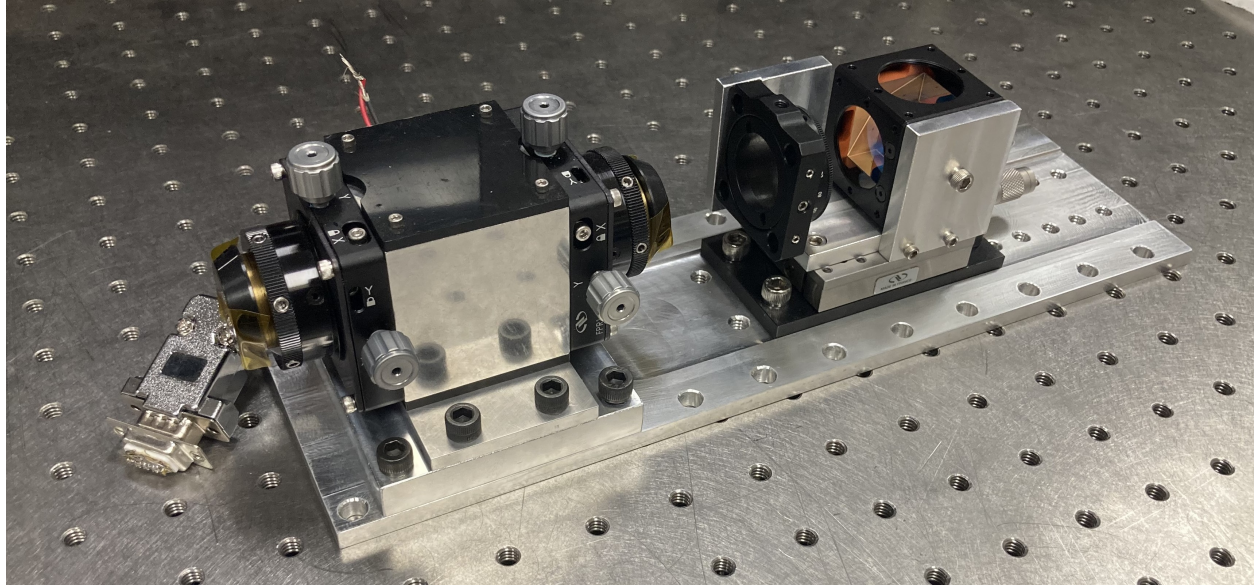


Figure 3.8: A photo of the TSOA assembly.

The first aspheric lens (Thorlabs CM230TMD-B, $F=4.51$ mm) focuses the incident light from the DBR laser onto the TSOA. This lens, held by a fiber positioner (Newport FPR1-C1A), focuses the incident light onto a TSOA (Eagleyard EYP-TPA-0780-03000-4006-CMT04-0000), which is held in an aluminum housing. The TSOA is driven with current

pulses to amplify the beam and create the lidar pulse train. The output beam from the TSOA is incident on a second aspheric lens, also held in a fiber positioner (same lens and positioner). The aluminum housing is temperature-stabilized with a TEC. This proprietary assembly (the two aspheric lenses, fiber positioners, and temperature-stabilized aluminum housing) was designed by engineers at NCAR, but an earlier prototype is available in Xiong's Ph.D. thesis [149].

After the aspheric lens, the beam is incident on a cylindrical lens (Thorlabs LJ1695RM-B, $f=50\text{mm}$) tilted downward at 3° . The output of the TSOA is astigmatic, so the aspheric and cylindrical lenses are used to create a circular, collimated beam. The downward tilt prevents direct retroreflections into the TSOA, addressing spectral purity issues caused by retroreflections. Subsequently, the beam continues through a circular polarizer (Thorlabs VC5-780) consisting of a PBS and a quarter waveplate. The PBS and quarter waveplate convert the beam to circular polarization, ensuring that any retroreflected light will be reflected by the PBS before reaching the TSOA. The circular polarizer adds a layer of safety by averting potential diode damage from amplification in the backward direction, which may destroy the entrance facet through COMD, and addresses spectral purity concerns.

The cylindrical lens and the circular polarizer are mounted on a linear translation stage (Newport UMR5.16). This feature allows fine adjustment for cylindrical lens position, making collimation easier. The entire assembly is mounted onto an aluminum base. Having all the components mounted onto a removable base allows the TSOA to be aligned on a laboratory optical table and moved to the lidar breadboard without losing alignment.

Key improvements, including the downward tilt of the cylindrical lens, consolidating the TSOA and collimation optics onto a single plate, and the addition of the circular polarizer, were recommended by Scott Spuler, who has noticed improvements after adding a similar system to NCAR's MPD systems [150].

Axicon Assembly

The axicon assembly (refer to Figure 3.7 for reference) reshapes the circular beam into an annular one. It consists of two axicons and an iris. A photo of the axicon assembly is shown in Figure 3.9, and the SolidWorks assembly drawing is shown in Appendix C.

The axicons (Thorlabs AX255-B) are mounted in two kinematic x-y translation mounts (Thorlabs ST1XY-A). An iris is placed in front of the first axicon, and the second axicon is mounted in an adjustable lens tube, allowing precise beam shaping. The axicon pair and the iris reshape the incident circular beam into an annular beam, where the iris aperture and

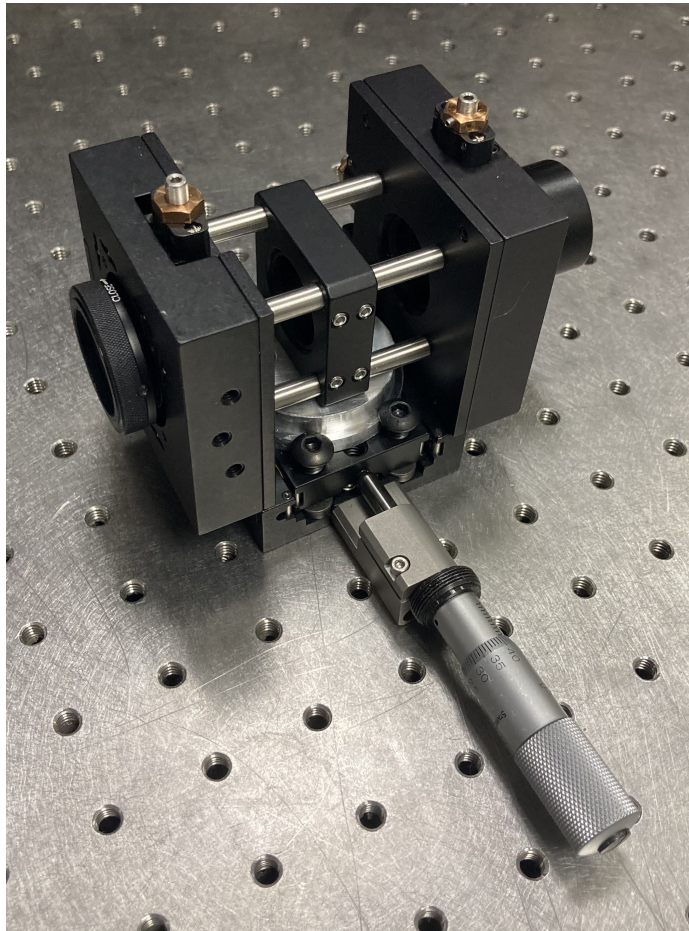


Figure 3.9: A photo of the axicon assembly.

the distance between each axicon determine the beam shape.

The axicon pair is mounted onto a custom rotating platform, which, in turn, is mounted on a linear translation stage (Newport M-460P-X). The rotating platform consists of a circular aluminum piece with a diameter that is slightly smaller than a hole pattern on the linear translation stage. The rotating platform is secured to the linear stage by button-head cap screws, which sit outside the platform and pinch it to the linear stage. Loosening the cap screws allows the entire assembly to be rotated on the translation mount.

This assembly is an improvement over previous designs because the rotating platform and the micrometer-adjust linear translation stage provide precise linear adjustment capabilities in the x-axis and rotation in the sagittal plane. In contrast to earlier systems that relied on delicate manual positioning and mounting the axicons with table clamps, the new assembly will be easier to align.

T/R Assembly

The T/R assembly (refer to Figure 3.7 for reference) serves two functions: expanding the transmitted beam into the telescope and collecting the backscattered light from the telescope into a multimode fiber. A photo of the T/R assembly is shown in Figure 3.10, and the assembly drawings are available in Appendix C.

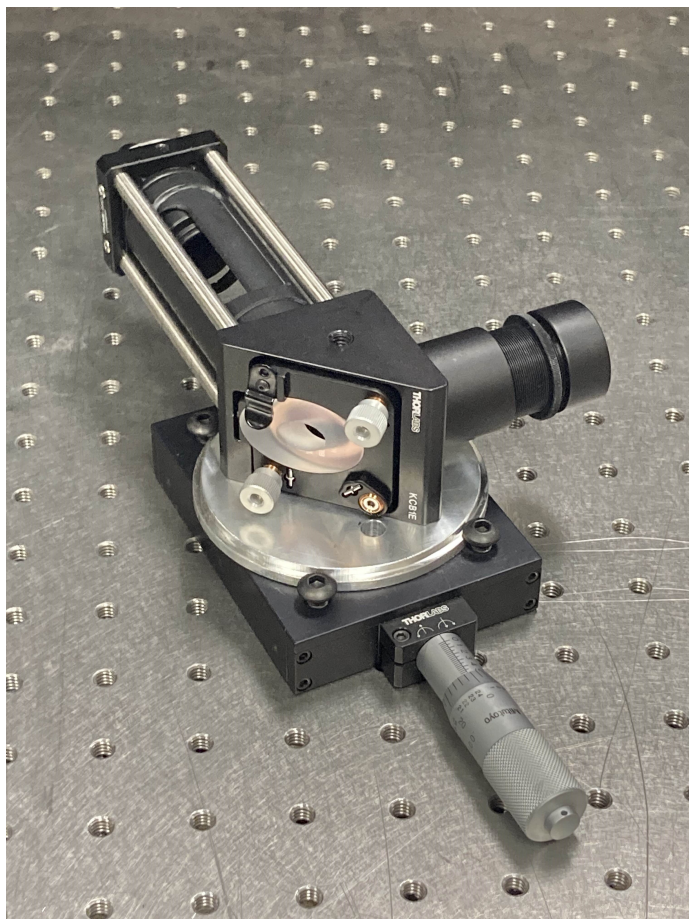


Figure 3.10: A photo of the T/R assembly.

The T/R assembly contains an elliptical mirror (Thorlabs BB1-E03) with a 10-mm hole bored through the center of it at a 45° angle (made by Perkins Precision Development) held in a kinematic mount (Thorlabs KCB1E). The annular beam passes through this center hole on the transmit path. Then, the laser pulse is focused by a lens (Thorlabs LA1509-B, $f=100\text{mm}$) in an adjustable lens tube, which is adjusted to form a matched focal point system with the telescope.

The return signal incident on the outer half of the primary mirror is imaged onto the elliptical mirror. This light is passed through a 4x beam reducer, created using two lenses (Thorlabs LA1509-B [$f=100\text{mm}$] and Thorlabs LA1054-B, [$f=-25\text{mm}$]), and incident on a fiber collimator (Thorlabs PAF2P-11B). The fiber collimator focuses light into a multimode optical fiber, which guides the signal to the second stage of the receiving optics. The entire T/R assembly is mounted onto a custom rotating platform, itself attached to a linear translation stage. This design is the same concept as in the axicon assembly. It represents an improvement over previous systems for the same reasons.

Cage rods were added along the beam reducer between the T/R mirror and the fiber collimator, enhancing rigidity and making misalignment less likely when attaching and detaching the optical fiber. This modification, suggested by Robert Stillwell, has provided better alignment stability in NCAR's MPD systems [151].

Etalon Temperature Stabilization

Summary

The DLB direct-detection DWL requires an etalon with a stable temperature. A stability of 5 mK would contribute $0.49 \frac{\text{m}}{\text{s}}$ to the wind speed retrieval error. This etalon stability was achieved with a temperature-stabilized mount, which was designed, simulated, and fabricated. **Typically, 1-hour temperature stabilities of 2 mK and 24-hour temperature stabilities of 10 mK have been achieved, with the best performance being a temperature stability of 1.15 mK observed for 96 hours.**

Introduction

The stability of the frequency discriminators in the receiving optics plays a crucial role in the double-edge wind retrieval technique. The frequency discriminators for the DLB-DWL are fused-silica solid etalons. The etalons are commonly used in lidar receivers as NBFs for blocking the solar background [152]. They have been used in satellite-based lidars like GLAS (Geoscience Laser Altimeter System) [153] and CALIOP (Cloud-Aerosol LiDAR with Orthogonal Polarization) [154] and several MPD instruments [103, 105, 107, 108].

While these etalons offer advantages in optomechanical stability and ease of use, they cannot be tuned with a piezoelectric transducer. Therefore, the etalons must be tuned in frequency by adjusting the temperature, which changes the cavity length due to thermal expansion. Most successful edge and double-edge DWLs have implemented air-gap etalons with a gap between the mirrors adjustable by piezoelectric transducers (e.g., [23, 29, 33]).

However, the conceptualized instrument MARLI (MARs Lidar), designed for measuring winds in the Martian atmosphere, will use fused-silica solid etalons [155].

To accurately retrieve the wind speed, it is crucial to control the temperature of the etalon precisely. According to a modeling paper by Repasky et al., a temperature stability of 5 mK would cause an uncertainty in the wind speed retrieval of $0.4 \frac{m}{s}$ (1.02 MHz) [113]). However, an update to the etalon properties has changed this value to $0.49 \frac{m}{s}$ (1.25 MHz). This analysis assumed the worst-case condition where the temperature in etalon a was correlated with etalon b. If the temperature stability between the two etalons is uncorrelated and random, the error in the wind speed retrieval will be $.346 \frac{m}{s}$ (887 kHz).

Achieving a temperature stability of 5 mK is challenging, but previous systems have demonstrated its feasibility. For example, Imaki built a DWL with an etalon that had a temperature stability of 7 mK [156], the ALADIN receiver had a long-term stability of 10 mK [66], and Ishii built a DWL with a temperature stability of 10 mK [157]. Cremons et al. expect to achieve a temperature stability of 5 mK in MARLI [155]. Furthermore, laser reference cavities (e.g., [158, 159]) and astronomical spectrographs (e.g., [160, 161]) regularly achieve sub-mK temperature stabilities in evacuated chambers, at the cost of long time constants. Savani et al. achieved sub-mK temperature control of a laser diode mount using commercial TECs, thermistors, and temperature controllers [162].

A temperature-stabilized etalon mount was designed, simulated, and fabricated. The best performance was a temperature stability of 1.15 mK for 96 hours. Typical performance shows 1-hour stability of better than 2 mK and 24-hour stability of better than 10 mK. The temperature-stabilized mount in its present form meets the stability criteria in some conditions. However, if a bias correction is implemented, the stringent temperature stability requirement of 5 mK may only be required for short-term stability. This bias correction involves periodically sending a small amount of laser light through the etalons to measure the low-frequency drift, as described in the Research Plan chapter. Ongoing efforts are focused on improving the stability under all conditions.

The following subsections will describe the mechanical design, the electronic design, and testing for the temperature-stabilized etalon mount.

Mechanical Design

The temperature-stabilized etalon mount consists of two layers of active temperature stabilization. In simplest terms, the second stage controls the temperature of the etalon, and the first stage provides a temperature-stabilized chamber to contain the second stage. The two stages of the temperature-stabilized etalon mount and how they interface will be described in greater detail. Figure 3.11 shows an image of the complete etalon mount. The assembly drawings for the most recent (fourth) prototype of the etalon mount are shown in Appendix D.

The second stage, shown in Figure 3.12, is similar to the etalon mounts in the MPD systems [103, 105, 107, 108]. It consists of a temperature-stabilized copper block holding the fused silica etalon at its center. The etalon is compressed into indium foil between the etalon and the copper block to ensure a thermally conductive interface. Two antireflective-coated windows surround the etalon and are held in place by retaining rings (Thorlabs SM1) and compressed into o-rings, which ensure an airtight seal. These windows prevent free-convection air from interacting with the etalon, increasing thermal stability. The copper block is surrounded by $\frac{1}{4}$ -inch-thick rubber foam insulation held in place by a 3D-printed plastic jacket. A thermistor is embedded in thermally conductive epoxy (Electrodag 5810) for temperature measurement, and the TEC is pressed against the top of the etalon mount between the etalon fixture and the heat sink. Graphite foil forms a thermally conductive interface between the TEC and the second stage.

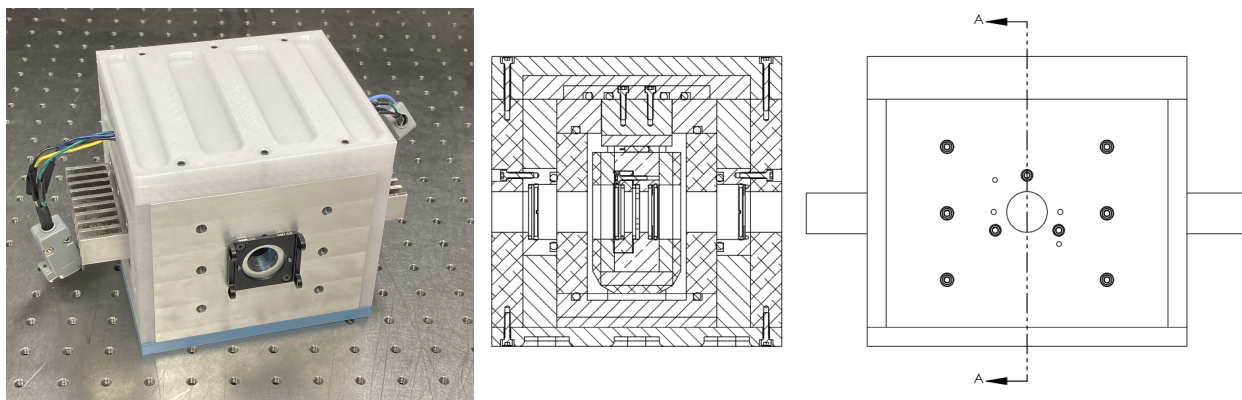


Figure 3.11: Left: A photo of the temperature-stabilized etalon mount prototype. Right: A SolidWorks drawing of the left, including a cross-sectional view.

The second stage is attached to a heat sink assembly, as shown in Figure 3.13. The second stage is attached to an aluminum heat sink, which passes through a hole in the Delrin lid of the first stage's central chamber. O-rings ensure an airtight seal at the interface between the heat sink and the lid. This design creates a heat path out of the first stage, which allows the control loop to use the ambient environment as a heat reservoir. The heat sink is pressed to the TEC by four screws with thermally insulating sleeve washers that attach the heat sink to the second stage. These screws pass through compression blocks, low-fill (5%) 3D-printed PET parts slightly taller than the TEC. These compression blocks (inspired by a design from engineers at NCAR [150]) deform as the screws are tightened and act like springs that pre-tension the screws before the TEC is compressed between the heat sink and the second stage. This pre-tensioning allows a secure fit without too much pressure on the TEC.

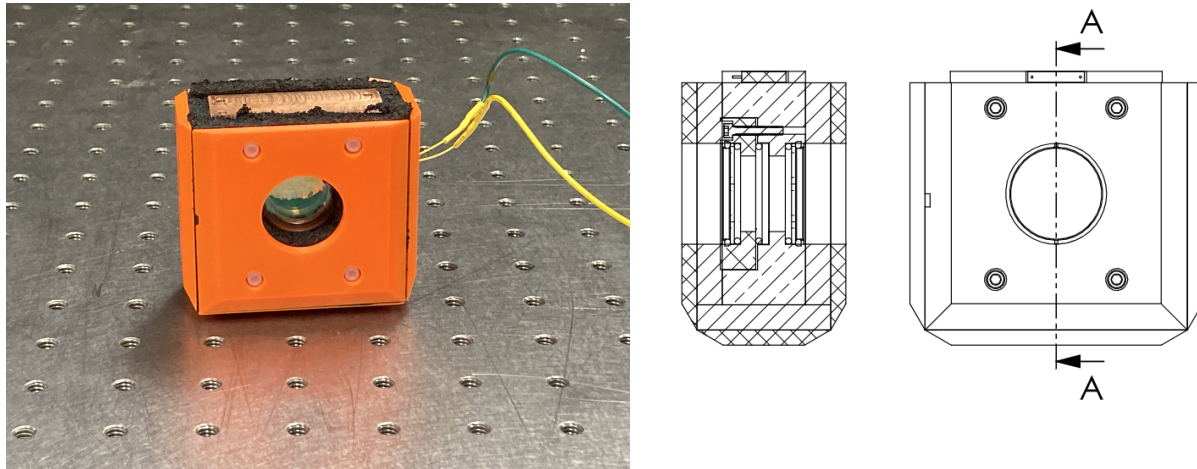


Figure 3.12: Left: A photo of the second stage of the temperature-stabilized etalon mount. Right: A SolidWorks drawing of the left, including a cross-sectional view.

The heat sink for the second stage is connected to the first stage's lid by button head cap screws, as shown in Figure 3.13. The hole pattern in the lid is aligned with slots in the heat sink, which allows rotational adjustment when the screws are loosened. This rotational adjustment allows coarse angular tuning of the etalon. The fine-tuning is achieved with temperature. The angular adjustment is preferred for coarse tuning because an adjustment over a full spectral range requires a temperature range of $\sim 20^\circ \text{ C}$, and the temperature-stabilized etalon mount works best when operating etalon about 5° C above room temperature. This rotating mount design is similar to the rotating platforms in the

axicon assembly and the T/R assembly. O-rings at the interface between the heat sink and the lid ensure an airtight seal, keeping the inside chamber isolated from the ambient environment.

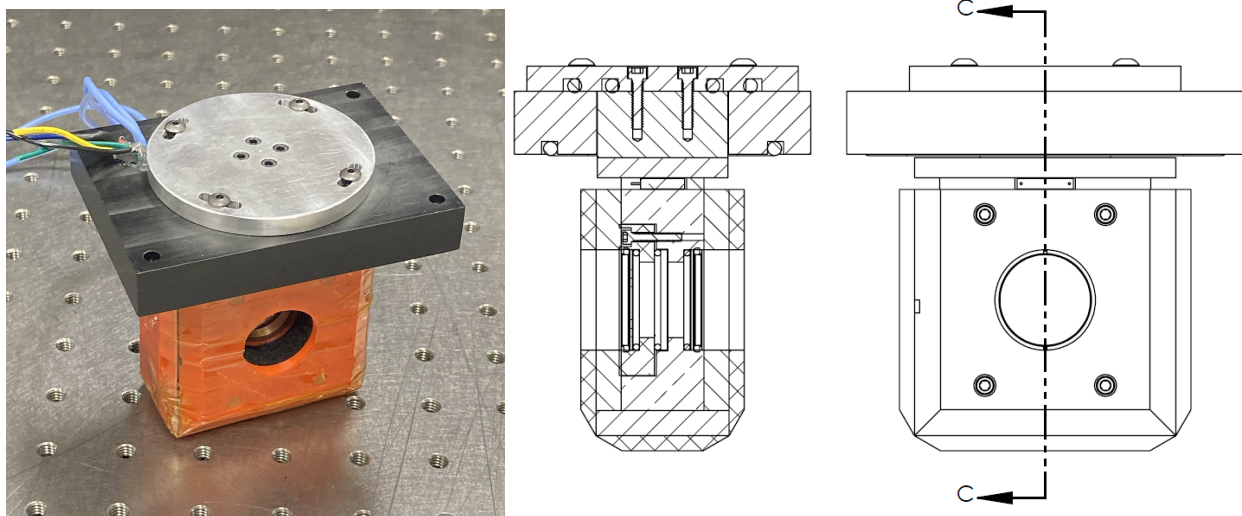


Figure 3.13: Left: A photo of the second stage of the temperature-stabilized etalon mount and its heat sink interfacing with the lid of the first stage. Right: A SolidWorks drawing of the left, including a cross-sectional view.

The first stage of the etalon mount is a hollow aluminum block that is temperature-controlled with TECs. The Delrin lid is attached to the first stage, with o-rings sealing the interface, creating an airtight chamber to contain the second stage. The chamber without the lid is shown in Figure 3.14, while the lid interfacing with the rest of the first stage to create an airtight chamber is shown in Figure 3.15. A thermistor is embedded in the first stage using thermally conductive epoxy (Electrodag 5810). The first stage is set to the same temperature as the second stage, which causes the air inside the first stage to become nearly isothermal, minimizing heat transfer. Antireflective-coated windows allow light to transmit through the first stage. They are held in place by retaining rings (Thorlabs SM1) with o-rings at the interface between the first stage and the window to make the chamber airtight. The first stage is designed to interface with the Thorlabs cage cube system, allowing easy connection with the rest of the receiver. The heat sinks for the first stage are connected using a 3D-printed compression mount and nylon sleeve to insulate the screws, similar to the heat sinks for the second stage. The first stage is insulated with $\frac{5}{8}$ -inch-thick rubber foam insulation and a 3D-printed jacket.

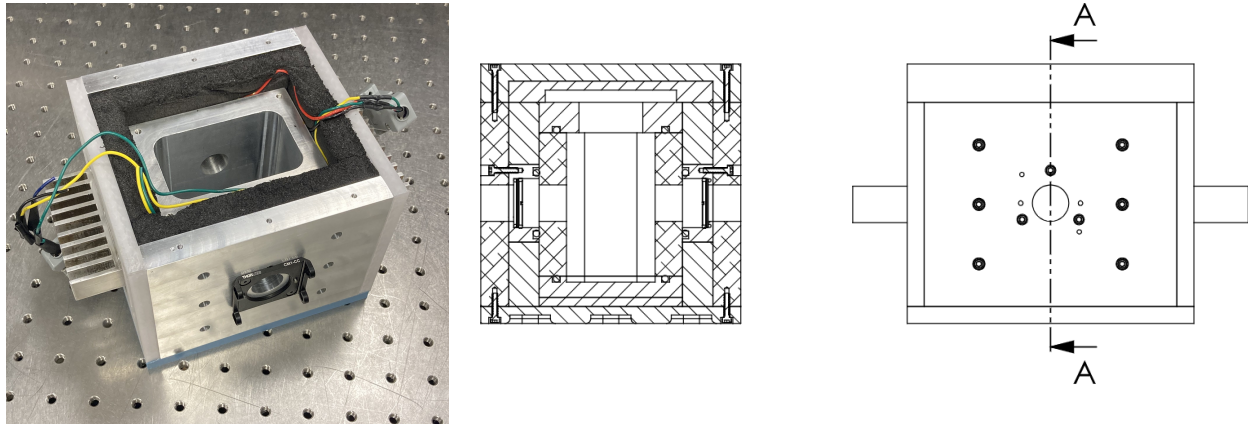


Figure 3.14: Left: A photo of the inner chamber of the first stage of the temperature-stabilized etalon mount. Right: A SolidWorks drawing of the left, including a cross-sectional view. The drawing is shown with the lid and the cover.

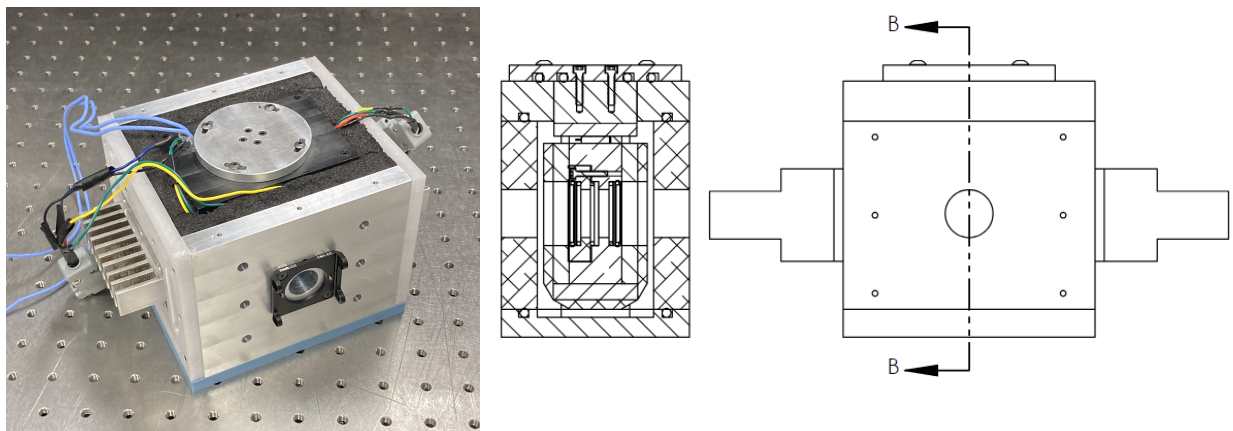


Figure 3.15: Left: A photo of the second stage of the receiver inside the first stage of the temperature-stabilized etalon mount. Right: A SolidWorks drawing of the left, including a cross-sectional view. The drawing shows the first stage chamber without insulation.

The heat sink for the second stage is insulated with a cover. The cover is made of two layers — a layer of insulating rubber foam and a 3D-printed shell. This cover prevents ambient air from interacting with the second-stage heat sink, thus improving the thermal stability of the etalon. The entire assembly with the cover can be seen in Figure 3.11. The first two versions of the etalon mount did not have this cover, and it was found that the heat sink conducted too much heat into the second stage, causing drifts in the etalon transmission.

Thermal simulations were conducted on the design of the temperature-stabilized etalon mount using SolidWorks. The results showed that during steady-state operation and ambient temperature being 10° C colder than the set temperature, the coldest point on the etalon would be 0.81 mK colder than the set temperature. The temperature gradients across the active area would be less than 0.80 mK. Additionally, the temperature of the inside face of the first stage would be within 20 mK of the set temperature for the same conditions.

The simulations assumed perfect isolation of the inside of the first stage from the ambient environment. A constant convective heat transfer coefficient of $21.7 \frac{W}{m^2 K}$ between the exterior of the first stage and the ambient was used, as recommended by Wavelength Electronic [163]. The air inside the first stage was assumed to be nearly quiescent, as the only forcing would be buoyantly driven flow in a nearly isothermal chamber. In quiescent air, the convective heat transfer coefficient is $0.21 \frac{W}{m^2 K}$ [164]. A conservative value of $1 \frac{W}{m^2 K}$ was chosen and applied to the second stage and the inner faces of the first stage.

Electronic Design

The temperature stabilization electronics consist of a temperature controller, a TEC (or series of TECs), and a thermistor. A block diagram of the electronics of the temperature-control scheme can be seen in Figure 3.16. During lidar operation, the etalon mount will be kept $\sim 5^\circ$ C above room temperature.

The control system uses Thorlabs temperature controllers (TED 8020) to regulate the temperature of the temperature-stabilized etalon mount. The TEC controller has a resistance measurement resolution of 0.3Ω and a 24-hour stability of 0.5Ω when operating with a $100 \mu\text{A}$ bias current. Laird TECs are used as the active heating element for the first and second stages. The first stage uses four CP08-63-06-L-RT-W4.5 TECs in series, and the second stage uses an OTX20-66-F0-1211-11-W2.25 TEC. The TECs and controllers' performance has been modeled based on Wavelength Electronics' technical notes [163, 165, 166]). The temperature can be maintained up to 14.5 degrees Celsius above room temperature, using a conservative estimate of $21.7 \frac{W}{m^2 K}$ for the convective heat transfer coefficient. The TCS-620

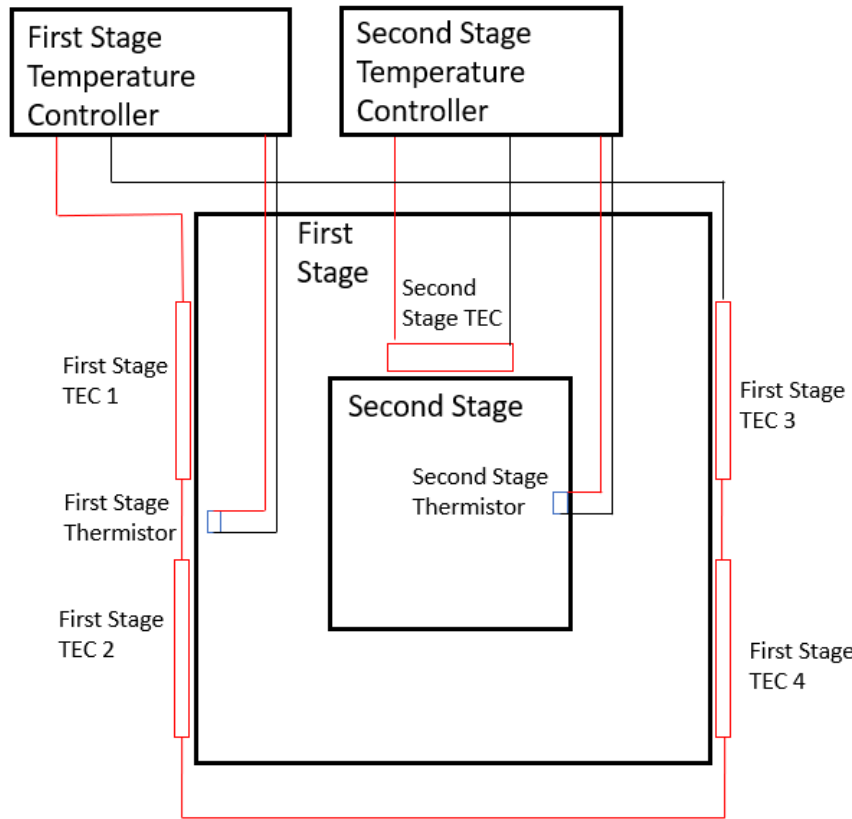


Figure 3.16: A block diagram of the temperature control electronics.

thermistor by wavelength electronics is used for the temperature probe. This thermistor has a slope of $880 \frac{\Omega}{K}$ at $25^\circ C$, which, when multiplied by the resistance measurement resolution of the TEC controller, gives a temperature measurement stability of 0.34 mK and a 24-hour stability of 0.56 mK .

Testing

Four temperature-stabilized etalon mount prototypes were created and tested. The laser was stabilized in these tests, as described in the Laser Stabilization section. The stabilized laser was incident on a 50/50 beamsplitter, where one leg was reflected onto a detector for a reference signal, and the other leg was passed through the temperature-stabilized etalon mount before being incident on a detector. The transmission of the etalon is the ratio of the detected signal through the etalon to the reference signal, normalized to the maximum transmission observed through the etalon. The etalon was temperature-tuned so that the laser frequency was located on the point of half-maximum transmission to maximize the

transmission slope. This test was run multiple times to identify and troubleshoot issues with the temperature-stabilized mount. Figure 3.17 shows the best performance. The etalon had a temperature stability of 1.15 mK for 96 hours. The room temperature varied by less than 0.4 K during this period.

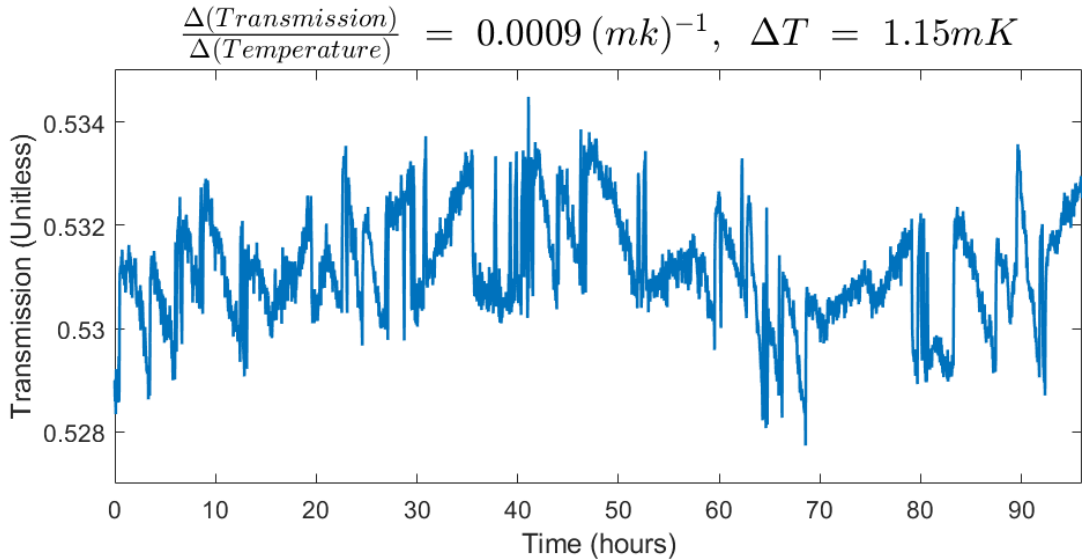


Figure 3.17: The best temperature stability performance of the temperature-stabilized etalon mount. This test recorded a stability of 1.15 mK over 96 hours.

Typically, the etalon is stable to 2 mK for 1-hour periods and 10 mK for 24-hour periods. The wind speed errors that would be caused by a 2 mK and 10 mK temperature stability would be $0.196 \frac{m}{s}$ and $0.98 \frac{m}{s}$, respectively, if the etalon temperatures are correlated and $0.138 \frac{m}{s}$ and $0.692 \frac{m}{s}$, respectively, if their errors were random. However, the etalon transmission drift appears strongly correlated with a changing room temperature, making the former scenario more likely. Efforts will continue to minimize the transmission drift caused by temperature drift in the etalon. However, the stringent temperature stability requirements cited by Repasky et al. [113] may not be necessary for long-term stability, as a bias correction can be implemented. Refer to the Research Plan section for details.

One issue is that the transmission drifts dramatically due to the mechanical elements shifting for approximately a week after the mount is assembled. Figure 3.18 shows an example of this type of drift. This effect disappears after approximately two weeks, but the temperature-stabilized etalon mounts will not be usable during that time. This effect is similar to the long-term instrument drift observed in the ALADIN double-edge receiver [167], which was corrected in the wind speed retrievals. A solution to this issue might not

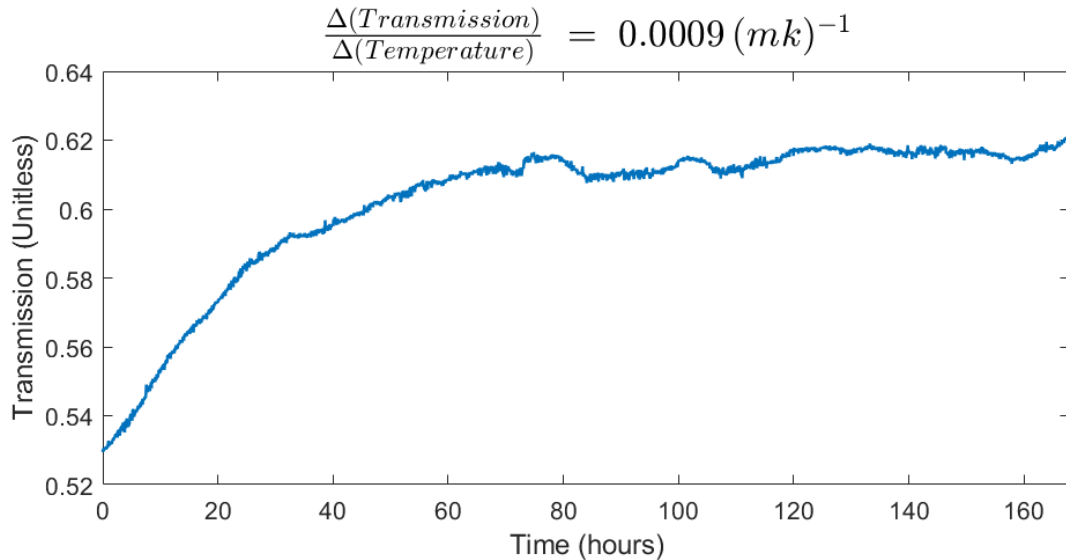


Figure 3.18: The long-term drift of the temperature-stabilized etalon mount caused by mechanical drift.

exist, and there will have to be a 2-week waiting period between assembling and using the temperature-stabilized etalon mounts.

Second-Stage Receiver

Summary

The lidar second-stage receiver was designed using previous MPD designs (e.g., [103, 105, 107, 108]) as a template, with adaptations made to incorporate the temperature-stabilized etalon mounts. Some parts for the second-stage receiver have been designed and machined. The second-stage receiver still needs to be completed.

Introduction

A block diagram of the second-stage receiver is shown in Figure 3.19. The second-stage receiver is based on the light-tight Thorlabs cage cube system, preventing unwanted photons from reaching the detector. The SolidWorks drawings of the second-stage receiver are shown in Appendix E. Details about the design will be given in the following subsection.

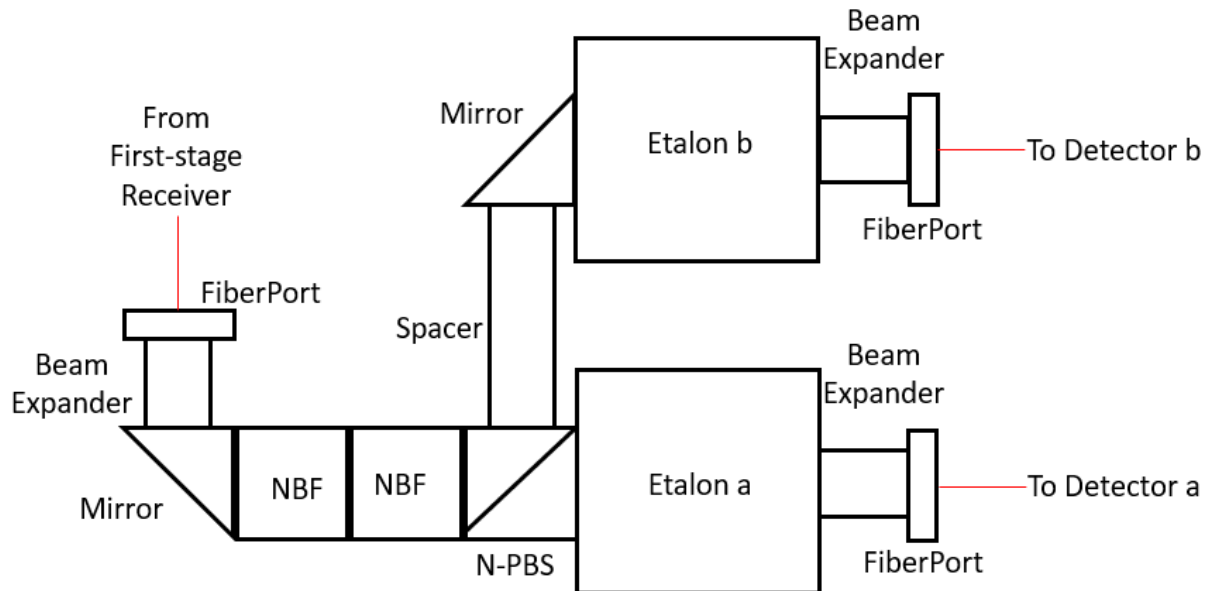


Figure 3.19: The second-stage receiver block diagram.

Design

Although previous MPD designs inspired the second-stage receiver, there are differences between the one in the DLB direct-detection DWL and those in previous instruments. The most significant difference is incorporating the temperature-stabilized etalon mounts in the receiver. The modular cage cube design allows easy attachment and removal of each component. Custom adapters were created to interface the fiber collimators with the cage cube system and to connect the compact cage cube components with the full-size components.

Light entering the system is collimated using a fiber collimator (Thorlabs, PAF2P-11B). The light is then expanded with a 2.25x beam expander (Thorlabs ACN127-020-B [$f = -20\text{mm}$] and AC254-045-B [$f = 45\text{ mm}$]). This expansion increases the effective finesse of the etalons, as larger beams have lower divergence angles. Identical beam expanders reduce the size of the beam for coupling into the multimode fibers, which lead to the APDs.

The NBFs (Alluxa 780.2-0.4 OD6) are mounted on kinematic mounts (Thorlabs B4CRP), enabling precise angular tuning to optimize transmission for the laser linewidths. With a bandwidth of 0.4 nm, these filters block most of the sky background. The etalons (Light Machinery OP-7423-1686-2) act as edge filters and effectively attenuate much of the remaining background, as they have a bandwidth of 0.12 nm. A field stop (the multimode

fiber core) limits the angles at the NBFs and the etalons to < 3 mrad [105], preventing range-dependent errors. These angles will lead to a slight degradation in the finesse of the etalon, but the double-edge technique will still work. The multimode fiber also mixes the spatial intensity distribution of the energy collected from each range bin, providing uniform angular distribution at the filters and etalons. This technique was described by Grund and Eloranta [168] and is implemented in several edge DWLs (e.g., [23, 29, 40, 45, 157]).

The beam is steered from the input to the multimode fibers that lead to the APDs using the position of the collimating lenses in the fiber ports and the tilt of the two mirrors. The beam from the input to detector a has six degrees of freedom (two at each fiber collimator and two at the mirror), and the beam from the input to detector b has eight degrees of freedom, four of which are independent of the beam path from the input to a, allowing the light to be guided through the system and coupled into the fibers leading to the APDs.

All lens tubes are reinforced with cage rods to maintain optomechanical stability when attaching and removing the multimode fibers, as recommended by Robert Stillwell [151]. Reflective mylar tape covers the rear of the mirrors, preventing stray light from entering the system.

In contrast to previous systems, custom aluminum spacers connected with cage cube connectors were used to provide spacing between receiver elements instead of lens tubes. The cage cube connectors provide better mechanical stability when aligning the system.

RESEARCH PLAN

The primary goal of the proposed research effort is the development and demonstration of a direct detection DWL based on the DLB architecture of the MPD. The following milestones and tasks must be completed to achieve this goal.

1. Instrument Development

- Develop the instrument hardware.
- Complete the assembly of the lidar transmitter and verify its performance.
- Complete the assembly of the lidar receiver and verify its performance.
- Assemble and align the lidar.

2. Software Development

- Develop the instrument control software, including data acquisition, background measurements, calibration scans, and bias correction measurements.
- Write the retrieval algorithm program, including etalon transmission modeling, wind speed retrievals, and mixing height retrievals.

3. Testing and Validation

- Test and troubleshoot the instrument.
- Validate the instrument with horizontal testing.

Approximate timelines for each milestone are given in the section title. An expected publications timeline is shown in the Publications chapter.

Instrument Development (February 2024 - June 2024)

Laser Transmitter (February 2024 - May 2024)

Some components for the laser transmitter have been fabricated (see the Laser Transmitter section), and the laser has been characterized. However, several steps remain, including mounting the TSOA in its housing, measuring the spectral purity of the TSOA, and assembling the laser transmitter on an optical breadboard.

The TSOA will be mounted in its housing and soldered to the coaxial connector. The seed laser will be coupled into the TSOA, and the beam will be aligned to optimize the power

output. The TSOA will be pulsed at 10 kHz with a $1\text{-}\mu\text{s}$ pulse length, and the spectral purity of the output will be measured using an optical spectrum analyzer. This measurement will check for broadband amplified spontaneous emission (ASE) [169]. When operated without a seed laser input, a TSOA will emit ASE from both facets with a broad spectral width ($\sim 20\text{-}30\text{nm}$). ASE is drastically reduced in the presence of a seed laser while operating the TSOA in a MOPA configuration. However, a small amount of ASE could cause systematic biases in the wind speed retrieval, especially range-dependent biases, as the ASE has a different divergence angle than the amplified seed laser [106]. The ASE can be reduced in the DLB direct-detection DWL by tuning the seed laser alignment and power and by adjusting the TSOA pulse current to ensure gain saturation [106, 169, 170].

Once the spectral purity of the TSOA is verified, the laser stabilization scheme and transmitter optics will be transferred to a $2'\times 4'$ optical breadboard to be aligned with the telescope.

Temperature-Stabilized Etalon Mount (February 2024 - April 2024)

Several prototype temperature-stabilized etalon mounts have been created (see the Etalon Temperature Stabilization section). The temperature-stabilized etalon mount is nearly complete but has not demonstrated long-term (weeks to months) stability at 5 mK. However, it has been achieved for several days at a time. Testing and troubleshooting to identify issues with the thermal stability is ongoing.

Biases due to the temperature drift in the etalon will be corrected using a similar method to those used by interferometric DWLs (e.g., [49, 57, 60]). A bias correction involves sending a small amount of the laser light into the receiver, observing the apparent Doppler shift from the unshifted light, and subtracting this instrument bias from the vertical wind speeds retrieved by the atmosphere. During lidar operation, the zero-bias measurement will be conducted by deactivating the TSOA and closing a camera shutter at the focal point of the field lens and telescope. In this state, the TSOA absorbs the laser light, allowing only a minimal amount to illuminate the shutter. The diffuse reflection from this shutter will be reflected into the lidar receiver.

Lidar Receiver (February 2024 - May 2024)

The lidar receiver has been designed, and some components have been fabricated (see the Second-Stage Receiver section). However, the entire receiver needs to be assembled and aligned. This alignment will be done by practices developed by the MPD group at MSU

and NCAR [150, 151]. Following successful alignment, the receiver will be mounted onto an optical breadboard.

Assemble and Align the Lidar (May 2024 - June 2024)

The laser transmitter and the lidar receiver need to be aligned with a telescope in a roofport laboratory. The lidar optics will be mounted onto a cart and transferred to Cobleigh Hall 616, where it will be aligned with an F-4.5 telescope using proven best practices developed by the MPD group [150, 151]. The beam will be transmitted to the sky through the roofport and can be operated while attended in dry conditions.

Software Development (July 2024 - September 2025)

Instrument Control and Data Acquisition Software (July 2024 - September 2024)

The instrument control and data acquisition software will be implemented using LabVIEW, leveraging the program that runs the O_2 DIAL system as a template. While much of the code can be reused, adjustments will be made to accommodate different hardware, such as Newport laser controllers replacing Thorlabs ones.

The data acquisition software will control the trigger pulses to the TSOAs and the MCS. User inputs will start the various functions, including data acquisition and calibration scans. Additionally, users can adjust parameters like the repetition rate (defaulting to 10 kHz) and pulse length (defaulting to 1 μ s).

Modifications are necessary for the laser stabilization software, such as adapting it for FMS instead of using a wavemeter. A laser stabilization monitor will be developed, triggering an error if the error signal voltage surpasses a specified threshold. The etalon temperature-stabilization software will also be refined. The calibration scan program for the HSRL will be reused for the DLB direct-detection DWL.

The data acquisition program will be modified to include a bias correction. This measurement involves turning off the TSOA and closing a camera shutter while recording data with the detector. This program (15 seconds to a minute long) will run every hour.

Afterpulsing, which is the delayed response of an APD caused by a high-powered pulse [171], causes a range-dependent false signal in the lidar profiles due to initial oversaturation of the APD by the outgoing laser pulse. Afterpulsing is analogous to seeing a ghost image of a bright light (like the sun) after looking away from the source. Afterpulsing measurements will be recorded after each instrument alignment using the method described by Campbell et al. for use in MicroPulse Lidars [98]. This measurement involves placing an absorptive

piece of black foam on top of the telescope in the transmitted beam path and measuring the time-dependent false signal.

Approximately 1% of the duty cycle will be used for background measurements. This measurement will involve not pulsing the TSOA while taking measurements from the detectors. APD dark counts will also be captured in the background measurement.

Data collected will be stored as NetCDF files containing timestamped lidar signal profiles integrated into 2-second intervals. It will also store housekeeping information like the laser temperature, current, and lock status.

Retrieval Algorithm (October 2024 - August 2025)

The retrieval algorithm must be developed to convert the raw photon count data to wind speeds. These programs will be implemented using MATLAB and Python.

A MATLAB code will be written to generate the transmission curves for the two etalon channels from the calibration scan data. This algorithm follows a similar process to the HSRL calibrations described in Colberg [109]. One difference between these programs is that the etalon transmission spectrum will be modeled to fit the measured data (equations 2-5 in Spuler et al. [105]). The etalons for the DLB direct-detection DWL are catalog products and have transmission properties slightly different than those modeled by Repasky et al. [113]. For this reason, the optimal etalon offset will need to be re-determined using the measured transmission curves.

These transmission curves can be tested and verified using a method described by Xia et al. [32]. The TSOA will be turned off in this verification test, and the bias correction program will be run. However, instead of a camera shutter, a rotating disk that spins at a known angular velocity is placed at the focal point of the field lens. The light scattered by the revolving disk into the detector has a known Doppler shift. The retrieved Doppler shift can be compared against the known Doppler shift to assess the accuracy of the transmission curves.

In the wind speed retrieval, the data will first be corrected for nonidealities caused by the APD deadtime (the time period after an avalanche event where the detector is unable to detect another photon) using multiphoton timing statistics [171]. Then, background and afterpulsing measurements will be subtracted from the lidar profiles, as described by Campbell et al. [98]. The algorithm will remove clouds and precipitation from the data using a method outlined in Colberg [109], which used the first two features in the features-extraction from Binietoglou et al. [172]. This method uses a 2-D edge finder (Sobel operator)

and the spatiotemporal variance of the signal. If the Sobel operator or the variance exceeds a manually selected threshold, the bin is flagged as cloudy and excluded from the wind speed retrieval. The HSRL-measured backscatter ratio profiles at 770 nm will be retrieved using the method described by Colberg [109]. The backscatter ratio at 780 nm will be estimated using the measured backscatter ratio at 770 nm, and the Angstrom exponent [173] measured by a nearby Aeronet solar radiometer [174].

The molecular backscattering spectrum relies on a model of the atmospheric temperature and pressure profiles. The temperature will be modeled using surface conditions as a boundary condition for a constant-lapse rate atmosphere. The pressure profile will be modeled using the barometric formula [175] and a measured surface pressure. Once the pressure and temperature profiles are modeled, the molecular backscatter spectrum will be generated from a principal component analysis (PCA) [176] trained with the Tenti-S6 model for Cabannes scattering [120]. PCA allows spectrum reconstruction in a single matrix multiplication process with high accuracy. When performing PCA, the first principal component of a set of variables is the linear combination of the original variables that explains the most variance. Each additional principal component explains the most variance of the remaining unexplained variance. Binietoglou et al. [176] demonstrated errors of less than 0.05% between the Tenti-S6 model and reconstructed spectra using four principal components. PCA significantly reduces processing time, as generating spectra from the Tenti-S6 code is computationally expensive, and spectra must be generated for every bin in the retrieval. A sensitivity analysis for the wind retrieval concerning the estimated temperature and pressure will be performed.

Once the atmosphere is modeled, transmission spectra through the etalons are known, and the corrected photon counts are obtained, the wind speed can be retrieved using Equation 2.14. The error will be estimated by linear propagation, including covariance between error sources [177].

After vertical wind speeds are retrieved, the variance of vertical wind speeds will be used to estimate the mixing height. The mixing height is the height to which aerosol or gaseous chemical species become well-mixed within the PBL. The mixing height is a crucial meteorological parameter for describing turbulent mixing and convective transfer. The convective PBL is characterized by turbulent eddies driven by heat flux and has high vertical velocity variances. Therefore, the mixing height can be found at the lowest altitude where the vertical velocity variance falls below a certain threshold. Although the statistical moments of the lidar signal are contaminated by random noise associated with photon counting, the

temporally correlated variance linked with turbulence can be extracted by the autocovariance extrapolation technique described by Lenschow et al. [178]. Tucker et al. used this technique to determine the mixing height using a heterodyne DWL [179], suggesting its applicability for the DLB direct-detection DWL. These mixing height retrievals will be compared to those found using the HSRL, using the method presented in Colberg et al. [124].

Denoising techniques, such as Poisson thinning [180], can be explored for their effectiveness in improving vertical wind speed retrievals. Poisson thinning is a process where smoothing filter widths are optimized to minimize random error due to Poisson noise while minimizing the blurring effects on correlated structures. It has been applied to the DLB-HSRL data [107] and significantly improved data in the free troposphere.

Testing and Validation (October 2024 - December 2025)

Testing and Troubleshooting (October 2024 - August 2025)

Challenges are anticipated while developing the DLB direct-detection DWL. During this period, the instrument will be tested and troubleshooted, the software will be debugged, and unforeseen issues will be fixed.

Horizontal Testing and Validation (September 2025 - December 2025)

The lidar can only be useful for a meteorological application if the wind speed can be verified. This validation will be conducted through horizontal testing and comparisons to an anemometer.

The lidar beam can be horizontally propagated using two methods. First, it can be achieved by placing a right-angle mirror on the roofport and reflecting the beam at a 90-degree angle. Alternatively, the beam can be directed horizontally by removing the window from the roofport room and aiming the telescope accordingly. The vector component of the wind speed can be compared to anemometer observations.

More precise validation methods, like comparison to radar wind profilers, other DWLs, or radiosondes, require expensive equipment. Comparison to models like the ECMWF reanalyses can be helpful but cannot replace the importance of validating findings with co-located measurements. Therefore, the in-situ measurements with an anemometer are the best option for validating the wind speed measurements made by the DLB direct-detection DWL.

PUBLICATIONS

This chapter provides a list of completed publications and planned future publications. Coauthored publications will be included in the Completed Publications section and only first-authored papers will be included in the Planned Publications section. Planned publications will be ordered by importance, and a brief description and expected time of submission will be given.

Completed Publications

Journal Articles

- **L. Colberg**, O. Cruikshank, and K. S. Repasky. Planetary Boundary Layer Height Retrieval from a Diode-Laser-Based High Spectral Resolution Lidar. *Journal of Applied Remote Sensing*, 16(2):024507, 2022. <https://doi.org/10.1117/1.JRS.16.024507>.
- K. S. Repasky, O. Cruikshank, and **L. Colberg**. Performance modeling of a diode-laser-based direct-detection Doppler lidar for vertical wind profiling. *Journal of Atmospheric and Oceanic Technology*, 39(11):1655 – 1668, 2022. <https://doi.org/10.1175/JTECH-D-22-0001.1>.

Conference Proceedings

- **L. Colberg**, O. Cruikshank, K. S. Repasky, S. M. Spuler, R. A. Stillwell, and M. Hayman. Planetary Boundary Layer Height Retrieval Using MicroPulse DIAL. In J. T. Sullivan, T. Leblanc, S. Tucker, B. Demoz, E. Eloranta, C. Hostetler, S. Ishii, L. Mona, F. Moshary, A. Papayannis, and K. Rupavatharam, editors, *Proceedings of the 30th International Laser Radar Conference*, pages 355-361, Remote, 2022. Springer International Publishing. ISBN 978-3-031-37818-8. https://doi.org/10.1007/978-3-031-37818-8_47.

- O. Cruikshank, **L. Colberg**, K. S. Repasky, R. A. Stillwell, and S. M. Spuler. MicroPulse Differential Absorption Lidar for Temperature Retrieval in the Lower Troposphere. In J. T. Sullivan, T. Leblanc, S. Tucker, B. Demoz, E. Eloranta, C. Hostetler, S. Ishii, L. Mona, F. Moshary, A. Papayannis, and K. Rupavatharam, editors, Proceedings of the 30th International Laser Radar Conference, pages 395-401, Remote, 2022. Springer International Publishing. ISBN 978-3-031-37818-8. https://doi.org/10.1007/978-3-031-37818-8_52.
- K. S. Repasky, O. Cruikshank, and **L. Colberg**. Performance Modeling of a Diode-Laser-Based Direct-Detection Doppler Lidar. In J. T. Sullivan, T. Leblanc, S. Tucker, B. Demoz, E. Eloranta, C. Hostetler, S. Ishii, L. Mona, F. Moshary, A. Papayannis, and K. Rupavatharam, editors, Proceedings of the 30th International Laser Radar Conference, pages 365-371, Remote, 2022. Springer International Publishing. ISBN 978-3-031-37818-8. https://doi.org/10.1007/978-3-031-37818-8_48.

Master's Thesis

- **L. Colberg**. Diode-Laser-Based High Spectral Resolution LiDAR. Master's thesis, Montana State University-Bozeman, Norm Asbjornson College of Engineering, Bozeman MT, United States of America, 2021. Available at <https://scholarworks.montana.edu/xmlui/bitstream/handle/1/16596/colberg-diode-laser-2021.pdf?sequence=1>.

Presentations

- **L. Colberg**, O. Cruikshank, and K. S. Repasky. Progress Toward a Diode-Laser-Based Doppler Wind Lidar. In 104th American Meteorological Society Annual Meeting, Baltimore MD, U.S.A., 2024. AMS.
- **L. Colberg**, O. Cruikshank, P. F. Morgan, K. S. Repasky, R. A. Stillwell, and S. M. Spuler. Improved Planetary Boundary Layer Height Retrievals from a Diode-Laser-Based High Spectral Resolution Lidar. In 103rd AMS Annual Meeting, Denver CO, U.S.A., 2023. AMS.
- **L. Colberg**, O. Cruikshank, K. S. Repasky, S. M. Spuler, R. A. Stillwell, and M. Hayman. Planetary Boundary Layer Height Measurements using Diode-Laser-Based High Spectral Resolution Lidar. In 102nd American Meteorological Society Annual Meeting, Remote., 2022. AMS.

- O. Cruikshank, **L. Colberg**, K. S. Repasky, R. A. Stillwell, and S. M. Spuler. Micropulse Differential Absorption Lidar for Temperature Retrieval in the Lower Troposphere Recent Improvements and Testing. In 103rd American Meteorological Society Annual Meeting, Denver CO, U.S.A., 2023. AMS.
- O. Cruikshank, **L. Colberg**, K. S. Repasky, R. A. Stillwell, S. M. Spuler, and M. Hayman. Micropulse Differential Absorption Lidar for Temperature Retrieval in the Lower Troposphere. In 102nd American Meteorological Society Annual Meeting, Remote, 2022. AMS.
- O. Cruikshank, **L. Colberg**, K. S. Repasky, R. A. Stillwell, M. Hayman, and S. M. Spuler. Modeling the Micro-Pulse DIAL (MPD) Performance at Low Ranges, and Improving Temperature Profiling Retrieval Algorithms. In 101st American Meteorological Society Annual Meeting, Remote, 2021. AMS.
- R. A. Stillwell, S. M. Spuler, M. Hayman, K. S. Repasky, O. Cruikshank, and **L. Colberg**. Progress toward the Network Deployment of Atmospheric Temperature Profiling Using Differential Absorption Lidar. In 101st American Meteorological Society Annual Meeting, Remote, 2021. AMS.

Planned Publications

Journal Articles

- Demonstration of a Diode-Laser-Based Direct-Detection Doppler Wind Lidar (Mid 2025).

This paper will describe the DLB direct-detection DWL and present results from validations compared to in-situ wind speed measurements.

- Mixing Height Retrievals using the Diode-Laser-Based Direct-Detection Doppler Wind Lidar (Late 2025).

This paper will describe the mixing height retrieval using the vertical wind profiles from the DLB direct-detection DWL with comparisons to radiosondes and the HSRL.

- Design and Demonstration of a Temperature-Stabilized Etalon Mount System for Solid Etalons, (Late 2024/Early 2025)

This paper will describe the design and testing of the temperature-stabilized etalon mount. It will also describe the bias correction reference measurement and implementation.

- Mixing Height Retrievals from the MicroPulse DIAL during the M2HATS Field Experiment (Late 2024/Early 2025)

This paper will present mixing height retrievals from water vapor and aerosol profiles retrieved by MPDs during the M2HATS field experiment with comparisons to radiosondes. This paper is a side project that continues the work presented at the International Laser Radar Conference in 2022 [181].

Presentations

- Preliminary Results from a Diode-Laser-Based Direct-Detection Doppler Wind Lidar, In 105th American Meteorological Society Annual Meeting, New Orleans LA, U.S.A., 2025. AMS. (January 2025).

This presentation will present any preliminary results obtained by January 2025 at the American Meteorological Society Annual Meeting.

REFERENCES CITED

- [1] T. Foken. *Springer Handbook of Atmospheric Measurements*. Springer International Publishing, Cham, Switzerland, 2021. ISBN 978-3-030-52170-7. doi:10.1007/978-3-030-52171-4.
- [2] R. B. Stull. *An Introduction to Boundary Layer Meteorology*. Springer Dordrecht, Dordrecht, Netherlands, 1988. ISBN 978-90-277-2768-8. doi:10.1007/978-94-009-3027-8.
- [3] J. R. Garratt. *The Atmospheric Boundary Layer*. Cambridge University Press, Cambridge, United Kingdom, 1992. ISBN 978-0-521-46745-2.
- [4] National Research Council. *Observing Weather and Climate from the Ground Up: A Nationwide Network of Networks*. The National Academies Press, Washington D.C., U.S.A., 2009. ISBN 978-0-309-12986-2. doi:10.17226/12540.
- [5] National Research Council. *When Weather Matters: Science and Services to Meet Critical Societal Needs*. The National Academies Press, Washington D.C., U.S.A., 2010. ISBN 978-0-309-15249-5. doi:10.17226/12888.
- [6] J. Teixeira, J. R. Piepmeier, A. R. Nehrir, C. O. Ao, S. S. Chen, C. A. Clayson, A. M. Fridlind, M. Lebsack, W. McCarty, H. Salmun, J. A. Santanello, D. D. Turner, Z. Wang, and X. Zeng. Toward a global planetary boundary layer observing system: The NASA PBL incubation study team report. Technical report, National Aeronautics and Space Administration, 2021. URL <https://ntrs.nasa.gov/api/citations/20230001633/downloads/AFridlindPBLTowardsReport.pdf>.
- [7] National Academies of Science, Engineering, and Medicine. *Thriving on Our Changing Planet: A Decadal Strategy for Earth Observation from Space*. The National Academies Press, Washington D.C., U.S.A., 2018. ISBN 978-0-309-46757-5. doi:10.17226/24938.
- [8] National Academies of Sciences, Engineering, and Medicine. *The Future of Atmospheric Boundary Layer Observing, Understanding, and Modeling: Proceedings of a Workshop*. The National Academies Press, Washington D.C., U.S.A., 2018. ISBN 978-0-309-47723-9. doi:10.17226/25138.
- [9] C. Weitkamp. *Lidar: Range-Resolved Optical Remote Sensing of the Atmosphere*. Springer New York, New York City, U.S.A., 2005. ISBN 978-0-387-40075-4. doi:10.1007/b106786.
- [10] C. F. Bohren and D. R. Huffman. *Absorption and Scattering of Light by Small Particles*. Wiley-VCH, Weinheim, Germany, 1998. ISBN 978-0-471-29340-8. doi:10.1002/9783527618156.

- [11] C. Werner. *Doppler Wind Lidar*, pages 325–354. Springer New York, New York City, U.S.A., 2005. ISBN 978-0-387-25101-1. doi:10.1007/0-387-25101-4_12.
- [12] O. Reitebuch. *Wind Lidar for Atmospheric Research*, pages 487–507. Springer Berlin Heidelberg, Berlin, Germany, 2012. doi:10.1007/978-3-642-30183-4_30.
- [13] O. Reitebuch and R. M. Hardesty. *Doppler Wind Lidar*, pages 759–797. Springer International Publishing, Cham, Switzerland, 2021. ISBN 978-3-030-52171-4. doi:10.1007/978-3-030-52171-4_27.
- [14] M. Shangguan, J. Qiu, J. Yuan, Z. Shu, L. Zhou, and H. Xia. Doppler wind lidar from UV to NIR: A review with case study examples. *Frontiers in Remote Sensing*, 2: 787111, 2022. doi:10.3389/frsen.2021.787111.
- [15] G. Benedetti-Michelangeli, F. Congeduti, and G. Fiocco. Measurement of aerosol motion and wind velocity in the lower troposphere by Doppler optical radar. *Journal of Atmospheric Sciences*, 29(5):906 – 910, 1972. doi:10.1175/1520-0469(1972)029<0906:MOAMAW>2.0.CO;2.
- [16] E. W. Eloranta, J. M. King, and J. A. Weinmann. The determination of wind speeds in the boundary layer by monostatic lidar. *Journal of Applied Meteorology and Climatology*, 14:1485 – 1489, 1975. doi:10.1175/1520-0450(1975)014<1485:TDOMSI>2.0.CO;2.
- [17] J. A. McKay. Modeling of direct detection Doppler wind lidar. I. The edge technique. *Applied Optics*, 37(27):6480–6486, 1998. doi:10.1364/AO.37.006480.
- [18] J. A. McKay. Modeling of direct detection Doppler wind lidar. II. The fringe imaging technique. *Applied Optics*, 37(27):6487–6493, 1998. doi:10.1364/AO.37.006487.
- [19] M. J. McGill and J. D. Spinhirne. Comparison of two direct-detection Doppler lidar techniques. *Optical Engineering*, 37(10):2675 – 2686, 1998. doi:10.1117/1.601804.
- [20] M. L. Chanin, A. Garnier, A. Hauchecorne, and J. Porteneuve. A Doppler lidar for measuring winds in the middle atmosphere. *Geophysical Research Letters*, 16(11): 1273–1276, 1989. doi:10.1029/GL016i011p01273.
- [21] A. Garnier and M. L. Chanin. Description of a Doppler Rayleigh LIDAR for measuring winds in the middle atmosphere. *Applied Physics B*, 55(1):35–40, 1992. doi:10.1007/BF00348610.
- [22] C. L. Korb, B. M. Gentry, and C. Y. Weng. Edge technique: theory and application to the lidar measurement of atmospheric wind. *Applied Optics*, 31(21):4202–4213, 1992. doi:10.1364/AO.31.004202.
- [23] C. L. Korb, B. M. Gentry, and S. X. Li. Edge technique Doppler lidar wind measurements with high vertical resolution. *Applied Optics*, 36(24):5976–5983, 1997. doi:10.1364/AO.36.005976.

- [24] C. L. Korb, B. M. Gentry, S. X. Li, and C. Flesia. Theory of the double-edge technique for Doppler lidar wind measurement. *Applied Optics*, 37(15):3097–3104, 1998. doi:10.1364/AO.37.003097.
- [25] C. Flesia and C. L. Korb. Theory of the double-edge molecular technique for Doppler lidar wind measurement. *Applied Optics*, 38(3):432–440, 1999. doi:10.1364/AO.38.000432.
- [26] C. Souprayen, A. Garnier, A. Hertzog, A. Hauchecorne, and J. Porteneuve. Rayleigh–Mie Doppler wind lidar for atmospheric measurements. I. Instrumental setup, validation, and first climatological results. *Applied Optics*, 38(12):2410–2421, 1999. doi:10.1364/AO.38.002410.
- [27] C. Souprayen, A. Garnier, and A. Hertzog. Rayleigh–Mie Doppler wind lidar for atmospheric measurements. II. Mie scattering effect, theory, and calibration. *Applied Optics*, 38(12):2422–2431, 1999. doi:10.1364/AO.38.002422.
- [28] S. M. Khaykin, A. Hauchecorne, R. Wing, P. Keckhut, S. Godin-Beekmann, J. Porteneuve, J.-F. Mariscal, and J. Schmitt. Doppler lidar at Observatoire de Haute-Provence for wind profiling up to 75 km altitude: performance evaluation and observations. *Atmospheric Measurement Techniques*, 13(3):1501–1516, 2020. doi:10.5194/amt-13-1501-2020.
- [29] B. M. Gentry, H. Chen, and S. X. Li. Wind measurements with 355-nm molecular Doppler lidar. *Optics Letters*, 25(17):1231–1233, 2000. doi:10.1364/OL.25.001231.
- [30] B. Gentry, M. McGill, G. Schwemmer, M. Hardesty, A. Brewer, T. Wilkerson, R. Atlas, M. Sirota, S. Lindemann, and F. Hovis. Development of an airborne molecular direct detection Doppler lidar for tropospheric wind profiling. In U. N. Singh, editor, *Lidar Remote Sensing for Environmental Monitoring VIII*, volume 6681, page 66810B. SPIE, 2007. doi:10.1117/12.739379.
- [31] B. M. Gentry and H. Chen. Performance validation and error analysis for a direct-detection molecular Doppler lidar. In U. N. Singh, T. Itabe, and Z. Liu, editors, *Lidar Remote Sensing for Industry and Environment Monitoring III*, volume 4893, pages 287 – 294. SPIE, 2003. doi:10.1117/12.466526.
- [32] H. Xia, D. Sun, Y. Yang, F. Shen, J. Dong, and T. Kobayashi. Fabry-Perot interferometer based Mie Doppler lidar for low tropospheric wind observation. *Applied Optics*, 46(29):7120–7131, 2007. doi:10.1364/AO.46.007120.
- [33] H. Xia, X. Dou, D. Sun, Z. Shu, X. Xue, Y. Han, D. Hu, Y. Han, and T. Cheng. Mid-altitude wind measurements with mobile Rayleigh Doppler lidar incorporating system-level optical frequency control method. *Optics Express*, 20(14):15286–15300, 2012. doi:10.1364/OE.20.015286.

- [34] X. Dou, Y. Han, D. Sun, H. Xia, Z. Shu, R. Zhao, M. Shangguan, and J. Guo. Mobile Rayleigh Doppler lidar for wind and temperature measurements in the stratosphere and lower mesosphere. *Optics Express*, 22(S5):A1203–A1221, 2014. doi:10.1364/OE.22.0A1203.
- [35] C.-Y. She, J. Yue, Z.-A. Yan, J. W. Hair, J.-J. Guo, S.-H. Wu, and Z.-S. Liu. Direct-detection Doppler wind measurements with a Cabannes–Mie lidar: A comparison between iodine vapor filter and Fabry–Perot interferometer methods. *Applied Optics*, 46(20):4434–4443, 2007. doi:10.1364/AO.46.004434.
- [36] C.-Y. She, J. Yue, Z.-A. Yan, J. W. Hair, J.-J. Guo, S.-H. Wu, and Z.-S. Liu. Direct-detection Doppler wind measurements with a Cabannes–Mie lidar: B. impact of aerosol variation on iodine vapor filter methods. *Applied Optics*, 46(20):4444–4454, 2007. doi:10.1364/AO.46.004444.
- [37] P. Piironen and E. W. Eloranta. Demonstration of a high-spectral-resolution lidar based on an iodine absorption filter. *Optics Letters*, 19(3):234–236, 1994. doi:10.1364/OL.19.000234.
- [38] Z.-S. Liu, W.-B. Chen, T.-L. Zhang, J. W. Hair, and C.-Y. She. An incoherent Doppler lidar for ground-based atmospheric wind profiling. *Applied Physics B*, 3(6):561–566, 1997. doi:10.1007/s003400050215.
- [39] Z.-S. Liu, D. Wu, J.-T. Liu, K.-L. Zhang, W.-B. Chen, X.-Q. Song, J. W. Hair, and C.-Y. She. Low-altitude atmospheric wind measurement from the combined Mie and Rayleigh backscattering by Doppler lidar with an iodine filter. *Applied Optics*, 41(33):7079–7086, 2002. doi:10.1364/AO.41.007079.
- [40] Z.-S. Liu, B.-Y. Liu, Z.-G. Li, Z.-A. Yan, S.-H. Wu, and Z.-B. Sun. Wind measurements with incoherent Doppler lidar based on iodine filters at night and day. *Applied Physics B*, 88(2):327–335, 2007. doi:10.1007/s00340-007-2674-y.
- [41] E. E. Eloranta. *High Spectral Resolution Lidar*, pages 143–163. Springer New York, New York City, U.S.A., 2005. ISBN 978-0-387-25101-1. doi:10.1007/0-387-25101-4_5.
- [42] J. S. Friedman, C. A. Tepley, P. A. Castleberg, and H. Roe. Middle-atmospheric Doppler lidar using an iodine-vapor edge filter. *Optics Letters*, 22(21):1648–1650, 1997. doi:10.1364/OL.22.001648.
- [43] G. Baumgarten. Doppler Rayleigh/Mie/Raman lidar for wind and temperature measurements in the middle atmosphere up to 80 km. *Atmospheric Measurement Techniques*, 3(6):1509–1518, 2010. doi:10.5194/amt-3-1509-2010.
- [44] W. Huang, X. Chu, B. P. Williams, S. D. Harrell, J. Wiig, and C.-Y. She. Na double-edge magneto-optic filter for Na lidar profiling of wind and temperature in the lower atmosphere. *Optics Letters*, 34(2):199–201, 2009. doi:10.1364/OL.34.000199.

- [45] W. Huang, X. Chu, J. Wiig, B. Tan, C. Yamashita, T. Yuan, J. Yue, S. D. Harrell, C.-Y. She, B. P. Williams, J. S. Friedman, and R. M. Hardesty. Field demonstration of simultaneous wind and temperature measurements from 5 to 50 km with a Na double-edge magneto-optic filter in a multi-frequency Doppler lidar. *Optics Letters*, 34(10): 1552–1554, 2009. doi:10.1364/OL.34.001552.
- [46] V. J. Abreu, J. E. Barnes, and P. B. Hays. Observations of winds with an incoherent lidar detector. *Applied Optics*, 31(22):4509–4514, 1992. doi:10.1364/AO.31.004509.
- [47] K. W. Fischer, V. J. Abreu, W. R. Skinner, J. E. Barnes, M. J. McGill, and T.D. Irgang. Visible wavelength Doppler lidar for measurement of wind and aerosol profiles during day and night. *Optical Engineering*, 34(2):499 – 511, 1995. doi:10.1117/12.188598.
- [48] M. J. McGill, W. R. Skinner, and T. D. Irgang. Validation of wind profiles measured with incoherent Doppler lidar. *Applied Optics*, 36(9):1928–1939, 1997. doi:10.1364/AO.36.001928.
- [49] T. D. Irgang, P. B. Hays, and W. R. Skinner. Two-channel direct-detection doppler lidar employing a charge-coupled device as a detector. *Applied Optics*, 41(6):1145–1155, 2002. doi:10.1364/AO.41.001145.
- [50] J. A. McKay. Assessment of a multibeam Fizeau wedge interferometer for Doppler wind lidar. *Applied Optics*, 41(9):1760–1767, 2002. doi:10.1364/AO.41.001760.
- [51] Z. Liu and T. Kobayashi. Differential discrimination technique for incoherent Doppler lidar to measure atmospheric wind and backscatter ratio. *Optical Review*, 3(1):1349–9432, 1996. doi:10.1007/s10043-996-0047-0.
- [52] D. Bruneau. Mach–Zehnder interferometer as a spectral analyzer for molecular Doppler wind lidar. *Applied Optics*, 40(3):391–399, 2001. doi:10.1364/AO.40.000391.
- [53] D. Bruneau and J. Pelon. Simultaneous measurements of particle backscattering and extinction coefficients and wind velocity by lidar with a Mach–Zehnder interferometer: principle of operation and performance assessment. *Applied Optics*, 42(6):1101–1114, 2003. doi:10.1364/AO.42.001101.
- [54] N. Cézard, A. Dolfi-Bouteyre, J.-P. Huignard, and P. H. Flamant. Performance evaluation of a dual fringe-imaging Michelson interferometer for air parameter measurements with a 355 nm Rayleigh-Mie lidar. *Applied Optics*, 48(12):2321–2332, 2009. doi:10.1364/AO.48.002321.
- [55] D. Bruneau, A. Garnier, A. Hertzog, and J. Porteneuve. Wind-velocity lidar measurements by use of a Mach–Zehnder interferometer, comparison with a Fabry–Perot interferometer. *Applied Optics*, 43(1):173–182, 2004. doi:10.1364/AO.43.000173.

- [56] D. Bruneau, J. Pelon, F. Blouzon, J. Spatazza, P. Genau, G. Buchholtz, N. Amarouche, A. Abchiche, and O. Aouji. 355-nm high spectral resolution airborne lidar LNG: system description and first results. *Applied Optics*, 54(29):8776–8785, 2015. doi:10.1364/AO.54.008776.
- [57] S. C. Tucker, C. S. Weimer, S. Baidar, and R. M. Hardesty. The Optical Autocovariance Wind Lidar. Part I: OAWL instrument development and demonstration. *Journal of Atmospheric and Oceanic Technology*, 35(10):2079 – 2097, 2018. doi:10.1175/JTECH-D-18-0024.1.
- [58] S. Baidar, S. C. Tucker, M. Beaubien, and R. M. Hardesty. The Optical Autocovariance Wind Lidar. Part II: Green OAWL (GrOAWL) airborne performance and validation. *Journal of Atmospheric and Oceanic Technology*, 35(10):2099 – 2116, 2018. doi:10.1175/JTECH-D-18-0025.1.
- [59] J. Herbst and P. Vrancken. Design of a monolithic Michelson interferometer for fringe imaging in a near-field, UV, direct-detection Doppler wind lidar. *Applied Optics*, 55(25):6910–6929, 2016. doi:10.1364/AO.55.006910.
- [60] P. Vrancken and J. Herbst. Aeronautics application of direct-detection Doppler wind lidar: An adapted design based on a fringe-imaging Michelson interferometer as spectral analyzer. *Remote Sensing*, 14(14), 2022. doi:10.3390/rs14143356.
- [61] A. Stoffelen, G. J. Marseille, F. Bouttier, D. Vasiljevic, S. de Haan, and C. Cardinali. ADM-Aeolus Doppler wind lidar observing system simulation experiment. *Quarterly Journal of the Royal Meteorological Society*, 132(619):1927–1947, 2006. doi:10.1256/qj.05.83.
- [62] ESA. Adm-aeolus science report. Technical report, European Space Agency, 2008. URL <https://esamultimedia.esa.int/multimedia/publications/SP-1311/SP-1311.pdf>.
- [63] O. Reitebuch. *The Spaceborne Wind Lidar Mission ADM-Aeolus*, pages 815–827. Springer Berlin Heidelberg, Berlin, Heidelberg, Germany, 2012. ISBN 978-3-642-30183-4. doi:10.1007/978-3-642-30183-4_49.
- [64] W. E. Baker, G. D. Emmitt, F. Robertson, R. M. Atlas, J. E. Molinari, D. A. Bowdle, J. Paegle, R. M. Hardesty, R. T. Menzies, R. T. Krishnamurti, R. A. Brown, M. J. Post, J. R. Anderson, A. C. Lorenc, and J. McElroy. Lidar-measured winds from space: A key component for weather and climate prediction. *Bulletin of the American Meteorological Society*, 76(6):869 – 888, 1995. doi:10.1175/1520-0477(1995)076<0869:LMWFSA>2.0.CO;2.
- [65] W. E. Baker, R. Atlas, C. Cardinali, A. Clement, G. D. Emmitt, B. M. Gentry, R. M. Hardesty, E. Källén, M. J. Kavaya, R. Langland, Z. Ma, M. Masutani, W. McCarty, R. B. Pierce, Z. Pu, L. P. Riishojgaard, J. Ryan, S. Tucker, M. Weissmann, and

- J. G. Yoe. Lidar-measured wind profiles: The missing link in the global observing system:. *Bulletin of the American Meteorological Society*, 95(4):543 – 564, 2014. doi:10.1175/BAMS-D-12-00164.1.
- [66] O. Reitebuch, C. Lemmerz, E. Nagel, U. Paffrath, Y. Durand, M. Endemann, F. Fabre, and M. Chaloupy. The airborne demonstrator for the direct-detection Doppler wind lidar ALADIN on ADM-Aeolus. Part I: Instrument design and comparison to satellite instrument. *Journal of Atmospheric and Oceanic Technology*, 26(12):2501 – 2515, 2009. doi:10.1175/2009JTECHA1309.1.
- [67] U. Paffrath, C. Lemmerz, O. Reitebuch, B. Witschas, I. Nikolaus, and V. Freudenthaler. The airborne demonstrator for the direct-detection Doppler wind lidar ALADIN on ADM-Aeolus. Part II: Simulations and Rayleigh receiver radiometric performance. *Journal of Atmospheric and Oceanic Technology*, 26(12):2516 – 2530, 2009. doi:10.1175/2009JTECHA1314.1.
- [68] O. Lux, C. Lemmerz, F. Weiler, U. Marksteiner, B. Witschas, S. Rahm, A. Schäfler, and O. Reitebuch. Airborne wind lidar observations over the North Atlantic in 2016 for the pre-launch validation of the satellite mission Aeolus. *Atmospheric Measurement Techniques*, 11(6):3297–3322, 2018. doi:10.5194/amt-11-3297-2018.
- [69] O. Lux, C. Lemmerz, F. Weiler, U. Marksteiner, B. Witschas, S. Rahm, A. Geiß, A. Schäfler, and O. Reitebuch. Retrieval improvements for the ALADIN airborne demonstrator in support of the Aeolus wind product validation. *Atmospheric Measurement Techniques*, 15(5):1303–1331, 2022. doi:10.5194/amt-15-1303-2022.
- [70] A. G. Straume, M. Rennie, L. Isaksen, J de Kloe, G. J. Marseille, A. Stoffelen, T. Flament, H. Stieglitz, A. Dabas, D. Huber, O. Reitebuch, C. Lemmerz, O. Lux, U. Marksteiner, F. Weiler, B. Witschas, M. Meringer, K. Schmidt, I. Nikolaus, A. Geiß, P. Flamant, T. Kanitz, D. Wernham, J. von Bismarck, S. Bley, T. Fehr, R. Floberghagen, and T. Parrinello. ESA’s space-based Doppler wind lidar mission Aeolus—first wind and aerosol product assessment results. In *EPJ Web of Conferences*, volume 237, page 01007. EDP Sciences, 2020. doi:10.1051/epjconf/202023701007.
- [71] O. Reitebuch, C. Lemmerz, O. Lux, U. Marksteiner, S. Rahm, F. Weiler, B. Witschas, M. Meringer, K. Schmidt, D. Huber, I. Nikolaus, A. Geiß, M. Vaughan, A. Dabas, T. Flament, H. Stieglitz, L. Isaksen, M. Rennie, J. de Kloe, G. J. Marseille, A. Stoffelen, D. Wernham, T. Kanitz, A. G. Straume, T. Fehr, J. von Bismarck, R. Floberghagen, and T. Parrinello. Initial assessment of the performance of the first wind lidar in space on Aeolus. In *EPJ Web of Conferences*, volume 237, page 01010. EDP Sciences, 2020. doi:10.1051/epjconf/202023701010.
- [72] K. M. Bedka, A. R. Nehrir, M. Kavaya, R. Barton-Grimley, M. Beaubien, B. Carroll, J. Collins, J. Cooney, G. D. Emmitt, S. Greco, S. Kooi, T. Lee, Z. Liu, S. Rodier, and G. Skofronick-Jackson. Airborne lidar observations of wind, water vapor,

- and aerosol profiles during the NASA Aeolus calibration and validation (cal/val) test flight campaign. *Atmospheric Measurement Techniques*, 14(6):4305–4334, 2021. doi:10.5194/amt-14-4305-2021.
- [73] H. Baars, J. Walchester, E. Basharova, H. Gebauer, M. Radenz, J. Bühl, B. Barja, U. Wandinger, and P. Seifert. Long-term validation of Aeolus L2B wind products at Punta Arenas, Chile, and Leipzig, Germany. *Atmospheric Measurement Techniques*, 16(16):3809–3834, 2023. doi:10.5194/amt-16-3809-2023.
 - [74] F. Weiler, M. Rennie, T. Kanitz, L. Isaksen, E. Checa, J. de Kloe, N. Okunde, and O. Reitebuch. Correction of wind bias for the lidar on board Aeolus using telescope temperatures. *Atmospheric Measurement Techniques*, 14(11):7167–7185, 2021. doi:10.5194/amt-14-7167-2021.
 - [75] F. Weiler, T. Kanitz, D. Wernham, M. Rennie, D. Huber, M. Schillinger, O. Saint-Pe, R. Bell, T. Parrinello, and O. Reitebuch. Characterization of dark current signal measurements of the ACCDs used on board the Aeolus satellite. *Atmospheric Measurement Techniques*, 14(7):5153–5177, 2021. doi:10.5194/amt-14-5153-2021.
 - [76] M. P. Rennie, L. Isaksen, F. Weiler, J. de Kloe, T. Kanitz, and O. Reitebuch. The impact of Aeolus wind retrievals on ECMWF global weather forecasts. *Quarterly Journal of the Royal Meteorological Society*, 147(740):3555–3586, 2021. doi:10.1002/qj.4142.
 - [77] S. Laroche and J. St-James. Impact of the Aeolus level-2B horizontal line-of-sight winds in the Environment and Climate Change Canada global forecast system. *Quarterly Journal of the Royal Meteorological Society*, 148(745):2047–2062, 2022. doi:10.1002/qj.4300.
 - [78] K. Garrett, H. Liu, K. Ide, R. N. Hoffman, and K. E. Lukens. Optimization and impact assessment of Aeolus HLOS wind assimilation in NOAA’s global forecast system. *Quarterly Journal of the Royal Meteorological Society*, 148(747):2703–2716, 2022. doi:10.1002/qj.4331.
 - [79] K. S. Arnold and C.-Y. She. Metal fluorescence lidar (light detection and ranging) and the middle atmosphere. *Contemporary Physics*, 44(1):35–49, 2003. doi:10.1080/00107510302713.
 - [80] C.-Y. She. On atmospheric lidar performance comparison: from power-aperture product to power-aperture-mixing ratio-scattering cross-section product. *Journal of Modern Optics*, 52(18):2723–2729, 2005. doi:10.1080/09500340500352618.
 - [81] C.-Y. She and J. R. Yu. Simultaneous three-frequency Na lidar measurements of radial wind and temperature in the mesopause region. *Geophysical Research Letters*, 21(17):1771–1774, 1994. doi:10.1029/94GL01417.

- [82] D. A. Krueger, C.-Y. She, and T. Yuan. Retrieving mesopause temperature and line-of-sight wind from full-diurnal-cycle Na lidar observations. *Applied Optics*, 54(32): 9469–9489, 2015. doi:10.1364/AO.54.009469.
- [83] C.-Y. She, A.-Z. Liu, T. Yuan, J. Yue, T. Li, C. Ban, and J. S. Friedman. *MLT Science Enabled by Atmospheric Lidars*, chapter 20, pages 395–450. American Geophysical Union (AGU), 2021. ISBN 9781119815631. doi:10.1002/9781119815631.ch20.
- [84] X. Chu and G. Yang. Future lidars for cutting-edge sciences in ionosphere-thermosphere-mesosphere-stratosphere physics and space-atmosphere coupling. In J. T. Sullivan, T. Leblanc, S. Tucker, B. Demoz, E. Eloranta, C. Hostetler, S. Ishii, L. Mona, F. Moshary, A. Papayannis, and K. Rupavatharam, editors, *Proceedings of the 30th International Laser Radar Conference*, pages 57–63, Big Sky, Montana, U.S.A., 2022. Springer International Publishing. ISBN 978-3-031-37818-8. doi:10.1007/978-3-031-37818-8_8.
- [85] G. J. Koch, J. Y. Beyon, B. W. Barnes, M. Petros, J. Yu, F. Amzajerdian, M. J. Kavaya, and U. N. Singh. High-energy 2 μm Doppler lidar for wind measurements. *Optical Engineering*, 46(11):116201, 2007. doi:10.1117/1.2802584.
- [86] G. J. Koch, J. Y. Beyon, P. E. Petzar, M. Petros, J. Yu, B. C. Trieu, M. J. Kavaya, U. N. Singh, E. A. Modlin, B. W. Barnes, and B. B. Demoz. Field testing of a high-energy 2- μm Doppler lidar. *Journal of Applied Remote Sensing*, 4(1):043512, 2010. doi:10.1117/1.3368726.
- [87] M. J. Kavaya, J. Y. Beyon, G. J. Koch, M. Petros, P. J. Petzar, U. N. Singh, B. C. Trieu, and J. Yu. The Doppler Aerosol Wind (DAWN) airborne, wind-profiling coherent-detection lidar system: Overview and preliminary flight results. *Journal of Atmospheric and Oceanic Technology*, 31(4):826 – 842, 2014. doi:10.1175/JTECH-D-12-00274.1.
- [88] R. K. Newsome and R. Krishnamurthy. Doppler Lidar (DL) Instrument Handbook. Technical report, U.S. Department of Energy, 2022. Available online at https://www.arm.gov/publications/tech_reports/handbooks/dl_handbook.pdf.
- [89] V.-M. Kumer, J. Reuder, and B. R. Furevik. A comparison of LiDAR and radiosonde wind measurements. *Energy Procedia*, 53:214–220, 2014. doi:10.1016/j.egypro.2014.07.230.
- [90] A. J. Illingworth, D. Cimini, A. Haefele, M. Haeffelin, Hervo M., S. Kotthaus, U. Löhnert, P. Martinet, I. Mattis, E. J. O'Connor, and R. Potthast. How can existing ground-based profiling instruments improve European weather forecasts? *Bulletin of the American Meteorological Society*, 100(4):605 – 619, 2019. doi:10.1175/BAMS-D-17-0231.1.

- [91] B. Shrestha, J. A. Brotzge, J. Wang, N. Bain, C. D. Thorncroft, E. Joseph, J. Freedman, and S. Perez. Overview and applications of the New York state mesonet profiler network. *Journal of Applied Meteorology and Climatology*, 60(11):1591 – 1611, 2021. doi:10.1175/JAMC-D-21-0104.1.
- [92] J. F. Barlow, T. M. Dunbar, E. G. Nemitz, C. R. Wood, M. W. Gallagher, F. Davies, E. O'Connor, and R. M. Harrison. Boundary layer dynamics over London, UK, as observed using Doppler lidar during REPARTEE-II. *Atmospheric Chemistry and Physics*, 11(5):2111–2125, 2011. doi:10.5194/acp-11-2111-2011.
- [93] I. Gultepe, H. J. S. Fernando, E. R. Pardyjak, S. W. Hoch, Z. Silver, E. Creegan, L. S. Leo, Z. Pu, S. F. J. De Wekker, and C. Hang. An overview of the MATERHORN fog project: Observations and predictability. *Pure and Applied Geophysics*, 173(5):2983–3010, 2016. doi:10.1007/s00024-016-1374-0.
- [94] H. J. S. Fernando, J. Mann, J. M. L. M. Palma, J. K. Lundquist, R. J. Barthelmie, M. Belo-Pereira, W. O. J. Brown, F. K. Chow, T. Gerz, C. M. Hocut, P. M. Klein, L. S. Leo, J. C. Matos, S. P. Oncley, S. C. Pryor, L. Bariteau, T. M. Bell, N. Bodini, M. B. Carney, M. S. Courtney, E. D. Creegan, R. Dimitrova, S. Gomes, M. Hagen, J. O. Hyde, S. Kigle, R. Krishnamurthy, J. C. Lopes, L. Mazzaro, J. M. T. Neher, R. Menke, P. Murphy, L. Oswald, S. Otarola-Bustos, A. K. Pattantyus, C. Veiga Rodrigues, A. Schady, N. Sirin, S. Spuler, E. Svensson, J. Tomaszewski, D. D. Turner, L. van Veen, N. Vasiljević, D. Vassallo, S. Voss, N. Wildmann, and Y. Wang. The Perdigão: Peering into microscale details of mountain winds. *Bulletin of the American Meteorological Society*, 100(5):799 – 819, 2019. doi:10.1175/BAMS-D-17-0227.1.
- [95] Metek: Lidar wind sensor wind scout. product data sheet (metek gmbh, elmshorn 2019). Available online at https://metek.de/wp-content/uploads/2018/05/20180521_Datenblatt_WindScout.pdf, 2019. Accessed: 2024-02-08.
- [96] S. M. Spuler, M. Hayman, and T. M. Weckwerth. *Water Vapor Differential Absorption Lidar*, pages 741–757. Springer International Publishing, Cham, Switzerland, 2021. ISBN 978-3-030-52171-4. doi:10.1007/978-3-030-52171-4_26.
- [97] J.D. Spinhirne. Micro pulse lidar. *IEEE Transactions on Geoscience and Remote Sensing*, 31(1):48–55, 1993. doi:10.1109/36.210443.
- [98] J. R. Campbell, D. L. Hlavka, E. J. Welton, C. J. Flynn, D. D. Turner, J. D. Spinhirne, V. S. Scott, and I. H. Hwang. Full-time, eye-safe cloud and aerosol lidar observation at Atmospheric Radiation Measurement program sites: Instruments and data processing. *Journal of Atmospheric and Oceanic Technology*, 19(4):431 – 442, 2002. doi:10.1175/1520-0426(2002)019<0431:FTESCA>2.0.CO;2.
- [99] A. R. Nehrir, K. S. Repasky, J. L. Carlsten, M. D. Olland, and J. A. Shaw. Water vapor profiling using a widely tunable, amplified diode-laser-based differential absorption

lidar (DIAL). *Journal of Atmospheric and Oceanic Technology*, 26(4):733 – 745, 2009. doi:10.1175/2008JTECHA1201.1.

- [100] A. R. Nehrir, K. S. Repasky, and J. L. Carlsten. Eye-safe diode-laser-based micropulse differential absorption lidar (DIAL) for water vapor profiling in the lower troposphere. *Journal of Atmospheric and Oceanic Technology*, 28(2):131 – 147, 2011. doi:10.1175/2010JTECHA1452.1.
- [101] A. R. Nehrir, K. S. Repasky, and J. L. Carlsten. Micropulse water vapor differential absorption lidar: transmitter design and performance. *Optics Express*, 20(22):25137–25151, 2012. doi:10.1364/OE.20.025137.
- [102] K. S. Repasky, D. Moen, S. Spuler, A. R. Nehrir, and J. L. Carlsten. Progress towards an autonomous field deployable diode-laser-based differential absorption lidar (DIAL) for profiling water vapor in the lower troposphere. *Remote Sensing*, 5(12):6241–6259, 2013. doi:10.3390/rs5126241.
- [103] S. M. Spuler, K. S. Repasky, B. Morley, D. Moen, M. Hayman, and A. R. Nehrir. Field-deployable diode-laser-based differential absorption lidar (DIAL) for profiling water vapor. *Atmospheric Measurement Techniques*, 8(3):1073–1087, 2015. doi:10.5194/amt-8-1073-2015.
- [104] T. M. Weckwerth, K. J. Weber, D. D. Turner, and S. M. Spuler. Validation of a water vapor micropulse differential absorption lidar (DIAL). *Journal of Atmospheric and Oceanic Technology*, 33(11):2353 – 2372, 2016. doi:10.1175/JTECH-D-16-0119.1.
- [105] S. M. Spuler, M. Hayman, R. A. Stillwell, J. Carnes, T. Bernatsky, and K. S. Repasky. MicroPulse DIAL (MPD) – a diode-laser-based lidar architecture for quantitative atmospheric profiling. *Atmospheric Measurement Techniques*, 14(6):4593–4616, 2021. doi:10.5194/amt-14-4593-2021.
- [106] S. M. Spuler, R. A. Stillwell, M. Hayman, and K. S. Repasky. Semiconductor lidar for quantitative atmospheric profiling. In J. T. Sullivan, T. Leblanc, S. Tucker, B. Demoz, E. Eloranta, C. Hostetler, S. Ishii, L. Mona, F. Moshary, A. Papayannis, and K. Rupavatharam, editors, *Proceedings of the 30th International Laser Radar Conference*, pages 41–47, Big Sky, Montana, U.S.A., 2022. Springer International Publishing. ISBN 978-3-031-37818-8. doi:10.1007/978-3-031-37818-8_6.
- [107] M. Hayman and S. Spuler. Demonstration of a diode-laser-based high spectral resolution lidar (HSRL) for quantitative profiling of clouds and aerosols. *Optics Express*, 25(24):A1096–A1110, 2017. doi:10.1364/OE.25.0A1096.
- [108] R. A. Stillwell, S. M. Spuler, M. Hayman, K. S. Repasky, and C. E. Bunn. Demonstration of a combined differential absorption and high spectral resolution lidar for profiling atmospheric temperature. *Optics Express*, 28(1):71–93, 2020. doi:10.1364/OE.379804.

- [109] L. Colberg. Diode-laser-based high spectral resolution LIDAR. Master's thesis, Montana State University-Bozeman, Norm Asbjornson College of Engineering, Bozeman MT, U.S.A., 2021. Available at <https://scholarworks.montana.edu/xmlui/bitstream/handle/1/16596/colberg-diode-laser-2021.pdf?sequence=1>.
- [110] K. S. Repasky, C. E. Bunn, M. Hayman, R. A. Stillwell, and S. M. Spuler. Modeling the performance of a diode laser-based (DLB) micro-pulse differential absorption lidar (MPD) for temperature profiling in the lower troposphere. *Optics Express*, 27(23):33543–33563, 2019. doi:10.1364/OE.27.033543.
- [111] T. M. Weckwerth, V. Wulfmeyer, R. M. Wakimoto, R. M. Hardesty, J. W. Wilson, and R. M. Banta. NCAR-NOAA lower-tropospheric water vapor workshop. *Bulletin of the American Meteorological Society*, 80:2339–2357, 1999. doi:10.1175/1520-0477(1999)080%3C2331:WOTOFE%3E2.0.CO;2.
- [112] V. Wulfmeyer, R. M. Hardesty, D. D. Turner, A. Behrendt, M. P. Cadeddu, P. Di Girolamo, P. Schlüssel, J. Van Baelen, and F. Zus. A review of the remote sensing of lower tropospheric thermodynamic profiles and its indispensable role for the understanding and the simulation of water and energy cycles. *Reviews of Geophysics*, 53(3):819–895, 2015. doi:10.1002/2014RG000476.
- [113] K. S. Repasky, O. Cruikshank, and L. Colberg. Performance modeling of a diode-laser-based direct-detection Doppler lidar for vertical wind profiling. *Journal of Atmospheric and Oceanic Technology*, 39(11):1655 – 1668, 2022. doi:10.1175/JTECH-D-22-0001.1.
- [114] A. Dabas, M. L. Denneulin, P. Flamant, C. Loth, A. Garnier, and A. Dolfi-Bouteyre. Correcting winds measured with a Rayleigh Doppler lidar from pressure and temperature effects. *Applied Optics*, 60(2):206—215, 2008. doi:10.1111/j.1600-0870.2007.00284.x.
- [115] B. Liu, M. Esselborn, M. Wirth, A. Fix, D. Bi, and G. Ehret. Influence of molecular scattering models on aerosol optical properties measured by high spectral resolution lidar. *Applied Optics*, 48(27):5143–5154, 2009. doi:10.1364/AO.48.005143.
- [116] B. Witschas. *Light Scattering on Molecules in the Atmosphere*, pages 69–83. Springer Berlin Heidelberg, Berlin, Germany, 2012. ISBN 978-3-642-30183-4. doi:10.1007/978-3-642-30183-4_5.
- [117] C.-Y. She. Spectral structure of laser light scattering revisited: bandwidths of nonresonant scattering lidars. *Applied Optics*, 40(27):4875–4884, 2001. doi:10.1364/AO.40.004875.
- [118] A. T. Young. Rayleigh scattering. *Applied Optics*, 20(4):533–535, 1981. doi:10.1364/AO.20.000533.

- [119] A. T. Young. Rayleigh scattering. *Physics Today*, 35(1):42–48, 1982. Available at <https://www.researchgate.net/profile/Hans-Moosmuller/post/Does-Rayleigh-Scattering-really-explain-blueness-of-sky/attachment/59d6338dc49f478072ea23ef/AS%3A273644943544335%401442253446960/download/Young1982PhysicsToday.pdf>.
- [120] G. Tenti, C. D. Boley, and R. C. Desai. On the kinetic model description of Rayleigh–Brillouin scattering from molecular gases. *Canadian Journal of Physics*, 52(4):285–290, 1974. doi:10.1139/p74-041.
- [121] A. T. Young and G. W. Kattawar. Rayleigh-scattering line profiles. *Applied Optics*, 22(23):3668–3670, 1983. doi:10.1364/AO.22.003668.
- [122] B. Witschas, M. O. Vieitez, E. van Duijn, O. Reitebuch, W. van de Water, and W. Ubachs. Spontaneous Rayleigh–Brillouin scattering of ultraviolet light in nitrogen, dry air, and moist air. *Applied Optics*, 49(22):4217–4227, 2010. doi:10.1364/AO.49.004217.
- [123] B. Witschas, C. Lemmerz, and O. Reitebuch. Horizontal lidar measurements for the proof of spontaneous Rayleigh–Brillouin scattering in the atmosphere. *Applied Optics*, 51(25):6207–6219, 2012. doi:10.1364/AO.51.006207.
- [124] L. Colberg, O. Cruikshank, and K. S. Repasky. Planetary boundary layer height retrieval from a diode-laser-based high spectral resolution lidar. *Journal of Applied Remote Sensing*, 16(2):024507, 2022. doi:10.1117/1.JRS.16.024507.
- [125] V. A. Kovalev and W. E. Eichinger. *Elastic lidar: theory, practice, and analysis methods*. John Wiley & Sons, Inc., Hoboken NJ, U.S.A., 2004. ISBN 9780471201717. doi:10.1002/0471643173.
- [126] K. S. Repasky, O. Cruikshank, and L. Colberg. Performance modeling of a diode laser-based direct detection Doppler lidar. In J. T. Sullivan, T. Leblanc, S. Tucker, B. Demoz, E. Eloranta, C. Hostetler, S. Ishii, L. Mona, F. Moshary, A. Papayannis, and K. Rupavatharam, editors, *Proceedings of the 30th International Laser Radar Conference*, pages 365–371, Cham, Switzerland, 2022. Springer International Publishing. ISBN 978-3-031-37818-8. doi:10.1007/978-3-031-37818-8_48.
- [127] Y. Xiong, S. Murphy, J. L. Carlsten, and K. S. Repasky. Design and characteristics of a tapered amplifier diode system by seeding with continuous-wave and mode-locked external cavity diode laser. *Optical Engineering*, 45(12):124205, 2006. doi:10.1117/1.2404925.
- [128] C.-Y. She, D. A. Krueger, Z.-A. Yan, and X. Hu. Atomic vapor filter revisited: a Cabannes scattering temperature/wind lidar at 770 nm. *Optics Express*, 29(3):4338–4362, 2021. doi:10.1364/OE.413442.

- [129] F. Shen, C. Xie, C. Qiu, and B. Wang. Fabry–Perot etalon-based ultraviolet trifrequency high-spectral-resolution lidar for wind, temperature, and aerosol measurements from 0.2 to 35 km altitude. *Applied Optics*, 57(31):9328–9340, 2018. doi:10.1364/AO.57.009328.
- [130] F. Shen, J. Ji, C. Xie, Z. Wang, and B. Wang. High-spectral-resolution Mie Doppler lidar based on a two-stage Fabry-Perot etalon for tropospheric wind and aerosol accurate measurement. *Applied Optics*, 58(9):2216–2225, 2019. doi:10.1364/AO.58.002216.
- [131] F. Shen, C. Xie, L. Yang, B. Wang, H. Zhou, and H. Xu. Rayleigh Doppler lidar technology based on a quadruple dual-pass Fabry–Perot interferometer. *Optics and Lasers in Engineering*, 174:107953, 2024. doi:10.1016/j.optlaseng.2023.107953.
- [132] G. C. Bjorklund. Frequency-modulation spectroscopy: a new method for measuring weak absorptions and dispersions. *Optics Letters*, 5(1):15–17, 1980. doi:10.1364/OL.5.000015.
- [133] G. C. Bjorklund, M. D. Levenson, W. Lenth, and C. Ortiz. Frequency modulation (FM) spectroscopy. *Applied Physics B*, 32(3):145–152, 1983. doi:10.1007/BF00688820.
- [134] R. W. P. Drever, J. L. Hall, F. V. Kowalski, J. Hough, G. M. Ford, A. J. Munley, and H. Ward. Laser phase and frequency stabilization using an optical resonator. *Applied Physics B*, 31(2):97–105, 1983. doi:10.1007/BF00702605.
- [135] E. D. Black. An introduction to Pound–Drever–Hall laser frequency stabilization. *American Journal of Physics*, 69(1):79–87, 01 2001. doi:10.1119/1.1286663.
- [136] J. W. Hair, C. A. Hostetler, A. L. Cook, D. B. Harper, R. A. Ferrare, T. L. Mack, W. Welch, L. R. Izquierdo, and F. E. Hovis. Airborne high spectral resolution lidar for profiling aerosol optical properties. *Applied Optics*, 47(36):6734–6752, 2008. doi:10.1364/AO.47.006734.
- [137] M. Esselborn, M. Wirth, A. Fix, M. Tesche, and G. Ehret. Airborne high spectral resolution lidar for measuring aerosol extinction and backscatter coefficients. *Applied Optics*, 47(3):346–358, 2008. doi:10.1364/AO.47.000346.
- [138] C. Affolderbach and G. Miletí. A compact laser head with high-frequency stability for Rb atomic clocks and optical instrumentation. *Review of Scientific Instruments*, 76(7):073108, 07 2005. ISSN 0034-6748. doi:10.1063/1.1979493.
- [139] X.-H. Qi, W.-L. Chen, L. Yi, D.-W. Zhou, T. Zhou, Q. Xiao, J. Duan, X.-J. Zhou, and X.-Z. Chen. Ultra-stable rubidium-stabilized external-cavity diode laser based on the modulation transfer spectroscopy technique. *Chinese Physics Letters*, 26(4):044205, 2009. doi:10.1088/0256-307X/26/4/044205.

- [140] T. Zhou, X. Qi, Q. Wang, W. Xiong, J. Duan, X. Zhou, and X. Chen. Frequency-stabilized diode laser at 780 nm with a continuously locked time over 100 h. *Chin. Opt. Lett.*, 8(5):496–498, May 2010. Available online at <https://citeserx.ist.psu.edu/document?repid=rep1&type=pdf&doi=960a3c6ef4a96d6100cb142271be302c87ea7642>.
- [141] F. Gruet, M. Pellaton, C. Affolderbach, T. Bandi, R. Matthey, and G. Mileti. Compact and frequency stabilized laser heads for rubidium atomic clocks. In Bruno Cugny, Errico Armandillo, and Nikos Karafolas, editors, *International Conference on Space Optics — ICSO 2012*, volume 10564, page 105642Y. International Society for Optics and Photonics, SPIE, 2012. doi:10.1117/12.2309135.
- [142] A. Strangfeld, S. Kanthak, M. Schiemangk, B. Wiegand, A. Wicht, A. Ling, and M. Krutzik. Prototype of a compact rubidium-based optical frequency reference for operation on nanosatellites. *J. Opt. Soc. Am. B*, 38(6):1885–1891, Jun 2021. doi:10.1364/JOSAB.420875.
- [143] T. Day. *Frequency-stabilized solid state lasers for coherent optical communications*. Ph.D. thesis, Stanford University, Stanford CA, U.S.A., 1990. Available online at <https://search.proquest.com/openview/47b34765ab8227217e2cdae8f9b3811a/1?pq-origsite=gscholar&cbl=18750&diss=y>.
- [144] M. Zhu and J. L. Hall. Frequency stabilization of tunable lasers. In F. B. Dunning and R. G. Hulet, editors, *Atomic, Molecular, and Optical Physics: Electromagnetic Radiation*, volume 29 of *Experimental Methods in the Physical Sciences*, pages 103–136. Academic Press, 1997. doi:10.1016/S0076-695X(08)60614-6.
- [145] P. A. Roos. *The Diode-Pumped Continuous-Wave Raman Laser: Classical, Quantum, and Thermo-Optic Fundamentals*. Ph.D. thesis, Montana State University, Bozeman MT, U.S.A., 2002. Available at online <https://www.proquest.com/docview/305495689?pq-origsite=gscholar&fromopenview=true&sourcetype=Dissertations%20&%20Theses>.
- [146] T. Böttger. *Laser Frequency Stabilization to Spectral Hole Burning Frequency References in Erbium-Doped Crystals: Material and Device Optimization*. Ph.D. thesis, Montana State University, Bozeman MT, U.S.A., 2002. Available online at <https://www.proquest.com/docview/305502128/fulltextPDF/3EA0135B976D42B8PQ/1?accountid=28148&sourcetype=Dissertations%20&%20Theses>.
- [147] L. S. Meng. *Continuous-wave Raman laser in hydrogen: Semi-classical theory and diode-pumping experiments*. Ph.D. thesis, Montana State University, Bozeman MT, U.S.A., 2002. Available online at <https://search.proquest.com/openview/92be5080eebd8b872bbf7ab91654a691/1?pq-origsite=gscholar&cbl=18750&diss=y>.

- [148] D. A. Steck. Rubidium 87 d line data, 2001. Available online at <https://steck.us/alkalidata/rubidium87numbers.1.6.pdf>.
- [149] Y. Xiong. *Mode-locked Raman laser in H₂ pumped by a mode-locked external cavity diode laser.* Ph.D. thesis, Montana State University, Bozeman MT, U.S.A., 2007. Available online at <https://search.proquest.com/openview/d460124f4105e933617012e175f1a335/1?pq-origsite=gscholar&cbl=18750>.
- [150] S. M. Spuler. National Center for Atmospheric Research, Earth Observing Laboratory, Personal communication, 2023.
- [151] R. A. Stillwell. National Center for Atmospheric Research, Earth Observing Laboratory, Personal communication, 2023.
- [152] D. M. Rust. Etalon filters. *Optical Engineering*, 33(10):3342 – 3348, 1994. doi:10.1117/12.179401.
- [153] M.A. Krainak, M.A. Stephen, A.J. Martino, R.S. Lancaster, G.R. Allan, and D.L. Lunt. Tunable solid-etalon filter for the icesat/glas 532 nm channel lidar receiver. In *IGARSS 2003. 2003 IEEE International Geoscience and Remote Sensing Symposium. Proceedings (IEEE Cat. No.03CH37477)*, volume 5, pages 3020–3022 vol.5, 2003. doi:10.1109/IGARSS.2003.1294667.
- [154] N. H. Zaun, C. Weimer, Y. Sidorin, and D. Lunt. Solid-etalon for the CALIPSO lidar receiver. In W. L. Barnes and J. J. Butler, editors, *Earth Observing Systems IX*, volume 5542, pages 141 – 145. International Society for Optics and Photonics, SPIE, 2004. doi:10.1117/12.559883.
- [155] D. R. Cremons, J. B. Abshire, X. Sun, G. Allan, H. Riris, M. D. Smith, S. Guzewich, A. Yu, and F. Hovis. Design of a direct-detection wind and aerosol lidar for mars orbit. *CEAS Space Journal*, 12(2):149–162, 2020. doi:10.1007/s12567-020-00301-z.
- [156] M. Imaki and T. Kobayashi. Ultraviolet high-spectral-resolution Doppler lidar for measuring wind field and aerosol optical properties. *Applied Optics*, 44(28):6023–6030, 2005. doi:10.1364/AO.44.006023.
- [157] S. Ishii, K. Kishibuchi, H. Takenaka, Y. Jin, T. Nishizawa, N. Sugimoto, H. Iwai, M. Aoki, S. Kawamura, and H. Okamoto. 355-nm direct-detection Doppler wind lidar for vertical atmospheric motion measurement. *Applied Optics*, 61(27):7925–7936, 2022. doi:10.1364/AO.460219.
- [158] J. C. Bergquist, W. M. Itano, and D. J. Wineland. Laser stabilization to a single ion. *Frontiers in laser spectroscopy*, pages 359–376, 1994. Available online at <https://tf.nist.gov/general/pdf/976.pdf>.

- [159] L. Marmet, A. A. Madej, K. J. Siemsen, J. E. Bernard, and B. G. Whitford. Precision frequency measurement of the $^2s_{1/2} - ^2d_{5/2}$ transition of Sr^+ with a 674-nm diode laser locked to an ultrastable cavity. *IEEE Transactions on Instrumentation and Measurement*, 46(2):169–173, 1997. doi:10.1109/19.571804.
- [160] F. Pepe, P. Molero, S. Cristiani, R. Rebolo, N.C. Santos, H. Dekker, D. Mégevand, F. M. Zerbi, A. Cabral, P. Di Marcantonio, M. Abreu, M. Affolter, M. Aliverti, C. Allende Prieto, M. Amate, G. Avila, V. Baldini, P. Bristow, C. Broeg, R. Cirami, J. Coelho, P. Conconi, I. Coretti, G. Cupani, V. D’Odorico, V. De Caprio, B. Delabre, R. Dorn, P. Figueira, A. Fragoso, S. Galeotta, L. Genolet, R. Gomes, J.I. González Hernández, I. Hughes, O. Iwert, F. Kerber, M. Landomi, J. L. Lizon, C. Lovis, C. Maire, M. Mannetta, C. Martins, M. Monteiro, A. Oliveira, E. Poretti, J. L. Rasilla, M. Riva, S. Santana Tschudi, P. Santos, D. Sosnowska, S. Sousa, P. Spanó, F. Tenegi, G. Toso, E. Vanzella, M. Viel, and M. R. Zapatero Osorio. ESPRESSO: The next European exoplanet hunter. *Astronomische Nachrichten*, 335(1):8–20, 2014. doi:10.1002/asna.201312004.
- [161] P. Robertson, T. Anderson, G. Stefansson, F. R. Hearty, A. Monson, S. Mahadevan, S. Blakeslee, C. Bender, J. P. Ninan, D. Conran, E. Levi, E. Lubar, A. Cole, A. Dykhouse, S. Kanodia, C. Nitroy, J. Smolsky, D. Tuggle, B. Blank, M. Nelson, C. Blake, S. Halverson, C. Henderson, K. F. Kaplan, D. Li, S. E. Logsdon, M. W. McElwain, J. Rajagopal, L. W. Ramsey, A. Roy, C. Schwab, R. Terrien, and J. T. Wright. Ultrastable environment control for the NEID spectrometer: design and performance demonstration. *Journal of Astronomical Telescopes, Instruments, and Systems*, 5(1):015003, 2019. doi:10.1117/1.JATIS.5.1.015003.
- [162] V. Savani and L. A. Johnson. Achieving millikelvin temperature stability. Application Note 38, ILX Lightwave, 2013. Available online at https://www.newport.com/medias/sys_master/images/images/hfb/h4d/8797050372126/AN38-Achieving-Millikelvin-Temperature-Stability.pdf.
- [163] Wavelength Electronics. Optimizing thermoelectric temperature control systems. Technical Note TC01, Wavelength Electronics, 2020. Available online at <https://teamwavelength.com/download/applicationtechnotes/tn-tc01.pdf>.
- [164] T. L. Bergman, A. S. Lavine, F. P. Incropera, and D. P. DeWitt. *Introduction to heat transfer*. John Wiley & Sons, Hoboken NJ, U.S.A., 2011. ISBN 978-0470-50196-2.
- [165] Wavelength Electronics. Specifying thermoelectric coolers. Application Note TC09, Wavelength Electronics, 2015. Available online at <https://www.teamwavelength.com/download/applicationtechnotes/an-tc09.pdf>.
- [166] Wavelength Electronics. Compliance voltage & temperature control design with multiple thermoelectric coolers. Application Note TC05, Wavelength Electronics, 2017. Available online at <https://www.teamwavelength.com/download/applicationtechnotes/an-tc15.pdf>.

- [167] B. Witschas, C. Lemmerz, O. Lux, U. Marksteiner, O. Reitebuch, F. Weiler, F. Fabre, A. Dabas, T. Flament, D. Huber, and M. Vaughan. Spectral performance analysis of the Aeolus Fabry–Pérot and Fizeau interferometers during the first years of operation. *Atmospheric Measurement Techniques*, 15(5):1465–1489, 2022. doi:10.5194/amt-15-1465-2022.
- [168] C. J. Grund and E. W. Eloranta. Fiber-optic scrambler reduces the bandpass range dependence of Fabry–Perot étalons used for spectral analysis of lidar backscatter. *Applied Optics*, 30(19):2668–2670, 1991. doi:10.1364/AO.30.002668.
- [169] W. W. Chow and R. R. Craig. Amplified spontaneous emission effects in semiconductor laser amplifiers. *IEEE Journal of Quantum Electronics*, 26(8):1363–1368, 1990. doi:10.1109/3.59683.
- [170] D. Voigt, E. C. Schilder, R. J. C. Spreeuw, and H. B. van Linden van den Heuvell. Characterization of a high-power tapered semiconductor amplifier system. *Applied Physics B*, 72(3):279–284, 2001. doi:10.1007/s003400100513.
- [171] M. Höbel and J. Ricka. Dead-time and afterpulsing correction in multiphoton timing with nonideal detectors. *Review of Scientific Instruments*, 65(7):2326–2336, 07 1994. doi:10.1063/1.1144684.
- [172] I. Binietoglou, G. D’Amico, H. Baars, L. Belegante, and E. Marinou. A methodology for cloud masking uncalibrated lidar signals. In *EPJ Web of Conferences, The 28th International Laser Radar Conference (ILRC 28)*, volume 176, page 05048. EDP Sciences, 2018. doi:10.1051/epjconf/201817605048.
- [173] T. F. Eck, B. N. Holben, J. S. Reid, O. Dubovik, A. Smirnov, N. T. O’Neill, I. Slutsker, and S. Kinne. Wavelength dependence of the optical depth of biomass burning, urban, anhd desert dust aerosols. *Journal of Geophysical Research: Atmospheres*, 104(D24): 31333–31349, 1999. doi:10.1029/1999JD900923.
- [174] B. N. Holben, T. F. Eck, I. Slutsker, D. Tanré, J. P. Buis, A. Setzer, E. Vermote, J. A. Reagan, Y. J. Kaufman, T. Nakajima, F. Lavenu, I. Jankowiak, and A. Smirnov. Aeronet—a federated instrument network and data archive for aerosol characterization. *Remote Sensing of Environment*, 66(1):1–16, 1998. ISSN 0034-4257. doi:10.1016/S0034-4257(98)00031-5.
- [175] G. Lente and K. Ősz. Barometric formulas: various derivations and comparisons to environmentally relevant observations. *ChemTexts*, 6(13), 2020. doi:10.1007/s40828-020-0111-6.
- [176] I. Binietoglou, P. Giampouras, and L. Belegante. Linear approximation of Rayleigh–Brillouin scattering spectra. *Applied Optics*, 55(27):7707–7711, Sep 2016. doi:10.1364/AO.55.007707.

- [177] J. R. Taylor and W. Thompson. *An introduction to error analysis: the study of uncertainties in physical measurements*, volume 2. University Science Books, Sausalito CA, U.S.A., 1982. ISBN 0-935702-42-3.
- [178] D. H. Lenschow, V. Wulfmeyer, and C. Senff. Measuring second- through fourth-order moments in noisy data. *Journal of Atmospheric and Oceanic Technology*, 17(10):1330 – 1347, 2000. doi:10.1175/1520-0426(2000)017<1330:MSTFOM>2.0.CO;2.
- [179] S. C. Tucker, C. J. Senff, A. M. Weickmann, W. A. Brewer, R. M. Banta, S. P. Sandberg, D. C. Law, and R. M. Hardesty. Doppler lidar estimation of mixing height using turbulence, shear, and aerosol profiles. *Journal of Atmospheric and Oceanic Technology*, 26(4):673 – 688, 2009. doi:10.1175/2008JTECHA1157.1.
- [180] M. Hayman, R. A. Stillwell, and S. M. Spuler. Optimization of linear signal processing in photon counting lidar using Poisson thinning. *Optics Letters*, 45(18):5213–5216, Sep 2020. doi:10.1364/OL.396498.
- [181] L. Colberg, O. Cruikshank, K. S. Repasky, S. M. Spuler, R. A. Stillwell, and M. Hayman. Planetary boundary layer height measurements using MicroPulse DIAL. In J. T. Sullivan, T. Leblanc, S. Tucker, B. Demoz, E. Eloranta, C. Hostetler, S. Ishii, L. Mona, F. Moshary, A. Papayannis, and K. Rupavatharam, editors, *Proceedings of the 30th International Laser Radar Conference*, pages 355–361, Cham, Switzerland, 2022. Springer International Publishing. ISBN 978-3-031-37818-8. doi:10.1007/978-3-031-37818-8_47.

APPENDIX: LIST OF ACRONYMS

A2D	ALADIN Airborne Demonstrator
ADM-Aeolus	Atmospheric Dynamics Mission - Aeolus
ALOMAR	Arctic Lidar Observatory for Middle Atmosphere Research
ALADIN	Atmospheric LAser Doppler INstrument
APD	Avalanche Photodiode
ARM	Atmospheric Radiation Measurement
ASE	Amplified Spontaneous Emission
CALIOP	Cloud and Aerosol LIdar with Orthogonal Polarization
CCD	Charge-Coupled Device
COMD	Catastrophic Optical Mirror Damage
CSU	Colorado State University
CW	Continuous-Wave
DBR	Distributed Bragg Reflector
DIAL	Differential Absorption Lidar
DLB	Diode-Laser-Based
DLR	Deutsches Zentrum für Luft- und Raumfahrt (German Aerospace Center)
DAWN	Doppler Aerosol WiNd
DWL	Doppler Wind Lidar
ECMWF	European Center for Medium-range Weather Forecasting
ESA	European Space Agency
EOM	Electro-Optic Modulator
FMS	Frequency Modulation Spectroscopy
GLAS	Geoscience Laser Altimeter System
GLOW	Goddard Lidar Observatory for Winds
GrOAWL	Green OAWL
HSRL	High Spectral Resolution Lidar
LNG	Lidar aerosols Nouvelle Génération (Next Generation aerosol Lidar)
LIF	Laser-Induced Fluorescence
LOS	Line-Of-Sight
MARLI	MARs LIdar
MCS	Multi-Channel Scaler
MOPA	Maser Oscillator Power Amplifier
MPD	MicroPulse Differential absorption lidar
MSU	Montana State University
NASA	National Aeronautic and Space Administration
NBF	Narrowband Filter
NCAR	National Center for Atmospheric Research
N-PBS	Non-Polarizing Beamsplitter

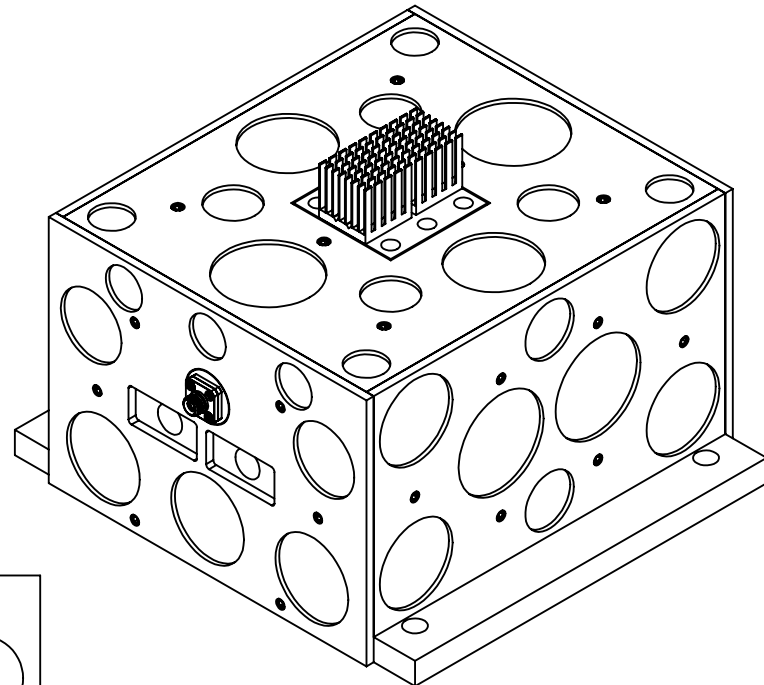
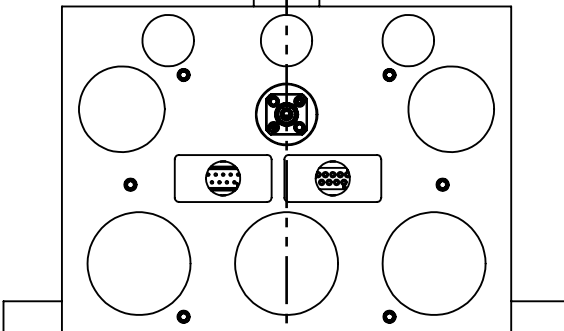
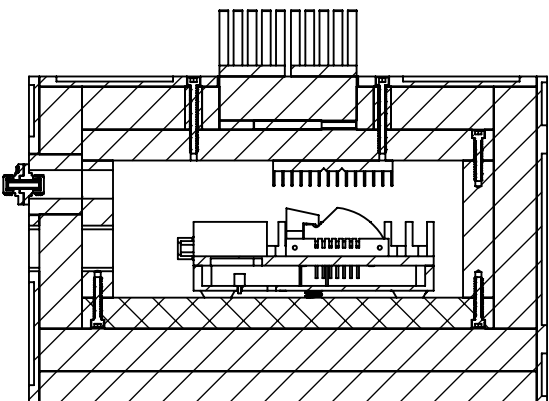
NWP	Numerical Weather Prediction
OAWL	Optical Autocovariance Wind Lidar
OHP	Observatoire de Haute-Provence (Haute-Province Observatory)
PBS	Polarizing Beamsplitter
PBL	Planetary Boundary Layer
PCA	Principal Component Analysis
RF	Radio Frequency
SPCM	Single-Photon-Counting Module
SPRL	Space Physics Research Laboratory
T/R	Transmit/Receive
TEC	Thermo-Electric Cooler
TSOA	Tapered Semiconductor Optical Amplifier
TWiLiTE	Tropospheric Wind Lidar Technology Experiment
UPS	Uninterruptible Power Supply
USTC	University of Science and Technology of China

APPENDIX: LASER STABILIZATION SOLIDWORKS DRAWINGS

2

1

Cross-section and Iso Views



SECTION A-A

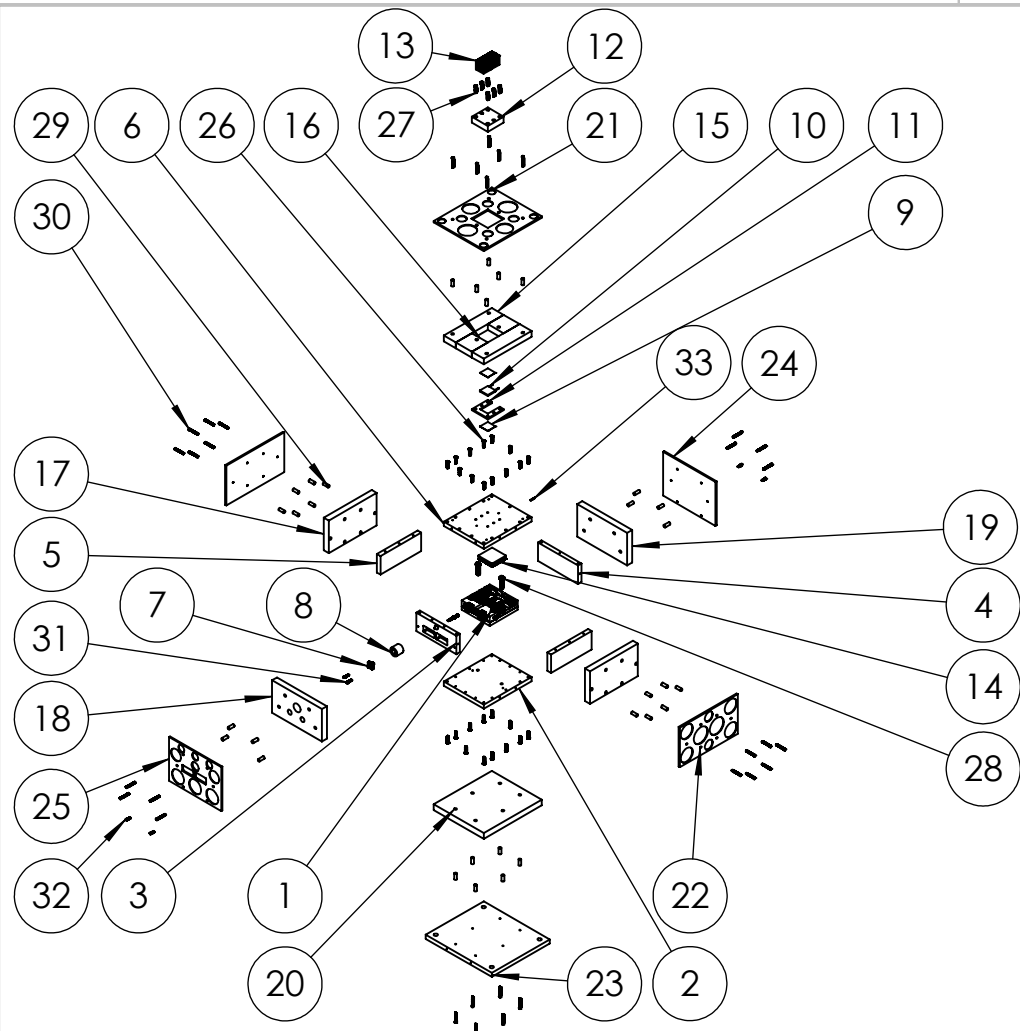
SCALE 1 : 2.8

PROPRIETARY AND CONFIDENTIAL
THE INFORMATION CONTAINED IN THIS DRAWING IS THE SOLE PROPERTY OF <INSERT COMPANY NAME HERE>. ANY REPRODUCTION IN PART OR AS A WHOLE WITHOUT THE WRITTEN PERMISSION OF <INSERT COMPANY NAME HERE> IS PROHIBITED.

		UNLESS OTHERWISE SPECIFIED:			DRAWN	NAME	DATE	TITLE: dbr_enclosure_assy				
		DIMENSIONS ARE IN INCHES TOLERANCES: FRACTIONAL \pm ANGULAR: MACH \pm BEND \pm TWO PLACE DECIMAL \pm THREE PLACE DECIMAL \pm										
		INTERPRET GEOMETRIC TOLERANCING PER: MATERIAL			CHECKED	ENG APPR.	MFG APPR.					
NEXT ASSY	USED ON	FINISH										
APPLICATION		DO NOT SCALE DRAWING			COMMENTS:							
A												
SIZE		DWG. NO.			REV							
A												
SCALE:1:2.8		WEIGHT:			SHEET 1 OF 3							

2

1



	PART NUMBER	DESCRIPTION	QTY.
1	LM14S2-Solidworks	ThorLabs	1
2	cage_bottom	Custom Delrin	1
3	cage_front	Custom Delrin	1
4	cage_back	Custom Delrin	1
5	cage_side	Custom Delrin	2
6	cage_top	Custom Delrin	1
7	ADAFC3-Solidworks	ThorLabs	1
8	optical_fiber_spacer	Custom Delrin	1
9	graphite_sheet	Panasonic	2
10	TEC	Laird Thermal Systems	1
11	TEC_compression_mount	Custom ABS	1
12	heat_sink	Custom Aluminum	1
13	8822T936	Adhesive-Mount Heat Sink	2
14	8822T959	Adhesive-Mount Heat Sink	1
15	insulation_top_p1	Custom Foam	2
16	insulation_top_p2	Custom Foam	2
17	insulation_side	Custom Foam	2
18	insulation_front	Custom Foam	1
19	insulation_back	Custom Foam	1
20	insulation_bottom	Custom Foam	1
21	shell_top	Custom ABS	1
22	shell_side	Custom ABS	2
23	shell_bottom	Custom Delrin	1
24	shell_back	Custom ABS	1
25	shell_front	Custom ABS	1
26	91251A112	Black-Oxide Alloy Steel Socket Head Screw	27
27	95868A196	Nylon Socket Head Screws	6
28	91251A542	Black-Oxide Alloy Steel Socket Head Screw	2
29	94639A204	Off-White Nylon Unthreaded Spacer	32
30	95868A115	Nylon Socket Head Screws	32
31	91251A081	Black-Oxide Alloy Steel Socket Head Screw	2
32	95868A108	Nylon Socket Head Screws	4
33	Thermistor	Wavelength Electronics	1

		UNLESS OTHERWISE SPECIFIED:	DRAWN	NAME	DATE
		DIMENSIONS ARE IN INCHES TOLERANCES: FRACTIONAL \pm ANGULAR: MACH \pm BEND \pm TWO PLACE DECIMAL \pm THREE PLACE DECIMAL \pm			
		INTERPRET GEOMETRIC TOLERANCING PER:	CHECKED	ENG APPR.	MFG APPR.
		MATERIAL			
		NEXT ASSY	USED ON	FINISH	
		APPLICATION		DO NOT SCALE DRAWING	

A A

TITLE: dbr_enclosure_assy

SIZE	DWG. NO.	REV
A		
SCALE: 1:17		WEIGHT:
		SHEET 2 OF 3

PROPRIETARY AND CONFIDENTIAL
THE INFORMATION CONTAINED IN THIS
DRAWING IS THE SOLE PROPERTY OF
<INSERT COMPANY NAME HERE>. ANY
REPRODUCTION IN PART OR AS A WHOLE
WITHOUT THE WRITTEN PERMISSION OF
<INSERT COMPANY NAME HERE> IS
PROHIBITED.

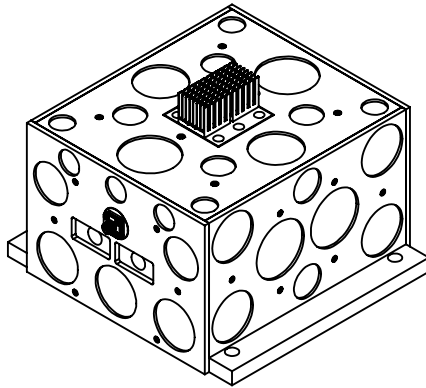
2

1

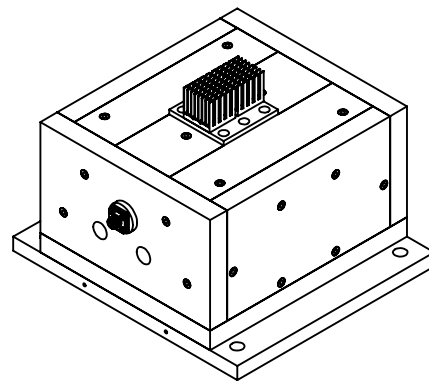
B

B

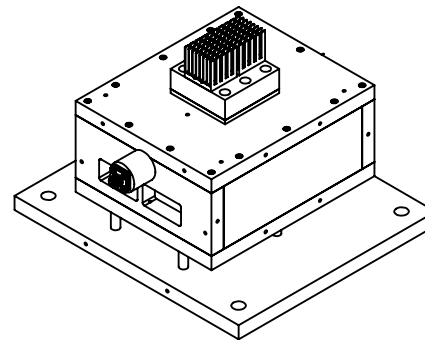
Complete



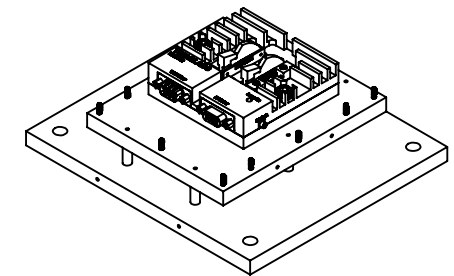
Shell Removed



Insulation Removed



Inner Cage and Heat Sink Removed



A

A

PROPRIETARY AND CONFIDENTIAL
THE INFORMATION CONTAINED IN THIS DRAWING IS THE SOLE PROPERTY OF <INSERT COMPANY NAME HERE>. ANY REPRODUCTION IN PART OR AS A WHOLE WITHOUT THE WRITTEN PERMISSION OF <INSERT COMPANY NAME HERE> IS PROHIBITED.

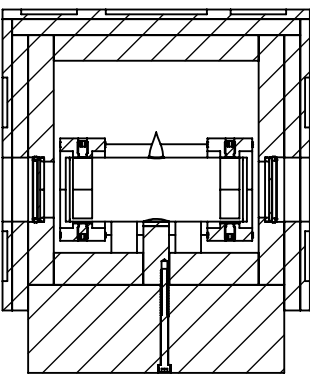
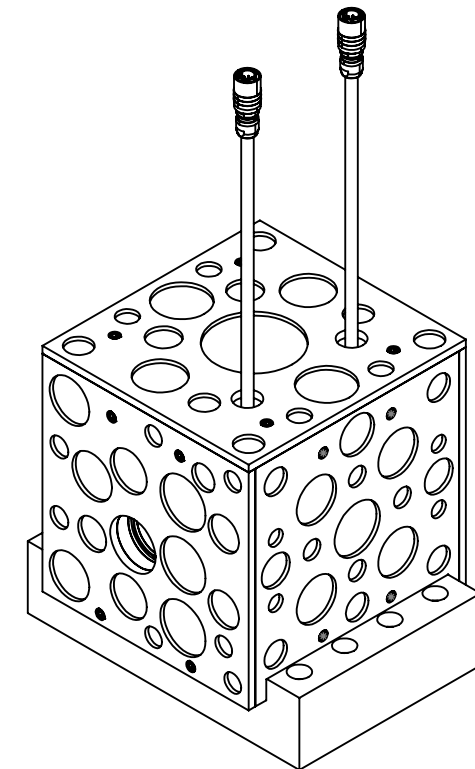
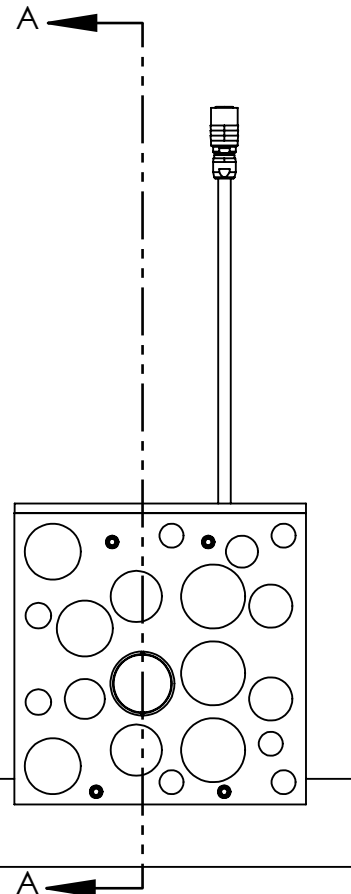
		UNLESS OTHERWISE SPECIFIED:		NAME	DATE	TITLE: dbr_enclosure_assy
		DIMENSIONS ARE IN INCHES	DRAWN			
		TOLERANCES:	CHECKED			
		FRACTIONAL \pm	ENG APPR.			
		ANGULAR: MACH \pm BEND \pm	MFG APPR.			
		TWO PLACE DECIMAL \pm	Q.A.			
		THREE PLACE DECIMAL \pm				
		INTERPRET GEOMETRIC TOLERANCING PER:				
		MATERIAL				
NEXT ASSY	USED ON	FINISH				
APPLICATION		DO NOT SCALE DRAWING				
SIZE	DWG. NO.					REV
A						
SCALE: 1:5	WEIGHT:					SHEET 3 OF 3

2

1

2

Cross Section and Iso Views

SECTION A-A
SCALE 1 : 3

PROPRIETARY AND CONFIDENTIAL
THE INFORMATION CONTAINED IN THIS DRAWING IS THE SOLE PROPERTY OF <INSERT COMPANY NAME HERE>. ANY REPRODUCTION IN PART OR AS A WHOLE WITHOUT THE WRITTEN PERMISSION OF <INSERT COMPANY NAME HERE> IS PROHIBITED.

		UNLESS OTHERWISE SPECIFIED:		DRAWN	NAME	DATE	TITLE: rb_cell_enclosure_assy				
		DIMENSIONS ARE IN INCHES TOLERANCES: FRACTIONAL \pm ANGULAR: MACH \pm BEND \pm TWO PLACE DECIMAL \pm THREE PLACE DECIMAL \pm									
		INTERPRET GEOMETRIC TOLERANCING PER: MATERIAL		CHECKED	ENG APPR.	MFG APPR.					
NEXT ASSY	USED ON	FINISH									
APPLICATION		DO NOT SCALE DRAWING		COMMENTS:							
SIZE	DWG. NO.										
A											
SCALE: 1:3		WEIGHT:		SHEET 1 OF 3							

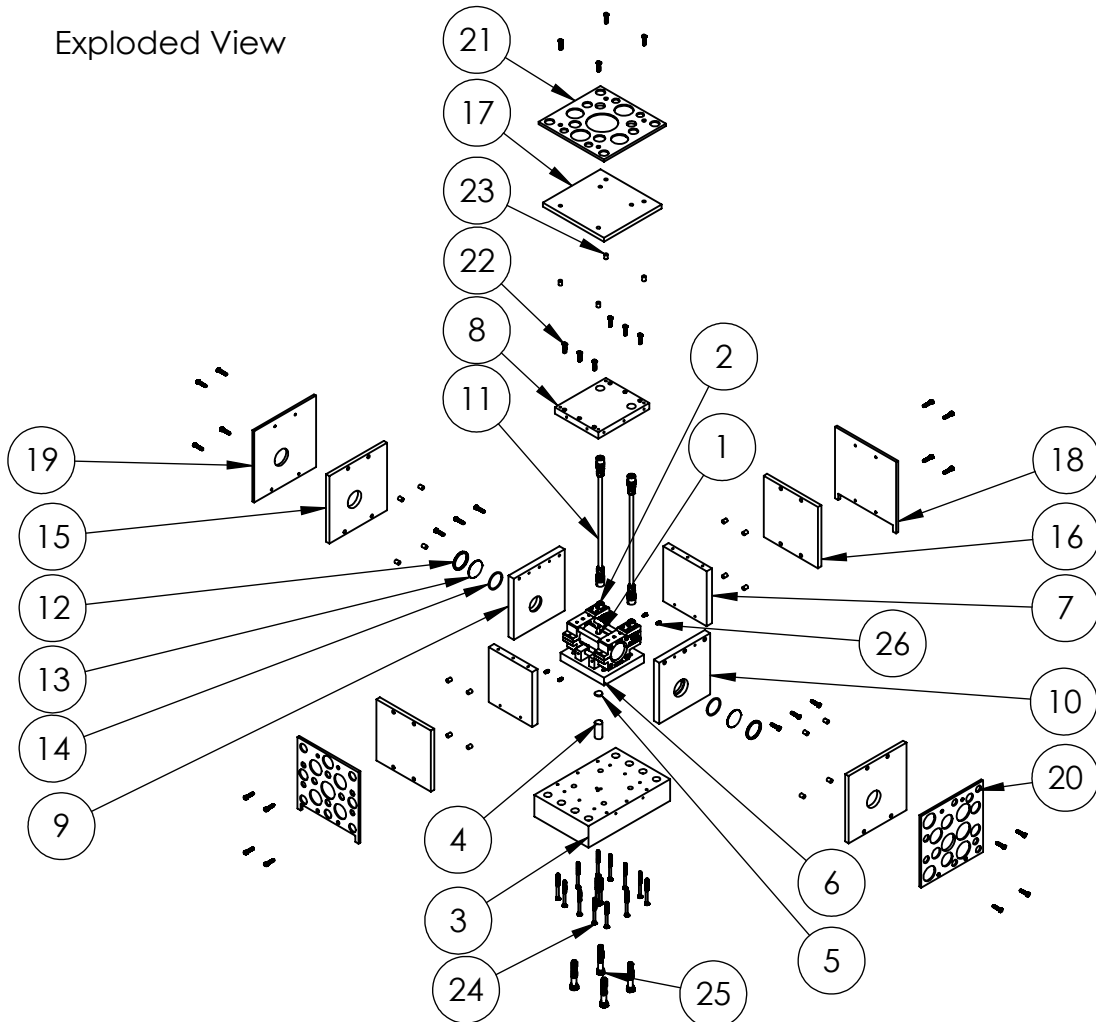
2

1

B

A

Exploded View



ITEM NO.	PART NUMBER	DESCRIPTION	QTY.
1	GC25075-RB-Solidworks	Rb Cell	1
2	GCH25-75-Solidworks	Rb Cell Heater	1
3	heat_sink	custom aluminum	1
4	heat_sink_pillar	custom aluminum	1
5	Thermal_pad	Bergquist Gap Pad	1
6	inner_chamber_bottom	custom delrin	1
7	inner_chamber_side	custom delrin	2
8	inner_chamber_top	custom delrin	1
9	inner_chamber_front	custom delrin	1
10	inner_chamber_back	custom delrin	1
11	HR10CAB1-Solidworks	Hirose Cable	2
12	SM1RR-Solidworks	retaining ring	2
13	WG41010-B-Solidworks	b-coated window	2
14	o-ring	o-ring	2
15	insulation_front_back	custom foam	2
16	insulation_side	custom foam	2
17	insulation_top	custom foam	1
18	jacket_side	custom abs	2
19	jacket_front	custom abs	1
20	jacket_back	custom abs	1
21	jacket_top	custom abs	1
22	91251A110	Black-Oxide Alloy Steel Socket Head Screw	32
23	94639A706	Off-White Nylon Unthreaded Spacer	20
24	91251A149	Black-Oxide Alloy Steel Socket Head Screw	15
25	91251A546	Black-Oxide Alloy Steel Socket Head Screw	4
26	94115A106	Alloy Steel Nylon-Tip Set Screws	4

UNLESS OTHERWISE SPECIFIED:		NAME	DATE
DIMENSIONS ARE IN INCHES			
TOLERANCES:			
FRACTIONAL \pm			
ANGULAR: MACH \pm BEND \pm			
TWO PLACE DECIMAL \pm			
THREE PLACE DECIMAL \pm			
INTERPRET GEOMETRIC TOLERANCING PER:			
MATERIAL			
NEXT ASSY	USED ON	FINISH	
APPLICATION	DO NOT SCALE DRAWING		

A A

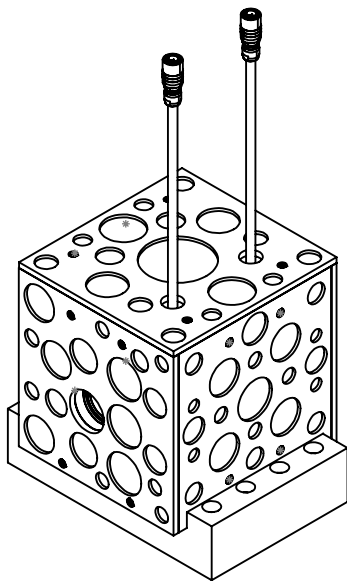
TITLE: rb_cell_enclosure_assy

SIZE	DWG. NO.	REV
A		
SCALE: 1:10	WEIGHT:	SHEET 2 OF 3

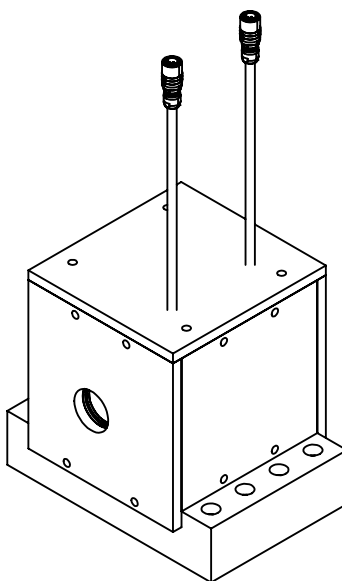
PROPRIETARY AND CONFIDENTIAL
THE INFORMATION CONTAINED IN THIS DRAWING IS THE SOLE PROPERTY OF <INSERT COMPANY NAME HERE>. ANY REPRODUCTION IN PART OR AS A WHOLE WITHOUT THE WRITTEN PERMISSION OF <INSERT COMPANY NAME HERE> IS PROHIBITED.

B

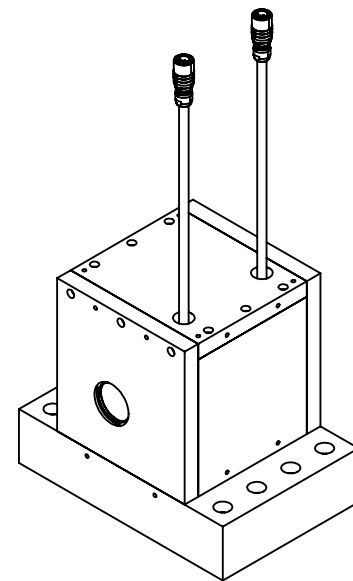
Complete



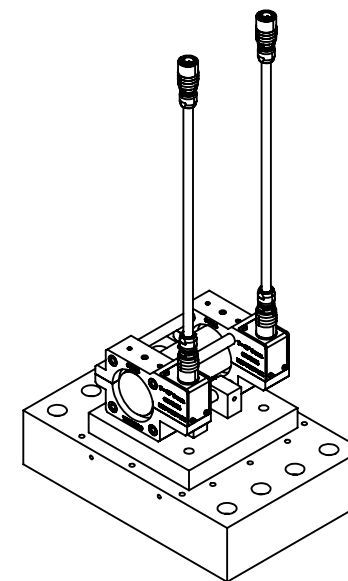
Jacket Removed



Insulation Removed



Inner Chamber Removed



B

A

A

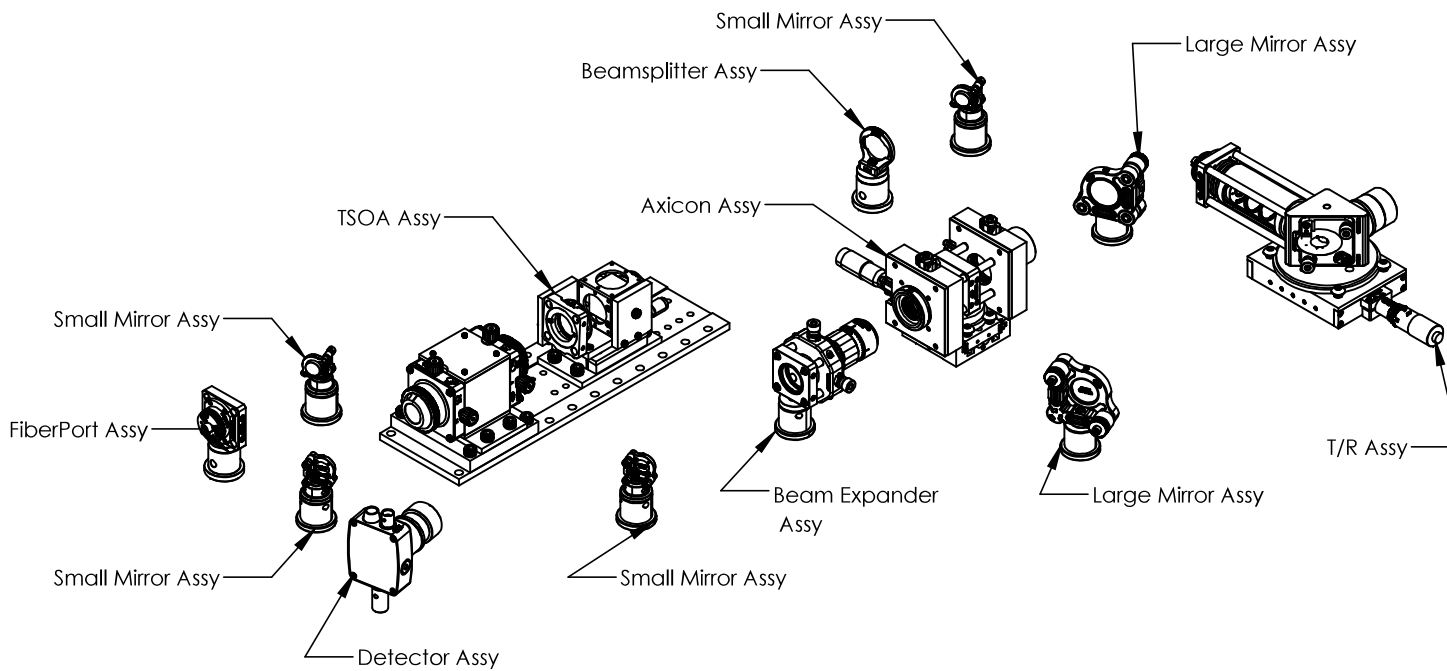
PROPRIETARY AND CONFIDENTIAL
THE INFORMATION CONTAINED IN THIS DRAWING IS THE SOLE PROPERTY OF
<INSERT COMPANY NAME HERE>. ANY
REPRODUCTION IN PART OR AS A WHOLE
WITHOUT THE WRITTEN PERMISSION OF
<INSERT COMPANY NAME HERE> IS
PROHIBITED.

		UNLESS OTHERWISE SPECIFIED:		NAME	DATE	TITLE: rb_cell_enclosure_assy		
		DIMENSIONS ARE IN INCHES						
		TOLERANCES:						
		FRACTIONAL \pm						
		ANGULAR: MACH \pm BEND \pm						
		TWO PLACE DECIMAL \pm						
		THREE PLACE DECIMAL \pm						
		INTERPRET GEOMETRIC TOLERANCING PER:						
		MATERIAL						
NEXT ASSY	USED ON	FINISH						
APPLICATION	DO NOT SCALE DRAWING							
SIZE	DWG. NO.						REV	
A								
SCALE: 1:3	WEIGHT:						SHEET 3 OF 3	

APPENDIX: TRANSMITTER SOLIDWORKS DRAWINGS

B

B



A

A

		UNLESS OTHERWISE SPECIFIED:		NAME	DATE	TITLE: Transmitter_assembly
		DIMENSIONS ARE IN INCHES	DRAWN			
		TOLERANCES:	CHECKED			
		FRACTIONAL \pm	ENG APPR.			
		ANGULAR: MACH \pm BEND \pm	MFG APPR.			
		TWO PLACE DECIMAL \pm	Q.A.			
		THREE PLACE DECIMAL \pm	COMMENTS:			
		INTERPRET GEOMETRIC TOLERANCING PER:				
		MATERIAL				
NEXT ASSY	USED ON	FINISH				
APPLICATION		DO NOT SCALE DRAWING				
			SIZE	DWG. NO.		REV
			A			
			SCALE: 1:6			WEIGHT: SHEET 1 OF 1

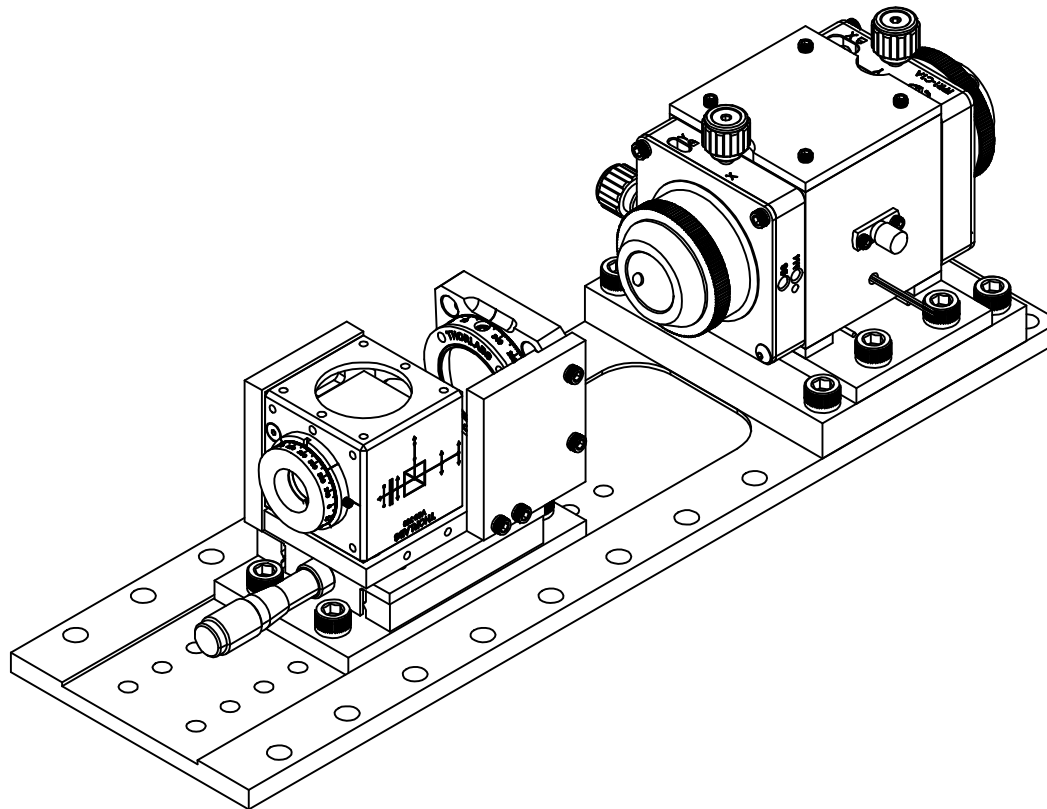
PROPRIETARY AND CONFIDENTIAL
THE INFORMATION CONTAINED IN THIS
DRAWING IS THE SOLE PROPERTY OF
<INSERT COMPANY NAME HERE>. ANY
REPRODUCTION IN PART OR AS A WHOLE
WITHOUT THE WRITTEN PERMISSION OF
<INSERT COMPANY NAME HERE> IS
PROHIBITED.

2

1

B

B



A

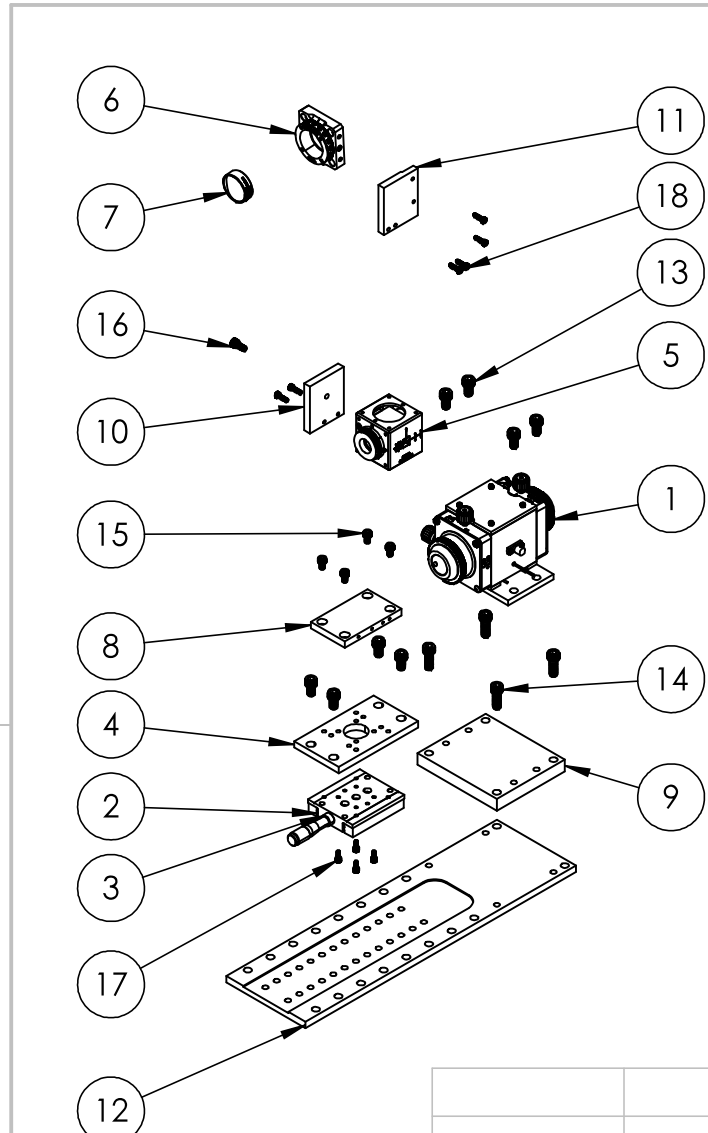
A

PROPRIETARY AND CONFIDENTIAL
 THE INFORMATION CONTAINED IN THIS
 DRAWING IS THE SOLE PROPERTY OF
 <INSERT COMPANY NAME HERE>. ANY
 REPRODUCTION IN PART OR AS A WHOLE
 WITHOUT THE WRITTEN PERMISSION OF
 <INSERT COMPANY NAME HERE> IS
 PROHIBITED.

		UNLESS OTHERWISE SPECIFIED:		NAME	DATE	TITLE: TSOA_assembly		
		DIMENSIONS ARE IN INCHES						
		TOLERANCES:						
		FRACTIONAL \pm						
		ANGULAR: MACH \pm BEND \pm						
		TWO PLACE DECIMAL \pm						
		THREE PLACE DECIMAL \pm						
		INTERPRET GEOMETRIC TOLERANCING PER:						
		MATERIAL						
NEXT ASSY	USED ON	FINISH	COMMENTS:					
APPLICATION	DO NOT SCALE DRAWING							
SIZE	DWG. NO.							
A								
SCALE: 1:2	WEIGHT:		REV					
			SHEET 1 OF 2					

2

1



ITEM NO.	PART NUMBER	DESCRIPTION	QTY.
1	Tapered_Amplifier_assy	Custom Assembly	1
2	Newport-UMR5_16	Linear Stage, Double-Row Ball Bearings, 0.63 in., 4-40, 8-32 and 1/4-20	1
3	Newport-BM11_16	Micrometer Head, Standard Resolution, 16 mm Travel, 9 lb. Load	1
4	Newport-M-PBN5	Base Plate, Used with UMR5 Series, MVN50 & UTR46 Series	1
5	VC5-780-Solidworks	30 mm Cage-Cube-Mounted Variable Circular Polarizer 780 nm, 8-32 Tap	1
6	CRM1L-Solidworks	Cage Rotation Mount for Ø1" Optics, Double Bored with Setscrew, 8-32 Tap	1
7	LJ1695RM-B-Solidworks	f = 50.0 mm, Ø1", N-BK7 Mounted Plano-Convex Round Cyl Lens, ARC: 650 - 1050 nm	1
8	translation_stage_adaptor_bottom	Custom Aluminum	1
9	TSOA_baseplate	Custom Aluminum	1
10	cir_pol_mount	Custom Aluminum	1
11	cyl_lens_mount	Custom Aluminum	1
12	TSOA_assembly_base	Custom Aluminum	1
13	91251A535	Black-Oxide Alloy Steel Socket Head Screw (1/4-20, L=3/8")	8
14	91251A539	Black-Oxide Alloy Steel Socket Head Screw (1/4-20, L=5/8")	4
15	91251A190	Black-Oxide Alloy Steel Socket Head Screw (8-32, L=1/4")	4
16	91251A192	Black-Oxide Alloy Steel Socket Head Screw (8-32, L=3/8")	1
17	91251A106	Black-Oxide Alloy Steel Socket Head Screw (4-40, L=1/4")	4
18	91251A108	Black-Oxide Alloy Steel Socket Head Screw (4-40, L=3/8")	6

PROPRIETARY AND CONFIDENTIAL
THE INFORMATION CONTAINED IN THIS DRAWING IS THE SOLE PROPERTY OF
<INSERT COMPANY NAME HERE>. ANY
REPRODUCTION IN PART OR AS A WHOLE
WITHOUT THE WRITTEN PERMISSION OF
<INSERT COMPANY NAME HERE> IS
PROHIBITED.

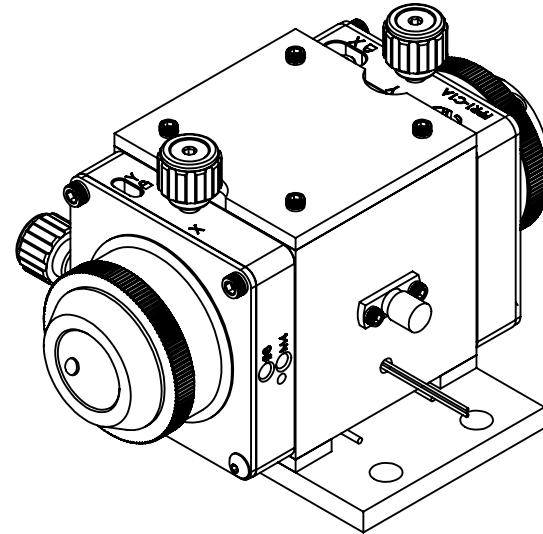
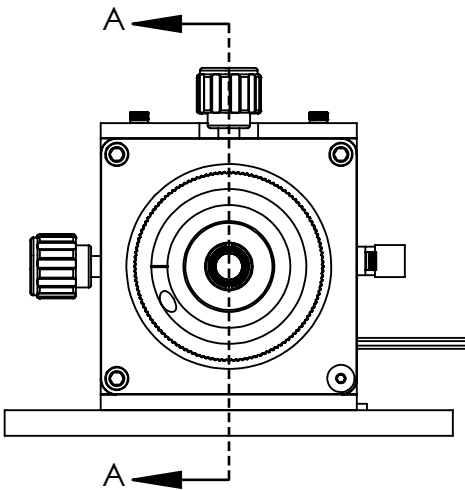
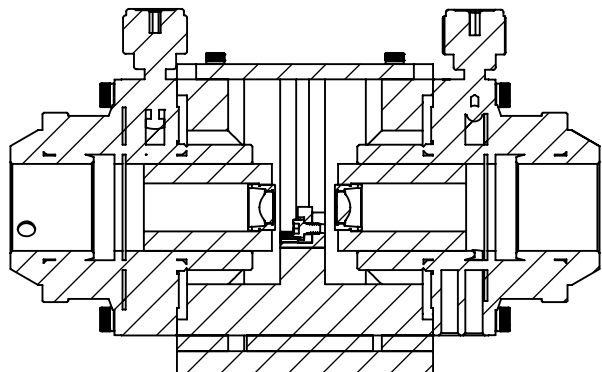
UNLESS OTHERWISE SPECIFIED:		NAME	DATE
DIMENSIONS ARE IN INCHES	DRAWN		
TOLERANCES: FRACTIONAL \pm ANGULAR: MACH \pm BEND \pm TWO PLACE DECIMAL \pm THREE PLACE DECIMAL \pm	CHECKED		
INTERPRET GEOMETRIC TOLERANCING PER:	ENG APPR.		
MATERIAL	MFG APPR.		
NEXT ASSY	Q.A.		
USED ON			
APPLICATION			
			COMMENTS:

TSOA_assembly

SIZE	DWG. NO.	REV
A		
SCALE: 1:6	WEIGHT:	SHEET 2 OF 2

2

1



SECTION A-A
SCALE 2 : 3

PROPRIETARY AND CONFIDENTIAL
THE INFORMATION CONTAINED IN THIS DRAWING IS THE SOLE PROPERTY OF <INSERT COMPANY NAME HERE>. ANY REPRODUCTION IN PART OR AS A WHOLE WITHOUT THE WRITTEN PERMISSION OF <INSERT COMPANY NAME HERE> IS PROHIBITED.

		UNLESS OTHERWISE SPECIFIED:		DRAWN	NAME	DATE	TITLE: Tapered_Amplifier_assy				
		DIMENSIONS ARE IN INCHES TOLERANCES: FRACTIONAL \pm ANGULAR: MACH \pm BEND \pm TWO PLACE DECIMAL \pm THREE PLACE DECIMAL \pm									
		INTERPRET GEOMETRIC TOLERANCING PER: MATERIAL		CHECKED	ENG APPR.	MFG APPR.					
		NEXT ASSY									
		USED ON		COMMENTS:							
		APPLICATION		FINISH							
		DO NOT SCALE DRAWING									
SIZE		DWG. NO.		REV							
A											
SCALE: 2:3		WEIGHT:		SHEET 1 OF 3							

2

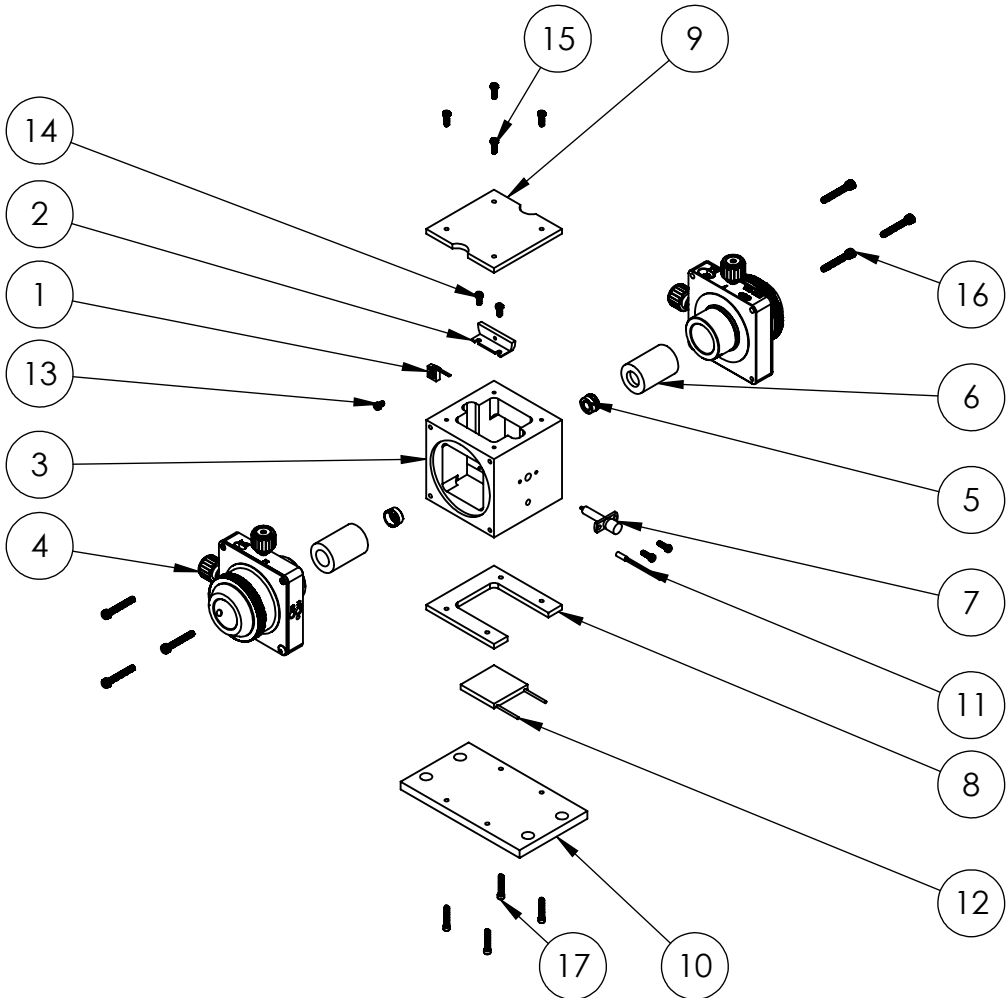
1

B

A

B

B



ITEM NO.	PART NUMBER	DESCRIPTION	QTY.
1	Tapered_Amplifier	Eagleyard (EYP-TPA-0780-03000-4006-CMT04-0000)	1
2	Tapered_Amplifier_Holder	Custom Aluminum	1
3	TA_mount_center	Custom Aluminum	1
4	Newport-FPR1-C1A	Fiber Optic Positioner	2
5	C230TMD-B-Solidworks	f = 4.51 mm, NA = 0.55, WD = 2.43 mm, Mounted Aspheric Lens, ARC: 600 - 1050 nm	2
6	lens_holder	Custom Aluminum	2
7	SMA_female_flange	Pasternack SMA Female Connector Solder Attachment 2 Hole Flange Mount Stub Terminal, .481 inch Hole Spacing, .050 inch Diameter, Gold Plated	1
8	TA_HS_compression_mount	Custom ABS	1
9	TA_mount_lid	Custom Delrin	1
10	TA_mount_base	Custom Aluminum	1
11	Thermistor	Thorlabs 10 kΩ Thermistor	1
12	TEC	Laird (CP08-127-05-L1-W4.5)	1
13	91251A072	Black-Oxide Alloy Steel Socket Head Screw (2-56, L=1/8")	1
14	91251A076	Black-Oxide Alloy Steel Socket Head Screw (2-56, L=3/16")	2
15	91251A077	Black-Oxide Alloy Steel Socket Head Screw (2-56, L=1/4")	6
16	91251A113	Black-Oxide Alloy Steel Socket Head Screw (4-40, L=3/4")	6
17	95868A126	Nylon Socket Head Screws (2-56, L=1/2")	4

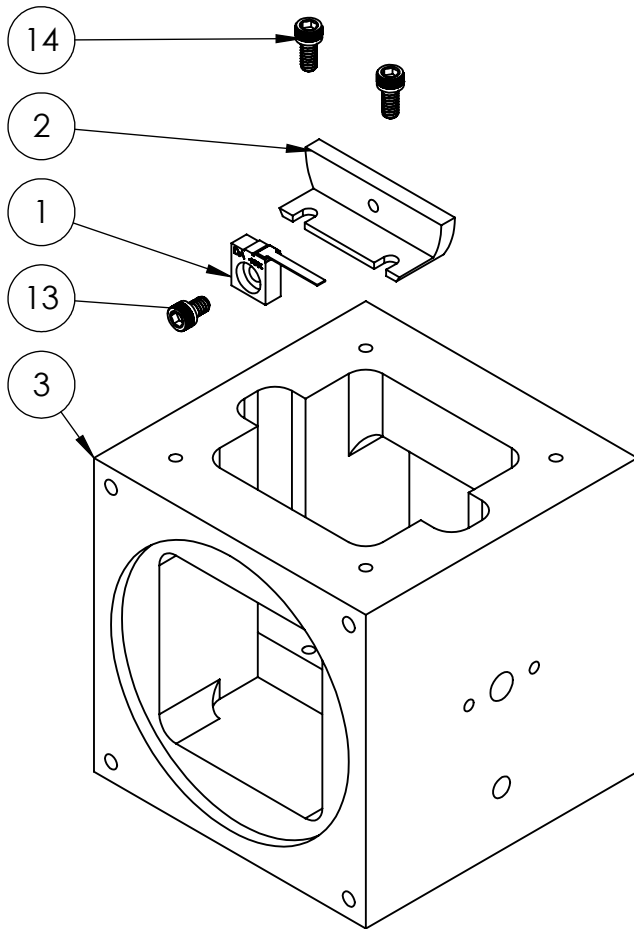
A

A

		UNLESS OTHERWISE SPECIFIED:	DRAWN	NAME	DATE
		DIMENSIONS ARE IN INCHES TOLERANCES: FRACTIONAL \pm ANGULAR: MACH \pm BEND \pm TWO PLACE DECIMAL \pm THREE PLACE DECIMAL \pm			
		INTERPRET GEOMETRIC TOLERANCING PER: MATERIAL	CHECKED	ENG APPR.	MFG APPR.
		NEXT ASSY	USED ON	FINISH	
		APPLICATION		DO NOT SCALE DRAWING	

TITLE:	Tapered_Amplifier_assy		
	SIZE	DWG. NO.	REV
A			
SCALE: 1:4		WEIGHT:	SHEET 2 OF 3

PROPRIETARY AND CONFIDENTIAL
 THE INFORMATION CONTAINED IN THIS DRAWING IS THE SOLE PROPERTY OF
 <INSERT COMPANY NAME HERE>. ANY
 REPRODUCTION IN PART OR AS A WHOLE
 WITHOUT THE WRITTEN PERMISSION OF
 <INSERT COMPANY NAME HERE> IS
 PROHIBITED.



B

ITEM NO.	PART NUMBER	DESCRIPTION	QTY.
1	Tapered_Amplifier	Eagleyard (EYP-TPA-0780-03000-4006-CMT04-0000)	1
2	Tapered_Amplifier_Holder	Custom Aluminum	1
3	TA_mount_center	Custom Aluminum	1
4	Newport-FPR1-C1A	Fiber Optic Positioner	2
5	C230TMD-B-Solidworks	f = 4.51 mm, NA = 0.55, WD = 2.43 mm, Mounted Aspheric Lens, ARC: 600 - 1050 nm	2
6	lens_holder	Custom Aluminum	2
7	SMA_female_flange	Pasternack SMA Female Connector Solder Attachment 2 Hole Flange Mount Stub Terminal, .481 inch Hole Spacing, .050 inch Diameter, Gold Plated	1
8	91251A076	Black-Oxide Alloy Steel Socket Head Screw (2-56, L=3/16")	2
9	91251A077	Black-Oxide Alloy Steel Socket Head Screw (2-56, L=1/4")	6
10	91251A113	Black-Oxide Alloy Steel Socket Head Screw (4-40, L=3/4")	6
11	91251A072	Black-Oxide Alloy Steel Socket Head Screw (2-56, L=1/8")	1
12	TA_mount_lid	Custom Delrin	1
13	TA_HS_compression_mount	Custom ABS	1
14	TA_mount_base	Custom Aluminum	1
15	95868A126	Nylon Socket Head Screws (2-56, L=1/2")	4
16	Thermistor	Thorlabs 10 kΩ Thermistor	1
17	TEC	Laird (CP08-127-05-L1-W4.5)	1

B

A

		UNLESS OTHERWISE SPECIFIED:		NAME	DATE	TITLE: Tapered_Amplifier_assy
		DIMENSIONS ARE IN INCHES	DRAWN			
		TOLERANCES:	CHECKED			
		FRACTIONAL \pm	ENG APPR.			
		ANGULAR: MACH \pm BEND \pm	MFG APPR.			
		TWO PLACE DECIMAL \pm	Q.A.			
		THREE PLACE DECIMAL \pm	COMMENTS:			
		INTERPRET GEOMETRIC TOLERANCING PER:				
		MATERIAL				
NEXT ASSY	USED ON	FINISH				
APPLICATION		DO NOT SCALE DRAWING				
			SIZE	DWG. NO.	REV	
			A			
			SCALE: 1:1 WEIGHT: SHEET 3 OF 3			

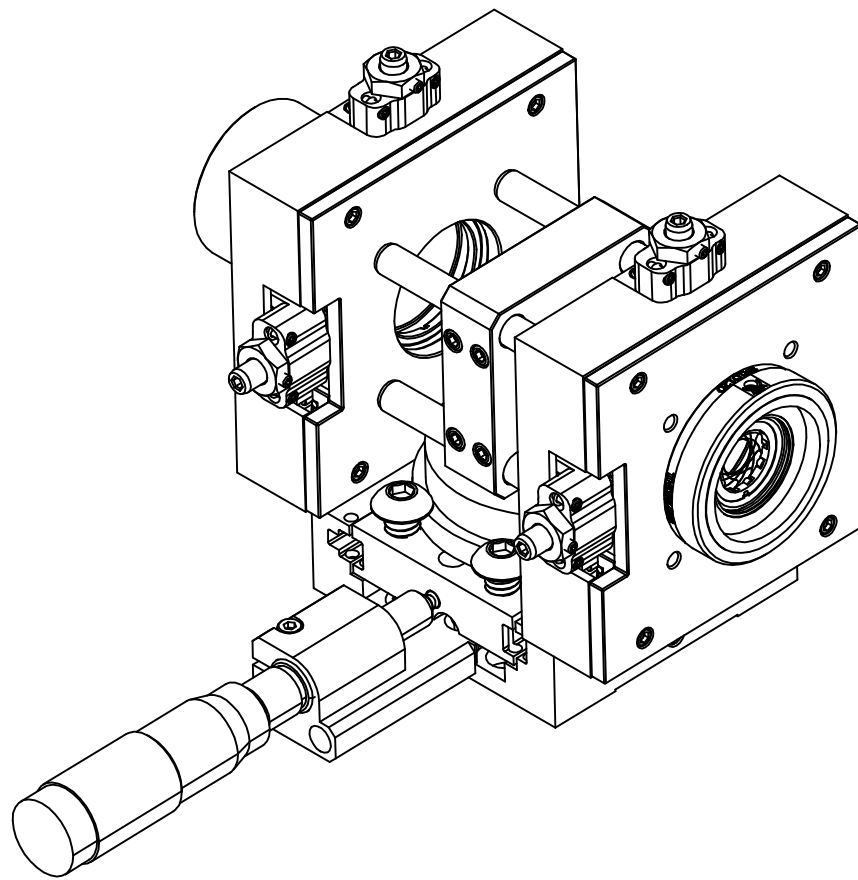
PROPRIETARY AND CONFIDENTIAL
THE INFORMATION CONTAINED IN THIS
DRAWING IS THE SOLE PROPERTY OF
<INSERT COMPANY NAME HERE>. ANY
REPRODUCTION IN PART OR AS A WHOLE
WITHOUT THE WRITTEN PERMISSION OF
<INSERT COMPANY NAME HERE> IS
PROHIBITED.

2

1

B

B



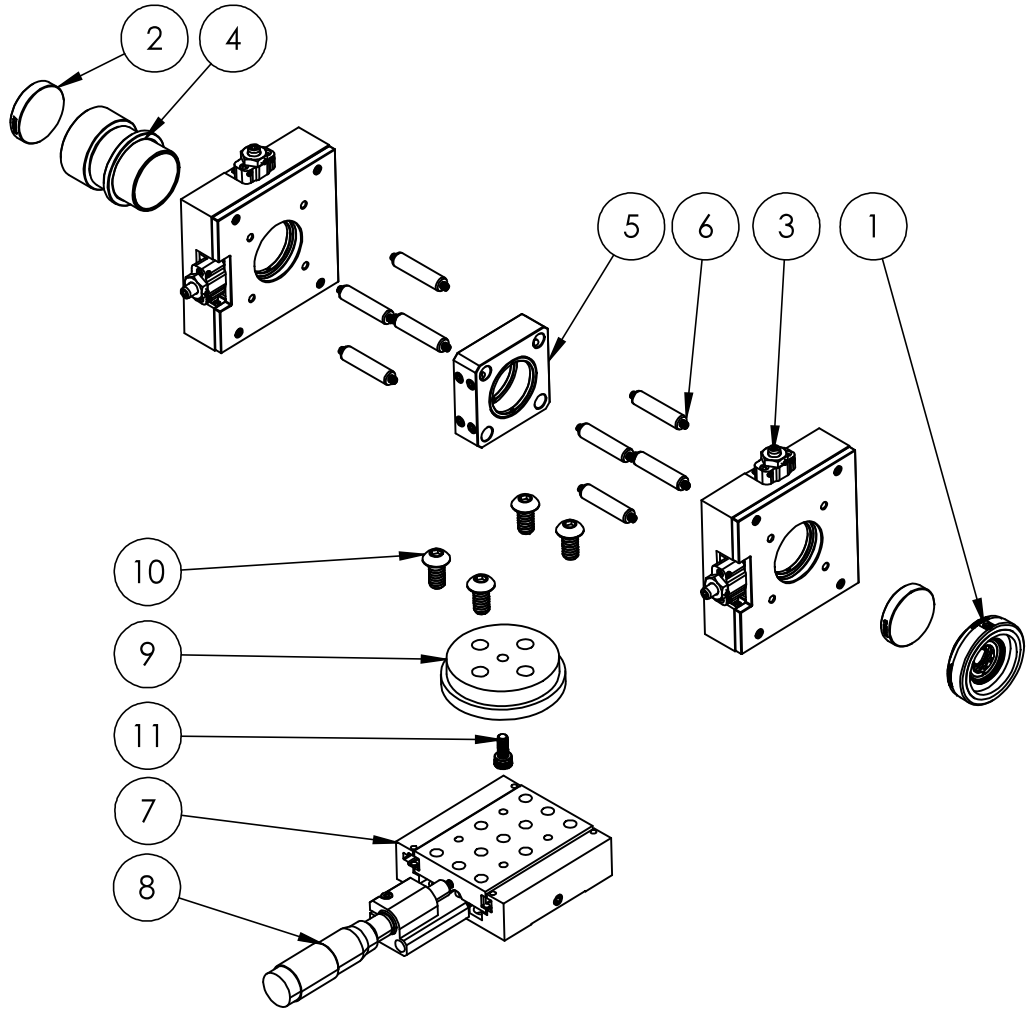
PROPRIETARY AND CONFIDENTIAL
THE INFORMATION CONTAINED IN THIS
DRAWING IS THE SOLE PROPERTY OF
<INSERT COMPANY NAME HERE>. ANY
REPRODUCTION IN PART OR AS A WHOLE
WITHOUT THE WRITTEN PERMISSION OF
<INSERT COMPANY NAME HERE> IS
PROHIBITED.

		UNLESS OTHERWISE SPECIFIED:		NAME	DATE	TITLE: Axicon_assembly
		DIMENSIONS ARE IN INCHES	DRAWN			
		TOLERANCES:	CHECKED			
		FRACTIONAL \pm	ENG APPR.			
		ANGULAR: MACH \pm BEND \pm	MFG APPR.			
		TWO PLACE DECIMAL \pm	Q.A.			
		THREE PLACE DECIMAL \pm				
		INTERPRET GEOMETRIC TOLERANCING PER:				
		MATERIAL				
NEXT ASSY	USED ON	FINISH				
APPLICATION		DO NOT SCALE DRAWING				

2

1

A



ITEM NO.	PART NUMBER	DESCRIPTION	QTY.
1	SM1D12D-Solidworks	SM1 Ring-Actuated Iris Diaphragm ($\varnothing 0.8$ - $\varnothing 12.0$ mm)	1
2	AX255-B-Solidworks	5.0°, 650 - 1050 nm AR Coated UVFS, $\varnothing 1"$ ($\varnothing 25.4$ mm) Axicon	2
3	ST1XY-A-Solidworks	XY Translator with 100 TPI Drives	2
4	SM1V10-Solidworks	$\varnothing 1"$ Adjustable Lens Tube, 0.81" Travel Range	1
5	CP33T-Solidworks	SM1-Threaded 30 mm Cage Plate, 0.50" Thick	1
6	ER1-Solidworks	Cage Assembly Rod ($L=1"$)	8
7	Newport-M-460P-X	X Linear Stage	1
8	Newport-SM-25	Vernier Micrometer	1
9	Axicon_mount	Custom Aluminum	1
10	91255A537	Button Head Hex Drive Screw (1/4-20, $L=1\frac{1}{2}"$)	4
11	91251A192	Black-Oxide Alloy Steel Socket Head Screw (8-32, $L=3/8"$)	1

PROPRIETARY AND CONFIDENTIAL
THE INFORMATION CONTAINED IN THIS DRAWING IS THE SOLE PROPERTY OF <INSERT COMPANY NAME HERE>. ANY REPRODUCTION IN PART OR AS A WHOLE WITHOUT THE WRITTEN PERMISSION OF <INSERT COMPANY NAME HERE> IS PROHIBITED.

		UNLESS OTHERWISE SPECIFIED:		NAME	DATE
		DIMENSIONS ARE IN INCHES		DRAWN	
		TOLERANCES:		CHECKED	
		FRACTIONAL \pm		ENG APPR.	
		ANGULAR: MACH \pm BEND \pm		MFG APPR.	
		TWO PLACE DECIMAL \pm		Q.A.	
		THREE PLACE DECIMAL \pm		COMMENTS:	
		INTERPRET GEOMETRIC TOLERANCING PER:			
		MATERIAL			
NEXT ASSY	USED ON	FINISH			
APPLICATION		DO NOT SCALE DRAWING			

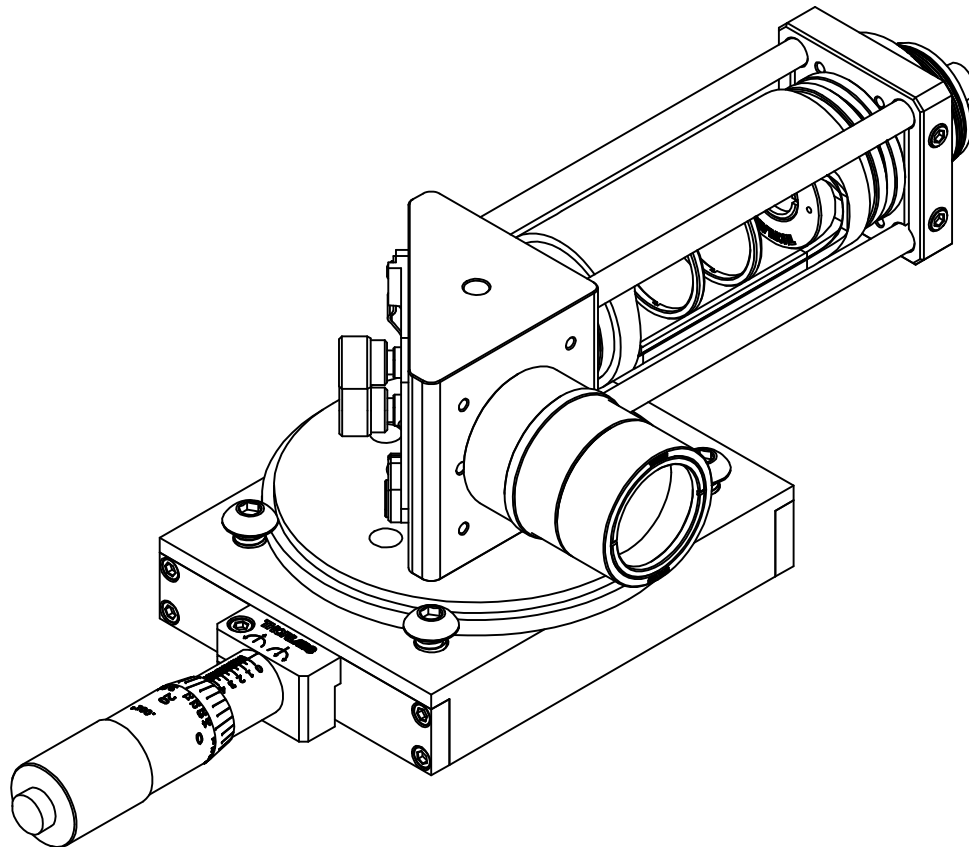
TITLE:

Axicon_assembly

SIZE	DWG. NO.	REV
A		
SCALE: 1:3	WEIGHT:	SHEET 2 OF 2

2

1



B

B

		UNLESS OTHERWISE SPECIFIED:				NAME	DATE	TITLE: TR_assembly
		DIMENSIONS ARE IN INCHES			DRAWN			
		TOLERANCES:			CHECKED			
		FRACTIONAL \pm			ENG APPR.			
		ANGULAR: MACH \pm BEND \pm			MFG APPR.			
		TWO PLACE DECIMAL \pm			Q.A.			
		THREE PLACE DECIMAL \pm			COMMENTS:			
		INTERPRET GEOMETRIC TOLERANCING PER:						
		MATERIAL						
		NEXT ASSY	USED ON	FINISH				
		APPLICATION		DO NOT SCALE DRAWING				

PROPRIETARY AND CONFIDENTIAL
THE INFORMATION CONTAINED IN THIS
DRAWING IS THE SOLE PROPERTY OF
<INSERT COMPANY NAME HERE>. ANY
REPRODUCTION IN PART OR AS A WHOLE
WITHOUT THE WRITTEN PERMISSION OF
<INSERT COMPANY NAME HERE> IS
PROHIBITED.

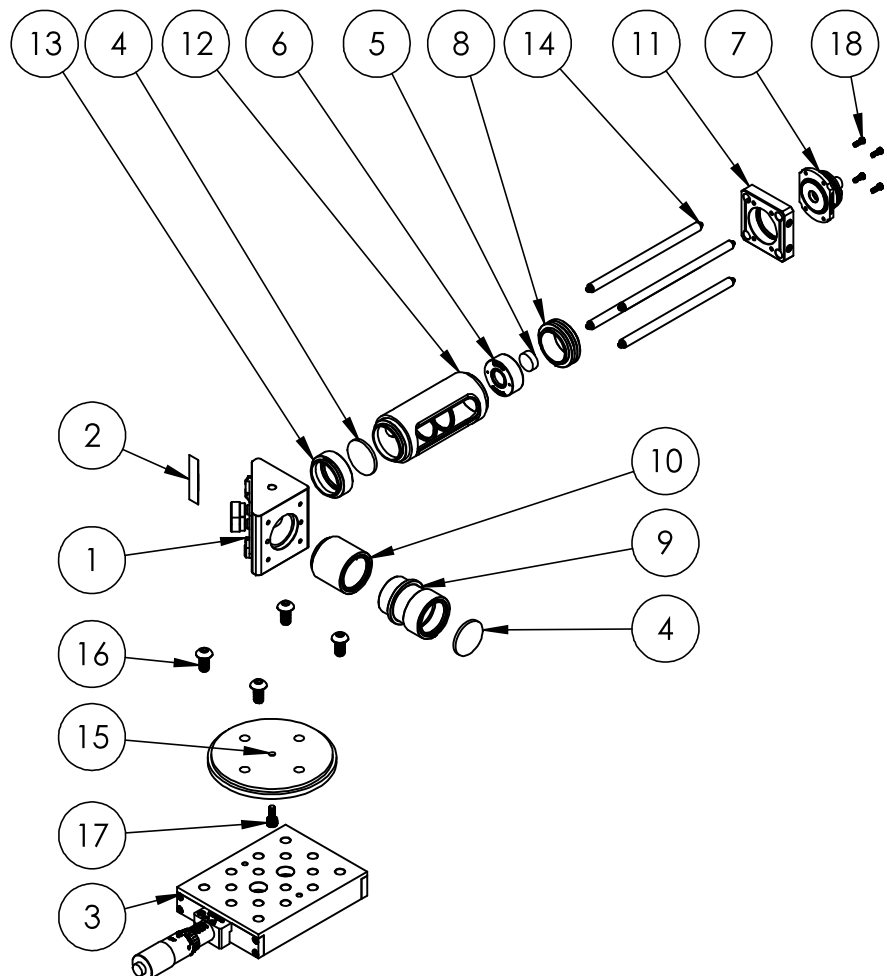
2

1

SIZE DWG. NO. REV
A

SCALE: 2:3 WEIGHT: SHEET 1 OF 2

A



B

B

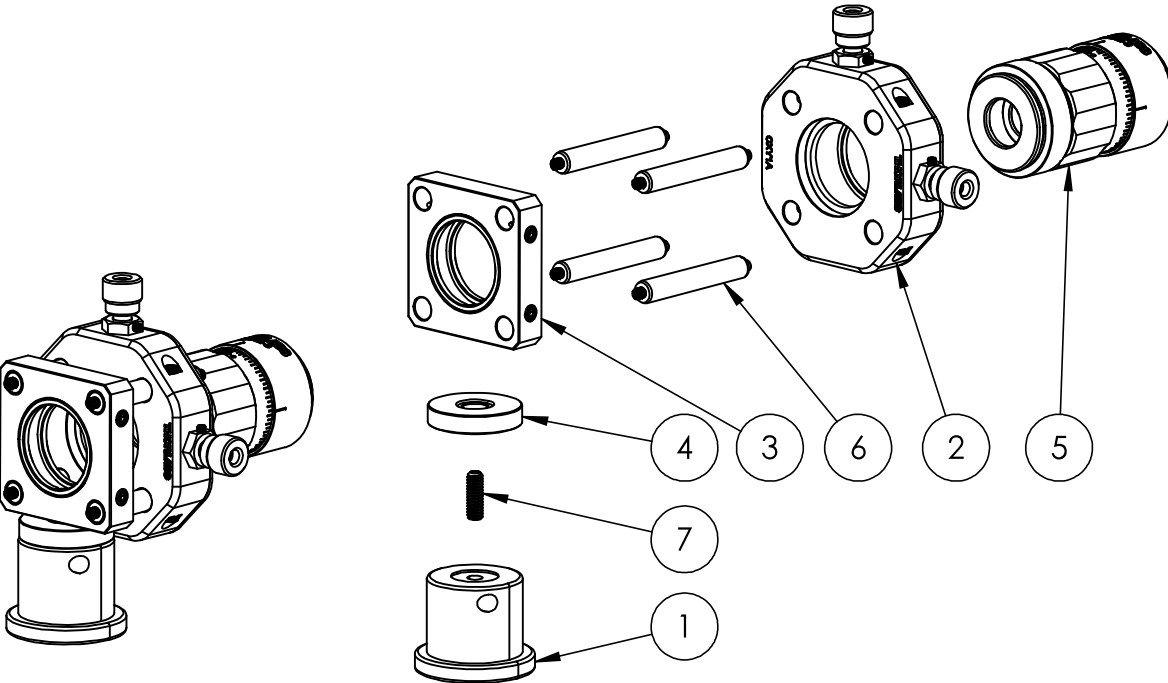
ITEM NO.	PART NUMBER	DESCRIPTION	QTY.
1	KCB1E-Solidworks	Right-Angle Kinematic Elliptical Mirror Mount with Tapped Cage Rod Holes, 30 mm Cage System and SM1 Compatible, 8-32 and 1/4"-20 Mounting Holes	1
2	BBE1-E03-modified	1" Broadband Dielectric Elliptical Mirror, 750 - 1100 nm with 10cm center bore hole	1
3	PT1-Solidworks	1" Translation Stage with Standard Micrometer, 1/4"-20 Taps	1
4	LA1509-B-Solidworks	N-BK7 Plano-Convex Lens, Ø1", f = 100 mm, AR Coating: 650 - 1050 nm	2
5	LC1054-B-Solidworks	N-BK7 Plano-Concave Lens, Ø1/2", f = -25.0 mm, AR Coating: 650-1050 nm	1
6	SM1A6T-Solidworks	Adapter with External SM1 Threads and Internal SM05 Threads, 0.40" Long	1
7	PAF2P-11B-Solidworks	FiberPort, FC/PC, f=11.0 mm, 600 - 1050 nm, Ø2.38 mm Waist	1
8	CMT2-Solidworks	C-Mount (1.00"-32) Coupler, External Threads, 0.5" Long	1
9	SM1V10-Solidworks	Ø1" Adjustable Lens Tube, 0.81" Travel Range	1
10	SM1L10-Solidworks	SM1 Lens Tube, 1.00" Thread Depth	1
11	CP08FP-Solidworks	FiberPort Adapter for 30 mm Cage System	1
12	SM1L30C-Solidworks	SM1 Slotted Lens Tube, 3" Thread Depth	1
13	SM1L03-Solidworks	SM1 Lens Tube, 0.30" Thread Depth	1
14	ER4-Solidworks	Cage Assembly Rod, 4" Long, Ø6 mm	4
15	TR_mount	Custom Aluminum	1
16	91255A537	Button Head Hex Drive Screw (1/4-20, L=1 1/2")	4
17	91251A192	Black-Oxide Alloy Steel Socket Head Screw (8-32, L=3/8")	1
18	91251A077	Black-Oxide Alloy Steel Socket Head Screw (2-56, L=1/4")	4

A

A

		UNLESS OTHERWISE SPECIFIED:		NAME	DATE	TITLE: TR_assembly
		DIMENSIONS ARE IN INCHES	DRAWN			
		TOLERANCES:	CHECKED			
		FRACTIONAL \pm	ENG APPR.			
		ANGULAR: MACH \pm BEND \pm	MFG APPR.			
		TWO PLACE DECIMAL \pm	Q.A.			
		THREE PLACE DECIMAL \pm	COMMENTS:			
		INTERPRET GEOMETRIC TOLERANCING PER:				
		MATERIAL				
NEXT ASSY	USED ON	FINISH				
APPLICATION		DO NOT SCALE DRAWING				
SIZE		DWG. NO.		REV		
A						
SCALE: 1:5		WEIGHT:		SHEET 2 OF 2		

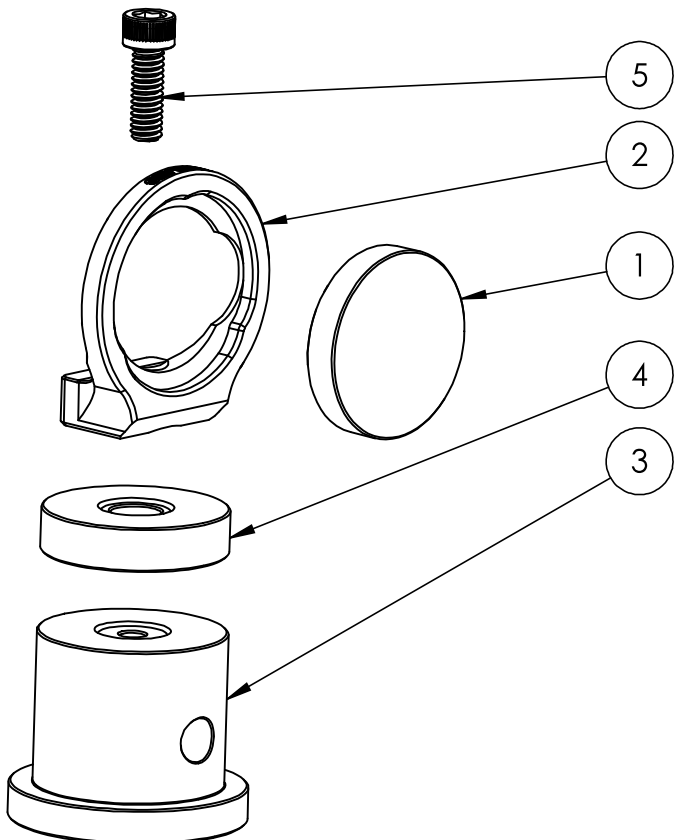
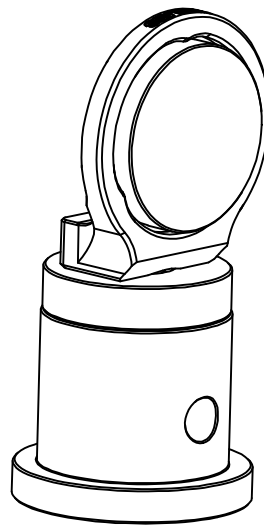
PROPRIETARY AND CONFIDENTIAL
THE INFORMATION CONTAINED IN THIS DRAWING IS THE SOLE PROPERTY OF
<INSERT COMPANY NAME HERE>. ANY
REPRODUCTION IN PART OR AS A WHOLE
WITHOUT THE WRITTEN PERMISSION OF
<INSERT COMPANY NAME HERE> IS
PROHIBITED.



PROPRIETARY AND CONFIDENTIAL
THE INFORMATION CONTAINED IN THIS DRAWING IS THE SOLE PROPERTY OF <INSERT COMPANY NAME HERE>. ANY REPRODUCTION IN PART OR AS A WHOLE WITHOUT THE WRITTEN PERMISSION OF <INSERT COMPANY NAME HERE> IS PROHIBITED.

ITEM NO.	PART NUMBER	DESCRIPTION	QTY.
1	Newport-9952	Optical Pedestal, Clean-Passivated, 1.0 in. Height, 1 in. Diameter, 8-32	1
2	CXY1A-Solidworks	30 mm Cage System, XY Translating Lens Mount for Ø1" Optics	1
3	CP33-Solidworks	SM1-Threaded 30 mm Cage Plate, 0.35" Thick, 2 Retaining Rings, 8-32 Tap	1
4	RS5M-Solidworks	Ø25.0 mm Post Spacer, Thickness = 5 mm	1
5	GBE02-B-Solidworks	2X Achromatic Galilean Beam Expander, AR Coated: 650 - 1050 nm	1
6	ER1.5-Solidworks	Cage Assembly Rod, 1.5" Long, Ø6 mm	4
7	91375A194	Alloy Steel Cup-Point Set Screw (8-32, L=1/2")	1

		UNLESS OTHERWISE SPECIFIED:		NAME	DATE	TITLE: Beam_expander_assembly
		DIMENSIONS ARE IN INCHES	DRAWN			
		TOLERANCES:	CHECKED			
		FRACTIONAL \pm	ENG APPR.			
		ANGULAR: MACH \pm BEND \pm	MFG APPR.			
		TWO PLACE DECIMAL \pm	Q.A.			
		THREE PLACE DECIMAL \pm	COMMENTS:			
		INTERPRET GEOMETRIC TOLERANCING PER:				
		MATERIAL				
NEXT ASSY	USED ON	FINISH				
APPLICATION		DO NOT SCALE DRAWING				
SIZE	DWG. NO.		REV		A	
SCALE: 1:2	WEIGHT:		SHEET 1 OF 1			



ITEM NO.	PART NUMBER	DESCRIPTION	QTY.
1	BSF10-B-Solidworks	Ø1" UVFS Beam Sampler for Beam Pick-Off, ARC: 650-1050 nm, 5 mm Thick	1
2	POLARIS-B1G-Solidworks	Polaris Ø1" Glue-In Fixed Mount, Optimized for Beamsplitters	1
3	RS1P8E-Solidworks	Ø1" Pedestal Pillar Post, 8-32 Taps, L = 1"	1
4	RS6M-Solidworks	Ø25.0 mm Post Spacer, Thickness = 6 mm	1
5	91251A194	Black-Oxide Alloy Steel Socket Head Screw (8-32, L=1/2")	1

B

B

A

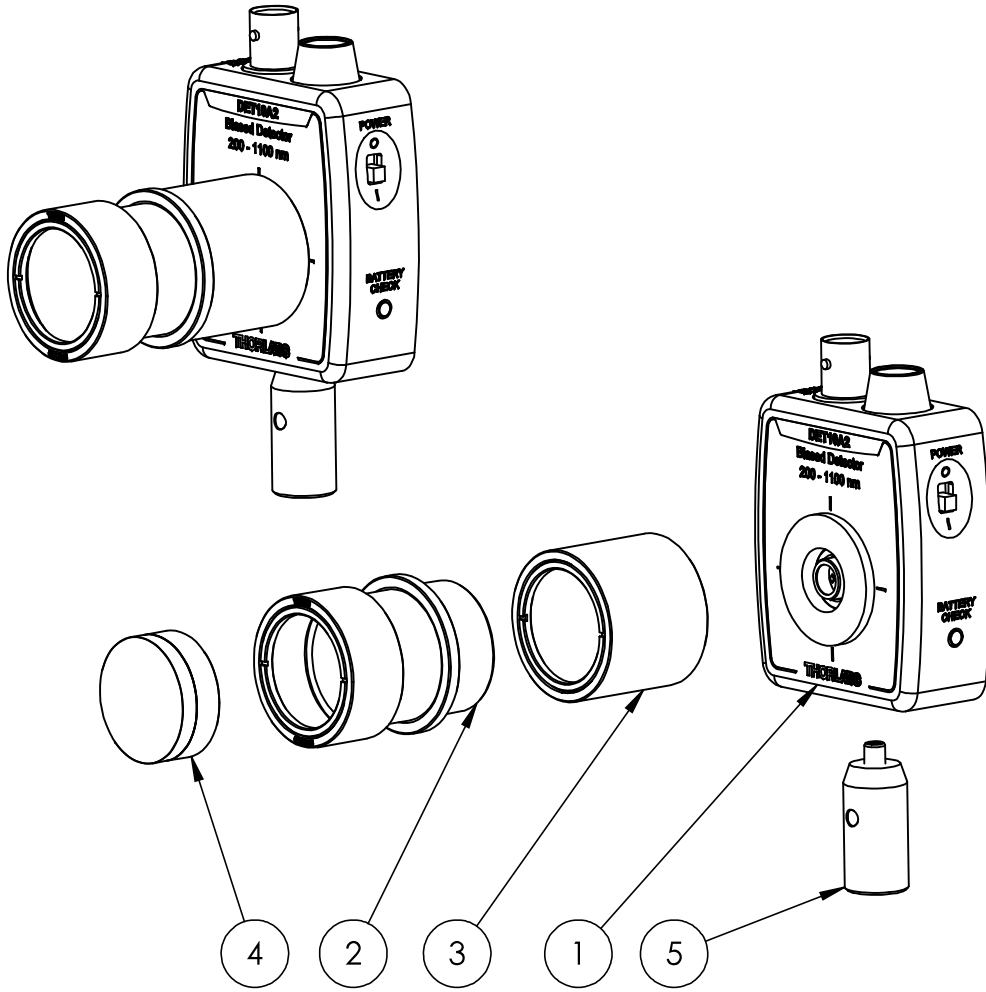
A

		UNLESS OTHERWISE SPECIFIED:		NAME	DATE	TITLE: Beamsplitter_assembly
		DIMENSIONS ARE IN INCHES	DRAWN			
		TOLERANCES:	CHECKED			
		FRACTIONAL \pm	ENG APPR.			
		ANGULAR: MACH \pm BEND \pm	MFG APPR.			
		TWO PLACE DECIMAL \pm	Q.A.			
		THREE PLACE DECIMAL \pm	COMMENTS:			
		INTERPRET GEOMETRIC TOLERANCING PER:				
		MATERIAL				
NEXT ASSY	USED ON	FINISH				
APPLICATION		DO NOT SCALE DRAWING				
			SIZE	DWG. NO.	REV	
			A			
			SCALE: 1:1	WEIGHT:	SHEET 1 OF 1	

PROPRIETARY AND CONFIDENTIAL
THE INFORMATION CONTAINED IN THIS
DRAWING IS THE SOLE PROPERTY OF
<INSERT COMPANY NAME HERE>. ANY
REPRODUCTION IN PART OR AS A WHOLE
WITHOUT THE WRITTEN PERMISSION OF
<INSERT COMPANY NAME HERE> IS
PROHIBITED.

2

1



ITEM NO.	PART NUMBER	DESCRIPTION	QTY.
1	DET10A2-Solidworks	Si Detector, 200 - 1100 nm, 1 ns Rise Time, 0.8 mm ² , Universal 8-32 / M4 Mounting Holes	1
2	SM1V10-Solidworks	Ø1" Adjustable Lens Tube, 0.81" Travel Range	1
3	SM1M10-Solidworks	SM1 Lens Tube Without External Threads, 1" Long	1
4	AC254-050-AB-Solidworks	f = 50.0 mm, Ø1" Achromatic Doublet, ARC: 650 - 1050 nm	1
5	TR1-Solidworks	Ø1/2" Optical Post, SS, 8-32 Setscrew, 1/4"-20 Tap, L = 1"	1

B

B

A

A

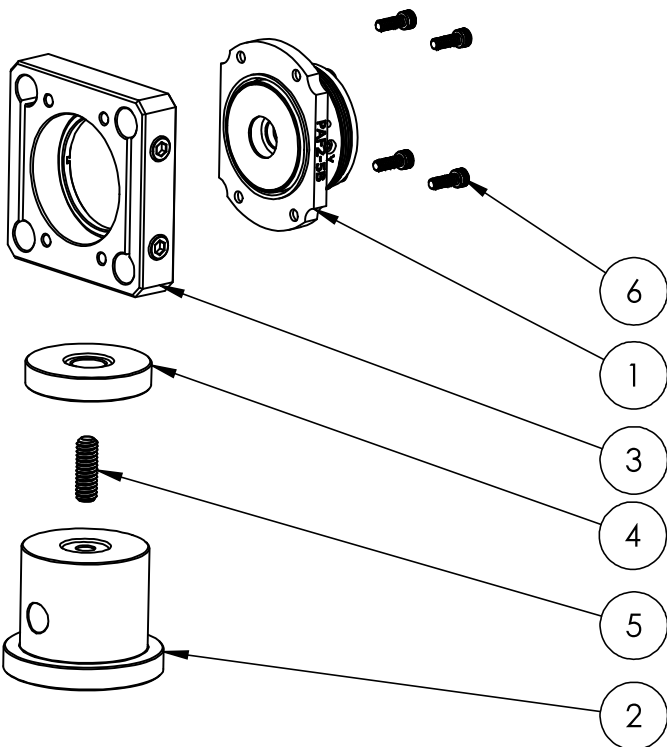
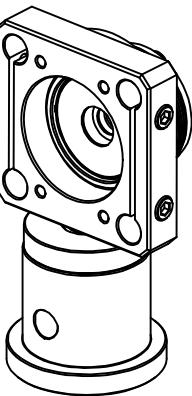
		UNLESS OTHERWISE SPECIFIED:		NAME	DATE	TITLE: detector_assembly
		DIMENSIONS ARE IN INCHES				
		TOLERANCES:				
		FRACTIONAL \pm				
		ANGULAR: MACH \pm BEND \pm				
		TWO PLACE DECIMAL \pm				
		THREE PLACE DECIMAL \pm				
		INTERPRET GEOMETRIC TOLERANCING PER:				
		MATERIAL				
		COMMENTS:				
NEXT ASSY	USED ON	FINISH				
APPLICATION		DO NOT SCALE DRAWING				
SIZE	DWG. NO.		REV			
A						
SCALE: 2:3		WEIGHT:	SHEET 1 OF 1			

2

1

PROPRIETARY AND CONFIDENTIAL
THE INFORMATION CONTAINED IN THIS DRAWING IS THE SOLE PROPERTY OF <INSERT COMPANY NAME HERE>. ANY REPRODUCTION IN PART OR AS A WHOLE WITHOUT THE WRITTEN PERMISSION OF <INSERT COMPANY NAME HERE> IS PROHIBITED.

B



ITEM NO.	PART NUMBER	DESCRIPTION	QTY.
1	PAF2-5B-Solidworks	FiberPort, FC/PC & FC/APC, f=4.6 mm, 600 - 1050 nm, Ø1.00 mm Waist	1
2	RS1P8E-Solidworks	Ø1" Pedestal Pillar Post, 8-32 Taps, L = 1"	1
3	CP08FP-Solidworks	FiberPort Adapter for 30 mm Cage System	1
4	RS5M-Solidworks	Ø25.0 mm Post Spacer, Thickness = 5 mm	1
5	91375A194	Alloy Steel Cup-Point Set Screw (8-32, L=1/2")	1
6	91251A077	Black-Oxide Alloy Steel Socket Head Screw (2-56, L=1/4")	4

A

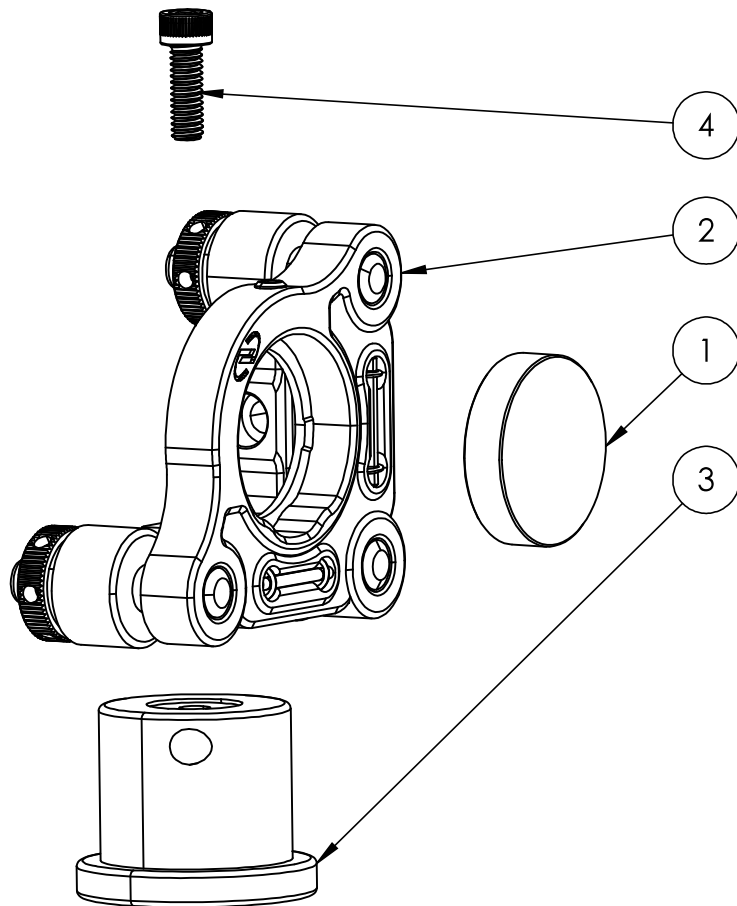
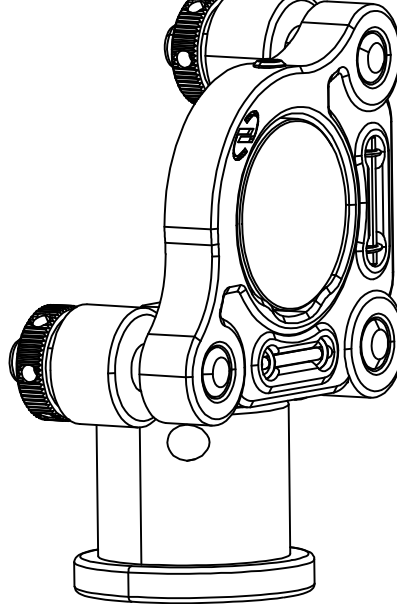
		UNLESS OTHERWISE SPECIFIED:		NAME	DATE	TITLE: FiberPort_assembly
		DIMENSIONS ARE IN INCHES	DRAWN			
		TOLERANCES:	CHECKED			
		FRACTIONAL \pm	ENG APPR.			
		ANGULAR: MACH \pm BEND \pm	MFG APPR.			
		TWO PLACE DECIMAL \pm	Q.A.			
		THREE PLACE DECIMAL \pm	COMMENTS:			
		INTERPRET GEOMETRIC TOLERANCING PER:				
		MATERIAL				
NEXT ASSY	USED ON	FINISH				
APPLICATION		DO NOT SCALE DRAWING				
SIZE	DWG. NO.		REV		A	
SCALE: 2:3	WEIGHT:		SHEET 1 OF 1			

PROPRIETARY AND CONFIDENTIAL
 THE INFORMATION CONTAINED IN THIS
 DRAWING IS THE SOLE PROPERTY OF
 <INSERT COMPANY NAME HERE>. ANY
 REPRODUCTION IN PART OR AS A WHOLE
 WITHOUT THE WRITTEN PERMISSION OF
 <INSERT COMPANY NAME HERE> IS
 PROHIBITED.

ITEM NO.	PART NUMBER	DESCRIPTION	QTY.
1	BB1-E03-Solidworks	Ø1" Broadband Dielectric Mirror, 750 - 1100 nm	1
2	Newport-SS100-F2H	Mirror Mount, Suprema®, 1.0 in, (2) 100-TPI Locking Hex-Broach Actuators	1
3	Newport-9952	Optical Pedestal, Clean-Passivated, 1.0 in. Height, 1 in. Diameter, 8-32	1
4	91251A194	Black-Oxide Alloy Steel Socket Head Screw (8-32, L=1/2")	1

B

B

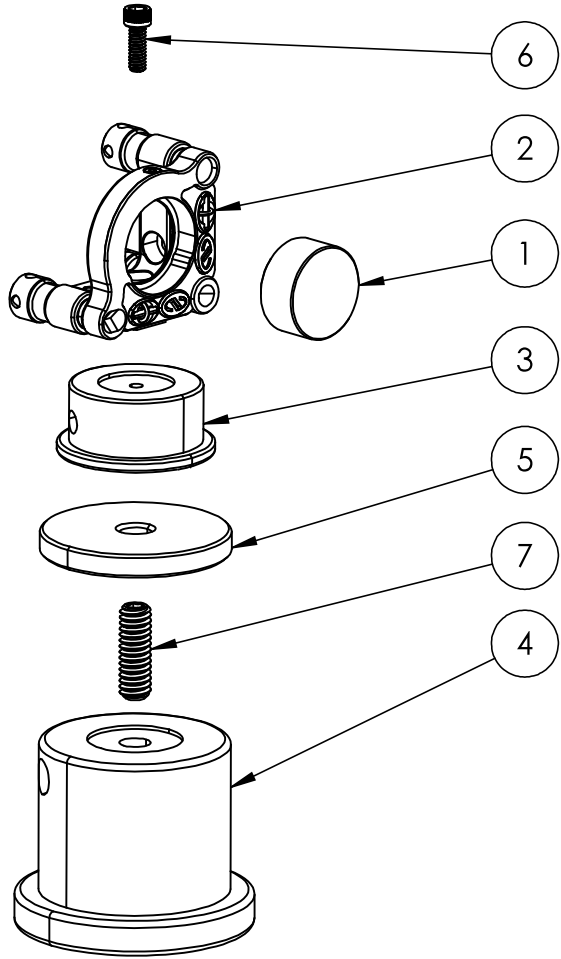
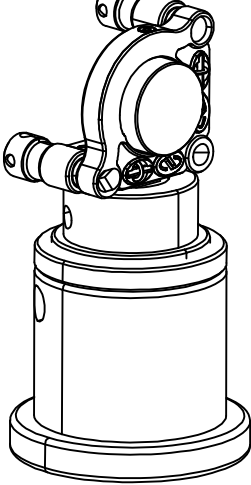


PROPRIETARY AND CONFIDENTIAL
THE INFORMATION CONTAINED IN THIS DRAWING IS THE SOLE PROPERTY OF <INSERT COMPANY NAME HERE>. ANY REPRODUCTION IN PART OR AS A WHOLE WITHOUT THE WRITTEN PERMISSION OF <INSERT COMPANY NAME HERE> IS PROHIBITED.

		UNLESS OTHERWISE SPECIFIED:		NAME	DATE	
		DIMENSIONS ARE IN INCHES	DRAWN			
		TOLERANCES:	CHECKED			
		FRACTIONAL \pm	ENG APPR.			
		ANGULAR: MACH \pm BEND \pm	MFG APPR.			
		TWO PLACE DECIMAL \pm	Q.A.			
		THREE PLACE DECIMAL \pm				
		INTERPRET GEOMETRIC TOLERANCING PER:	COMMENTS:			
		MATERIAL				
NEXT ASSY	USED ON	FINISH				
APPLICATION		DO NOT SCALE DRAWING				
SIZE		DWG. NO.			REV	
A						
SCALE: 1:1		WEIGHT:			SHEET 1 OF 1	

2

1



ITEM NO.	PART NUMBER	DESCRIPTION	QTY.
1	BB05-E03-Solidworks	$\varnothing 1/2"$ Broadband Dielectric Mirror, 750 - 1100 nm	1
2	Newport-SS050-F3	Mirror Mount, Suprema®, 0.5 in., (3) 100-TPI Locking Allen-Key Actuators	1
3	Newport-9942	Optical Pedestal, 3/8 in. Height, 0.7 in. Diameter, 2-56 Thread	1
4	Newport-9952	Optical Pedestal, Clean-Passivated, 1.0 in. Height, 1 in. Diameter, 8-32	1
5	Newport-PS-0_125	Pedestal Spacer, 0.125 in. Thick, 1 in. Diameter Posts, 8-32 (M4) CLR	1
6	91251A077	Black-Oxide Alloy Steel Socket Head Screw (2-56, L=1/4")	1
7	91375A194	Alloy Steel Cup-Point Set Screw (8-32, L=1/2")	1

PROPRIETARY AND CONFIDENTIAL
THE INFORMATION CONTAINED IN THIS DRAWING IS THE SOLE PROPERTY OF <INSERT COMPANY NAME HERE>. ANY REPRODUCTION IN PART OR AS A WHOLE WITHOUT THE WRITTEN PERMISSION OF <INSERT COMPANY NAME HERE> IS PROHIBITED.

		UNLESS OTHERWISE SPECIFIED:		NAME	DATE	TITLE: Mirror_assembly_small
		DIMENSIONS ARE IN INCHES	DRAWN			
		TOLERANCES:	CHECKED			
		FRACTIONAL \pm	ENG APPR.			
		ANGULAR: MACH \pm BEND \pm	MFG APPR.			
		TWO PLACE DECIMAL \pm	Q.A.			
		THREE PLACE DECIMAL \pm	COMMENTS:			
		INTERPRET GEOMETRIC TOLERANCING PER:				
		MATERIAL				
NEXT ASSY	USED ON	FINISH				
APPLICATION		DO NOT SCALE DRAWING				
SIZE		DWG. NO.		REV		
A						
SCALE: 1:1		WEIGHT:		SHEET 1 OF 1		

2

1

APPENDIX: TEMPERATURE-STABILIZED ETALON MOUNT SOLIDWORKS

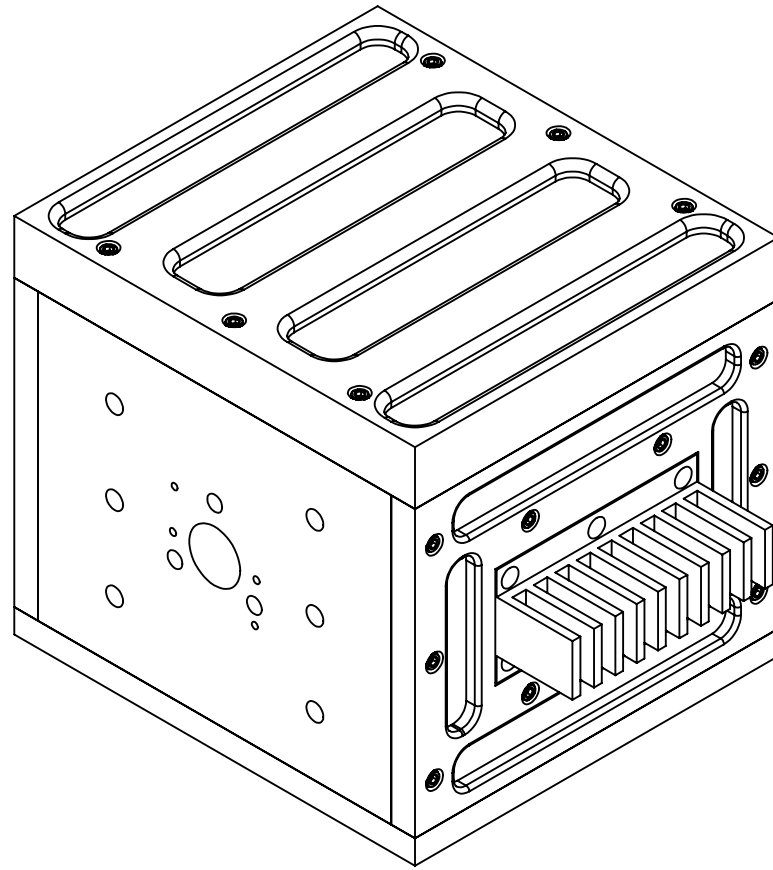
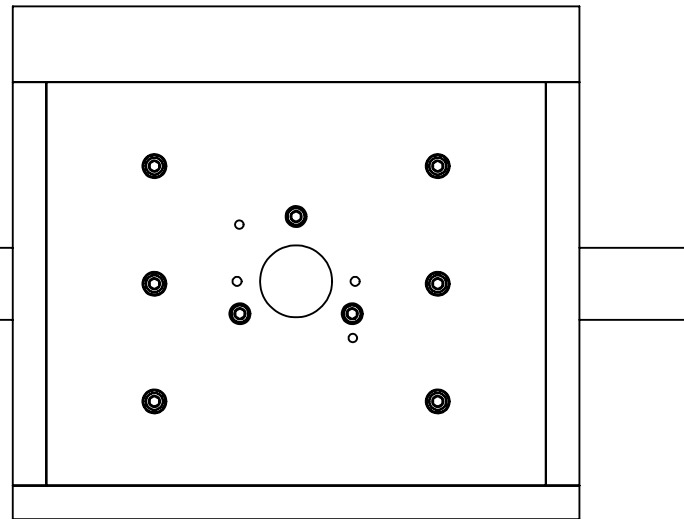
DRAWINGS

2

1

B

B

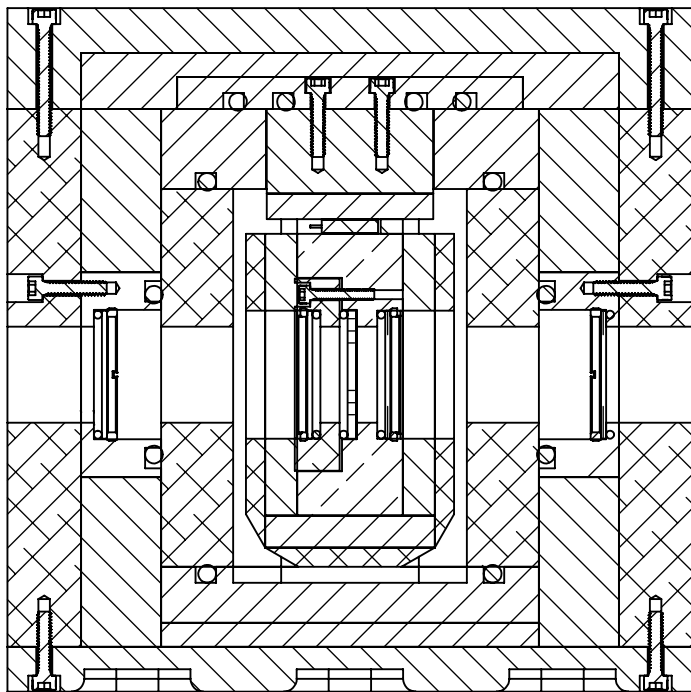


PROPRIETARY AND CONFIDENTIAL
THE INFORMATION CONTAINED IN THIS DRAWING IS THE SOLE PROPERTY OF
<INSERT COMPANY NAME HERE>. ANY
REPRODUCTION IN PART OR AS A WHOLE
WITHOUT THE WRITTEN PERMISSION OF
<INSERT COMPANY NAME HERE> IS
PROHIBITED.

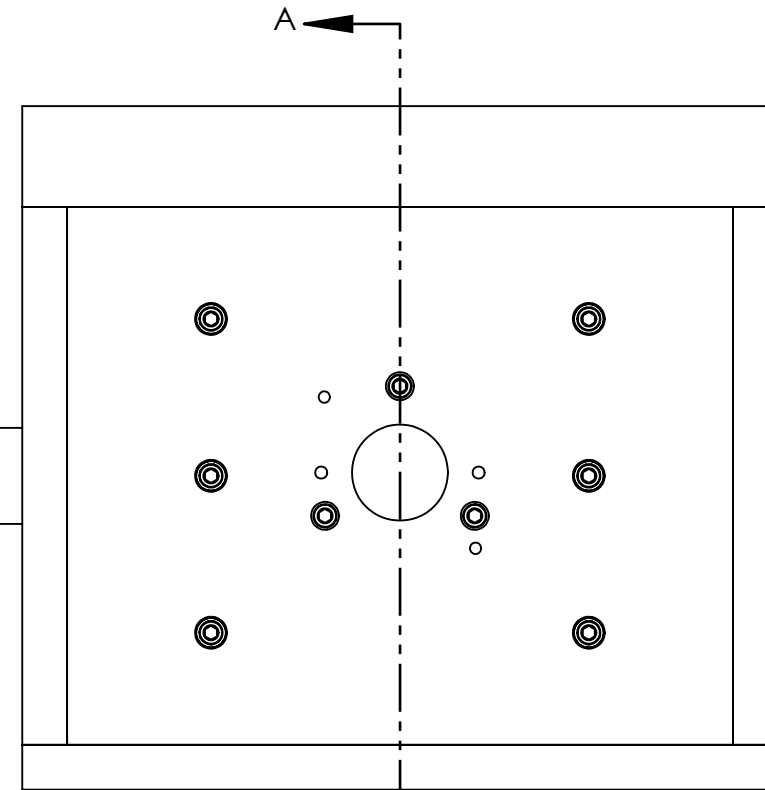
		UNLESS OTHERWISE SPECIFIED:			NAME	DATE	TITLE: Temperature_Stabilized_Mount	
		DIMENSIONS ARE IN INCHES		DRAWN				
		TOLERANCES:		CHECKED				
		FRACTIONAL \pm		ENG APPR.				
		ANGULAR: MACH \pm BEND \pm		MFG APPR.				
		TWO PLACE DECIMAL \pm		Q.A.				
		THREE PLACE DECIMAL \pm		COMMENTS:				
		INTERPRET GEOMETRIC TOLERANCING PER:						
		MATERIAL						
		NEXT ASSY		FINISH				
		APPLICATION		DO NOT SCALE DRAWING				

2

1



SECTION A-A
SCALE 2 : 3



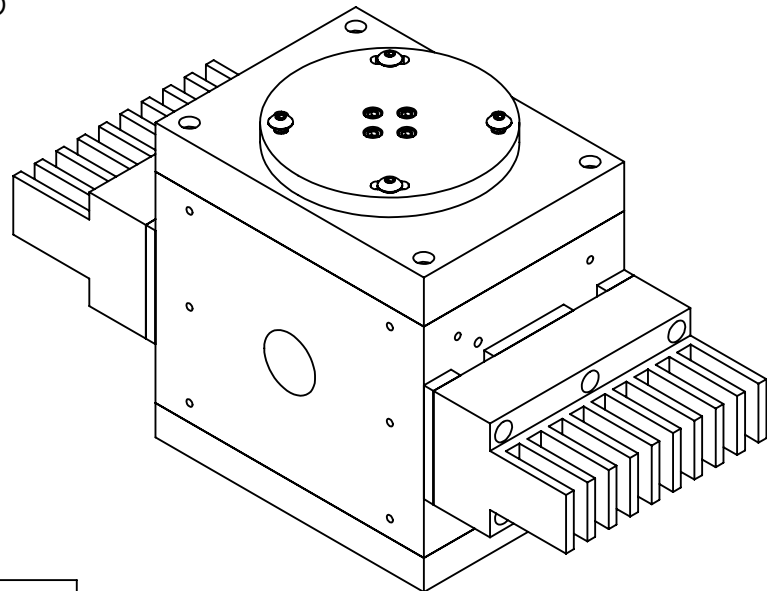
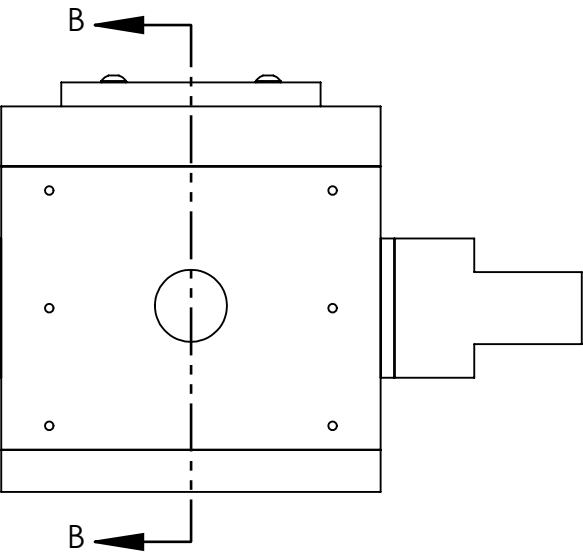
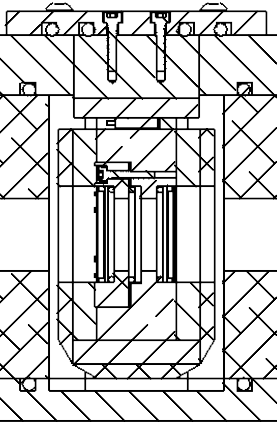
PROPRIETARY AND CONFIDENTIAL
THE INFORMATION CONTAINED IN THIS DRAWING IS THE SOLE PROPERTY OF <INSERT COMPANY NAME HERE>. ANY REPRODUCTION IN PART OR AS A WHOLE WITHOUT THE WRITTEN PERMISSION OF <INSERT COMPANY NAME HERE> IS PROHIBITED.

		UNLESS OTHERWISE SPECIFIED:		DRAWN	NAME	DATE	TITLE: Temperature_Stabilized_Mount		
		DIMENSIONS ARE IN INCHES TOLERANCES: FRACTIONAL \pm ANGULAR: MACH \pm BEND \pm TWO PLACE DECIMAL \pm THREE PLACE DECIMAL \pm							
		INTERPRET GEOMETRIC TOLERANCING PER: MATERIAL		CHECKED	ENG APPR.	MFG APPR.			
		NEXT ASSY							
		USED ON		FINISH		COMMENTS:			
		APPLICATION		DO NOT SCALE DRAWING		SIZE DWG. NO.			
						REV			
						A			
				SCALE: 2:3		WEIGHT:			
				SHEET 2 OF 5					

2

1

JACKET AND INSULATION REMOVED



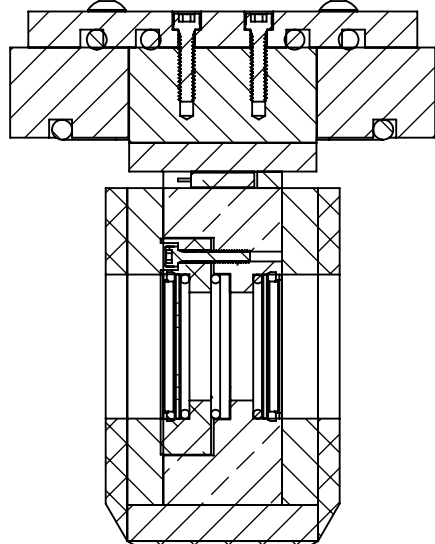
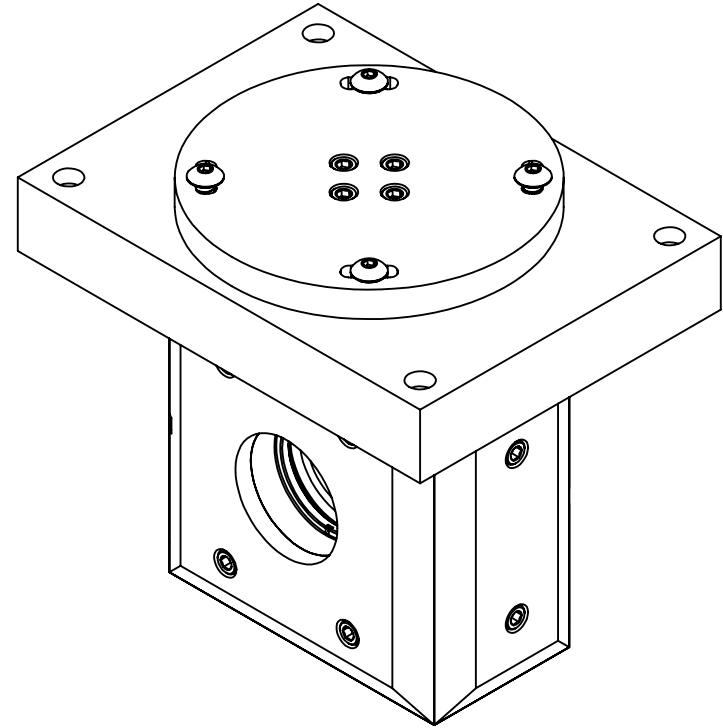
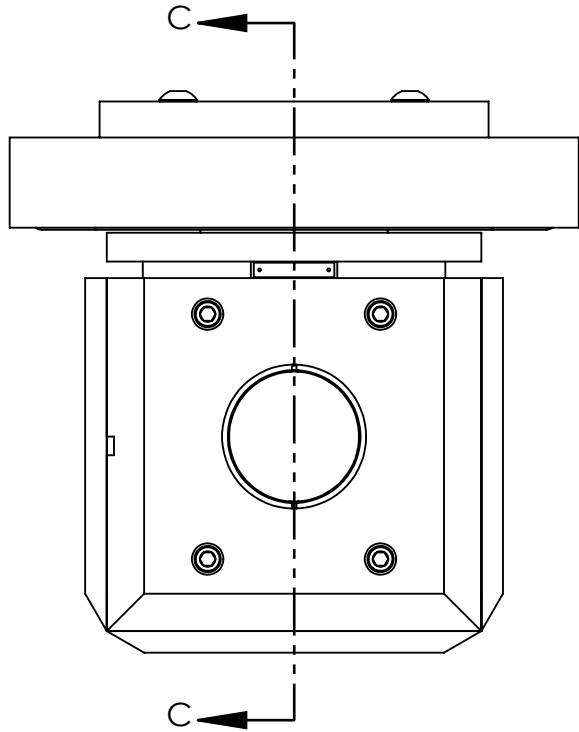
PROPRIETARY AND CONFIDENTIAL
THE INFORMATION CONTAINED IN THIS DRAWING IS THE SOLE PROPERTY OF <INSERT COMPANY NAME HERE>. ANY REPRODUCTION IN PART OR AS A WHOLE WITHOUT THE WRITTEN PERMISSION OF <INSERT COMPANY NAME HERE> IS PROHIBITED.

		UNLESS OTHERWISE SPECIFIED:			NAME	DATE	TITLE: Temperature_Stabilized_Mount
		DIMENSIONS ARE IN INCHES		DRAWN			
		TOLERANCES:		CHECKED			
		FRACTIONAL \pm		ENG APPR.			
		ANGULAR: MACH \pm BEND \pm		MFG APPR.			
		TWO PLACE DECIMAL \pm		Q.A.			
		THREE PLACE DECIMAL \pm		COMMENTS:			
		INTERPRET GEOMETRIC TOLERANCING PER:					
		MATERIAL					
NEXT ASSY	USED ON	FINISH					
APPLICATION		DO NOT SCALE DRAWING		SIZE	DWG. NO.		REV
				A			
				SCALE: 1:2	WEIGHT:	SHEET 3 OF 5	

2

1

FIRST STAGE REMOVED

SECTION C-C
SCALE 3 : 4

PROPRIETARY AND CONFIDENTIAL
THE INFORMATION CONTAINED IN THIS DRAWING IS THE SOLE PROPERTY OF <INSERT COMPANY NAME HERE>. ANY REPRODUCTION IN PART OR AS A WHOLE WITHOUT THE WRITTEN PERMISSION OF <INSERT COMPANY NAME HERE> IS PROHIBITED.

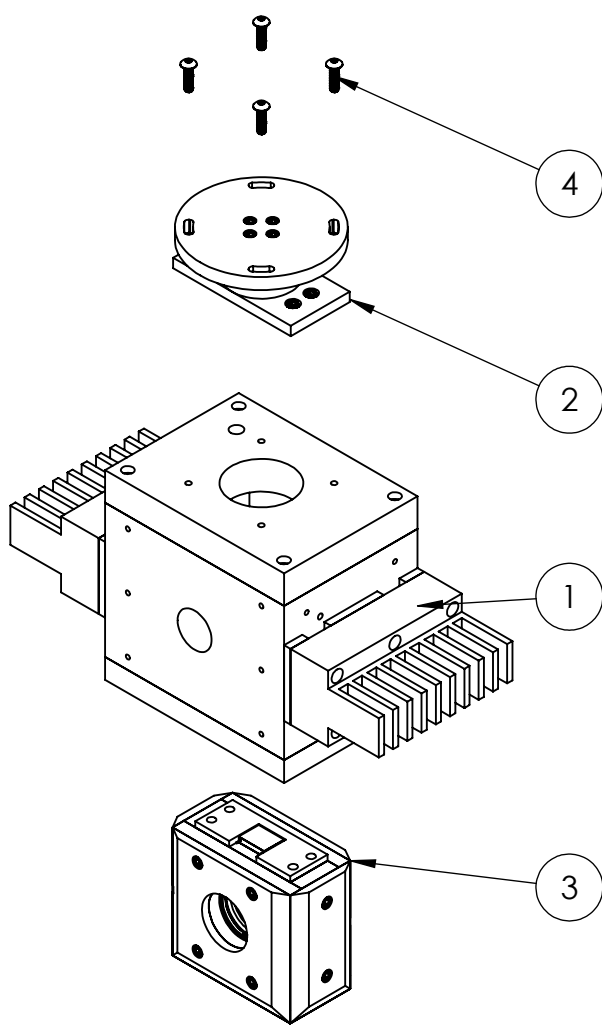
		UNLESS OTHERWISE SPECIFIED:		DRAWN	NAME	DATE	TITLE: Temperature_Stabilized_Mount		
		DIMENSIONS ARE IN INCHES TOLERANCES: FRACTIONAL \pm ANGULAR: MACH \pm BEND \pm TWO PLACE DECIMAL \pm THREE PLACE DECIMAL \pm							
		INTERPRET GEOMETRIC TOLERANCING PER: MATERIAL		CHECKED	ENG APPR.	MFG APPR.			
		NEXT ASSY							
		USED ON		FINISH		COMMENTS:			
		APPLICATION		DO NOT SCALE DRAWING					
SIZE		DWG. NO.		REV					
A									
SCALE: 3:4		WEIGHT:		SHEET 4 OF 5					

2

1

2

1



ITEM NO.	PART NUMBER	DESCRIPTION	QTY.
1	First_Stage	Assembly_1	1
2	heat_sink_assembly	Assembly_2	1
3	Second_Stage	Assembly_3	1
4	91255A148	Button Head Hex Drive Screw (6-32, L=1/2")	4

B

B

A

A

PROPRIETARY AND CONFIDENTIAL
THE INFORMATION CONTAINED IN THIS DRAWING IS THE SOLE PROPERTY OF
<INSERT COMPANY NAME HERE>. ANY
REPRODUCTION IN PART OR AS A WHOLE
WITHOUT THE WRITTEN PERMISSION OF
<INSERT COMPANY NAME HERE> IS
PROHIBITED.

		UNLESS OTHERWISE SPECIFIED:			DRAWN	NAME	DATE	TITLE: Temperature_Stabilized_Mount
		DIMENSIONS ARE IN INCHES TOLERANCES: FRACTIONAL \pm ANGULAR: MACH \pm BEND \pm TWO PLACE DECIMAL \pm THREE PLACE DECIMAL \pm						
		INTERPRET GEOMETRIC TOLERANCING PER:			CHECKED			
		MATERIAL						
NEXT ASSY	USED ON	FINISH			ENG APPR.			
APPLICATION		DO NOT SCALE DRAWING			COMMENTS:			
SIZE		DWG. NO.			REV			
A								
SCALE: 1:3		WEIGHT:			SHEET 5 OF 5			

2

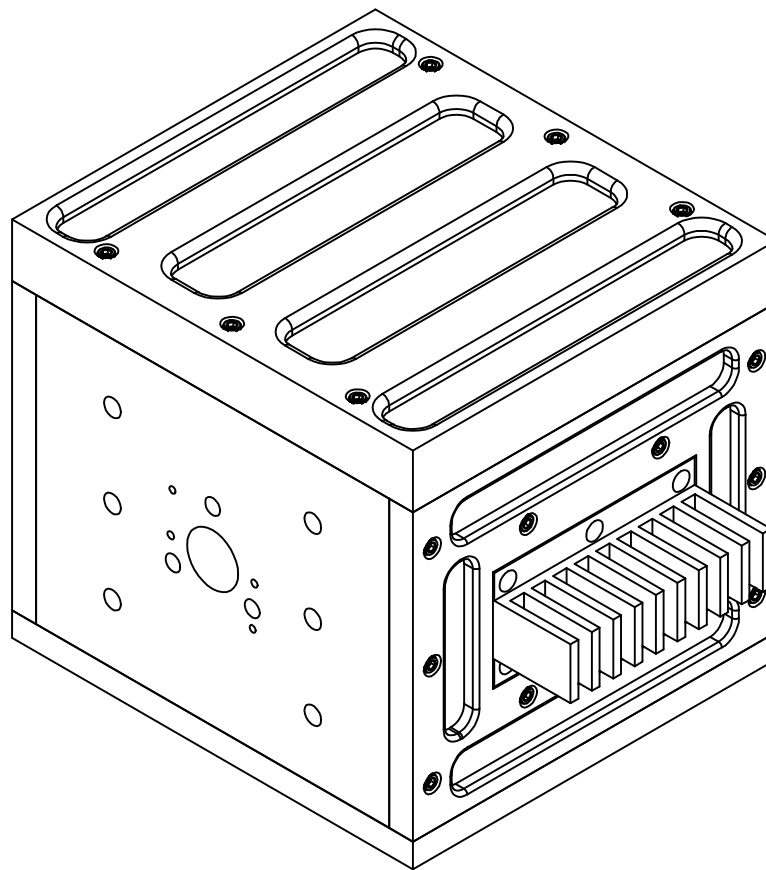
1

2

1

B

B



A

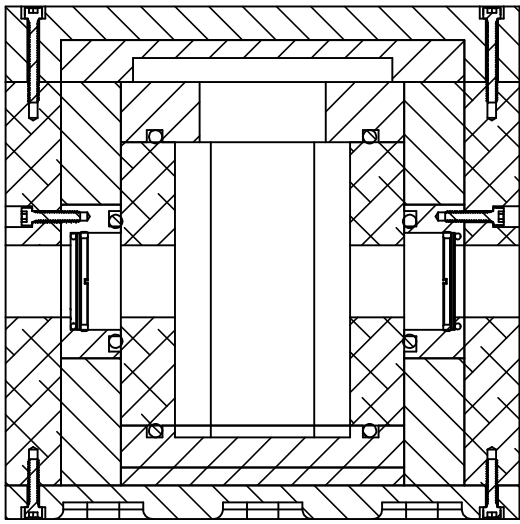
A

PROPRIETARY AND CONFIDENTIAL
 THE INFORMATION CONTAINED IN THIS
 DRAWING IS THE SOLE PROPERTY OF
 <INSERT COMPANY NAME HERE>. ANY
 REPRODUCTION IN PART OR AS A WHOLE
 WITHOUT THE WRITTEN PERMISSION OF
 <INSERT COMPANY NAME HERE> IS
 PROHIBITED.

		UNLESS OTHERWISE SPECIFIED:		NAME	DATE	TITLE: First_Stage
		DIMENSIONS ARE IN INCHES	DRAWN			
		TOLERANCES:	CHECKED			
		FRACTIONAL \pm	ENG APPR.			
		ANGULAR: MACH \pm BEND \pm	MFG APPR.			
		TWO PLACE DECIMAL \pm	Q.A.			
		THREE PLACE DECIMAL \pm				
		INTERPRET GEOMETRIC TOLERANCING PER:				
		MATERIAL				
NEXT ASSY	USED ON	FINISH				
APPLICATION		DO NOT SCALE DRAWING				
SIZE	DWG. NO.					REV
A						
SCALE: 1:2	WEIGHT:					SHEET 1 OF 7

2

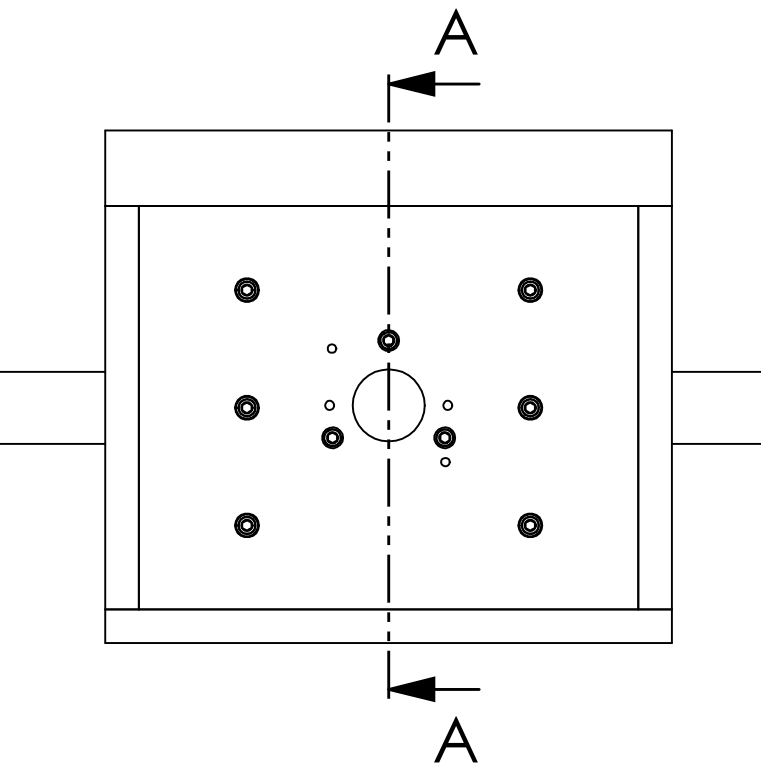
1



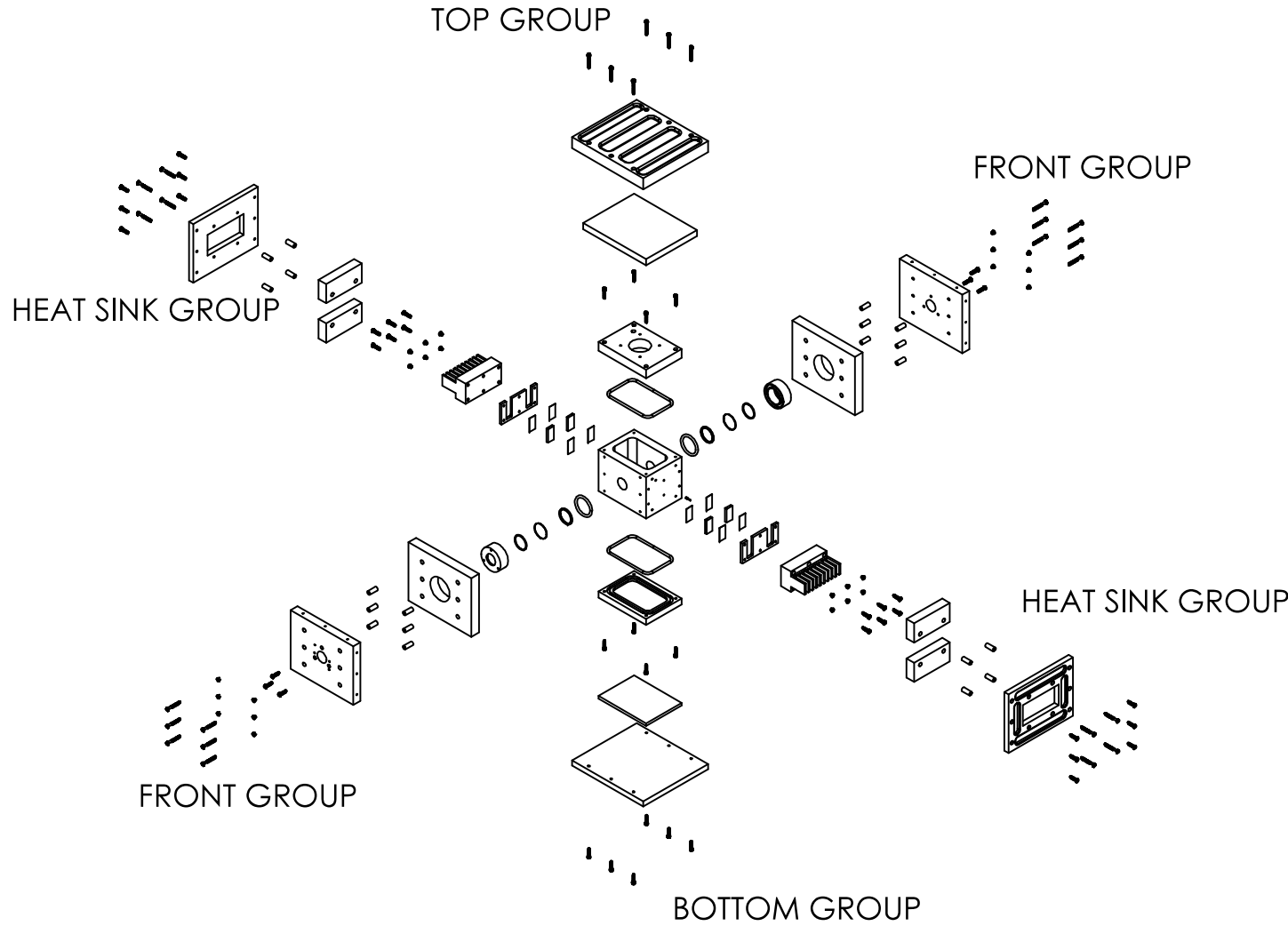
SECTION A-A

SCALE 1 : 2

PROPRIETARY AND CONFIDENTIAL
THE INFORMATION CONTAINED IN THIS
DRAWING IS THE SOLE PROPERTY OF
<INSERT COMPANY NAME HERE>. ANY
REPRODUCTION IN PART OR AS A WHOLE
WITHOUT THE WRITTEN PERMISSION OF
<INSERT COMPANY NAME HERE> IS
PROHIBITED.



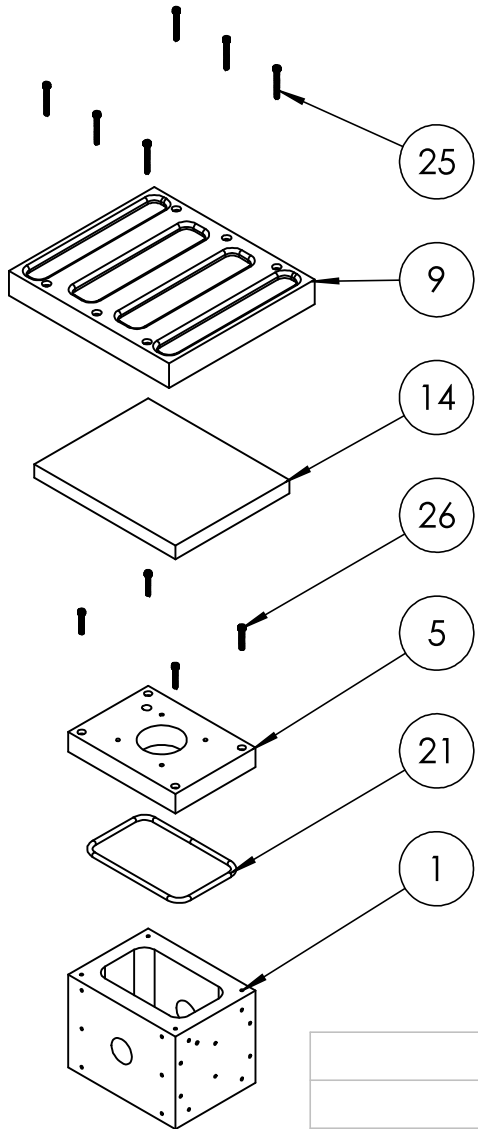
		UNLESS OTHERWISE SPECIFIED:				NAME	DATE	TITLE:
		DIMENSIONS ARE IN INCHES			DRAWN			
		TOLERANCES:			CHECKED			
		FRACTIONAL \pm			ENG APPR.			
		ANGULAR: MACH \pm	BEND \pm		MFG APPR.			
		TWO PLACE DECIMAL \pm			Q.A.			
		THREE PLACE DECIMAL \pm			COMMENTS:			
		INTERPRET GEOMETRIC TOLERANCING PER:						
		MATERIAL						
NEXT ASSY	USED ON	FINISH						
		APPLICATION	DO NOT SCALE DRAWING			SIZE DWG. NO.		
						REV		
						SCALE: 1:2 WEIGHT: SHEET 2 OF 7		



PROPRIETARY AND CONFIDENTIAL
THE INFORMATION CONTAINED IN THIS
DRAWING IS THE SOLE PROPERTY OF
<INSERT COMPANY NAME HERE>. ANY
REPRODUCTION IN PART OR AS A WHOLE
WITHOUT THE WRITTEN PERMISSION OF
<INSERT COMPANY NAME HERE> IS
PROHIBITED.

		UNLESS OTHERWISE SPECIFIED:			NAME	DATE	TITLE: First_Stage					
		DIMENSIONS ARE IN INCHES TOLERANCES: FRACTIONAL \pm ANGULAR: MACH \pm BEND \pm TWO PLACE DECIMAL \pm THREE PLACE DECIMAL \pm										
		INTERPRET GEOMETRIC TOLERANCING PER: MATERIAL			COMMENTS:							
NEXT ASSY		USED ON		FINISH								
APPLICATION			DO NOT SCALE DRAWING									
A		DWG. NO.		REV								
A												
SCALE: 1:10		WEIGHT:		SHEET 3 OF 7								

TOP GROUP

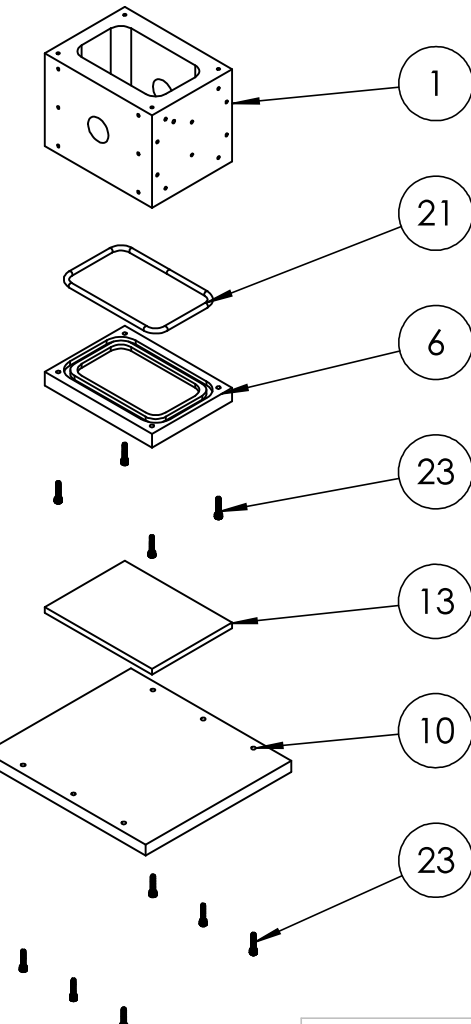


ITEM NO.	PART NUMBER	DESCRIPTION	QTY.
1	CAGE_BOTTOM	CUSTOM 6061-AL	1
2	CAGE_HEAT_SINK	CUSTOM 6061-AL	2
3	CAGE_JACKET_FRONT	CUSTOM 6061-AL	2
4	CAGE_JACKET_FRONT_SPACER	CUSTOM DELRIN	2
5	CAGE_TOP_O_RING	CUSTOM DELRIN	1
6	CAGE_BOTTOM_O_RING	CUSTOM DELRIN	1
7	CAGE_TEC_COMPRESSION_MOUNT	CUSTOM LOW-FILL ABS	2
8	JACKET_SIDE	CUSTOM PET	2
9	JACKET_TOP	CUSTOM PET	1
10	JACKET_BOTTOM	CUSTOM PET	1
11	FOAM_SIDE	CUSTOM RUBBER FOAM	4
12	FOAM_FRONT	CUSTOM RUBBER FOAM	2
13	FOAM_BOTTOM	CUSTOM RUBBER FOAM	1
14	FOAM_TOP	CUSTOM RUBBER FOAM	1
15	LAIRD_TEC_CP08-63-06-L1-W4.5	LAIRD TEC	4
16	THERMISTOR	WAVELENGTH ELECTRONICS TCS620	1
17	SM1RR-SOLIDWORKS	1-IN RETAINING RING	2
18	WG41010-B-SOLIDWORKS	B-COATED 1-IN WINDOW	2
19	CAGE_HEAT_SINK_GRAPHITE	PANASONIC GRAPHITE SHEET	8
20	9452K36	OIL-RESISTANT BUNA-N O-RING	2
21	O_RING_CUSTOM	CUSTOM O-RING FROM 0.139" STOCK	2
22	O-RING	1-IN DIA, 1/16-IN TH	2
23	91251A110	BLACK-OXIDE ALLOY STEEL SOCKET HEAD SCREW (4-40, L = 1/2")	40
24	91251A115	BLACK-OXIDE ALLOY STEEL SOCKET HEAD SCREW (4-40, L=1")	20
25	91251A114	BLACK-OXIDE ALLOY STEEL SOCKET HEAD SCREW (4-40, L = 7/8")	6
26	91251A112	BLACK-OXIDE ALLOY STEEL SOCKET HEAD SCREW (4-40, L=5/8")	4
27	94639A204	OFF-WHITE NYLON UNTHREADED SPACER (L=0.625, OD=0.25, ID=0.115)	20
28	91145A129	ELECTRICAL-INSULATING NYLON 6/6 SLEEVE WASHER (FOR #4 SCREWS)	24

		UNLESS OTHERWISE SPECIFIED:			
		DIMENSIONS ARE IN INCHES			
		TOLERANCES:			
		FRACTIONAL \pm			
		ANGULAR: MACH \pm BEND \pm			
		TWO PLACE DECIMAL \pm			
		THREE PLACE DECIMAL \pm			
		INTERPRET GEOMETRIC TOLERANCING PER:			
		MATERIAL			
NEXT ASSY	USED ON	FINISH			
APPLICATION		DO NOT SCALE DRAWING			

DRAWN	NAME	DATE	TITLE: First_Stage		
Q.A.	COMMENTS:				
SIZE	DWG. NO.			REV	
A					
SCALE: 1:5			WEIGHT:	SHEET 4 OF 7	

PROPRIETARY AND CONFIDENTIAL
THE INFORMATION CONTAINED IN THIS DRAWING IS THE SOLE PROPERTY OF <INSERT COMPANY NAME HERE>. ANY REPRODUCTION IN PART OR AS A WHOLE WITHOUT THE WRITTEN PERMISSION OF <INSERT COMPANY NAME HERE> IS PROHIBITED.



BOTTOM GROUP

BOM ON SHEET 4

B

B

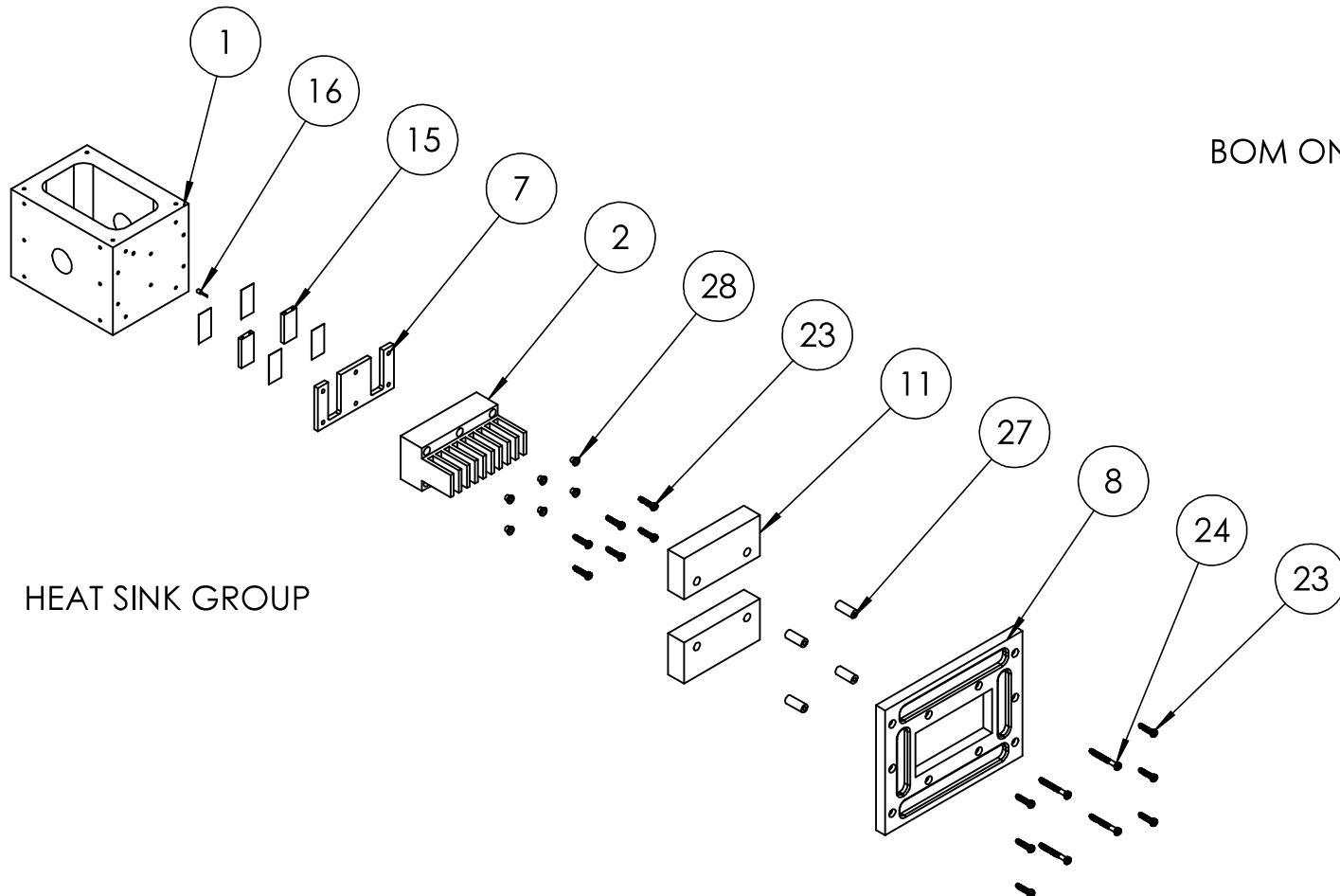
PROPRIETARY AND CONFIDENTIAL
THE INFORMATION CONTAINED IN THIS
DRAWING IS THE SOLE PROPERTY OF
<INSERT COMPANY NAME HERE>. ANY
REPRODUCTION IN PART OR AS A WHOLE
WITHOUT THE WRITTEN PERMISSION OF
<INSERT COMPANY NAME HERE> IS
PROHIBITED.

		UNLESS OTHERWISE SPECIFIED:		NAME	DATE
		DIMENSIONS ARE IN INCHES	DRAWN		
		TOLERANCES:	CHECKED		
		FRACTIONAL \pm	ENG APPR.		
		ANGULAR: MACH \pm BEND \pm	MFG APPR.		
		TWO PLACE DECIMAL \pm	Q.A.		
		THREE PLACE DECIMAL \pm			
		INTERPRET GEOMETRIC TOLERANCING PER:			
		MATERIAL			
NEXT ASSY	USED ON	FINISH			
APPLICATION		DO NOT SCALE DRAWING			

TITLE: First_Stage	SIZE A	DWG. NO.	REV
COMMENTS:			
SCALE: 1:5	WEIGHT:	SHEET 5 OF 7	

2

1

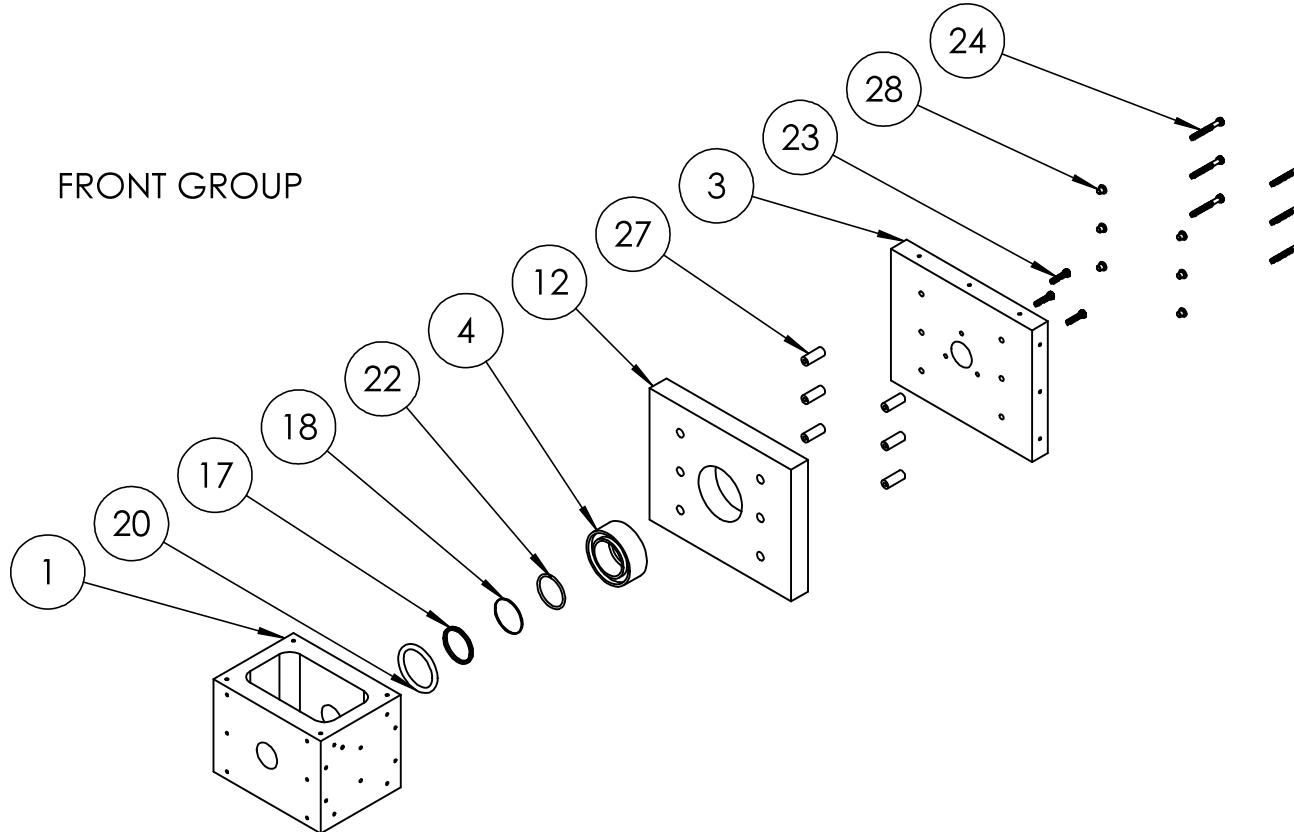


		UNLESS OTHERWISE SPECIFIED:		DRAWN	NAME	DATE	TITLE: First_Stage		
		DIMENSIONS ARE IN INCHES TOLERANCES: FRACTIONAL \pm ANGULAR: MACH \pm BEND \pm TWO PLACE DECIMAL \pm THREE PLACE DECIMAL \pm							
		INTERPRET GEOMETRIC TOLERANCING PER: MATERIAL		CHECKED	ENG APPR.	MFG APPR.			
		NEXT ASSY							
		USED ON		FINISH		COMMENTS:			
		APPLICATION		DO NOT SCALE DRAWING					
PROPRIETARY AND CONFIDENTIAL									
THE INFORMATION CONTAINED IN THIS DRAWING IS THE SOLE PROPERTY OF <INSERT COMPANY NAME HERE>. ANY REPRODUCTION IN PART OR AS A WHOLE WITHOUT THE WRITTEN PERMISSION OF <INSERT COMPANY NAME HERE> IS PROHIBITED.									

2

1

FRONT GROUP



BOM ON SHEET 4

PROPRIETARY AND CONFIDENTIAL
THE INFORMATION CONTAINED IN THIS
DRAWING IS THE SOLE PROPERTY OF
<INSERT COMPANY NAME HERE>. ANY
REPRODUCTION IN PART OR AS A WHOLE
WITHOUT THE WRITTEN PERMISSION OF
<INSERT COMPANY NAME HERE> IS
PROHIBITED.

		UNLESS OTHERWISE SPECIFIED:		NAME	DATE	TITLE: First_Stage
		DIMENSIONS ARE IN INCHES	DRAWN			
		TOLERANCES:	CHECKED			
		FRACTIONAL \pm	ENG APPR.			
		ANGULAR: MACH \pm BEND \pm	MFG APPR.			
		TWO PLACE DECIMAL \pm	Q.A.			
		THREE PLACE DECIMAL \pm	COMMENTS:			
		INTERPRET GEOMETRIC TOLERANCING PER:				
		MATERIAL				
NEXT ASSY	USED ON	FINISH				
APPLICATION		DO NOT SCALE DRAWING				
SIZE	DWG. NO.					REV
A						
SCALE: 1:5	WEIGHT:					SHEET 7 OF 7

2

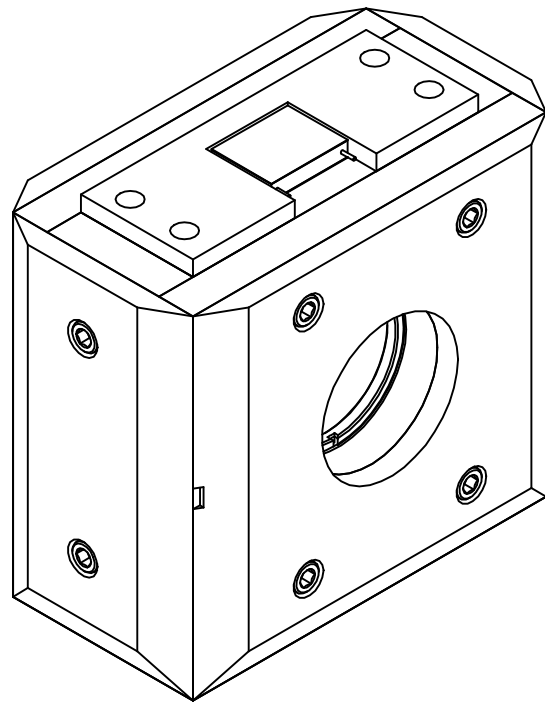
1

2

1

B

B



A

A

PROPRIETARY AND CONFIDENTIAL
 THE INFORMATION CONTAINED IN THIS DRAWING IS THE SOLE PROPERTY OF
 <INSERT COMPANY NAME HERE>. ANY
 REPRODUCTION IN PART OR AS A WHOLE
 WITHOUT THE WRITTEN PERMISSION OF
 <INSERT COMPANY NAME HERE> IS
 PROHIBITED.

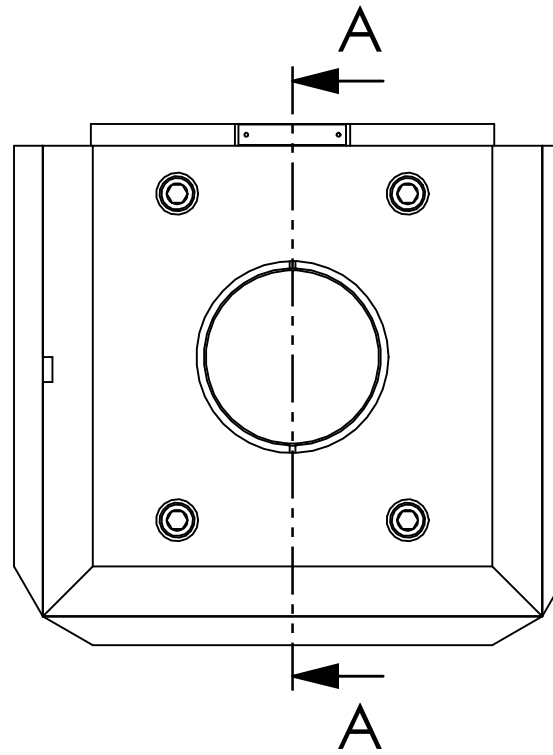
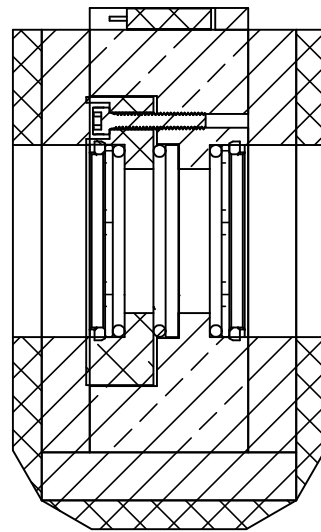
		UNLESS OTHERWISE SPECIFIED:		NAME	DATE	TITLE: Second_Stage
		DIMENSIONS ARE IN INCHES	DRAWN			
		TOLERANCES:	CHECKED			
		FRACTIONAL \pm	ENG APPR.			
		ANGULAR: MACH \pm BEND \pm	MFG APPR.			
		TWO PLACE DECIMAL \pm	Q.A.			
		THREE PLACE DECIMAL \pm				
		INTERPRET GEOMETRIC TOLERANCING PER:				
		MATERIAL				
NEXT ASSY	USED ON	FINISH				
APPLICATION		DO NOT SCALE DRAWING				
SIZE	DWG. NO.					REV
A						
SCALE: 1:1	WEIGHT:					SHEET 1 OF 4

2

1

B

B



SECTION A-A

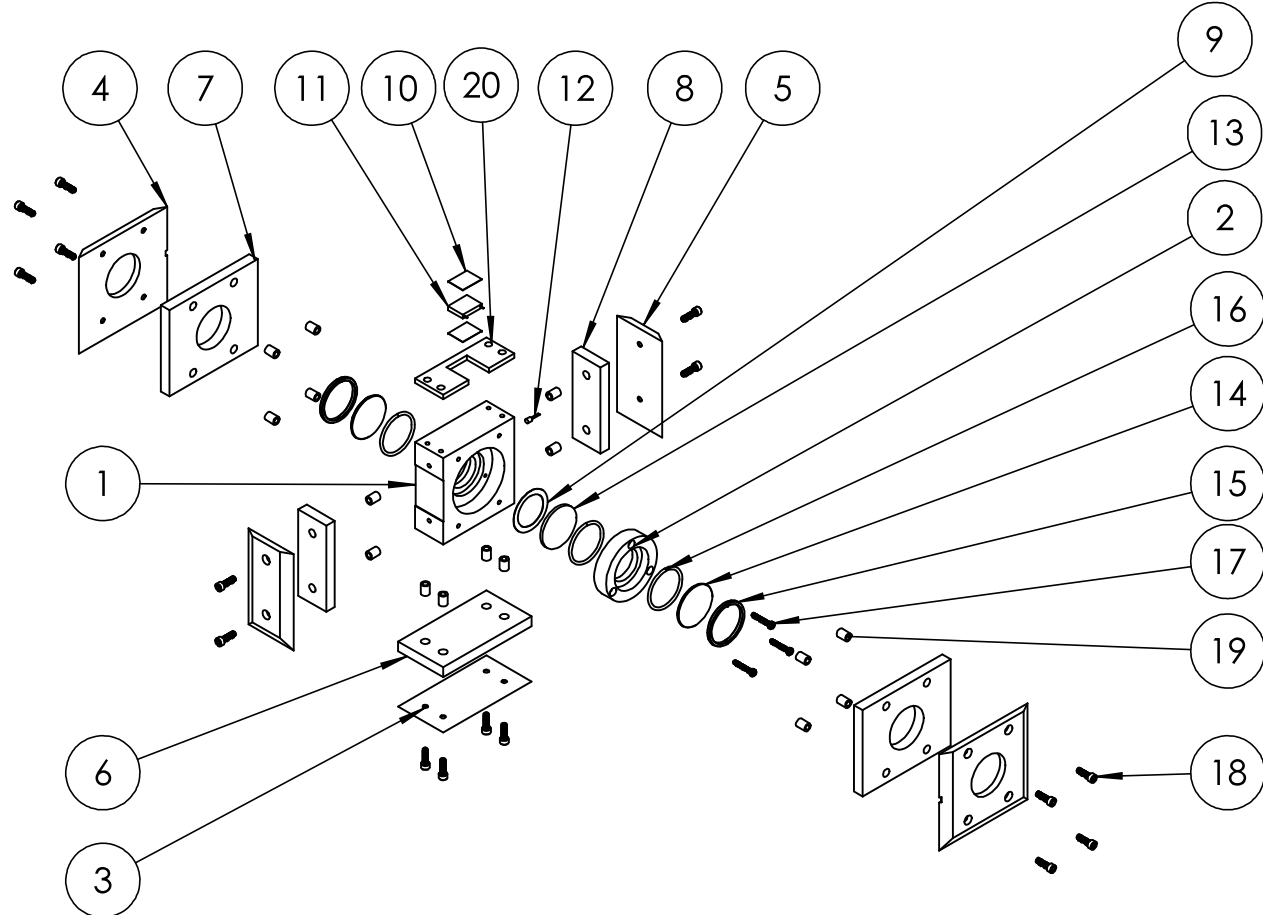
SCALE 1 : 1

PROPRIETARY AND CONFIDENTIAL
THE INFORMATION CONTAINED IN THIS
DRAWING IS THE SOLE PROPERTY OF
<INSERT COMPANY NAME HERE>. ANY
REPRODUCTION IN PART OR AS A WHOLE
WITHOUT THE WRITTEN PERMISSION OF
<INSERT COMPANY NAME HERE> IS
PROHIBITED.

		UNLESS OTHERWISE SPECIFIED:		DRAWN	NAME	DATE	TITLE: Second_Stage			
		DIMENSIONS ARE IN INCHES TOLERANCES: FRACTIONAL \pm ANGULAR: MACH \pm BEND \pm TWO PLACE DECIMAL \pm THREE PLACE DECIMAL \pm								
		INTERPRET GEOMETRIC TOLERANCING PER: MATERIAL		CHECKED	ENG APPR.	MFG APPR.				
NEXT ASSY	USED ON	FINISH								
APPLICATION		DO NOT SCALE DRAWING				SIZE DWG. NO.				
						REV				
						A				
		SCALE: 1:1				WEIGHT:				
		SHEET 2 OF 4								

2

1



ITEM NO.	PART NUMBER	DESCRIPTION	QTY.
1	etalon_mount	Custom Cu-145	1
2	etalon_retaining_ring	Custom 6061-Al	1
3	etalon_jacket_bottom	Custom Delrin	1
4	etalon_jacket_front	Custom Delrin	2
5	etalon_jacket_side	Custom Delrin	2
6	etalon_foam_bottom	Custom Rubber Foam	1
7	etalon_foam_front	Custom Rubber Foam	2
8	etalon_foam_side	Custom Rubber Foam	2
9	Indium_Foil_Etalon	Custom indium foil 0.004-th	1
10	TEC_graphite_sheet	Panasonic Graphite Sheet	2
11	TEC_OTX12-66-F0-1211-11-W2.25	Laird TEC	1
12	thermistor	Wavelength Electronics TCS620	1
13	etalon	LightMachinery Etalon	1
14	WG41010-B-Solidworks	B-coated 1-in window	2
15	SM1RR-Solidworks	1-in retaining ring	2
16	o-ring	1-in dia, 1/16-in th	3
17	91251A081	(2-56 UNC, L=0.5) Black-Oxide Alloy Steel Socket Head Screw	3
18	95868A108	(4-40 UNC, L=0.375) Nylon Socket Head Screws	16
19	94639A706	(L = 1/4", OD = 3/16", ID = .115") Off-White Nylon Unthreaded Spacer	16
20	heat_sink_compression_plate	Custom PET	1

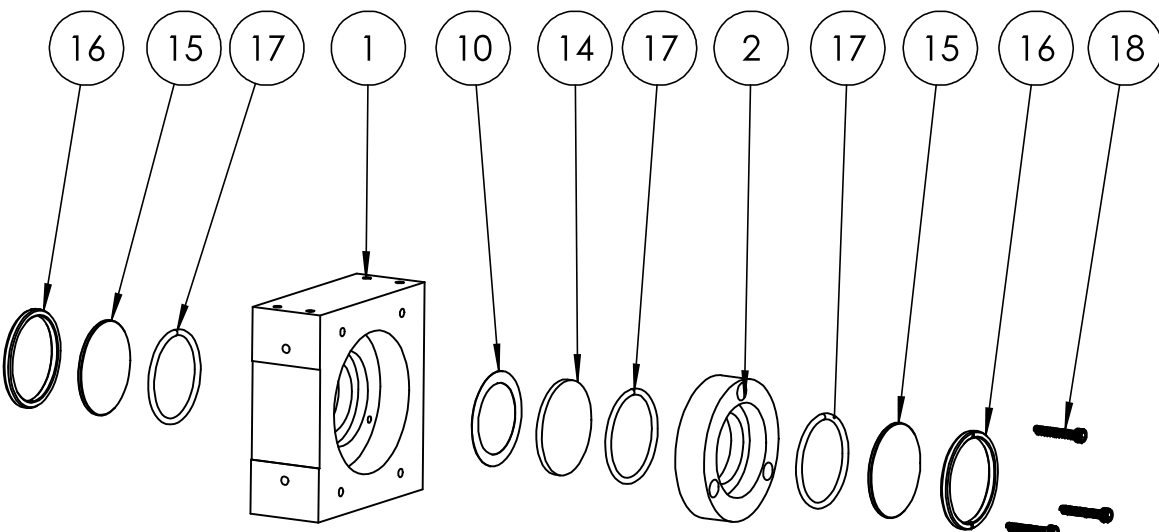
PROPRIETARY AND CONFIDENTIAL
THE INFORMATION CONTAINED IN THIS
DRAWING IS THE SOLE PROPERTY OF
[REDACTED COMPANY NAME HERE]. ANY
PRODUCTION IN PART OR AS A WHOLE
WITHOUT THE WRITTEN PERMISSION OF
[REDACTED COMPANY NAME HERE] IS
PROHIBITED.

		UNLESS OTHERWISE SPECIFIED:		NAME	DATE	TITLE: Second_Stage
		DIMENSIONS ARE IN INCHES TOLERANCES: FRACTIONAL \pm ANGULAR: MACH \pm BEND \pm TWO PLACE DECIMAL \pm THREE PLACE DECIMAL \pm	DRAWN			
			CHECKED			
			ENG APPR.			
			MFG APPR.			
		INTERPRET GEOMETRIC TOLERANCING PER:	Q.A.			
		MATERIAL	COMMENTS:			
		FINISH				
NEXT ASSY	USED ON					
APPLICATION		DO NOT SCALE DRAWING	SIZE	DWG. NO.		REV
			A			
			SCALE: 1:4	WEIGHT:	SHEET 3 OF 4	

2

1

FOAM, JACKET, AND TEC SUPRESSED



ITEM NO.	PART NUMBER	DESCRIPTION	QTY.
1	etalon_mount	Custom Cu-145	1
2	etalon_retaining_ring	Custom 6061-AI	1
3	etalon_jacket_bottom	Custom Delrin	1
4	etalon_jacket_front	Custom Delrin	2
5	etalon_jacket_side	Custom Delrin	2
6	etalon_foam_bottom	Custom Rubber Foam	1
7	etalon_foam_front	Custom Rubber Foam	2
8	etalon_foam_side	Custom Rubber Foam	2
9	heat_sink_compression_plate	Custom PET	1
10	Indium_Foil_Etalon	Custom Indium foil 0.004-th	1
11	TEC_graphite_sheet	Panasonic Graphite Sheet	2
12	TEC_OTX12-66-F0-1211-11-W2.25	Laird TEC	1
13	thermistor	Wavelength Electronics TCS620	1
14	etalon	LightMachinery Etalon	1
15	WG41010-B-Solidworks	B-coated 1-in window	2
16	SM1RR-Solidworks	1-in retaining ring	2
17	O-ring	1-in dia, 1/16-in th	3
18	91251A081	(2-56 UNC, L=0.5) Black-Oxide Alloy Steel Socket Head Screw	3
19	95868A108	(4-40 UNC, L=0.375) Nylon Socket Head Screws	16
20	94639A706	(L = 1/4", OD = 3/16", ID = .115") Off-White Nylon Unthreaded Spacer	16

		UNLESS OTHERWISE SPECIFIED:	DRAWN	NAME	DATE
		DIMENSIONS ARE IN INCHES TOLERANCES: FRACTIONAL \pm ANGULAR: MACH \pm BEND \pm TWO PLACE DECIMAL \pm THREE PLACE DECIMAL \pm			
		INTERPRET GEOMETRIC TOLERANCING PER:	CHECKED	ENG APPR.	MFG APPR.
		MATERIAL			
NEXT ASSY	USED ON	FINISH	Q.A.	COMMENTS:	
APPLICATION		DO NOT SCALE DRAWING			

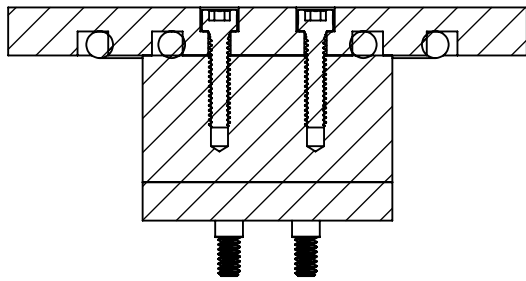
PROPRIETARY AND CONFIDENTIAL
THE INFORMATION CONTAINED IN THIS
DRAWING IS THE SOLE PROPERTY OF
<INSERT COMPANY NAME HERE>. ANY
REPRODUCTION IN PART OR AS A WHOLE
WITHOUT THE WRITTEN PERMISSION OF
<INSERT COMPANY NAME HERE> IS
PROHIBITED.

A
TITLE:
Second_Stage

SIZE	DWG. NO.	REV
A		
SCALE: 1:2		WEIGHT:
		SHEET 4 OF 4

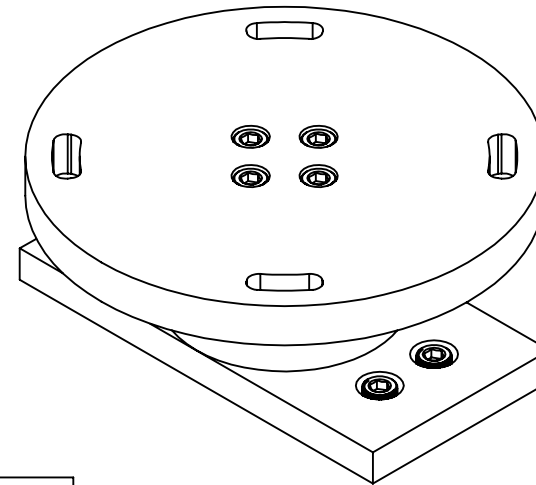
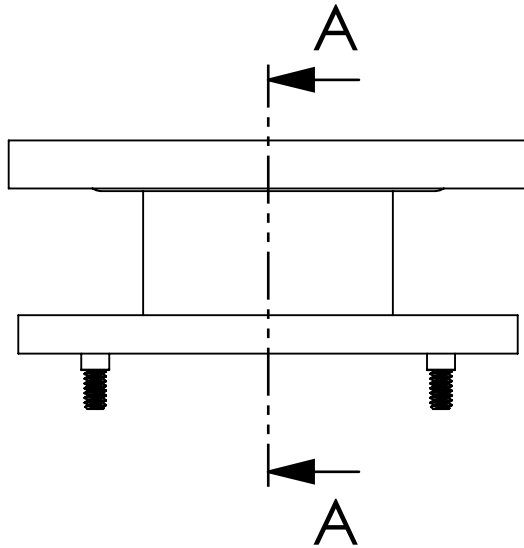
2

1



SECTION A-A

SCALE 1 : 1



PROPRIETARY AND CONFIDENTIAL
THE INFORMATION CONTAINED IN THIS DRAWING IS THE SOLE PROPERTY OF <INSERT COMPANY NAME HERE>. ANY REPRODUCTION IN PART OR AS A WHOLE WITHOUT THE WRITTEN PERMISSION OF <INSERT COMPANY NAME HERE> IS PROHIBITED.

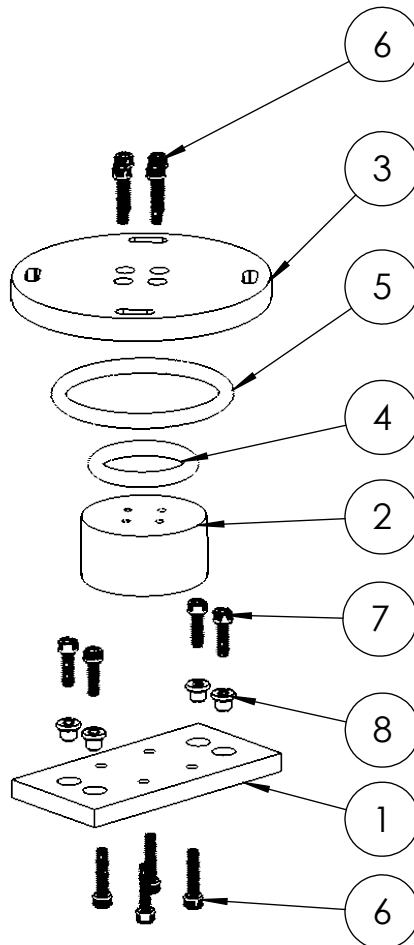
		UNLESS OTHERWISE SPECIFIED:			NAME	DATE	TITLE: heat_sink_assembly
		DIMENSIONS ARE IN INCHES TOLERANCES: FRACTIONAL \pm ANGULAR: MACH \pm BEND \pm TWO PLACE DECIMAL \pm THREE PLACE DECIMAL \pm		DRAWN			
		INTERPRET GEOMETRIC TOLERANCING PER:		CHECKED			
		MATERIAL		ENG APPR.			
		NEXT ASSY		MFG APPR.			
		USED ON		Q.A.			
		FINISH		COMMENTS:			
APPLICATION		DO NOT SCALE DRAWING		SIZE	DWG. NO.		REV
				A			
				SCALE: 1:1	WEIGHT:		SHEET 1 OF 2

2

1

B

A



ITEM NO.	PART NUMBER	DESCRIPTION	QTY.
1	heat_sink_contact_plate	Custom 6061-AL	1
2	heat_sink_middle	Custom 6061-AL	1
3	heat_sink_upper	Custom 6061-AL	1
4	9452K32	Oil-Resistant Buna-N O-Ring	1
5	9452K61	Oil-Resistant Buna-N O-Ring	1
6	91251A110	Black-Oxide Alloy Steel Socket Head Screw (4-40, L = 1/2")	8
7	91251A108	Black-Oxide Alloy Steel Socket Head Screw (4-40, L=3/8")	4
8	91145A129	Electrical-Insulating Nylon 6/6 Sleeve Washer (for #4 screws)	4

B

B

A

A

PROPRIETARY AND CONFIDENTIAL
THE INFORMATION CONTAINED IN THIS DRAWING IS THE SOLE PROPERTY OF <INSERT COMPANY NAME HERE>. ANY REPRODUCTION IN PART OR AS A WHOLE WITHOUT THE WRITTEN PERMISSION OF <INSERT COMPANY NAME HERE> IS PROHIBITED.

		UNLESS OTHERWISE SPECIFIED:		NAME	DATE	TITLE: heat_sink_assembly
		DIMENSIONS ARE IN INCHES	DRAWN			
		TOLERANCES:	CHECKED			
		FRACTIONAL \pm	ENG APPR.			
		ANGULAR: MACH \pm BEND \pm	MFG APPR.			
		TWO PLACE DECIMAL \pm	Q.A.			
		THREE PLACE DECIMAL \pm	COMMENTS:			
		INTERPRET GEOMETRIC TOLERANCING PER:				
		MATERIAL				
NEXT ASSY	USED ON	FINISH				
APPLICATION		DO NOT SCALE DRAWING				
SIZE	DWG. NO.		REV		A	
SCALE: 1:2	WEIGHT:		SHEET 2 OF 2			

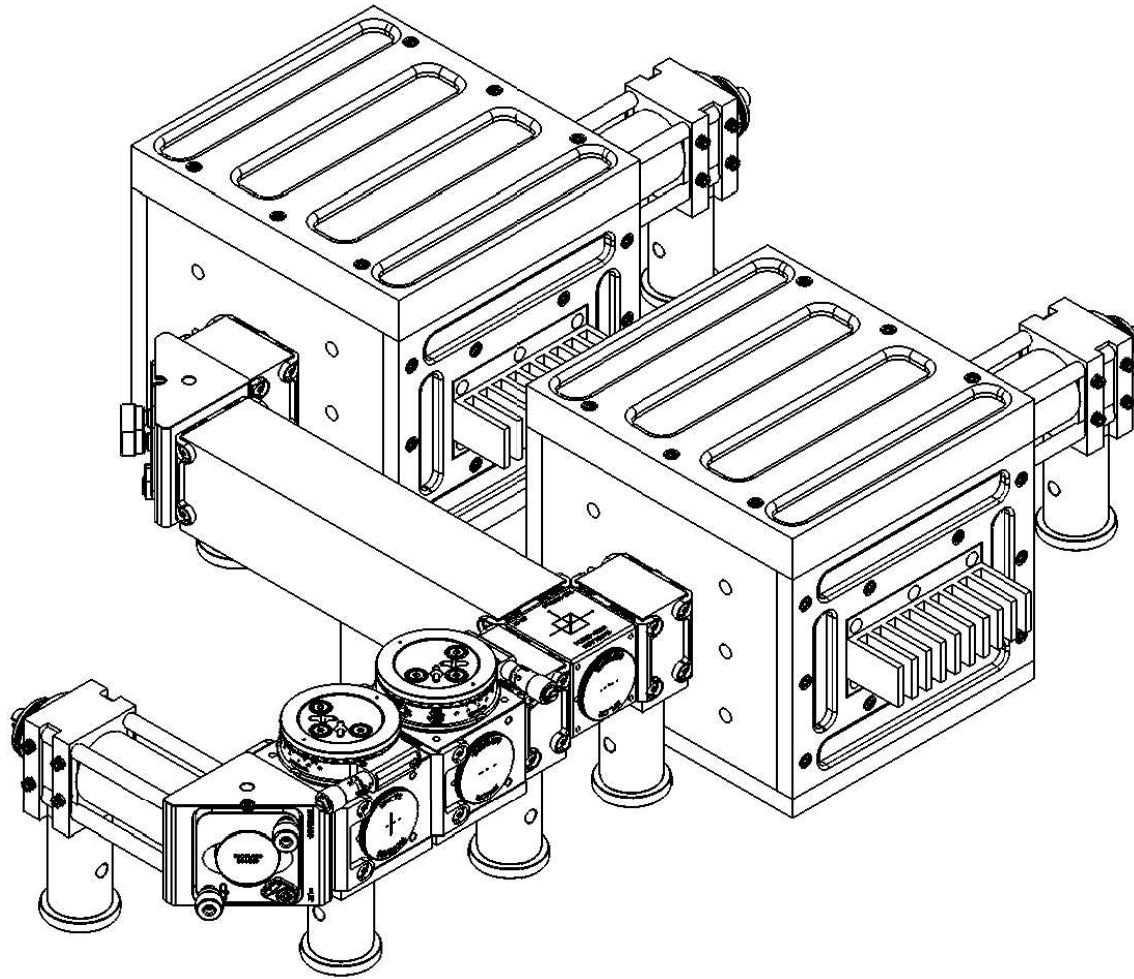
APPENDIX: SECOND-STAGE RECEIVER SOLIDWORKS DRAWINGS

2

1

B

B



A

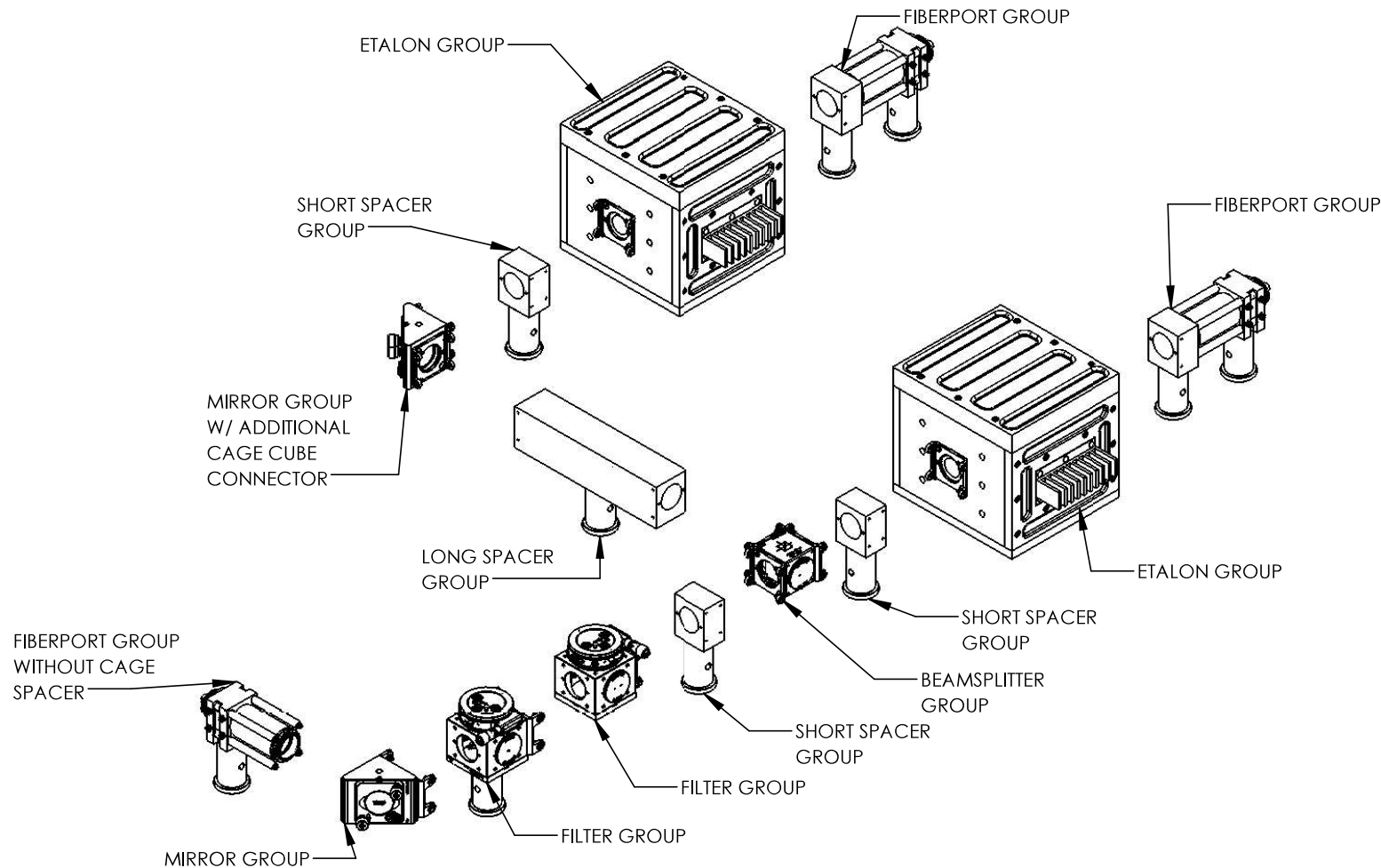
A

PROPRIETARY AND CONFIDENTIAL
 THE INFORMATION CONTAINED IN THIS DRAWING IS THE SOLE PROPERTY OF
 <INSERT COMPANY NAME HERE>. ANY
 REPRODUCTION IN PART OR AS A WHOLE
 WITHOUT THE WRITTEN PERMISSION OF
 <INSERT COMPANY NAME HERE> IS
 PROHIBITED.

		UNLESS OTHERWISE SPECIFIED:		NAME	DATE	TITLE: Receiver
		DIMENSIONS ARE IN INCHES	DRAWN			
		TOLERANCES:	CHECKED			
		FRACTIONAL \pm	ENG APPR.			
		ANGULAR: MACH \pm BEND \pm	MFG APPR.			
		TWO PLACE DECIMAL \pm	Q.A.			
		THREE PLACE DECIMAL \pm	COMMENTS:			
		INTERPRET GEOMETRIC TOLERANCING PER:				
		MATERIAL				
		NEXT ASSY	USED ON	FINISH		
	APPLICATION			DO NOT SCALE DRAWING		
SIZE	DWG. NO.					REV
A						
SCALE: 1:3	WEIGHT:					SHEET 1 OF 9

2

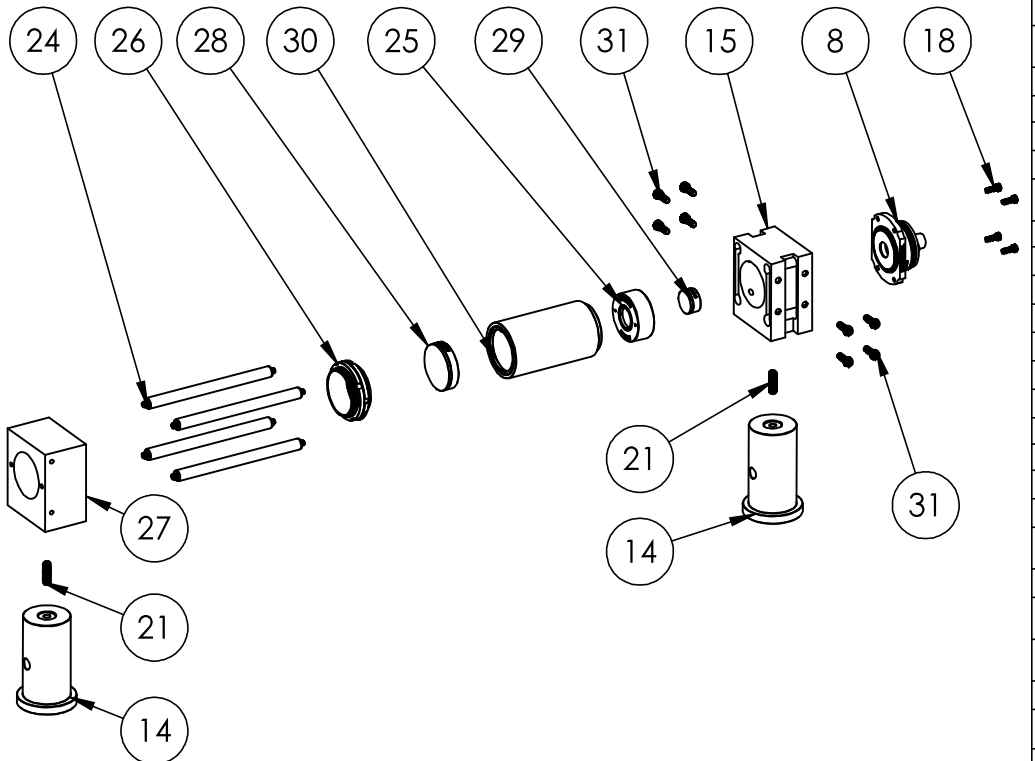
1



		UNLESS OTHERWISE SPECIFIED:		DRAWN	NAME	DATE	TITLE: Receiver				
		DIMENSIONS ARE IN INCHES TOLERANCES: FRACTIONAL \pm ANGULAR: MACH \pm BEND \pm TWO PLACE DECIMAL \pm THREE PLACE DECIMAL \pm									
		INTERPRET GEOMETRIC TOLERANCING PER: MATERIAL									
NEXT ASSY	USED ON	FINISH									
APPLICATION		DO NOT SCALE DRAWING									
SIZE		DWG. NO.									
A											
SCALE: 1:6		WEIGHT:		REV							
SHEET 2 OF 9											

PROPRIETARY AND CONFIDENTIAL
THE INFORMATION CONTAINED IN THIS
DRAWING IS THE SOLE PROPERTY OF
<INSERT COMPANY NAME HERE>. ANY
REPRODUCTION IN PART OR AS A WHOLE
WITHOUT THE WRITTEN PERMISSION OF
<INSERT COMPANY NAME HERE> IS
PROHIBITED.

FIBERPORT GROUP



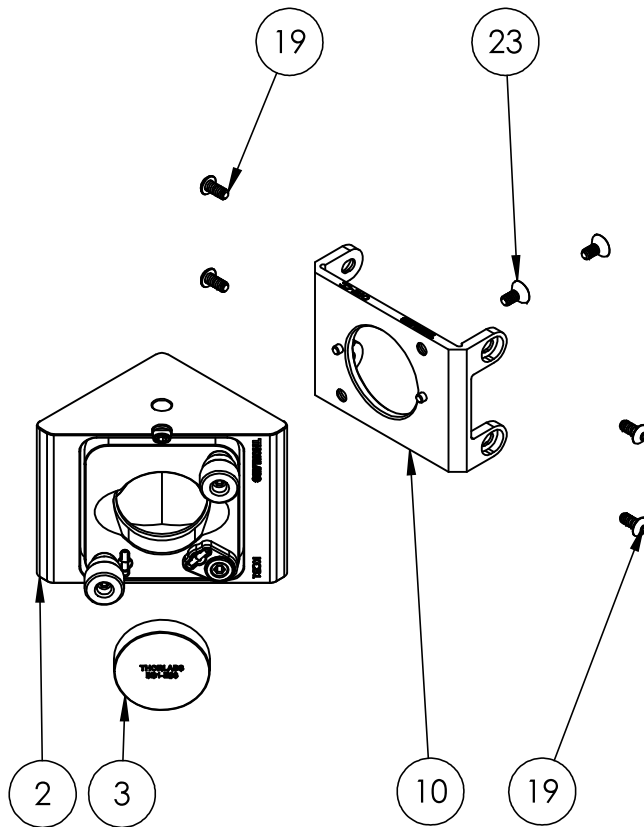
ITEM NO.	PART NUMBER	DESCRIPTION	QTY.
1	Temperature_Stabilized_Mount	Temperature-Stabilized Etalon Mount Assembly	2
2	KCB1-Solidworks	Right-Angle Kinematic Mirror Mount with Tapped Cage Rod Holes, 30 mm Cage System and SM1 Compatible, 8-32 and 1/4"-20 Mounting Holes	2
3	BB1-E03-Solidworks	Ø1" Broadband Dielectric Mirror, 750 - 1100 nm	2
4	CCM1-B\$014-Solidworks	30 mm Cage Cube-Mounted Non-Polarizing Beamsplitter, 700 - 1100 nm, 8-32 Tap	1
5	B4CRP-Thorlabs_Rotation_Stage	30 mm Cage Cube Precision Kinematic Rotation Platform	2
6	B5CT2-Solidworks	Ø1" Optic Mount with SM1-Threaded Bore for 30 mm Cage Cube, Mounts Optics up to 6.3 mm Thick	2
7	Alluxa_Filter	780.2-1 OD6 Ultra Narrow Bandpass Filter	2
8	PAF2A-11B-Solidworks	PAF2A-11B	3
9	C4W-Solidworks	30 mm Cage Cube	2
10	C4W-CC-Solidworks	THORLABS 30mm cage cube connector	2
11	CM1-CC-Solidworks	Cage Cube Connector for Compact 30 mm Cage Cubes	10
12	B1C-Solidworks	Blank Cover Plate	2
13	SM1CP2-Solidworks	Externally SM1-Threaded End Cap	5
14	RS2P8E-Solidworks	Ø1" Pedestal Pillar Post, 8-32 Taps, L = 2.5"	10
15	FiberPort_Cage_Adapter	Custom Aluminum	3
16	Cage_Spacer	Custom Aluminum	3
17	Cage_Spacer_Long	Custom Aluminum	1
18	91251A077	Black-Oxide Alloy Steel Socket Head Screw (2-56, L=1/4")	12
19	91255A106	Button Head Hex Drive Screw (4-40, L=1/4")	48
20	91255A103	Button Head Hex Drive Screw (4-40, L=1/8")	2
21	91375A194	Alloy Steel Cup-Point Set Screw (8-32, L=1/2")	10
22	91251A108	Black-Oxide Alloy Steel Socket Head Screw (4-40, L=3/8")	8
23	91253A106	Black-Oxide Alloy Steel Hex Drive Flat Head Screw (4-40, L=1/4")	24
24	ER3-Solidworks	Cage Assembly Rod, 3" Long, Ø6 mm	12
25	SM1A6T-Solidworks	Adapter with External SM1 Threads and Internal SM05 Threads: 0.40" Long	3
26	SM1T4-Solidworks	SM1 (1.035"-40) Coupler, External Threads, Fixed Shoulder and Locking Ring	3
27	Cube_to_Rod_Cage_Adapter	Custom Aluminum	2
28	AC254-045-B-Solidworks	f = 45.0 mm, Ø1" Achromatic Doublet, ARC: 650 - 1050 nm	3
29	ACN127-020-B-Solidworks	f = -20.0 mm, Ø1/2" Achromatic Doublet, ARC: 650 - 1050 nm	3
30	SM1L20-Solidworks	SM1 Lens Tube, 2.00" Thread Depth	3
31	91251A107	Black-Oxide Alloy Steel Socket Head Screw (4-40, L=5/16")	24

		UNLESS OTHERWISE SPECIFIED:	DRAWN	NAME	DATE	
		DIMENSIONS ARE IN INCHES TOLERANCES: FRACTIONAL \pm ANGULAR: MACH \pm BEND \pm TWO PLACE DECIMAL \pm THREE PLACE DECIMAL \pm				
		INTERPRET GEOMETRIC TOLERANCING PER: MATERIAL	CHECKED	TITLE:		
NEXT ASSY	USED ON	FINISH		Receiver		
APPLICATION		DO NOT SCALE DRAWING	ENG APPR.	MFG APPR.	Q.A.	
			COMMENTS:			

PROPRIETARY AND CONFIDENTIAL
THE INFORMATION CONTAINED IN THIS DRAWING IS THE SOLE PROPERTY OF <INSERT COMPANY NAME HERE>. ANY REPRODUCTION IN PART OR AS A WHOLE WITHOUT THE WRITTEN PERMISSION OF <INSERT COMPANY NAME HERE> IS PROHIBITED.

SIZE	DWG. NO.	REV
A		
SCALE: 1:4	WEIGHT:	SHEET 3 OF 9

MIRROR GROUP



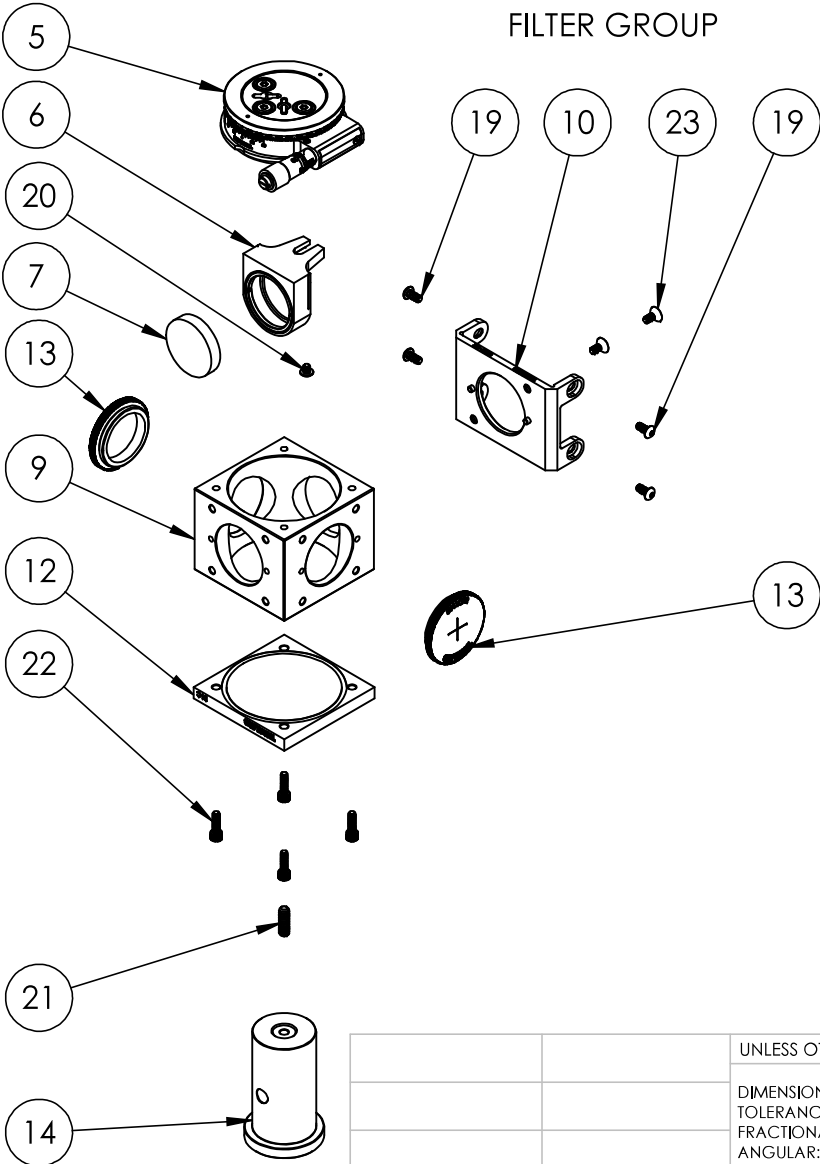
ITEM NO.	PART NUMBER	DESCRIPTION	QTY.
1	Temperature_Stabilized_Mount	Temperature-Stabilized Etalon Mount Assembly	2
2	KCB1-Solidworks	Right-Angle Kinematic Mirror Mount with Tapped Cage Rod Holes, 30 mm Cage System and SM1 Compatible, 8-32 and 1/4"-20 Mounting Holes	2
3	BB1-E03-Solidworks	Ø1" Broadband Dielectric Mirror, 750 - 1100 nm	2
4	CCM1-BS014-Solidworks	30 mm Cage Cube-Mounted Non-Polarizing Beamsplitter, 700 - 1100 nm; 8-32 Tap	1
5	B4CRP-Thorlabs_Rotation_Stage	30 mm Cage Cube Precision Kinematic Rotation Platform	2
6	B5CT2-Solidworks	Ø1" Optic Mount with SM1-Threaded Bore for 30 mm Cage Cube, Mounts Optics up to 6.3 mm Thick	2
7	Alluxa_Filter	780.2-1 OD6 Ultra Narrow Bandpass Filter	2
8	PAF2A-11B-Solidworks	PAF2A-11B	3
9	C4W-Solidworks	30 mm Cage Cube	2
10	C4W-CC-Solidworks	THORLABS 30mm cage cube connector	2
11	CM1-CC-Solidworks	Cage Cube Connector for Compact 30 mm Cage Cubes	10
12	B1C-Solidworks	Blank Cover Plate	2
13	SM1CP2-Solidworks	Externally SM1-Threaded End Cap	5
14	RS2P8E-Solidworks	Ø1" Pedestal Pillar Post, 8-32 Taps, L = 2.5"	10
15	FiberPort_Cage_Adapter	Custom Aluminum	3
16	Cage_Spacer	Custom Aluminum	3
17	Cage_Spacer_Long	Custom Aluminum	1
18	91251A077	Black-Oxide Alloy Steel Socket Head Screw (2-56, L=1/4")	12
19	91255A106	Button Head Hex Drive Screw (4-40, L=1/4")	48
20	91255A103	Button Head Hex Drive Screw (4-40, L=1/8")	2
21	91375A194	Alloy Steel Cup-Point Set Screw (8-32, L=1/2")	10
22	91251A108	Black-Oxide Alloy Steel Socket Head Flat Head Screw (4-40, L=3/8")	8
23	91253A106	Black-Oxide Alloy Steel Hex Drive Flat Head Screw (4-40, L=1/4")	24
24	ER3-Solidworks	Cage Assembly Rod, 3" Long, Ø6 mm	12
25	SM1A6T-Solidworks	Adapter with External SM1 Threads and Internal SM05 Threads, 0.40" Long	3
26	SM1T4-Solidworks	SM1 (1.035"-40) Coupler, External Threads, Fixed Shoulder and Locking Ring	3
27	Cube_to_Rod_Cage_Adapter	Custom Aluminum	2
28	AC254-045-B-Solidworks	f = 45.0 mm, Ø1" Achromatic Doublet, ARC: 650 - 1050 nm	3
29	ACN127-020-B-Solidworks	f = -20.0 mm, Ø1/2" Achromatic Doublet, ARC: 650 - 1050 nm	3
30	SM1L20-Solidworks	SM1 Lens Tube, 2.00" Thread Depth	3
31	91251A107	Black-Oxide Alloy Steel Socket Head Screw (4-40, L=5/16")	24

		UNLESS OTHERWISE SPECIFIED:		NAME	DATE	TITLE: Receiver
		DIMENSIONS ARE IN INCHES	DRAWN			
		TOLERANCES:	CHECKED			
		FRACTIONAL \pm	ENG APPR.			
		ANGULAR: MACH \pm BEND \pm	MFG APPR.			
		TWO PLACE DECIMAL \pm	Q.A.			
		THREE PLACE DECIMAL \pm	COMMENTS:			
		INTERPRET GEOMETRIC TOLERANCING PER:				
		MATERIAL				
NEXT ASSY	USED ON	FINISH				
APPLICATION		DO NOT SCALE DRAWING				

PROPRIETARY AND CONFIDENTIAL
THE INFORMATION CONTAINED IN THIS DRAWING IS THE SOLE PROPERTY OF
<INSERT COMPANY NAME HERE>. ANY
REPRODUCTION IN PART OR AS A WHOLE
WITHOUT THE WRITTEN PERMISSION OF
<INSERT COMPANY NAME HERE> IS
PROHIBITED.

SIZE DWG. NO. REV
A _____ REV
SCALE: 1:2 WEIGHT: SHEET 4 OF 9

FILTER GROUP



PROPRIETARY AND CONFIDENTIAL
THE INFORMATION CONTAINED IN THIS
DRAWING IS THE SOLE PROPERTY OF
<INSERT COMPANY NAME HERE>. ANY
REPRODUCTION IN PART OR AS A WHOLE
WITHOUT THE WRITTEN PERMISSION OF
<INSERT COMPANY NAME HERE> IS
PROHIBITED.

		UNLESS OTHERWISE SPECIFIED:			
		DIMENSIONS ARE IN INCHES			
		TOLERANCES:			
		FRACTIONAL \pm			
		ANGULAR: MACH \pm BEND \pm			
		TWO PLACE DECIMAL \pm			
		THREE PLACE DECIMAL \pm			
		INTERPRET GEOMETRIC TOLERANCING PER:			
		MATERIAL			
NEXT ASSY	USED ON	FINISH			
APPLICATION		DO NOT SCALE DRAWING			

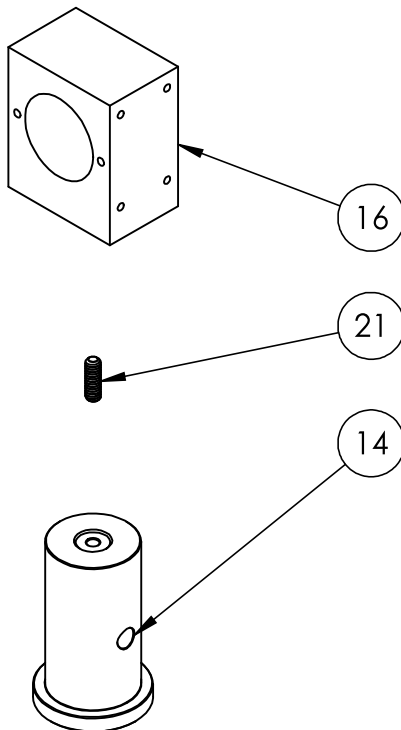
PART NUMBER	DESCRIPTION	QTY.
1	Temperature_Stabilized_Mount	2
2	KCB1-Solidworks	2
3	BB1-E03-Solidworks	2
4	CCM1-BS014-Solidworks	1
5	B4CRP-ThorLabs_Rotation_Stage	2
6	BSCT2-Solidworks	2
7	Alluxa_Filter	2
8	PAF2A-11B-Solidworks	3
9	C4W-Solidworks	2
10	C4W-CC-Solidworks	2
11	CM1-CC-Solidworks	10
12	B1C-Solidworks	2
13	SM1CP2-Solidworks	5
14	RS218E-Solidworks	10
15	FiberPort_Cage_Adapter	3
16	Cage_Spacer	3
17	Cage_Spacer_Long	1
18	91251A077	12
19	91255A106	48
20	91255A103	2
21	91375A194	10
22	91251A108	8
23	91253A106	24
24	ER3-Solidworks	12
25	SM1A6T-Solidworks	3
26	SM1T4-Solidworks	3
27	Cube_to_Rod_Cage_Adapter	2
28	AC254-045-B-Solidworks	3
29	ACN127-020-B-Solidworks	3
30	SM1L20-Solidworks	3
31	91251A107	24

TITLE:

Receiver

SIZE	DWG. NO.	REV
A		
SCALE: 1:3	WEIGHT:	SHEET 5 OF 9

SHORT SPACER GROUP

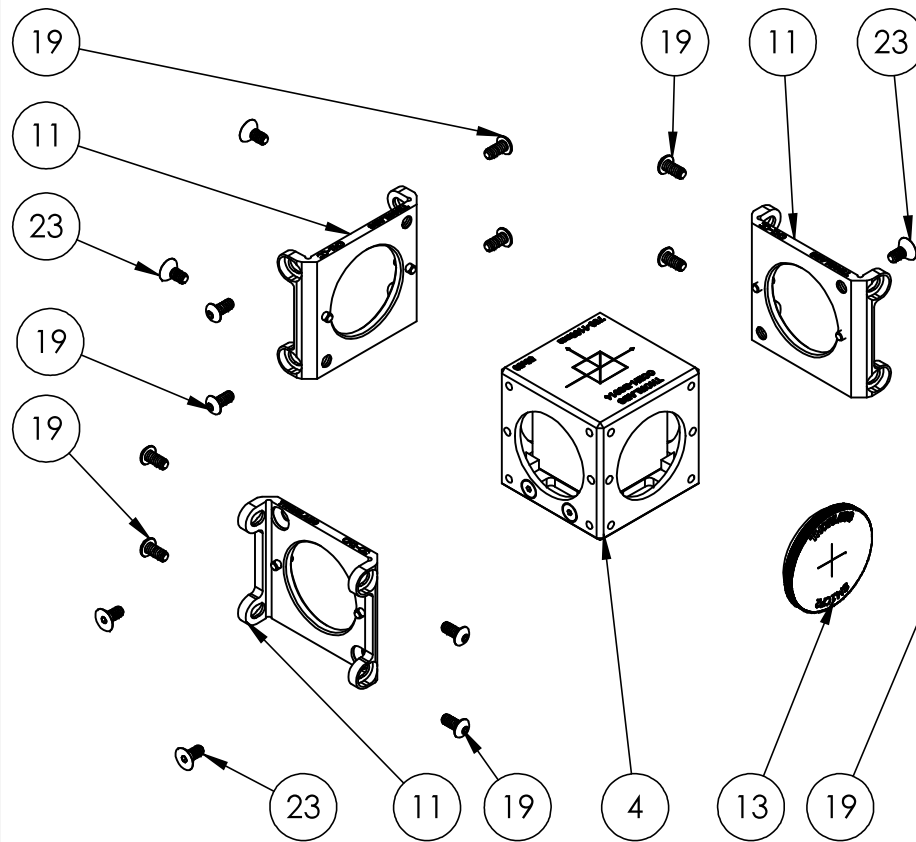


ITEM NO.	PART NUMBER	DESCRIPTION	QTY.
1	Temperature_Stabilized_Mount	Temperature-Stabilized Etalon Mount Assembly	2
2	KCB1-Solidworks	Right-Angle Kinematic Mirror Mount with Tapped Cage Rod Holes, 30 mm Cage System and SM1 Compatible, 8-32 and 1/4"-20 Mounting Holes	2
3	BB1-E03-Solidworks	Ø1" Broadband Dielectric Mirror, 750 - 1100 nm	2
4	CCM1-BS014-Solidworks	30 mm Cage Cube-Mounted Non-Polarizing Beamsplitter, 700 - 1100 nm, 8-32 Tap	1
5	B4CRP-Thorlabs_Rotation_Stage	30 mm Cage Cube Precision Kinematic Rotation Platform	2
6	B5CT2-Solidworks	Ø1" Optic Mount with SM1-Threaded Bore for 30 mm Cage Cube, Mounts Optics up to 6.3 mm Thick	2
7	Alluxa_Filter	780.2-1 OD6 Ultra Narrow Bandpass Filter	2
8	PAF2A-11B-Solidworks	PAF2A-11B	3
9	C4W-Solidworks	30 mm Cage Cube	2
10	C4W-CC-Solidworks	THORLABS 30mm cage cube connector	2
11	CM1-CC-Solidworks	Cage Cube Connector for Compact 30 mm Cage Cubes	10
12	B1C-Solidworks	Blank Cover Plate	2
13	SM1CP2-Solidworks	Externally SM1-Threaded End Cap	5
14	RS2P8E-Solidworks	Ø1" Pedestal Pillar Post, 8-32 Taps, L = 2.5"	10
15	FiberPort_Cage_Adapter	Custom Aluminum	3
16	Cage_Spacer	Custom Aluminum	3
17	Cage_Spacer_Long	Custom Aluminum	1
18	91251A077	Black-Oxide Alloy Steel Socket Head Screw (2-56, L=1/4")	12
19	91255A106	Button Head Hex Drive Screw (4-40, L=1/4")	48
20	91255A103	Button Head Hex Drive Screw (4-40, L=1/8")	2
21	91375A194	Alloy Steel Cup-Point Set Screw (8-32, L=1/2")	10
22	91251A108	Black-Oxide Alloy Steel Socket Head Screw (4-40, L=3/8")	8
23	91253A106	Black-Oxide Alloy Steel Hex Drive Flat Head Screw (4-40, L=1/4")	24
24	ER3-Solidworks	Cage Assembly Rod, 3" Long, Ø6 mm	12
25	SM1A6T-Solidworks	Adapter with External SM1 Threads and Internal SM05 Threads, 0.40" Long	3
26	SM1T4-Solidworks	SM1 (1.035"-40) Coupler, External Threads, Fixed Shoulder and Locking Ring	3
27	Cube_to_Rod_Cage_Adapter	Custom Aluminum	2
28	AC254-045-B-Solidworks	f = 45.0 mm, Ø1" Achromatic Doublet, ARC: 650 - 1050 nm	3
29	ACN127-020-B-Solidworks	f = -20.0 mm, Ø1/2" Achromatic Doublet, ARC: 650 - 1050 nm	3
30	SM1L20-Solidworks	SM1 Lens Tube, 2.00" Thread Depth	3
31	91251A107	Black-Oxide Alloy Steel Socket Head Screw (4-40, L=5/16")	24

		UNLESS OTHERWISE SPECIFIED:		NAME	DATE	TITLE: Receiver
		DIMENSIONS ARE IN INCHES	DRAWN			
		TOLERANCES:	CHECKED			
		FRACTIONAL \pm	ENG APPR.			
		ANGULAR: MACH \pm BEND \pm	MFG APPR.			
		TWO PLACE DECIMAL \pm	Q.A.			
		THREE PLACE DECIMAL \pm	COMMENTS:			
		INTERPRET GEOMETRIC TOLERANCING PER:				
		MATERIAL				
NEXT ASSY	USED ON	FINISH				
APPLICATION		DO NOT SCALE DRAWING				
SIZE	DWG. NO.		REV		A	
SCALE: 1:2	WEIGHT:		SHEET 6 OF 9			

PROPRIETARY AND CONFIDENTIAL
THE INFORMATION CONTAINED IN THIS DRAWING IS THE SOLE PROPERTY OF
<INSERT COMPANY NAME HERE>. ANY
REPRODUCTION IN PART OR AS A WHOLE
WITHOUT THE WRITTEN PERMISSION OF
<INSERT COMPANY NAME HERE> IS
PROHIBITED.

BEAMSPPLITTER GROUP



ITEM NO.	PART NUMBER	DESCRIPTION	QTY.
1	Temperature_Stabilized_Mount	Temperature-Stabilized Etalon Mount Assembly	2
2	KCB1-Solidworks	Right-Angle Kinematic Mirror Mount with Tapped Cage Rod Holes, 30 mm Cage System and SM1 Compatible, 8-32 and 1/4"-20 Mounting Holes	2
3	BB1-E03-Solidworks	Ø1" Broadband Dielectric Mirror, 750 - 1100 nm	2
4	CCM1-BS014-Solidworks	30 mm Cage Cube-Mounted Non-Polarizing Beamsplitter, 700 - 1100 nm, 8-32 Tap	1
5	B4CRP-Thorlabs_Rotation_Stage	30 mm Cage Cube Precision Kinematic Rotation Platform	2
6	B5CT2-Solidworks	Ø1" Optic Mount with SM1-Threaded Bore for 30 mm Cage Cube, Mounts Optics up to 6.3 mm Thick	2
7	Alluxa_Filter	780.2-1 OD6 Ultra Narrow Bandpass Filter	2
8	PAF2A-11B-Solidworks	PAF2A-11B	3
9	C4W-Solidworks	30 mm Cage Cube	2
10	C4W-CC-Solidworks	THORLABS 30mm cage cube connector	2
11	CM1-CC-Solidworks	Cage Cube Connector for Compact 30 mm Cage Cubes	10
12	B1C-Solidworks	Blank Cover Plate	2
13	SM1 CP2-Solidworks	Externally SM1-Threaded End Cap	5
14	RS2P8E-Solidworks	Ø1" Pedestal Pillar Post, 8-32 Taps, L = 2.5"	10
15	FiberPort_Cage_Adapter	Custom Aluminum	3
16	Cage_Spacer	Custom Aluminum	3
17	Cage_Spacer_Long	Custom Aluminum	1
18	91251A077	Black-Oxide Alloy Steel Socket Head Screw (2-56, L=1/4")	12
19	91255A106	Button Head Hex Drive Screw (4-40, L=1/4")	48
20	91255A103	Button Head Hex Drive Screw (4-40, L=1/8")	2
21	91375A194	Alloy Steel Cup-Point Set Screw (8-32, L=1/2")	10
22	91251A108	Black-Oxide Alloy Steel Socket Head Screw (4-40, L=3/8")	8
23	91253A106	Black-Oxide Alloy Steel Hex Drive Flat Head Screw (4-40, L=1/4")	24
24	ER3-Solidworks	Cage Assembly Rod, 3" Long, Ø6 mm	12
25	SM1A6T-Solidworks	Adapter with External SM1 Threads and Internal SM05 Threads, 0.40" Long	3
26	SM1T4-Solidworks	SM1 (1.035"-40) Coupler, External Threads, Fixed Shoulder and Locking Ring	3
27	Cube_to_Rod_Cage_Adapter	Custom Aluminum	2
28	AC254-045-B-Solidworks	f = 45.0 mm, Ø1" Achromatic Doublet, ARC: 650 - 1050 nm	3
29	ACN127-020-B-Solidworks	f = -20.0 mm, Ø1/2" Achromatic Doublet, ARC: 650 - 1050 nm	3
30	SM1L20-Solidworks	SM1 Lens Tube, 2.00" Thread Depth	3
31	91251A107	Black-Oxide Alloy Steel Socket Head Screw (4-40, L=5/16")	24

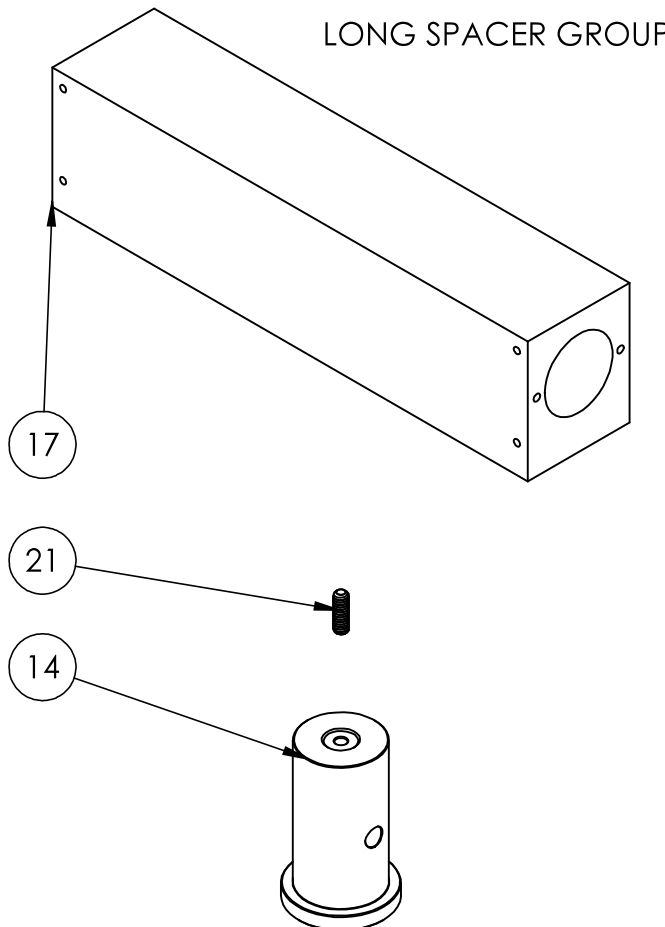
PROPRIETARY AND CONFIDENTIAL
THE INFORMATION CONTAINED IN THIS DRAWING IS THE SOLE PROPERTY OF
<INSERT COMPANY NAME HERE>. ANY
REPRODUCTION IN PART OR AS A WHOLE
WITHOUT THE WRITTEN PERMISSION OF
<INSERT COMPANY NAME HERE> IS
PROHIBITED.

UNLESS OTHERWISE SPECIFIED:			
DIMENSIONS ARE IN INCHES			
TOLERANCES:			
FRACTIONAL \pm			
ANGULAR: MACH \pm BEND \pm			
TWO PLACE DECIMAL \pm			
THREE PLACE DECIMAL \pm			
INTERPRET GEOMETRIC			
TOLERANCING PER:			
MATERIAL			
NEXT ASSY	USED ON	FINISH	
APPLICATION		DO NOT SCALE DRAWING	

TITLE:

Receiver

SIZE	DWG. NO.	REV
A		
SCALE: 1:2	WEIGHT:	SHEET 7 OF 9



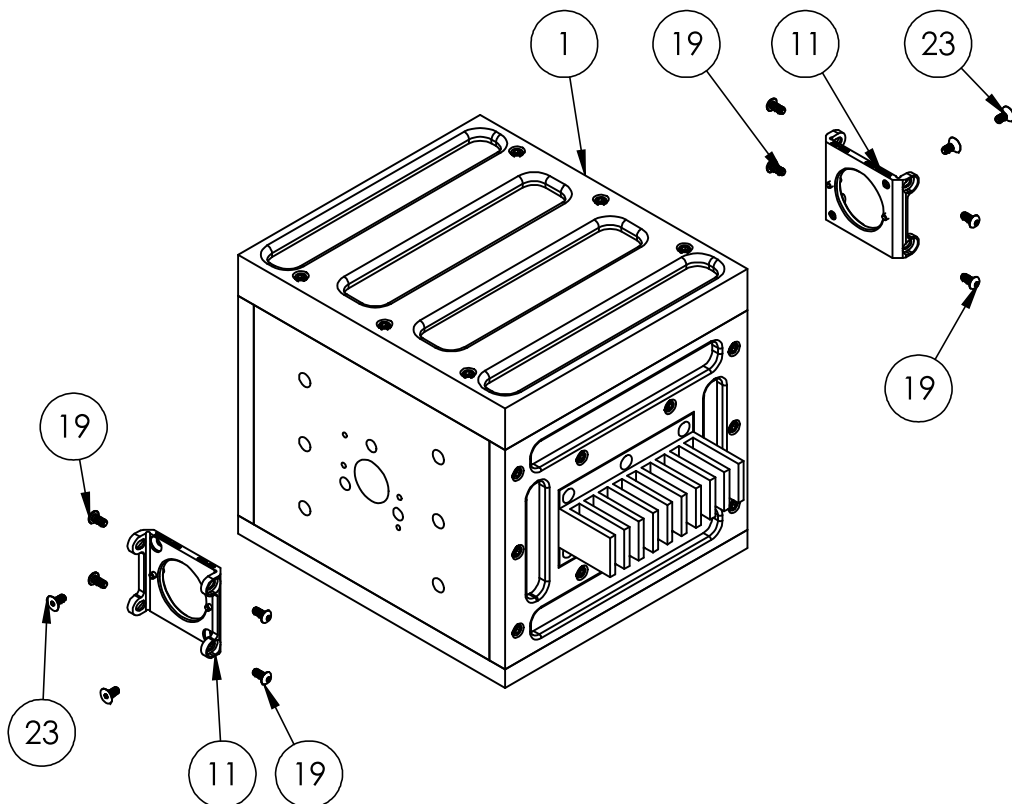
ITEM NO.	PART NUMBER	DESCRIPTION	QTY.
1	Temperature_Stabilized_Mount	Temperature-Stabilized Etalon Mount Assembly	2
2	KCB1-Solidworks	Right-Angle Kinematic Mirror Mount with Tapped Cage Rod Holes, 30 mm Cage System and SM1 Compatible, 8-32 and 1/4-20 Mounting Holes	2
3	BB1-E03-Solidworks	Ø1" Broadband Dielectric Mirror, 750 - 1100 nm	2
4	CCM1-BS014-Solidworks	30 mm Cage Cube-Mounted Non-Polarizing Beamsplitter, 700 - 1100 nm, 8-32 Tap	1
5	B4CRP-Thorlabs_Rotation_Stage	30 mm Cage Cube Precision Kinematic Rotation Platform	2
6	B5CT2-Solidworks	Ø1" Optic Mount with SM1-Threaded Bore for 30 mm Cage Cube, Mounts Optics up to 6.3 mm Thick	2
7	Alluxa_Filter	780.2-1 OD6 Ultra Narrow Bandpass Filter	2
8	PAF2A-11B-Solidworks	PAF2A-11B	3
9	C4W-Solidworks	30 mm Cage Cube	2
10	C4W-CC-Solidworks	THORLABS 30mm cage cube connector	2
11	CM1-CC-Solidworks	Cage Cube Connector for Compact 30 mm Cage Cubes	10
12	B1C-Solidworks	Blank Cover Plate	2
13	SM1CP2-Solidworks	Externally SM1-Threaded End Cap	5
14	RS2P8E-Solidworks	Ø1" Pedestal Pillar Post, 8-32 Taps, L= 2.5"	10
15	FiberPort_Cage_Adapter	Custom Aluminum	3
16	Cage_Spacer	Custom Aluminum	3
17	Cage_Spacer_Long	Custom Aluminum	1
18	91251A077	Black-Oxide Alloy Steel Socket Head Screw (2-56, L=1/4")	12
19	91255A106	Button Head Hex Drive Screw (4-40, L=1/4")	48
20	91255A103	Button Head Hex Drive Screw (4-40, L=1/8")	2
21	91375A194	Alloy Steel Cup-Point Set Screw (8-32, L=1/2")	10
22	91251A108	Black-Oxide Alloy Steel Socket Head Screw (4-40, L=3/8")	8
23	91253A106	Black-Oxide Alloy Steel Hex Drive Flat Head Screw (4-40, L=1/4")	24
24	ER3-Solidworks	Cage Assembly Rod, 3" Long, Ø6 mm	12
25	SM1A6T-Solidworks	Adapter with External SM1 Threads and Internal SM05 Threads, 0.40" Long	3
26	SM1T4-Solidworks	SM1 (1.035"-40) Coupler, External Threads, Fixed Shoulder and Locking Ring	3
27	Cube_to_Rod_Cage_Adapter	Custom Aluminum	2
28	AC254-045-B-Solidworks	f = 45.0 mm, Ø1" Achromatic Doublet, ARC: 650 - 1050 nm	3
29	ACN127-020-B-Solidworks	f = -20.0 mm, Ø1/2" Achromatic Doublet, ARC: 650 - 1050 nm	3
30	SM1L20-Solidworks	SM1 Lens Tube, 2.00" Thread Depth	3
31	91251A107	Black-Oxide Alloy Steel Socket Head Screw (4-40, L=5/16")	24

		UNLESS OTHERWISE SPECIFIED:		NAME	DATE	TITLE: Receiver
		DIMENSIONS ARE IN INCHES	DRAWN			
		TOLERANCES:	CHECKED			
		FRACTIONAL \pm	ENG APPR.			
		ANGULAR: MACH \pm BEND \pm	MFG APPR.			
		TWO PLACE DECIMAL \pm	Q.A.			
		THREE PLACE DECIMAL \pm	COMMENTS:			
		INTERPRET GEOMETRIC TOLERANCING PER:				
		MATERIAL				
NEXT ASSY	USED ON	FINISH				
APPLICATION		DO NOT SCALE DRAWING				

PROPRIETARY AND CONFIDENTIAL
THE INFORMATION CONTAINED IN THIS
DRAWING IS THE SOLE PROPERTY OF
<INSERT COMPANY NAME HERE>. ANY
REPRODUCTION IN PART OR AS A WHOLE
WITHOUT THE WRITTEN PERMISSION OF
<INSERT COMPANY NAME HERE> IS
PROHIBITED.

SIZE	DWG. NO.	REV
A		
SCALE: 1:2	WEIGHT:	SHEET 8 OF 9

ETALON GROUP



ITEM NO.	PART NUMBER	DESCRIPTION	QTY.
1	Temperature_Stabilized_Mount	Temperature-Stabilized Etalon Mount Assembly	2
2	KCB1-Solidworks	Right-Angle Kinematic Mirror Mount with Tapped Cage Rod Holes, 30 mm Cage System and SM1 Compatible, 8-32 and 1/4"-20 Mounting Holes	2
3	BB1-E03-Solidworks	Ø1" Broadband Dielectric Mirror, 750 - 1100 nm	2
4	CCM1-B8014-Solidworks	30 mm Cage Cube-Mounted Non-Polarizing Beamsplitter, 700 - 1100 nm, 8-32 Tap	1
5	B4CRP-Thorlabs_Rotation_Stage	30 mm Cage Cube Precision Kinematic Rotation Platform	2
6	B5CT2-Solidworks	Ø1" Optic Mount with SM1-Threaded Bore for 30 mm Cage Cube, Mounts Optics up to 6.3 mm Thick	2
7	Alluxa_Filter	780.2-1 OD6 Ultra Narrow Bandpass Filter	2
8	PAF2A-11B-Solidworks	PAF2A-11B	3
9	C4W-Solidworks	30 mm Cage Cube	2
10	C4W-CC-Solidworks	THORLABS 30mm cage cube conector	2
11	CM1-CC-Solidworks	Cage Cube Connector for Compact 30 mm Cage Cubes	10
12	B1C-Solidworks	Blank Cover Plate	2
13	SM1CP2-Solidworks	Externally SM1-Threaded End Cap	5
14	RS2P8E-Solidworks	Ø1" Pedestal Pillar Post, 8-32 Taps, L = 2.5"	10
15	FiberPort_Cage_Adapter	Custom Aluminum	3
16	Cage_Spacer	Custom Aluminum	3
17	Cage_Spacer_Long	Custom Aluminum	1
18	91251A077	Black-Oxide Alloy Steel Socket Head Screw (2-56, L=1/4")	12
19	91255A106	Button Head Hex Drive Screw (4-40, L=1/4")	48
20	91255A103	Button Head Hex Drive Screw (4-40, L=1/8")	2
21	91375A194	Alloy Steel Cup-Point Set Screw (8-32, L=1/2")	10
22	91251A108	Black-Oxide Alloy Steel Socket Head Screw (4-40, L=3/8")	8
23	91253A106	Black-Oxide Alloy Steel Hex Drive Flat Head Screw (4-40, L=1/4")	24
24	ER3-Solidworks	Cage Assembly Rod, 3" Long, Ø6 mm	12
25	SM1A6T-Solidworks	Adapter with External SM1 Threads and Internal SM05 Threads, 0.40" Long	3
26	SM1T4-Solidworks	SM1 (1.035"-40) Coupler, External Threads, Fixed Shoulder and Locking Ring	3
27	Cube_to_Rod_Cage_Adapter	Custom Aluminum	2
28	AC254-045-B-Solidworks	f = 45.0 mm, Ø1" Achromatic Doublet, ARC: 650 - 1050 nm	3
29	ACN127-020-B-Solidworks	f = -20.0 mm, Ø1/2" Achromatic Doublet, ARC: 650 - 1050 nm	3
30	SM1L20-Solidworks	SM1 Lens Tube, 2.00" Thread Depth	3
31	91251A107	Black-Oxide Alloy Steel Socket Head Screw (4-40, L=5/16")	24

		UNLESS OTHERWISE SPECIFIED:	NAME	DATE	TITLE: Receiver
		DIMENSIONS ARE IN INCHES			
		TOLERANCES:			
		FRACTIONAL \pm			
		ANGULAR: MACH \pm BEND \pm			
		TWO PLACE DECIMAL \pm			
		THREE PLACE DECIMAL \pm			
		INTERPRET GEOMETRIC TOLERANCING PER:			
		MATERIAL			
NEXT ASSY	USED ON	FINISH			
APPLICATION		DO NOT SCALE DRAWING			

PROPRIETARY AND CONFIDENTIAL
THE INFORMATION CONTAINED IN THIS DRAWING IS THE SOLE PROPERTY OF
<INSERT COMPANY NAME HERE>. ANY
REPRODUCTION IN PART OR AS A WHOLE
WITHOUT THE WRITTEN PERMISSION OF
<INSERT COMPANY NAME HERE> IS
PROHIBITED.

SIZE	DWG. NO.	REV
A		
SCALE: 1:3		WEIGHT:
		SHEET 9 OF 9